Politecnico di Torino

Corso di Laurea
A.a. 2025/2026
Sessione di Laurea Aprile 2026

Atmospheric Pressure Plasma Synthesis of Pyrrole-Based Nanoparticles with Potential Biomedical Applications

Relatori:
De Geyter Nathalie
Morent Rino
Mattu Clara

Candidati:
Mannu Lavinia

Aknowledgements

Un sentito ringraziamento alla Prof.ssa Mattu, per la disponibilità e il sostegno offerti durante il mio percorso universitario. Il suo insegnamento mi ha permesso di appassionarmi al tema, consentendomi una crescita sia personale che accademica.

I am deeply grateful to Prof. dr. ir. Nathalie De Geyter and Prof. dr. Rino Morent from Ugent for granting me the opportunity to undertake this thesis project, which has truly captured my interest and passion. Their availability and support throughout the process have been greatly appreciated and made this experience all the more enriching.

My heartfelt thanks go to my supervisor, Tinea Jelinek, whose expertise and guidance have been a constant source of direction and motivation. Her encouragement and unwavering support have inspired me to push my limits and give my very best at every stage of this journey.

I am also profoundly thankful to my family and friends for their continuous support, patience, and belief in me. Their presence has been a pillar of strength and an invaluable part of this academic and personal journey.

Permission for usage

Date:

Signature:

Declaration on the use of AI Tools

Artificial intelligence tools, specifically ChatGPT by OpenAI, were used during the writing of this thesis exclusively to improve the linguistic clarity and style of the English text. No scientific content, data interpretation, or original ideas were generated by the AI; all content and conclusions are the result of the author's own work.

Abstract — **The development of eco-friendly synthesis routes for biocompatible nanoparticles is of growing interest in biomedical research. This thesis aims to explore the use of a non-thermal Atmospheric Pressure Plasma Jet array (APPJ-array) device for the synthesis of pyrrole-based nanoparticles (NPs), investigating the influence of precursor flow rate, capillary-to-substrate distance, and voltage on: particle morphology, size distribution, and surface composition. Scanning electron microscopy analysis revealed that low flow rates, reduced distances, and moderate voltages lead to more uniform and spherical nanoparticle formation, while excessive values resulted in irregular aggregation of the NPs. FTIR and XPS demonstrated the presence of characteristic chemical groups of polypyrrole, such as C=C and N–H bonds, and suggested partial surface oxidation, likely due to interaction with reactive plasma species. OES provided insight into the plasma phase, highlighting the presence of excited nitrogen and oxygen species, which may play a role in NP surface modification. The synthesized NPs show promising physicochemical characteristics (such as nanoscale size, spherical shape, and surface chemistry) that make them candidates for further exploration in biomedical contexts. Overall, this study demonstrates that APPJ-array-assisted synthesis offers a rapid, solvent-free, and customizable route to produce pyrrole-based nanoparticles under ambient conditions. The findings provide a basis for future investigations into the biological performance of these materials, including cytocompatibility, functionalization strategies, and therapeutic integration.**

Keywords — Atmospheric Pressure Plasma Jet-array, Biomedical Applications, Pyrrole-based Nanoparticles, Eco-friendly Synthesis.

Atmospheric Pressure Plasma Synthesis of Pyrrole-Based Nanoparticles With Potential Biomedical Applications

Lavinia Mannu

Supervisors: Prof. dr. ir. Nathalie De Geyter, Prof. dr. Rino Morent, Prof. dr. ir. Mattu Clara

Counsellor: Jasna-Tinea Jelinek

***Abstract*— In this thesis, an eco-friendly approach for the synthesis of pyrrole-based nanoparticles (NPs) with potential biomedical applications is investigated using a non-thermal Atmospheric Pressure Plasma Jet (APPJ) - array. The study focuses on how precursor flow rate, capillaries-to-substrate distance, and peak-to-peak voltage influence the morphology and surface chemistry of the NPs. Findings reveal that lower flow rates, shorter distances, and moderate voltages promote the formation of spherical NPs, whereas higher values of the given parameters lead to irregular aggregation. Fourier Transform Infrared Spectroscopy (FTIR) and X-ray Photoelectron Spectroscopy (XPS) analyses confirm the incorporation of functional chemical groups. Optical Emission Spectroscopy (OES) allows for the identification of key species within the plasma, such as excited nitrogen and oxygen, which correspond to the surface composition of the NPs. The resulting pyrrole-based NPs, with controlled size and surface properties, show strong potential for biomedical applications in drug delivery, tissue engineering, and antibacterial treatments. This work demonstrates that this way of synthesis is a clean, scalable, and versatile method to produce functionalized organic nanoparticles, overcoming some of the limitations associated to traditional synthesis methods.**

***Keywords*— Atmospheric Pressure Plasma Jet Array, Biomedical Applications, Pyrrole-based Nanoparticles.**

INTRODUCTION

Nanotechnology offers new opportunities in biomedical applications through the use of nanoparticles (NPs) with high surface-to-volume ratios, tunable surface properties, and controlled compositions [1]. These properties enable their use in targeted drug delivery, regenerative medicine, biosensing, and diagnostic imaging [2], [3]. In particular, the development of organic polymer-based nanoparticles provides a biocompatible and often biodegradable alternative to inorganic systems. Among these, polypyrrole (PPy), a conductive polymer, has garnered significant attention due to its unique combination of chemical stability, electrical conductivity, and biocompatibility [4], [5].

PPy nanoparticles are of particular interest in the field of photothermal therapy, where they convert near-infrared (NIR) light into heat, inducing localized hyperthermia for cancer ablation [6]. They have also demonstrated potential in photoacoustic imaging, enabling deep tissue visualization with high contrast [7], and in biosensing, for instance through their use in highly selective hormone detection platforms [8]. Despite their promising applications, conventional methods for synthesizing PPy nanoparticles often involve toxic solvents, complex multistep reactions, and post-synthesis functionalization steps that limit scalability and clinical translation [9].

In this context, plasma-based techniques, especially Atmospheric Pressure Plasma (APP), have emerged as a clean, solvent-free alternative, capable of producing functional nanoparticles under ambient conditions [10]. APP systems can simultaneously initiate polymerization and deposit nanoparticles directly on a substrate, allowing for in-situ surface functionalization. By modulating plasma parameters, such as gas composition, input voltage, flow rates, and substrate distance, researchers can precisely control nanoparticle size, morphology, and surface chemistry [11].

This study explores the synthesis of pyrrole-based nanoparticles using a custom-built Atmospheric Pressure Plasma Jet (APPJ) array device. The objective is to investigate the influence of three key process parameters such as precursor flow rate, distance from the jet to the substrate, and peak-to-peak voltage on the morphological and chemical properties of the resulting nanoparticles. The ultimate goal is to establish an efficient, reproducible, and environmentally sustainable method for generating pyrrole-based nanoparticles tailored for biomedical applications.

MATERIALS & METHODS

A. Single electrode APPJ array

The device used consists of seven quartz capillaries, each with a length of 7 cm, an inner diameter of 1 mm, and an outer diameter of 3 mm, enclosed in a quartz glass tube, 10 cm in length with an inner diameter of 3 cm, as shown in Figure 1. It includes a high voltage electrode connected to a custom-made alternating current (AC) power supply, precursor/bubbling gas tube, and a discharge gas tube.

For precise control of the bubbling and discharge gas flows, two separate mass flow controllers (Bronkhorst) were

employed. The mass flow controller for the discharge gas has a maximum flow rate of 500 standard cubic centimeters per minute (sccm), while the one for the bubbling gas has a maximum flow rate of 10 standard liters per minute (slm).

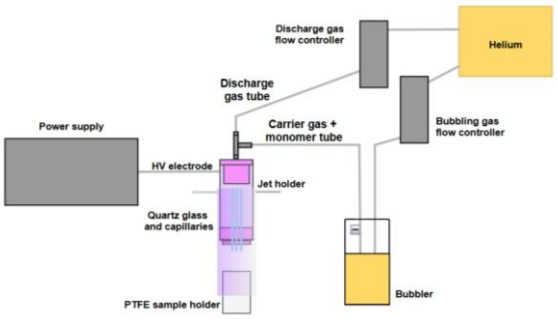

Figure 1: Schematic representation of the employed APPJ array

The precursor vapor is generated by passing the bubbling gas, same as the discharge gas, through a precursor-containing bubbler, mixing the vaporized precursor with the bubbling gas. Inside the plasma-containing capillaries, energetic species from the plasma break the precursor's chemical bonds, creating reactive radicals. These radicals recombine to start polymerization, forming oligomers and, if abundant, nanoparticles that grow by precursor addition or fusion [12].

B. *Surface characterization*

The morphological analysis and size distribution of the synthesized nanoparticles were carried out using a scanning electron microscope (JEOL JSM-6010PLUS). SEM images were acquired from both top-view and cross-sectional perspectives at magnifications of 7000x and 10,000x, respectively. Prior to imaging, the samples were sputter-coated with a thin gold layer using a JFC-130 coater to improve conductivity and avoid charging effects. The analysis was conducted at accelerating voltages of 5 or 7 kV to ensure optimal resolution. Particle size distribution was evaluated using ImageJ software, measuring at least 100 nanoparticles across multiple sample areas to ensure statistical relevance.

Chemical characterization was performed through Fourier-Transform Infrared Spectroscopy (FTIR) using a Bruker Tensor 27 spectrometer with a ZnSe ATR crystal. To prevent crystal damage, the nanoparticles were deposited onto a 0.18 mm low-density polyethylene (LDPE) film.The FTIR spectra enabled the identification of functional groups, providing insight into the chemical structure of the synthetized nanoparticles.

Surface chemical composition was further investigated by X-ray Photoelectron Spectroscopy (XPS), conducted with a PHI 5000 Versaprobe II system using a monochromatic Al Kα source (1486.6 eV, 50 W). Survey scans were performed at a pass energy of 187.85 eV to detect key elements (C1s, N1s, O1s). Data was analyzed with Multipak software based on relative sensitivity factors, averaging results from six different locations on each sample to account for surface variability.

Finally, Optical Emission Spectroscopy (OES) was employed to examine the reactive species generated during plasma discharge using an Ocean Optics S2000 spectrometer (1.4 nm resolution, 200–900 nm range). Three configurations were analyzed: (1) helium plasma alone, (2) helium plasma with a cylindrical polytetrafluoroethylene (PTFE) sample holder (24 mm diameter), and (3) helium plasma with pyrrole injection. The optical fiber was placed ~1 cm from the discharge center. Emission lines corresponding to excited helium, nitrogen species, and fragments from pyrrole breakdown were identified, offering insights into plasma chemistry and discharge dynamics during nanoparticle formation.

C. *Sample preparation*

For all experimental sets, both the discharge and carrier gases were helium (Air Liquide-Alphagaz 1, 99.999% purity), while the precursor was pyrrole (Sigma-Aldrich, reagent grade, 98%). The substrate used for all experiments, except for the FTIR analysis, was standard microscope glass slides, a dielectric material, circular, with a diameter of 25 mm.

D. *Varied experimental conditions.*

The samples were prepared by varying one parameter at a time while keeping the others constant. First, the ratio between the discharge gas and the carrier gas containing pyrrole was adjusted, maintaining a total gas flow of 2 slm, as shown in Table 1. For all conditions in this set, the input voltage was fixed at 9 kV, the distance from the capillaries to the substrate was set at 5 cm, and the deposition time was 60 seconds.

Table 1: Tested ratios between discharge gas and precursor+carrier gas flows

Monomer + carrier gas flow rate (sccm)	Discharge gas flow rate (slm)
10	1.99
25	1.975
50	1.95
100	1.90
150	1.85
200	1.80
250	1.75
300	1.70
350	1.65
400	1.60
450	1.55
500	1.50

The conditions that resulted in the formation of nanoparticles, rather than continuous films, and produced size distributions closest to the 1–100 nm range were selected for further testing.

Next, the distance between the capillaries and the substrate was varied from 3 to 7 cm, while maintaining the input voltage at 9 kV and the deposition time at 60 seconds.

Finally, after identifying the optimal combination of monomer flow and distance (one for each flow condition), the effect of input voltage was investigated, ranging from 6 to 10 kV, with 6 kV being the minimum required to sustain plasma.

RESULTS & DISCUSSION

A. *Nanoparticles morphology*

1) *Influence of the monomer flow*

The first investigated condition involved varying the ratio between the discharge gas and the precursor flow, keeping the total flow constant at 2 standard litres per minute (slm). Other parameters such as input voltage were kept constant at 9 kV. The distance between the tips of the capillaries and the substrate was fixed at 5 cm. The reaction was carried out for 60 s. Figure 2 shows the results of the nanoparticles size distribution using different pyrrole precursor flow rates.

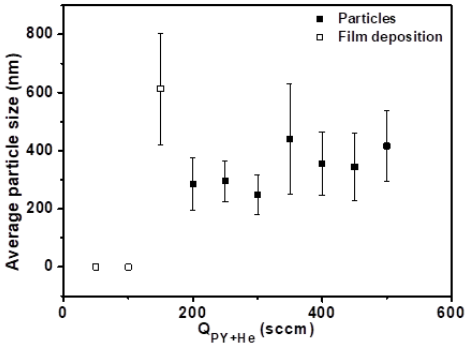

Figure 2: Size distribution of nanoparticles using precursor+bubbling gas flow rates

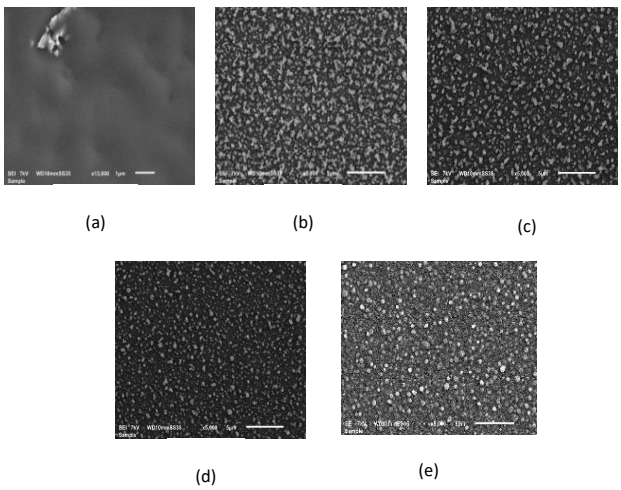

Figure 3: SEM images of He 1.900 slm Q_{py+he} 100 sccm (a), He 1.800 slm Q_{py+he} 200 sccm (b), He 1.750 slm Q_{py+he} 250 sccm (c), He 1.700 slm Q_{py+he} 300 sccm (d), He 1.600 slm Q_{py+he} 400 sccm (e)

At very low precursor flows (50–100 sccm), no nanoparticles were observed; instead, uniform films formed on the substrate (Fig. 2(a)). This is attributed to the insufficient radical concentration generated at low monomer levels, which inhibits nucleation and promotes direct film deposition. These findings align with the XPS analysis by Gomez et al. [13], who showed that crosslinking in plasma-polymerized pyrrole requires adequate radical density, enabled by sufficient monomer concentration and dehydrogenation energy.

At higher precursor flows (350–500 sccm), radical concentration increases significantly, accelerating nucleation and leading to the formation of clusters and aggregates (Fig. 2(e)). This condition results in larger average nanoparticle diameters. Heredia-Rivera et al. [14] similarly reported that higher precursor concentrations enhance crosslinking and conjugation length in PPy, indicating more intense polymerization. However, excessive precursor also leads to lower energy per molecule due to plasma energy distribution, reducing fragmentation efficiency and potentially causing incomplete reactions, as noted by Friedrich [15].

The optimal balance was observed at intermediate precursor flows (200–300 sccm), which yielded smaller and well-dispersed nanoparticles (Fig. 2(b), 2(c), 2(d)). At these concentrations, radical density is sufficient to support nucleation without triggering excessive aggregation. This trend is consistent with findings by Liang et al. [16], who showed that intermediate oxidant levels in chemical PPy synthesis lead to more controlled and uniform nanostructures. Overall, an optimal precursor-to-carrier gas ratio exists that promotes effective nucleation and controlled nanoparticle growth.

2) *Influence of the distance from the capillaries to the substrate*

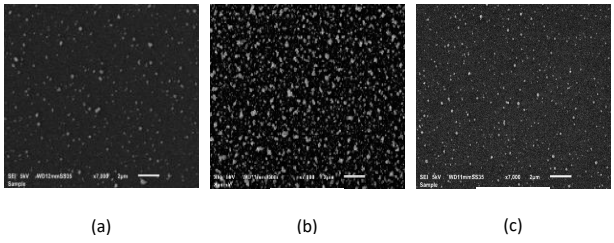

Figure 4: SEM images of the best results obtained by varying the distance (He 1.800 slm Q_{py+he} 200 sccm – 5 cm (a), He 1.750 slm Q_{py+he} 250 sccm – 3 cm (b), He 1.700 slm Q_{py+he} 300 sccm – 4 cm (c)).

The study of different capillary–substrate distances (3–7 cm) at three pyrrole flow rates (300, 250, and 200 sccm) demonstrated that this parameter critically affects nanoparticle size. At short distances (3 cm), limited residence time in the plasma restricts crosslinking and favors early deposition of small nuclei, as described by Friedrich [15]. Intermediate distances (4–6 cm) allow more growth due to longer exposure, but reduced plasma energy leads to larger, less uniform particles, consistent with Dufour's CAP model [17]. At 7 cm, with the substrate outside the quartz tube, oxygen from ambient air quenches reactive species, drastically lowering deposition and particle size, similar to Kautz's findings on oxygen effects in laser ablation [18]. Particles from 250 sccm flows were generally smaller than those from 300 sccm, likely due to higher discharge gas velocity enhancing radical formation and nucleation, in line

with Müller's observations [19]. Under 200 sccm, lower monomer availability increased sensitivity to distance changes: small variations produced significant size shifts, echoing Kadhem's results under monomer-limited regimes [20]. Overall, plasma energy, residence time, and precursor concentration together define a balance between nucleation and growth, which governs nanoparticle morphology. Figure 4 shows the SEM images of the optimal distance for each different pyrrole flow rate (5 cm for Q_{py+he} 200 sccm, 3 cm for Q_{py+he} 250 sccm and 4 cm for Q_{py+he} 300 sccm).

3) *Influence of the input voltage*

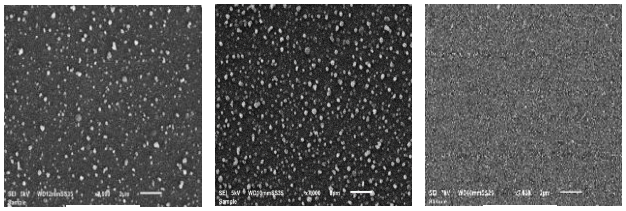

(a) (b) (c)

Figure 5: SEM images of the best results obtained by varying the input voltage (He 1.800 slm Q_{py+he} 200 sccm – 5 cm – 7 kV (a), He 1.750 slm Q_{py+he} 250 sccm – 3 cm – 7 kV (b), He 1.700 slm Q_{py+he} 300 sccm – 4 cm – 6 kV (c))

Across all tested conditions, increasing the input voltage led to a consistent rise in average nanoparticle size, confirming a strong link between plasma energy and nanoparticle growth. Higher input voltage enhances the electric field, which increases the energy transferred to the plasma and boosts the generation of reactive species. As shown by Yasuda [21] and Wang [22], this favors monomer fragmentation and radical formation but also promotes growth over nucleation, as existing nuclei have more energy and time to grow before new ones are formed. SEM images at high voltages also revealed cluster formation, likely due to particle aggregation or partial melting caused by excessive heat. This is supported by the work of Xu et al. [23], who reported that increased electron density and temperature under strong electric fields enhance plasma reactivity and heat transfer, leading to conditions that can promote both particle enlargement and agglomeration. Figure 5 shows the SEM images of the optimal input flow for each different pyrrole flow rate (7 kV for Q_{py+he} 200 sccm, 7 kV for Q_{py+he} 250 sccm and 6 kV for Q_{py+he} 300 sccm).

B. *Chemical Structure (FTIR)*

1) *Optimal precursor flows*

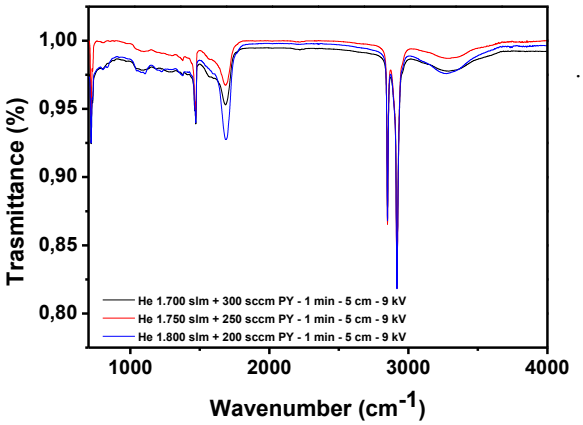

Figure 6: FTIR spectra under the best precursor flow conditions

The FTIR spectra of pyrrole-based nanoparticles synthesized at precursor flow rates between 200 and 300 sccm (Fig. 6) showed the presence of the characteristic absorption bands of LDPE at 2917, 2850, 1471, and 718 cm^{-1}, corresponding to CH_2 stretching and deformation modes [24]. Upon introducing pyrrole, new bands appeared, including 3284 cm^{-1} (N–H stretching) and 1685 cm^{-1} (C=C in-plane stretching) [25], [26]. A shoulder at 1570 cm^{-1} indicated C–C/C=C interchain crosslinking, and a peak at 1069 cm^{-1} was assigned to C–H in-plane bending in the pyrrole ring [26]. Across all flow conditions, the main PPy bands were consistently observed, suggesting no substantial chemical differences between samples. At 1.800 slm He + 200 sccm PY, increased intensity at 1685 cm^{-1} and new peaks at 801 cm^{-1} (associated with open-ring or alkene structures) and 1369 cm^{-1} (C–N stretching) were noted [27], [28], likely due to plasma-induced fragmentation and structural rearrangements. These results indicate that minor variations in precursor flow do not significantly affect the chemical composition, and that the APP process enables stable and reproducible surface chemistry in PPy nanoparticle synthesis.

2) *Optimal precursor flows and distances from the capillaries to the substrate*

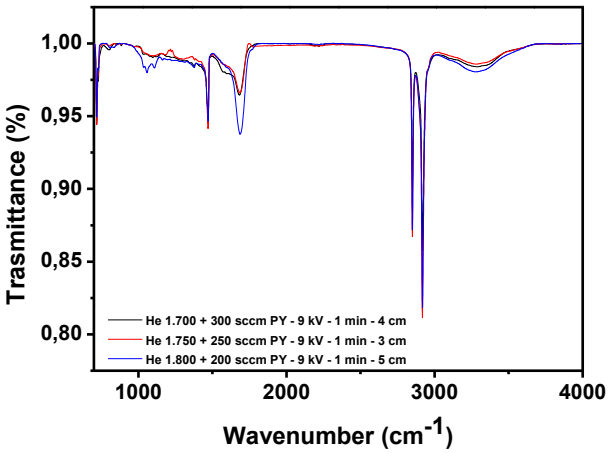

Figure 7: FTIR spectra at the optimal distance for each precursor flow rate.

FTIR spectra acquired at the optimal distances for each flow condition (4 cm for 300 sccm, 3 cm for 250 sccm, and 5 cm for 200 sccm PY, Fig. 7) revealed consistent chemical profiles, with clear bands from both the PE substrate (2917, 2850, 1471, 718 cm^{-1}) and PPy-related peaks (3284, 1685, 1570, 1069 cm^{-1}). At 300 sccm – 4 cm, the weak peak at 801 cm^{-1} suggests the presence of alkene or ring-opened structures [27] However, the relatively low intensity of most PPy-related peaks may reflect a lower deposition yield or plasma-induced fragmentation. The 250 sccm – 3 cm condition produced a similar spectrum but lacked the 801 cm^{-1} peak, indicating fewer fragmented species. This absence, possibly due to higher energy density near the nozzle, suggests enhanced precursor fragmentation and reduced retention of labile structures, consistent with SEM results showing smaller, less crosslinked nanoparticles. In contrast, the 200 sccm – 5 cm sample showed more intense absorption bands across the spectrum, pointing to improved deposition yield and greater incorporation of PPy functionalities. This may result from a longer residence time in the plasma zone, allowing more effective precursor-plasma interactions and polymerization [15]. Overall, longer distances favoured chemical retention and nanoparticle growth, whereas shorter distances promoted fragmentation and limited particle development. These findings align with the principle that plasma energy density and residence time are critical for controlling nanoparticle chemistry and morphology [29].

3) *Optimal process conditions*

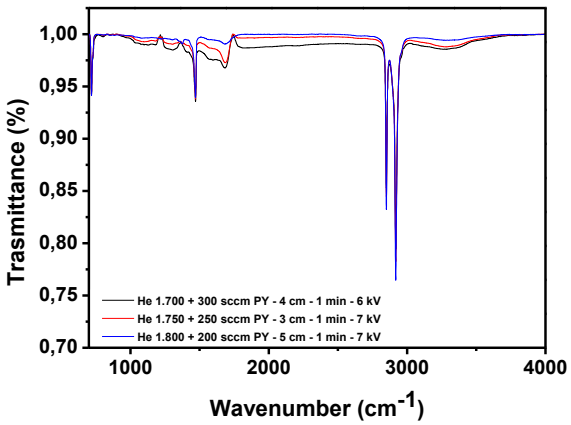

Figure 6: FTIR spectra at the optimal input flow for each precursor flow rate

Figure 8 shows the FTIR spectra at the optimal input voltage for each of the three combination of precursor flow and distance. At 300 sccm–4 cm–6 kV, strong and well-defined PPy-related peaks (3284, 1685, 1570, 1069 cm^{-1}) were observed alongside the characteristic PE bands, indicating efficient nanoparticle deposition. At 250 sccm–3 cm–7 kV, the same peaks were present but slightly weaker, with the 801 cm^{-1} band, previously linked to ring-opened structures, absent, suggesting less fragmentation but slightly lower yield. In contrast, 200 sccm–5 cm–7 kV showed significantly weaker pyrrole-related peaks, suggesting that, under low precursor flow, higher input voltage may negatively impact nanoparticle synthesis. A direct comparison across these three conditions shows that input voltage plays a critical role. At 300 sccm and 6 kV, deposition was efficient; however, increasing voltage to 7 kV at lower flows (250 and especially 200 sccm) resulted in weakened signals. This suggests that higher plasma energy can disrupt polymer growth by enhancing monomer fragmentation and reducing conjugation, as previously reported [27]. These results underscore the importance of balancing plasma energy density with precursor flow to optimize nanoparticle yield and chemical structure.

C. Surface Composition (XPS)

XPS analysis was performed in six different points for each sample, and the results showed in the Table 3 represent the average elemental composition across these measurements.

Table 2: Average atomic percentages of C1s, N1s, O1s for optimal monomer flow rates and distances (rows 1-3) and input voltages (rows 4-6)

He (slm)	Q_{PY+He} (sccm)	Voltage (kV)	Deposition Time (min)	Distance (cm)	C1s (%)	N1s (%)	O1s (%)
1.7	300	9	1	4	77,3 ± 0,5	14,6 ± 0,5	8,0 ± 0,5
1.7	300	6	1	4	75,8 ± 0,7	14,7 ± 0,5	9,5 ± 0,6
1.75	250	9	1	3	76,5 ± 0,8	15,0 ± 0,5	8,5 ± 0,4
1.75	250	7	1	3	77,4 ± 0,3	14,5 ± 0,3	8,0 ± 0,5
1.8	200	9	1	5	75,9 ± 0,9	15,3 ± 0,5	8,7 ± 0,8
1.8	200	7	1	5	73,2 ± 1,5	14,3 ± 0,8	12,4 ± 1,5

XPS analysis showed that all samples primarily contained carbon (C 1s), nitrogen (N 1s), and oxygen (O 1s), reflecting fragments from pyrrole, which is rich in carbon and nitrogen [30]. Oxygen, not originally present in pyrrole, appeared due to plasma-induced surface modifications and atmospheric contamination during synthesis and handling, introducing oxygen-containing groups such as carboxyl, hydroxyl, and esters [31], [32], [33]. Pure pyrrole has a theoretical N/C atomic ratio of 0.25 (~80% C, 20% N), but measured values were lower, especially nitrogen (14–15%), consistent with literature on plasma-polymerized pyrrole exposed to air, where nitrogen loss is linked to hydrolysis of reactive nitrile groups into carboxylic acids, releasing ammonia and increasing oxygen content [34].

Elemental percentages remained stable with minor variation except at 200 sccm flow, 7 kV voltage, and 5 cm distance, where oxygen increased significantly and carbon decreased, indicating enhanced surface oxidation due to

plasma, promoting oxygen-functional group formation and increased hydrophilicity [31], [32].

These XPS findings correlate well with FTIR data showing characteristic polypyrrole bands (N–H stretching, C=C, C–N), while oxygen enrichment and nitrogen reduction detected by XPS align with FTIR evidence of structural changes under stronger plasma exposure. This suggests plasma polymerization combined with ambient air humidity causes partial hydrolysis and chemical rearrangements on nanoparticle surfaces, modifying their chemical nature. The combined spectroscopic evidence confirms that plasma conditions and environmental exposure jointly influence the final composition and structure of synthesized nanoparticles.

D. Plasma Characterization (OES)

1) Optimal precursor flows

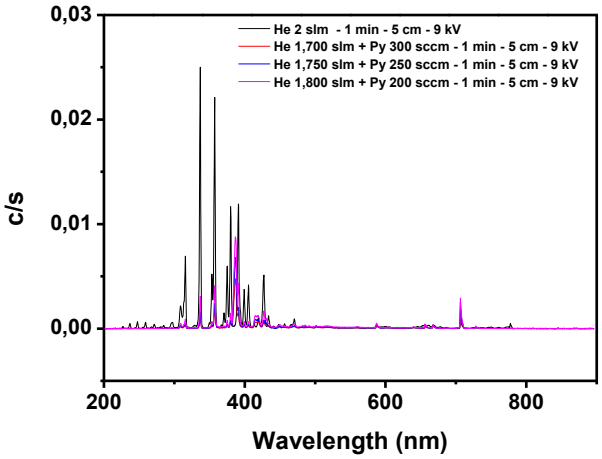

Figure 7: OES spectra under the condition without precursor flow and with the best precursor flow conditions

Spectroscopic analysis was performed by introducing a PTFE support positioned 5 cm from the tip of the capillary, in order to evaluate the active species generated in the helium plasma in the presence of a solid substrate. The resulting spectrum showed a composition similar to that of pure helium plasma, with the presence of peaks at 287 nm corresponds to the OH transition $A^2\Sigma^+$ (v = 0, 1) → $X^2\Pi$ ($\Delta v = 1$) [35], at 315, 337, 370, 375, and 380 nm related to the presence of excited N_2 molecules [36], at 355 nm and 390 nm attributed to C—N fragmentation transitions [37], at 400 nm and 405 nm that are part of the extended N_2 emission band [36], at 413, 430 and 433 nm corresponding to the CH radical [37], at 447 nm related to the He transition 4d3D → $2p^3P$ [38], at 468 nm associated with C_2 [37] and at 501, 588, 668 and 706, all related to He transitions [35].

Moreover, there was the appearance of several low-intensity peaks at 237, 247, 259, 271, 308, and 777 nm. The first four peaks were attributed to emissions from excited NO molecules, corresponding to the NOγ system [36], while the peak at 308 nm was associated with the OH transition ($A^2\Sigma^+$ → $X^2\Pi$, $\Delta v = 0$) [35]. The emission at 777 nm was assigned to the atomic oxygen transition ($3p^5P$ → $2s^5S$) [37]. These species likely originate from interactions between the plasma and components of the surrounding air or adsorbed residues on the support.

Subsequently, the monomer was introduced at a flow rate of 300 sccm, with an input voltage of 9 kV and the capillary-to-substrate distance maintained at 5 cm. The spectrum exhibited several significant changes compared to the plasma without monomer. Some of the previously observed peaks, such as those at 337, 357, and 430 nm, showed a marked decrease in intensity. Conversely, the intensity of the helium line at 706 nm increased, and new peaks emerged: the most prominent at 388 nm, attributed to the CN radical ($B^2\Sigma^+$ → $X^2\Sigma^+$) [37], one at 656 nm corresponding to the Hα transition (2p → 3d) [35], and another at 728 nm (He transition)[35]. Very similar spectra, characterised by the appearance of the same three new peaks, were obtained using a precursor flow of 250 and 200 sccm, with 5 cm of distance and 9 kV of input voltage. These results suggest that the introduction of pyrrole significantly alters the plasma chemistry, promoting the formation of carbon-, nitrogen-, and hydrogen-containing species, particularly the CN radical arising from precursor fragmentation.

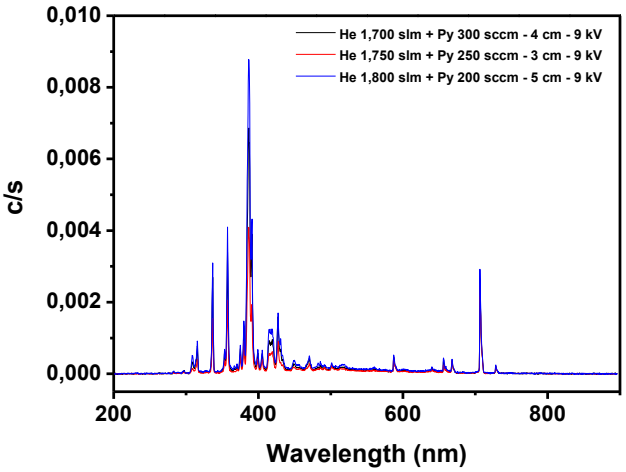

Figure 8: OES spectra at the optimal distance for each precursor flow rate

Figure 10 shows the OES spectra at the optimal distances. When this parameter was varied, the three new peaks previously indentified appeared in all spectra (388, 656, and 728 nm).

Overall, the spectral intensities were lower compared to the previous set of conditions. Lower monomer flow rates resulted in enhanced nitrogen-related peaks at 337, 357, and 388 nm, suggesting more efficient excitation and energy transfer to ambient air species. This behaviour is attributed to the reduced concentration of the organic monomer in the plasma, which lowers the competition for electron energy and allows more efficient excitation of N_2 molecules, thereby intensifying their characteristic emission lines [39].

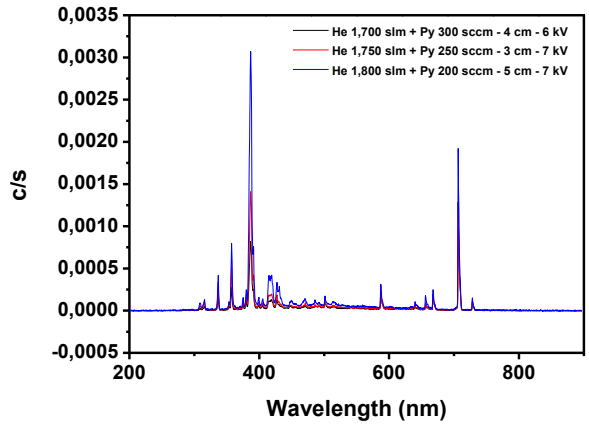

Figure 9: OES spectra spectra at the optimal inpu voltage for each precursor flow rate

A decrease in input voltage, under the condition of 300 sccm flow rate, led to an overall reduction in emission intensities, except for the helium peak at 706 nm, which increased. This behaviour can be attributed to a greater accumulation of metastable helium species at lower voltages. As reported by Naidis [40], reduced electric fields favour the formation of long-lived excited states such as He(2^3S), which emit at 706 nm and play a key role in sustaining the plasma through stepwise excitation and energy transfer.

At lower pyrrole flow rates, the spectra remained consistent with only slight variations in intensity. Interestingly, nitrogen-related peaks at 337, 357, and 388 nm were enhanced, again suggesting more efficient energy transfer to atmospheric species. As described by Bárdos and Baránková [39], this effect arises from a decreased monomer concentration, which reduces the consumption of electron energy by the organic species and enhances the excitation of air molecules.

Voltage optimization at these flow rates confirmed the dominance of the 706 nm helium peak at 7 kV, in agreement with literature findings that helium plasmas can maintain stable populations of reactive species under different operating conditions [40].

CONCLUSIONS

This study demonstrates the effective synthesis of pyrrole-based nanoparticles using an Atmospheric Pressure Plasma Jet (APPJ) array under ambient conditions. The results highlight the critical influence of precursor flow rate, substrate distance, and input voltage on nanoparticle morphology, size distribution, and chemical composition. Optimal conditions were identified at intermediate pyrrole flow rates (200–300 sccm) and moderate distances (3–5 cm), yielding smaller and well-dispersed nanoparticles with consistent PPy chemical signatures. Increasing input voltage generally promoted nanoparticle growth, enhancing aggregation.

The plasma characterization by Optical Emission Spectroscopy revealed dynamic changes in reactive species when introducing pyrrole vapor, providing insight into the plasma-chemical interactions governing polymerization and nanoparticle formation. The presence of biologically relevant reactive oxygen and nitrogen species further supports the potential biomedical applicability of the synthesized nanoparticles.

Overall, the atmospheric pressure plasma approach offers a scalable, environmentally friendly alternative to conventional chemical methods, producing functionalized pyrrole-based nanoparticles without toxic solvents or complex post-processing. Future work will focus on further optimizing plasma parameters, exploring functionalization routes for targeted biomedical applications, and evaluating the in vitro and in vivo performance of the synthesized nanoparticles.

REFERENCES

[1] S. Roszkowski and Z. Durczynska, “Advantages and limitations of nanostructures for biomedical applications,” *Advances in Clinical and Experimental Medicine*, vol. 34, no. 3, pp. 447–456, Jun. 2024, doi: 10.17219/acem/186846.

[2] S. Andrade, M. J. Ramalho, and J. A. Loureiro, “Polymeric Nanoparticles for Biomedical Applications,” *Polymers (Basel)*, vol. 16, no. 2, p. 249, Jan. 2024, doi: 10.3390/polym16020249.

[3] K. McNamara and S. A. M. Tofail, “Nanoparticles in biomedical applications,” *Adv Phys X*, vol. 2, no. 1, pp. 54–88, Jan. 2017, doi: 10.1080/23746149.2016.1254570.

[4] U. Omar, O. Roberto, G. Rafael, and M. Juan, “Interaction of polypyrrole nanoparticles synthesized by plasma with cell lines whit potential biomedical applications,” *Front Bioeng Biotechnol*, vol. 4, 2016, doi: 10.3389/conf.FBIOE.2016.01.01382.

[5] L. Hao, C. Dong, L. Zhang, K. Zhu, and D. Yu, “Polypyrrole Nanomaterials: Structure, Preparation and Application,” *Polymers (Basel)*, vol. 14, no. 23, p. 5139, Nov. 2022, doi: 10.3390/polym14235139.

[6] M. Wang, “Emerging Multifunctional NIR Photothermal Therapy Systems Based on Polypyrrole Nanoparticles,” *Polymers (Basel)*, vol. 8, no. 10, p. 373, Oct. 2016, doi: 10.3390/polym8100373.

[7] Z. Zha *et al.*, “Biocompatible polypyrrole nanoparticles as a novel organic photoacoustic contrast agent for deep tissue imaging,” *Nanoscale*, vol. 5, no. 10, p. 4462, 2013, doi: 10.1039/c3nr00627a.

[8] O. S. Kwon *et al.*, “Ultrasensitive and Selective Recognition of Peptide Hormone Using Close-Packed Arrays of hPTHR-Conjugated Polymer Nanoparticles,” *ACS Nano*, vol. 6, no. 6, pp. 5549–5558, Jun. 2012, doi: 10.1021/nn301482x.

[9] B. V. N. Nagavarma, H. Yadav, A. Ayaz, L. Vasudha, and H. Shivakumar, “Different techniques for preparation of polymeric nanoparticles - A review,” *Asian Journal of Pharmaceutical and Clinical Research*, vol. 5, pp. 16–23, 2012.

[10] M. Singh, M. Vajpayee, and L. Ledwani, “Eco-friendly Surface Modification and Nanofinishing of Textile Polymers to Enhance

Functionalisation," 2020, pp. 529–559. doi: 10.1007/978-3-030-33774-2_23.

[11] H. Shang, W. Ning, S. Shen, R. Wang, D. Dai, and S. Jia, "Atmospheric pressure plasma jet for surface treatment: a review," *Rev Mod Plasma Phys*, vol. 9, no. 1, p. 3, Dec. 2024, doi: 10.1007/s41614-024-00177-0.

[12] X. Zheng *et al.*, "Different Polymerizing Characteristics of Ar/He Atmospheric Pressure Plasma Jets at Room Temperature," *Plasma Processes and Polymers*, vol. 10, no. 4, pp. 379–387, Apr. 2013, doi: 10.1002/ppap.201200125.

[13] L. M. Gomez, G. J. Cruz, M. G. Olayo, M. Gonzalez-Torres, F. Gonzalez-Salgado, and O. G. Lopez-Gracia, "Analysis of crosslinking in polypyrrole particles synthesized by plasma," *Polymer Bulletin*, vol. 71, no. 12, pp. 3275–3287, Dec. 2014, doi: 10.1007/s00289-014-1249-4.

[14] U. Heredia-Rivera *et al.*, "Cold atmospheric plasma deposition of antibacterial polypyrrole–silver nanocomposites on wearable electronics for prolonged performance," *J Mater Chem C Mater*, vol. 12, no. 31, pp. 11861–11876, 2024, doi: 10.1039/D4TC00844H.

[15] J. Friedrich, "Mechanisms of Plasma Polymerization – Reviewed from a Chemical Point of View," *Plasma Processes and Polymers*, vol. 8, no. 9, pp. 783–802, Sep. 2011, doi: 10.1002/ppap.201100038.

[16] L. Liang, G. Chen, and C.-Y. Guo, "Polypyrrole nanostructures and their thermoelectric performance," *Mater Chem Front*, vol. 1, no. 2, pp. 380–386, 2017, doi: 10.1039/C6QM00061D.

[17] T. Dufour, "From Basics to Frontiers: A Comprehensive Review of Plasma-Modified and Plasma-Synthesized Polymer Films," *Polymers (Basel)*, vol. 15, no. 17, p. 3607, Aug. 2023, doi: 10.3390/polym15173607.

[18] E. J. Kautz *et al.*, "Impact of environmental oxygen on nanoparticle formation and agglomeration in aluminum laser ablation plumes," *J Chem Phys*, vol. 159, no. 17, Nov. 2023, doi: 10.1063/5.0167400.

[19] M. Müller, M. Dworschak, J. Benedikt, and L. Kienle, "Tungsten Nanoparticles Generated in an Atmospheric Pressure Plasma Jet," *Particle & Particle Systems Characterization*, vol. 41, no. 9, Sep. 2024, doi: 10.1002/ppsc.202400037.

[20] S. J. Kadhem, "Studying of Plasma- Polymerized Pyrrole at Variable Gas Flow Rates Via Plasma Jet," *Iraqi Journal of Physics*, vol. 19, no. 48, pp. 44–51, Mar. 2021, doi: 10.30723/ijp.v19i48.593.

[21] H. K. Yasuda, "Some Important Aspects of Plasma Polymerization," *Plasma Processes and Polymers*, vol. 2, no. 4, pp. 293–304, May 2005, doi: 10.1002/ppap.200400071.

[22] T. Wang *et al.*, "Effect of electrode configurations on the characteristics of the ring–ring typed atmospheric pressure plasma jet and its modification on polymer film," *Plasma Processes and Polymers*, vol. 19, no. 2, Feb. 2022, doi: 10.1002/ppap.202100139.

[23] Y. Xu *et al.*, "Enhancements of electric field and afterglow of non-equilibrium plasma by Pb(ZrxTi1−x)O3 ferroelectric electrode," *Nat Commun*, vol. 15, no. 1, p. 3092, Apr. 2024, doi: 10.1038/s41467-024-47230-7.

[24] J. V. Gulmine, P. R. Janissek, H. M. Heise, and L. Akcelrud, "Polyethylene characterization by FTIR," *Polym Test*, vol. 21, no. 5, pp. 557–563, 2002, doi: 10.1016/S0142-9418(01)00124-6.

[25] U. Heredia-Rivera *et al.*, "Cold Atmospheric Plasma-Assisted Direct Deposition of Polypyrrole-Ag Nanocomposites for Flexible Electronic Sensors," *ACS Appl Mater Interfaces*, vol. 15, no. 13, pp. 17078–17090, Apr. 2023, doi: 10.1021/acsami.2c20798.

[26] H. J. Jang, B. J. Shin, E. Y. Jung, G. T. Bae, J. Y. Kim, and H.-S. Tae, "Polypyrrole film synthesis via solution plasma polymerization of liquid pyrrole," *Appl Surf Sci*, vol. 608, p. 155129, Jan. 2023, doi: 10.1016/j.apsusc.2022.155129.

[27] P. Yang, J. Zhang, and Y. Guo, "Synthesis of intrinsic fluorescent polypyrrole nanoparticles by atmospheric pressure plasma polymerization," *Appl Surf Sci*, vol. 255, no. 15, pp. 6924–6929, May 2009, doi: 10.1016/j.apsusc.2009.03.016.

[28] M. Vasquez-Ortega, M. Ortega, J. Morales, M. G. Olayo, G. J. Cruz, and R. Olayo, "Core–shell polypyrrole nanoparticles obtained by atmospheric pressure plasma polymerization," *Polym Int*, vol. 63, no. 12, pp. 2023–2029, Dec. 2014, doi: 10.1002/pi.4756.

[29] C. Oehr, "Plasma surface modification of polymers for biomedical use," *Nucl Instrum Methods Phys Res B*, vol. 208, pp. 40–47, Aug. 2003, doi: 10.1016/S0168-583X(03)00650-5.

[30] S.-K. Pang, "Comprehensive study of polymerization of pyrrole: A theoretical approach," *Journal of Electroanalytical Chemistry*, vol. 859, p. 113886, Feb. 2020, doi: 10.1016/j.jelechem.2020.113886.

[31] P. Chu, "Plasma-surface modification of biomaterials," *Materials Science and Engineering: R: Reports*, vol. 36, no. 5–6, pp. 143–206, Mar. 2002, doi: 10.1016/S0927-796X(02)00004-9.

[32] J. Siegel, A. Řezníčková, A. Chaloupka, P. Slepička, and V. Švorčík, "Ablation and water etching of plasma-treated polymers," *Radiation Effects and Defects in Solids*, vol. 163, no. 9, pp. 779–788, Sep. 2008, doi: 10.1080/10420150801969654.

[33] R. Ghobeira, P. S. Esbah Tabaei, A. Nikiforov, R. Morent, and N. De Geyter, "Unraveling Exclusive In-Plasma Initiated Oxidation Processes Occurring at Polymeric Surfaces upon O2 Admixtures to Medium Pressure Ar and N2 DBD Treatments," *Polymers (Basel)*, vol. 15, no. 14, p. 2978, Jul. 2023, doi: 10.3390/polym15142978.

[34] Y. Iriyama and M. Hanawa, “Plasma Polymerization of Pyrrole and Structures and Properties of the Polymerized Films,” *Polym J*, vol. 33, no. 5, pp. 419–423, May 2001, doi: 10.1295/polymj.33.419.

[35] M. Thiyagarajan, A. Sarani, and C. Nicula, “Optical emission spectroscopic diagnostics of a non-thermal atmospheric pressure helium-oxygen plasma jet for biomedical applications,” *J Appl Phys*, vol. 113, no. 23, Jun. 2013, doi: 10.1063/1.4811339.

[36] I. Burducea *et al.*, “Helium Atmospheric Pressure Plasma Jet Effects on Two Cultivars of Triticum aestivum L.,” *Foods*, vol. 12, no. 1, p. 208, Jan. 2023, doi: 10.3390/foods12010208.

[37] C. Li, J. H. Hsieh, and Y. T. Lee, “Effects of radio frequency power on the microstructures and properties of plasma polymerized polypyrrole thin films,” *Vacuum*, vol. 140, pp. 132–138, Jun. 2017, doi: 10.1016/j.vacuum.2016.09.009.

[38] Q. Xiong, A. Y. Nikiforov, M. Á. González, C. Leys, and X. P. Lu, “Characterization of an atmospheric helium plasma jet by relative and absolute optical emission spectroscopy,” *Plasma Sources Sci Technol*, vol. 22, no. 1, p. 015011, Dec. 2012, doi: 10.1088/0963-0252/22/1/015011.

[39] L. Bárdos and H. Baránková, “Cold atmospheric plasma: Sources, processes, and applications,” *Thin Solid Films*, vol. 518, no. 23, pp. 6705–6713, Sep. 2010, doi: 10.1016/j.tsf.2010.07.044.

[40] G. V. Naidis, “Modeling of helium plasma jets emerged into ambient air: Influence of applied voltage, jet radius, and helium flow velocity on plasma jet characteristics,” *J Appl Phys*, vol. 112, no. 10, Nov. 2012, doi: 10.1063/1.4766297.

List of figures

List of tables

List of abbreviations

NPs	Nanoparticles
PPy	Polypyrrole
APP	Atmospheric Pressure Plasma
OES	Optical Emission Spectroscopy
FTIR	Fourier Transform Infrared Spectroscopy
XPS	X-ray Photoelectron Spectroscopy
SEM	Scanning Electron Microscopy
NIR	Near Infra-red
DOX	Doxorubicin
PAI	Photoacoustic imaging
PAT	Photoacoustic tomography
CNFs	Carbon nanofibers
CNTs	Carbon nanotubes
PNPs	Polymer Nanoparticles
EPR	Enhanced Permeability and Retention
BBB	Blood-brain barrier
He	Helium
MRI	Magnetic Resonance Imaging
RF	Radio frequency
sccm	Standard cubic centimetres per minute
slm	Standard litres per minute
ROS	Reactive Oxygen Species
PNPs	Polymeric nanoparticles
RF	Radio Frequency

Table of Contents

CHAPTER 1

Introduction

1.1 Scientific context and motivation for the research

The rapid development of nanotechnology has opened new opportunities in biomedical research, particularly through the use of nanoparticles (NPs) as therapeutic and diagnostic agents [1]. NPs have been widely studied for their suitable properties, including high surface-area-to-volume ratio, tuneable surface chemistry, chemical stability, and the ability to interact with biological systems at the molecular level [2]. Among all the NPs, polymeric NPs stand out for their biocompatibility and versatility, making them ideal candidates for drug delivery, imaging, and regenerative medicine [3].

Conductive polymer polypyrrole (PPy), has gained great interest due to its potential biomedical applications. Its electrical conductivity, chemical stability, and biocompatibility allow it to effectively interface with biological tissues [4]. This has led to promising research in areas such as neural stimulation, biosensors, and drug delivery [5], [6]. However, traditional synthesis methods of PPy NPs are often complex chemical routes which require multiple steps for surface functionalization and may involve toxic solvents or by-products [7].

Trying to overcome such limitations, plasma-based techniques have emerged as an innovative solution. Atmospheric Pressure Plasma (APP) technology allows for NPs synthesis under ambient conditions, offering advantages such as solvent-free processing, reduced risk of contamination from toxic reagents or residual solvents, and direct surface functionalization during deposition [8]. Moreover, APP process parameters, such as gas flow rate, applied voltage, and residence time, can be precisely tuned to modulate particle size, distribution, and surface properties [9].

This study is driven by the need for cleaner, more controllable, and scalable synthesis methods for pyrrole-based NPs, with APP offering a promising solution. APP technology represents an eco-friendly alternative with the potential to enhance the biomedical applicability of these NPs, allowing the functionalization of the NPs during synthesis, without the need for additional chemical processing [9].

This study aims to explore the potential of APP for the synthesis of pyrrole-based NPs, investigating how different plasma parameters influence the morphology, composition, and surface characteristics of the resulting NPs. The goal is to bridge the gap between scalable APP-assisted NP production and biomedical application, potentially contributing to advances in targeted drug delivery, tissue engineering, and biosensing technologies.

1.2 Objectives of the thesis

The aim of this thesis project is to explore the use of non-thermal at APP as an environmentally friendly technology capable of synthesising organic NPs with a potential for biomedical applications. Specifically, the project focuses on the synthesis of pyrrole-based NPs by varying several process parameters, including precursor flow, input voltage, and distance to achieve optimal NP characteristics such as uniform size distributions and high deposition yield. Following synthesis, the NPs were analysed through careful characterisation using advanced surface analysis techniques, including Optical Emission Spectroscopy (OES), Fourier Transform Infrared Spectroscopy (FTIR), X-ray Photoelectron Spectroscopy (XPS) and Scanning Electron Microscopy (SEM). The approach taken aims to provide new sustainable and efficient solutions to produce organic NPs, with a significant impact on therapeutic research, paving the way for innovative and scalable synthesis methods for future biomedical applications.

1.3 Biomedical potential of pyrrole-based nanoparticles

As previously mentioned, pyrrole-based NPs have gained increasing interest due to the electrical conductivity, chemical stability, and biocompatibility, making them particularly promising for a wide range of applications in the biomedical field [5].

Among pyrrole-based NPs, PPy NPs stand out as particularly promising [10]. PPy NPs have strong absorption in the near infra-red (NIR) region (700–1100 nm), where biological tissues exhibit minimal light absorption and scattering. When exposed to NIR laser irradiation, these NPs efficiently convert light energy into heat. When targeted to the tumour site and irradiated with a NIR light, these NPs will cause a localized and controlled hyperthermia capable of selectively destroying cancer cells while sparing surrounding healthy tissue [11]. PPy NPs can be used to combine photothermal therapy and chemotherapy to achieve a synergistic effect against cancer, because in addition to their NIR absorption and photothermal properties, they can also function as drug delivery vehicles [12]. Chen et al. [12] reported the successful loading of doxorubicin (DOX) onto the surface of PPy NPs via π–π stacking and electrostatic interactions, followed by a controlled release triggered by pH and temperature stimuli. In their study, the authors demonstrated that DOX release was significantly enhanced under acidic conditions (pH 5.5) and upon NIR irradiation, simulating the tumour microenvironment and laser treatment, respectively. Moreover, this group presented the temperature evolution of PPy NP solutions under 808 nm laser irradiation at different concentrations. The temperature increased rapidly with both time and NPs concentration, reaching over 55°C at the highest concentration (200 μg/mL) after 10 minutes of irradiation. These results demonstrate the high photothermal conversion efficiency of PPy NPs and support their potential for effective tumour ablation through hyperthermia. The dose-dependent response also highlights the tunability of the system, allowing for precise control over the thermal dose delivered to the target tissue [12].

In addition to its therapeutic applications, PPy also shows great potential in photoacoustic imaging (PAI) [5]. In their study, Zha et al. [13] introduced PPy NPs as a novel solution for photoacoustic tomography (PAT), demonstrating their exceptional optical and biocompatible properties. Synthesised through a

straightforward aqueous dispersion method, these NPs exhibited strong NIR absorption and generated photoacoustic signals eight times stronger than water at a concentration of 100 μg/mL. With a uniform diameter of approximately 46 nm, the NPs were optimally sized for prolonged circulation in the bloodstream, evading rapid clearance by the reticuloendothelial system. Key findings from the study included deep-tissue imaging capabilities, with PPy NPs enabling the visualization of agar phantoms embedded in chicken breast muscle at depths of up to 4.3 cm, achieving a noise-equivalent sensitivity of 9.32 μg/mL. In vivo experiments showed that intravenous injection of PPy NPs (100 μL, 2 mg/mL) in mice enhanced brain vasculature imaging, resulting in a 20% increase in photoacoustic signal intensity and an improved contrast-to-noise ratio. Histological analysis confirmed no acute toxicity in vital organs (heart, liver, spleen, lungs, kidneys) 15 days post-injection, further validating the biocompatibility of PPy. Compared to gold-based contrast agents such as nanoshells and nanorods, PPy NPs offer several advantages: lower cost, simpler synthesis, biodegradability, and a molar extinction coefficient (~2.4×10^{10} M^{-1} cm^{-1} at 808 nm) that is five orders of magnitude higher than that of hemoglobin, enabling high-contrast imaging at minimal doses [13].

Pyrrole-based NPs can also be employed in the field of biosensing [14]. Monitoring levels of parathyroid hormone (PTH) is clinically important for diagnosing and managing conditions such as hyperparathyroidism, osteoporosis, and chronic kidney disease, where calcium-phosphate metabolism is disrupted [14]. Kwon et al. [14] developed a highly sensitive and selective biosensor using carboxylated polypyrrole NPs (CPPyNPs) conjugated with the human parathyroid hormone receptor (hPTHR), a member of the G-protein-coupled receptor (GPCR) family. By forming a close-packed array of CPPyNPs on a field-effect transistor (FET) platform, the system was capable of detecting PTH at femtomolar concentrations, even in complex biological fluids like fetal bovine serum. This sensor not only demonstrated excellent selectivity and long-term stability but also enabled functional analysis of GPCR–ligand interactions, revealing enhanced receptor activation with increasing peptide length. These findings underscore the potential of pyrrole-based NPs for the development of next-generation diagnostic tools with high sensitivity and specificity.

Beyond hormone detection, pyrrole-based NPs have also shown great promise as enzyme mimics for biosensing applications [15]. Tao et al. [15] reported that PPy NPs possess intrinsic peroxidase-like activity, enabling the catalytic oxidation of typical substrates such as 3,3',5,5'-tetramethylbenzidine (TMB) in the presence of hydrogen peroxide (H_2O_2). This catalytic property allows for the colorimetric detection of H_2O_2 with high sensitivity and stability. Monitoring H_2O_2 levels is crucial in biomedical research, as it plays a central role in redox signalling and is involved in numerous physiological and pathological processes, including inflammation, apoptosis, cancer progression, and neurodegenerative diseases. Abnormal concentrations of H_2O_2 are often associated with oxidative stress, making it a key biomarker for early diagnosis and therapeutic monitoring. In their study, the authors successfully applied the PPy NP-based nanozyme system to detect H_2O_2 released by activated macrophages, demonstrating its potential for real-time monitoring of immune responses and oxidative states in disease conditions.

These biomedical applications of pyrrole-based NPs underline their potential as a multifunctional platform for cancer therapy, bioimaging and biosensing. The capacity to synthesize these NPs through clean and scalable methods, such as APP, further amplifies their clinical applicability by offering solvent-free processing and direct surface functionalization, reducing both production costs and environmental impact.

CHAPTER 2

Theoretical Background

2.1 Nanomaterials and nanoparticles: overview

The famous lecture 'There is Plenty of Room at the Bottom' given by Richard Feynman on 29 December 1959 marked the beginning of a new scientific era, predicting the rising of nanotechnology [16]. He hypothesised the possibility of manipulating atoms at the nanoscale level and invited researchers of the time to study physical phenomena at the nanoscale, which could differ from the phenomena at the macroscale [17]. However, it was not until the 1980s that this vision was realised with the rising of nanotechnology, a science that studies materials smaller than 100 nm, including NPs, nanorods, nanotubes, nanowires, nanocrystals and nanofibers[18], [19].

Today, nanomaterials are being used in numerous fields due to their distinctive characteristics, which derive from two main factors: surface effects and quantum effects, which significantly modify their mechanical, thermal, magnetic, electronic, optical, and catalytic properties [20].

Surface effects are primarily due to the high surface-area-to-volume ratio that nanomaterials possess [21]. When materials are reduced to the nanoscale, a larger fraction of atoms is located at or near the surface compared to their bulk counterparts [20], [22]. This high density of surface atoms increases chemical reactivity, as these atoms are less coordinated and have unsatisfied bonds, making them more likely to interact with other molecules [23]. For example, gold is chemically inert in bulk form, but it becomes highly reactive at the nanoscale, enhancing catalytic activity [24], [25]. Additionally, the structural properties of nanomaterials can change due to surface effects: metals like gold and silver exhibit a marked reduction in melting temperature when in nanoparticle form, while ceramics that are typically brittle at the macroscale show increased ductility at the nanoscale [20], [26], [27]. These structural changes are driven by the minimization of surface energy, leading to atomic rearrangements that do not occur in larger materials [21].

Quantum effects, on the other hand, emerge when the size of nanomaterials approaches the exciton Bohr radius, typically in the range of 1–100 nm [23]. One of the most significant quantum phenomena at this scale is quantum confinement, which affects conduction electrons, the free-moving electrons responsible for electric current in metals and semiconductors [28]. In bulk materials, electrons can move relatively freely, but in nanomaterials, their movement is restricted to a very small volume, causing discretization of energy levels [29]. This confinement alters the band gap, which is the energy difference between the valence band and the conduction band, in semiconductors, affecting their electronic and optical properties. For instance, quantum dots of cadmium selenide (CdSe) emit different colours of light depending on their size due to variations in energy levels caused by quantum confinement [30].

Quantum effects also lead to unexpected magnetic properties [31]. Metals like palladium, platinum, and gold, typically non-magnetic in bulk, exhibit magnetism at the nanoscale due to changes in electronic structure [20]. Additionally, quantum confinement influences the electronic affinity of nanomaterials, enhancing their ability to accept or donate electrical charges, which further improves their catalytic properties [20].

In the field of nanomaterials, NPs can be considered as the heart of nanotechnology. The definition by The International Organization for Standardization (ISO) states that NPs are nano-objects with all external dimensions in the nanoscale, ranging from 1 nm to 100 nm [32]. According to this definition, the lengths of the longest and the shortest axes of the nano-object do not differ significantly from each other [33].

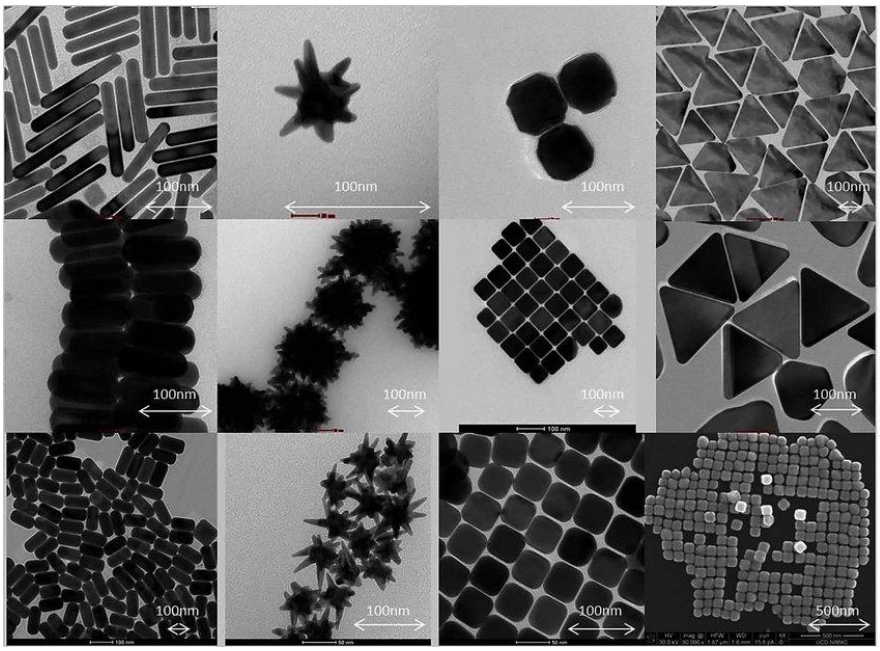

Figure 1: Representative examples of NPs with different shapes. Image taken from Bouloudenine et al. [287]

Generally, NPs can exhibit various morphologies, including spherical, cylindrical, tubular, conical, and many more (**Figure 1**) [34]. Surfaces can be smooth and homogeneous, or uneven and wavy, and they can have a crystalline or amorphous structure, with single- or multi-crystalline solids that are dispersed or aggregated [35]. The combination of these various features allows NPs to have distinctive properties, which can prove to be highly adaptable materials capable of meeting specific needs in a wide range of technological and industrial applications, including drug delivery, where NPs enhance targeted therapeutic effects [36]; optoelectronics, where they improve light absorption and emission properties [37]; biosensors, where their high surface area and surface tunability enable enhanced sensitivity and detection capabilities [38]; biofuel production, where NPs serve as catalysts to improve conversion efficiency [39]; food technology, where they contribute to food preservation and enhanced packaging materials [40]; and textile applications, where they are used to impart antimicrobial properties, enhance durability, and provide functional coatings [41].

A first fundamental classification concerns their chemical nature, which divides them into organic, inorganic and carbon-based nanoparticles [42].

2.1.1 Inorganic nanoparticles

Inorganic NPs are generally composed of metals or ceramics and involve particles with the absence of carbon [33]. Among these, bimetallic NPs can form homogeneous alloys like gold-silver (Au-Ag) with atomic-level mixing of metals, as demonstrated by co-reduction synthesis, or they may adopt core-shell configurations such as gold-core/silver-shell (Au@Ag) structures produced through seeded growth methods [43]. They exhibit unique optical, electrical, thermal, and magnetic properties, making them highly suitable for a wide range of applications across various fields [34], [44]. For instance, gold-silver (Au-Ag) NPs are particularly valued for their exceptional optical properties. Due to the phenomenon of localized surface plasmon resonance (LSPR), these NPs can significantly enhance Raman signals, making them powerful tools for biomolecule detection through Surface-Enhanced Raman Scattering (SERS), which is widely applied in sensitive diagnostic techniques [45]. From an electrical perspective, bimetallic NPs such as platinum-palladium (Pt-Pd) are employed in fuel cells, where their high electron conductivity and large catalytic surface area significantly improve the efficiency of electrochemical reactions. This makes them promising candidates for the development of clean and sustainable energy technologies [46]. Regarding thermal properties, copper-silver (Cu-Ag) NPs are used in nanofluids to enhance thermal conductivity, improving heat dissipation and potentially contributing to the reliability of cooling systems in electronic devices [47]. Finally, iron-platinum (Fe-Pt) NPs incorporated in montmorillonite (FePt@MMT) exhibit remarkable magnetic properties that make them suitable for magnetic hyperthermia in cancer treatment. In this application, alternating magnetic fields induce localized heating within the NPs, contributing to the selective ablation of cancer cells. Moreover, the porous structure of montmorillonite allows for combined chemotherapy delivery, enhancing therapeutic outcomes [48].

Ceramic NPs, composed of oxides and other inorganic compounds, are prized for their stability and load-bearing capacity [49], and they are used in catalysis, photonics, and degradation of pollutants [50], [51]. Organically modified silica-based NPs doped with photosensitizers (SiNP@PS), developed by Roy et al. [52], demonstrate excellent stability and efficient generation of reactive oxygen species under light irradiation, making them promising carriers for photodynamic therapy in cancer treatment. In this approach, the porous ceramic matrix allows oxygen diffusion while protecting the photosensitizer, enabling selective tumour cell destruction upon irradiation. Additionally, their small size and surface modifiability facilitate targeted delivery and reduced systemic toxicity. Huinan Hao [53] demonstrated that ceramic NPs like hydroxyapatite, tricalcium phosphate, and bioactive glass significantly enhance bone tissue engineering. Their incorporation in 3D printed scaffolds enables controlled porosity, improved mechanical strength, and bioactivity, promoting bone regeneration and stem cell differentiation. Strontium-doped bioactive glass scaffolds also provide sustained drug release, making ceramic NPs crucial for advanced regenerative medicine applications. Beyond biomedical uses, Chen et al. [54] showed that incorporating zirconium dioxide (ZrO_2) NPs into the phosphor layer of white LEDs can significantly enhance their optical performance. By leveraging the strong light-scattering properties of ZrO_2, the nanoparticles improve both luminous efficiency and colour uniformity. This approach helps mitigate common issues like uneven colour distribution, while maintaining high brightness, making it a

promising strategy for next-generation solid-state lighting. Wang et al. [55] reported that nickel-silicon oxycarbonitride (Ni/SiOCN) ceramic nanocomposites exhibit efficient catalytic performance in the dry reforming of methane (DRM), a key process that converts methane (CH_4) and carbon dioxide (CO_2) into syngas (CO + H_2), an essential mixture for the production of fuels and chemicals. In this application, the SiOCN ceramic matrix provides high thermal stability and ensures uniform dispersion of Ni NPs, effectively preventing their aggregation and extending the catalyst's lifespan. Furthermore, these materials display remarkable catalytic activity, making them highly promising for industrial applications under harsh conditions. Zinatloo-Ajabshir et al. [56] demonstrated that sonochemically synthesised cerium oxide (CeO_2) NPs, capped with glucose, exhibit enhanced photocatalytic activity for the degradation of organic pollutants under visible light. This approach improves the surface properties of CeO_2 by preventing agglomeration and increasing stability, achieving degradation efficiencies up to 99.1% for contaminants such as Captopril and Malachite Green. These findings highlight the strong potential of glucose-capped CeO_2 NPs for effective environmental remediation in wastewater treatment.

2.1.2 Carbon-based nanoparticles

Particular attention needs to be paid to carbon-based NPs, which comprise several materials with unique properties, enabling their application in areas such as electronics, energy, and biomedicine [57].

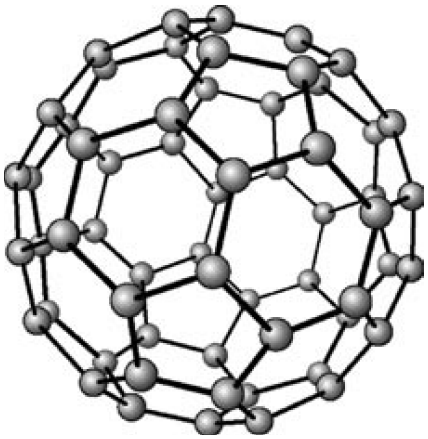

Figure 2: Representation of the structure of a C_{60} fullerene taken from Tikhomirov et al. [288]

Fullerenes (C60), due to their cage-like structure, composed of 20 hexagonal and 12 pentagonal rings (**Figure 2**), and distinctive physicochemical properties, have found applications in nanoscience, particularly in the development of organic photovoltaics, superconductors, and innovative materials such as polymer composites, thanks to their reactivity [58], [59]. The incorporation of fullerenes into polymer matrices, such as Polyvinyl Acetate (PVAc), Polymethyl Methacrylate (PMMA) enables significant modulation of optical absorption, photoluminescence, and energy band structure. Fullerene-doped polymers exhibit reduced energy band gaps, enhanced photoluminescence intensity, and improved fluorescence quantum yield, making them promising candidates for optoelectronic applications, including luminescent downshifters in silicon solar cells and efficient host matrices for solar concentrators [60]. The use of fullerenes in the field of photovoltaics is primarily driven by their

exceptional electron-accepting capabilities and high electron mobility, which enable efficient charge separation and transport in organic photovoltaic (OPV) devices, significantly enhancing their energy conversion efficiency [61]. In the biomedical sector, fullerenes are actively researched for drug delivery systems and photodynamic therapy due to their ability to generate reactive oxygen species (ROS) upon light irradiation, which can induce cell apoptosis in cancer cells [62]. For example, research conducted by Shi et al. [63] presented a novel biomedical application of fullerenes (C60) for combined chemotherapy and photodynamic therapy (PDT). Researchers developed a DOX-loaded poly(ethyleneimine) (PEI) derivatized fullerene (C60–PEI–DOX), where DOX is covalently attached via pH-sensitive hydrazone linkages. This functionalization enhances tumour targeting and controlled drug release, significantly improving antitumour efficacy compared to free DOX. Furthermore, the C60-based system also serves as an effective photosensitizer for PDT, generating ROS upon visible light irradiation, which induces cytotoxic effects in cancer cells. This dual-action platform, leveraging the unique properties of fullerenes, demonstrates great promise for targeted cancer therapy with minimal side effects.

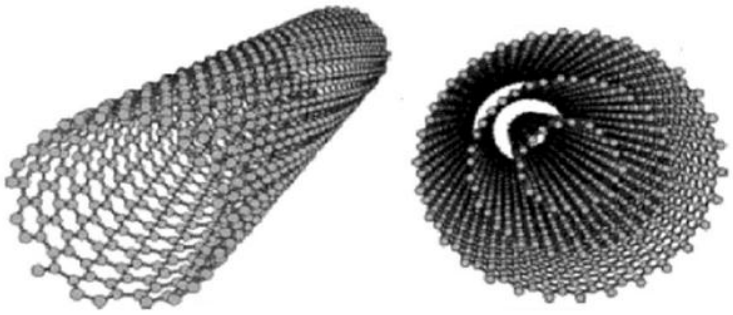

Figure 3: Representation of the structure of carbon nanotubes single-walled (left) and multi-walled (right). Image taken from Malhotra et al. [289]

Carbon nanotubes (CNTs), which can be classified into single-walled (SWCNTs) and multi-walled (MWCNTs) types, are distinguished by their structural composition: SWCNTs consist of a single layer of graphene rolled into a cylindrical shape, whereas MWCNTs are composed of multiple concentric graphene cylinders, as shown in **Figure 3** [64]. This structural difference influences their properties, SWCNTs typically exhibit higher flexibility and electronic conductivity, while MWCNTs are generally stronger and more resilient under mechanical stress due to their multi-layered structure [57]. CNTs are widely applied in fields such as electronics, energy storage, and biomedicine, with promising uses in drug delivery systems, nanocomposites for prosthetic devices, and materials for bone regeneration [65]. Peng et al. [66] demonstrated that the integration of CNTs into field-effect transistors (FETs) enables enhanced carrier mobility, high saturation velocity, and superior electrostatic control, leading to low power consumption and minimized short-channel effects. CNT-based FETs are explored for high-performance and energy-efficient integrated circuits, offering promising advancements over traditional silicon-based CMOS technology. Mazzatenta et al. [67], by exploring the coupling mechanisms between SWCNTs and hippocampal neurons, demonstrated that SWCNT substrates not only support neuronal

growth but can also directly stimulate brain circuit activity. Their findings underscore the potential of SWCNTs as a highly effective platform for neural interfaces, capable of modulating synaptic pathways and enhancing network connectivity, paving the way for advanced neuroprosthetic applications and deeper insights into neuron-material interactions. Furthermore, Zhang et al. [68] provided compelling evidence that embedding SWCNT into chitosan-based scaffolds enriched with nanocrystalline hydroxyapatite not only significantly promotes osteoblast proliferation compared to pristine hydrogel matrices but also leads to notable improvements in the mechanical properties of the scaffold, including enhanced tensile strength and compressive modulus. These findings suggest that the synergistic effect of SWCNT and hydroxyapatite within the chitosan matrix optimally supports cellular growth while reinforcing the structural integrity of the scaffold, making it a promising candidate for bone tissue engineering applications.

Carbon nanofibers (CNFs), although similar in structure to CNTs, are generally more cost-effective due to simpler production processes and lower purity requirements [57]. CNFs are used as reinforcement in polymer and metal matrices to enhance electrical conductivity, mechanical strength, and thermal properties. In polymer composites such as polypropylene and nylon, the incorporation of CNFs significantly reduces volume resistivity, improves tensile strength, and increases thermal stability, enabling their use in advanced electronic and structural applications. Moreover, in metal matrices like aluminium and magnesium alloys, CNFs contribute to superior thermal conductivity and adjustable coefficients of thermal expansion (CTE), addressing challenges in heat dissipation for aerospace and automotive industries [69]. Additionally, Victor Leung and Frank Ko [70] have investigated the potential biomedical applications of CNFs, highlighting their promising role in advancing tissue regeneration, wound care, and drug delivery systems. Due to their high surface area, porous structure, and similarity to the extracellular matrix (ECM), CNFs facilitate enhanced cell adhesion, proliferation, and nutrient transport, making them ideal candidates for tissue engineering scaffolds. Furthermore, their structural properties allow for the development of advanced wound dressings that promote faster healing and better integration with biological tissues. In drug delivery, CNFs offer a high loading capacity and controlled release of therapeutic agents, which could significantly improve the efficacy of anticancer treatments and other targeted therapies. These unique characteristics underline the transformative potential of carbon nanofibers in biomedical applications, driving ongoing research to optimize their performance and biocompatibility.

2.1.3 Organic nanoparticles

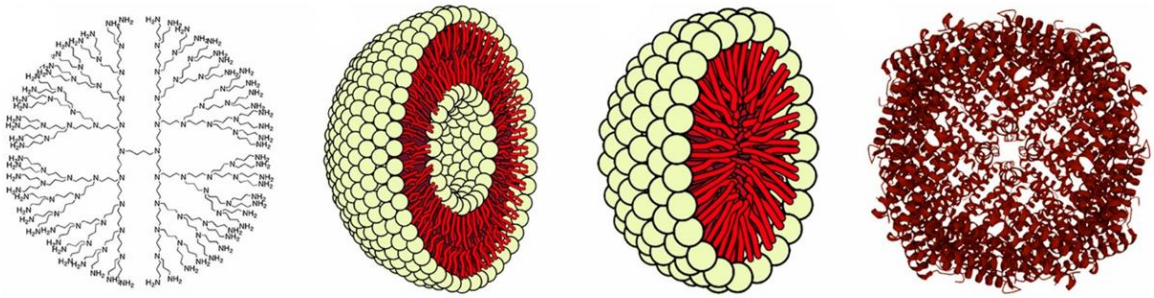

Figure 4: Types of organic nanoparticles: dendrimers, liposomes, micelles, ferritin (from left to right). Image taken from Joudeh et al. [33]

Organic NPs, typically smaller than 100 nm in size, are synthesised from organic materials and they can be composed of proteins, carbohydrates, lipids, polymers, or other organic compounds. These include dendrimers, liposomes, micelles and protein complexes such as ferritin [33], showed in **Figure 4**.

Dendrimers represent a promising class of nanomaterials for cancer therapy, particularly in targeted drug delivery. Their unique branched structure allows for high drug-loading capacity and controlled release, enhancing the specificity and efficacy of anticancer treatments while minimizing systemic toxicity. In addition to their role as drug carriers, dendrimers exhibit theragnostic capabilities, enabling simultaneous treatment and monitoring of cancer progression. Despite their potential, clinical applications in colorectal cancer remain limited, with only a few trials exploring their effectiveness. However, ongoing research continues to optimize dendrimer-based platforms for improved targeting, biocompatibility, and therapeutic outcomes, positioning them as a valuable tool in nanomedicine for cancer treatment [71].

Liposomes with a positive surface charge have demonstrated significant potential as immunoadjuvants by effectively enhancing cell-mediated immune responses. Their cationic nature facilitates the efficient delivery of soluble protein antigens into the cytoplasm of macrophages, leading to improved antigen processing and presentation via class I MHC molecules. This targeted delivery mechanism supports stronger activation of cytotoxic T lymphocytes, suggesting that positively charged liposomes could serve as powerful carriers in the development of advanced vaccines and immunotherapies [72].

Micelles engineered with polyethylene glycol (PEG) have proven effective for glucose-responsive insulin delivery, offering a promising strategy for diabetes management. Phenylboronic acid (PBA)-based micelles demonstrate high sensitivity to glucose levels, enabling an "on–off" release mechanism that responds dynamically to changes in blood sugar. Studies have shown that these micelles can effectively release insulin when exposed to hyperglycemic conditions (2 g/L glucose) while maintaining biocompatibility, highlighting their potential for self-regulated insulin delivery in diabetic therapy [73].

In general, organic NPs offer significant advantages, being typically non-toxic, biodegradable, and sensitive to thermal and electromagnetic radiation, such as heat and light [34]. They are formed through non-covalent intermolecular interactions, which enhance their stability and facilitate natural clearance from the body [74].

2.1.4 Polymeric nanoparticles

Among organic NPs, polymeric nanoparticles (PNPs) stand out in nanomedicine for the wide range of polymers available and their biocompatibility, biodegradability, and design versatility. Typically made from natural (chitosan, alginate) or synthetic polymers (PLA, PLGA, PCL), PNPs can safely degrade into non-toxic byproducts, ensuring minimal biological impact [75].

Due to their small size and high reactivity, PNPs interact more effectively with their surroundings and offer superior performance compared to traditional bulk polymers [76]. They are solid colloidal particles of nanometre size derived from polymers, characterised by innovative properties that are highly dependent on their structure. At the nanoscale level, quantum effects become predominant, and the surface-to-volume ratio increases significantly, affecting the overall properties of the material. This improvement favours mixing with other components in composites, optimises battery performance and reduces the use of resources in catalytic processes, contributing to a decrease in waste [76]. Moreover, the chemical structure of polymers enables precise control over the size, shape, surface charge, and functionalization of the NPs, allowing for the development of smart delivery systems that respond to specific physiological stimuli like pH, temperature, enzymatic activity or also external stimuli [77].

In the study conducted by Wang et al. [78], the researchers focused on the synthesis and characterization of polymeric nanoparticles with controlled size and morphology. Their objective was to explore how variations in polymerization conditions, such as monomer concentration and reaction temperature, influence particle structure and surface properties. By self-assembling block copolymers in solution and stabilizing them through core cross-linking, they produced core-shell NPs with diverse shapes, spheres, hollow spheres, and strings, demonstrating scalability for industrial applications. The NPs, featuring a highly cross-linked core and an elastomeric shell, exhibited enhanced reinforcing capabilities in rubber vulcanizates, reduced hysteresis, and strong mechanical properties, highlighting their potential for use in nanocomposites and targeted drug delivery.

As reported by Overney et al. [79], nanoscale confinement dramatically alters the glass transition behaviour of polymers. The glass transition temperature (Tg) marks the point at which polymer chains gain enough thermal energy to transition from a brittle, rigid state to a more elastic and ductile form. This parameter is crucial as it defines the temperature range over which the polymer shifts its mechanical properties, impacting its suitability for various applications. At the nanoscale, the restricted mobility of polymer chains and the increased energy required for molecular motion result in a higher Tg. This phenomenon is particularly important for technological applications, where the material's operational limits, stiff and brittle below Tg, flexible and impact-resistant above Tg, determine its effectiveness in uses such as polymeric membranes and drug delivery systems [80].

Moreover, Khan et al. [81] investigated the effect of nanoparticles on polymer crystallization, demonstrating that the interaction with NPs and spatial confinement induce higher crystallinity and greater morphological stability compared to bulk polymers. This more ordered structure, driven by the restricted mobility of polymer chains, enhances mechanical properties such as hardness, elastic modulus, and tensile strength. Additionally, the compactness and intertwining of polymer chains at the nanoscale reduce structural defects, contributing to greater thermal and mechanical stability.

2.1.5 Application of nanoparticles

As stated in the previous paragraphs, PNPs find applications in various fields: pharmaceutical applications [82], environmental and sustainability [83], energy [84] and electrochemical devices [83], cosmetics [85] and food Industry [83]. Among these, their use in biomedical engineering represents one of the most promising developments in recent years [86].

From a pharmaceutical point of view, one of the main limitations in the treatment of cancer is the difficulty of drugs in reaching and selectively accumulating in the desired target [87].

Often, the ineffectiveness of a therapy is due to the lack of selective accumulation at the target site, resulting in random dispersion of the drug in the body, that contributes to side effects such as myelosuppression (decreased production of white blood cells causing immunosuppression), mucositis (inflammation of the lining of the digestive tract), alopecia (hair loss), organ dysfunction, systemic toxicity, and insufficient concentration in the target area [88]. To solve this problem, several strategies have been investigated, including the use of PNPs as carriers to achieve targeted accumulation of the drug of interest [87].

Numerous studies have been conducted in this area. Gomez et al. [89] synthesised Poly Lactic-co-Glycolic Acid (PLGA) NPs loaded with corticosteroids, anti-inflammatory drugs used in the treatment of diseases of the posterior segment of the eye. Using these NPs, promising results were obtained, including successful encapsulation of dexamethasone in a stable and biocompatible form, as well as rapid and complete drug release in vitro. This approach helps to overcome the common challenges of delivering corticosteroids effectively to the target area, improving the potential for therapeutic efficacy.

In the field of drug delivery, NPs are widely studied in anti-cancer therapies, through two main approaches: passive targeting and active targeting [90].

In the case of passive targeting, NPs exploit the EPR (Enhanced Permeability and Retention) effect, which allows them to selectively accumulate within solid tumours such as hepatomas, sarcomas, carcinomas (e.g., colon and renal cell carcinoma), melanomas, and metastatic tumours (e.g., lymph node and bone metastases). This occurs because tumour blood vessels in these malignancies are more permeable and disorganized than those in healthy tissue, while lymphatic drainage is often impaired. As a result, NPs can extravasate and accumulate more efficiently in the tumour microenvironment due to their small size, so there is no specific molecular recognition of cancer cells, the selectivity is driven primarily by the unique vascular and lymphatic abnormalities of solid tumours [91].

On the other hand, active targeting involves modifying the NPs by binding specific ligands on their surface that recognise receptors abnormally present on the tumour cell membrane. These receptors vary depending on the tumour type, with certain cancers such as breast, lung, colorectal, and prostate cancer showing high expression of specific targets. This allows the NPs to interact in a targeted manner with the diseased cells, improving the selectivity and efficacy of the treatment [92].

One of the ongoing applications involves the controlled release of inhibitors of heme oxygenase (HO-1), an enzyme that cancer cells overexpress to protect themselves from oxidative stress by producing antioxidant molecules like bilirubin [93]. Inhibiting HO-1 can increase oxidative stress in tumour cells, enhancing their vulnerability to treatment. Zinc protoporphyrin (ZnPP) is a well-known HO-1 inhibitor, but its poor water solubility has limited its application [94]. Iyer et al. [95] initially used PEGylation (conjugation with polyethylene glycol) to improve solubility and facilitate tumour targeting via the EPR effect. Although successful in targeting, PEG–ZnPP showed low loading capacity (1.5% w/w) and high

viscosity, limiting its practicality for injection. To address these issues, amphiphilic styrene–maleic acid (SMA) copolymer was employed to encapsulate ZnPP, forming micelles (SMA–ZnPP) with high loading (up to 60% w/w), excellent solubility, and good stability in water. These micelles demonstrated effective HO-1 inhibition and cytotoxicity against cancer cells, presenting a promising strategy for targeted cancer therapy.

Many chemotherapeutic drugs, such as paclitaxel and DOX, experience rapid clearance from the bloodstream due to first-pass metabolism in the liver. This process, known as the first-pass effect, results in a substantial reduction of the active drug concentration before it reaches the target tissue, diminishing its therapeutic potential [96], [97]. To overcome this limitation, Araki et al. [98] studied paclitaxel-loaded PNPs composed of polyethylene glycol (PEG) and polylactic acid (PLA) block copolymers. The PNPs exhibited a mean particle size of approximately 80 nm and a nearly neutral zeta potential, favouring prolonged blood circulation and reduced opsonization by plasma proteins. In vivo studies on Colon-26 (C26) tumour-bearing mice demonstrated that the PNPs enhanced paclitaxel distribution within tumour tissues while minimizing uptake by the liver and spleen, which are typical sites of nonspecific NP accumulation. These results highlight the potential of PEG-PLA NPs as promising drug carriers to improve the therapeutic index of hydrophobic chemotherapeutic agents like paclitaxel, effectively overcoming the limitations associated with conventional formulations. Pieper et al. [99] employed polymeric NPs composed of PLGA, PLA, and PEGylated PLGA as carriers for DOX. In this study, these nanoparticles were demonstrated to improve the anticancer efficacy of DOX by enhancing its cellular uptake and providing controlled drug release. NPs showed substantial benefits in terms of increasing drug loading, prolonging drug release, and improving overall anticancer activity in neuroblastoma cells.

Drug delivery is particularly complex in the central nervous system due to the blood-brain barrier (BBB), which prevents the passage of several therapeutic molecules, recognising them as foreign [87]. The use of NPs for drug encapsulation enables bypassing the restrictive nature of the BBB, thanks to their small size and surface properties that facilitate their passage through the vascular endothelium. This capability was demonstrated in the study by Kreuter et al. [100], where dalargin, a hexapeptide that typically cannot cross the BBB, was successfully delivered to the central nervous system using poly(butyl cyanoacrylate) (PBCA) NPs coated with polysorbate 80. Intravenous administration of this NP formulation induced a significant analgesic effect in mice, which was not observed in control groups receiving the drug in solution or simple mixtures with NPs and surfactant. Microscopic analyses revealed that the polysorbate 80 coating facilitated the phagocytic uptake of the NPs by brain endothelial cells, allowing dalargin to reach the brain tissue. This study highlights the potential of polymeric NPs to enhance drug delivery across the BBB, opening new avenues for central nervous system therapies.

One of the major advantages of polymers is that there are so many chemical structures of polymer chains that have the ability to chemically or physically connect with other molecules, protect therapeutic substances, and respond to internal stimuli, such as pH [101], temperature [102] or other external stimuli, such as magnetic field [103] , ultrasound [104], or light [105]

Among the most promising polymers in this field is PPy, a conductive polymer with excellent optical properties in the NIR region. This characteristic makes it ideal for PAT, a therapeutic approach that uses the heat generated by light to selectively destroy cancer cells. PAT using PPy particles allows the release of heat by irradiating the particles with NIR laser, which causes the electrons to become excited and

release energy in the form of heat. This increase in temperature is enough to cause irreversible damage to tumour cells, leading to their death by necrosis or apoptosis, while the surrounding healthy tissues remain unharmed due to their greater ability to dissipate heat [106].
PPy NPs are also characterised by biocompatibility and stability, making them particularly interesting for clinical applications [107].

2.1.6 Traditional synthesis of nanoparticles: bottom-up

Numerous methods have been developed to synthesise PNPs with tailored chemical and physical properties suitable for specific applications, but generally these techniques are based on two main approaches: top-down and bottom-up [108].

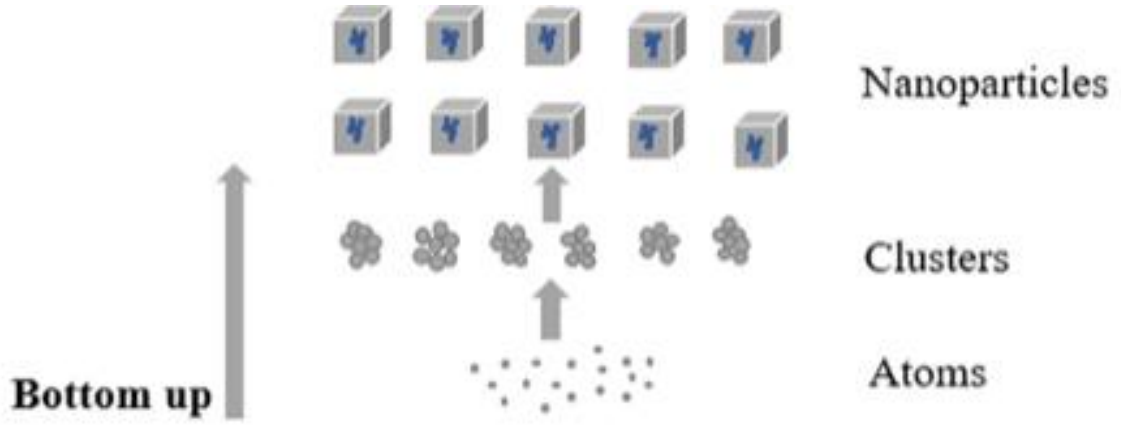

Figure 5: Bottom-up approach. Image taken from Abid et al. [108]

Figure 5 illustrates the bottom-up approach, which involves the formation of nanostructures starting from individual atoms or molecules, which gradually assemble into larger, organized structures [109].
The first method developed is solvent evaporation, the most widely used technique that uses the dispersion of a pre-formed polymer [110]. It is an emulsion-based method, which can be single, oil-in-water (o/w), or double emulsion (water-in-oil) in water (w/o/w) and requires the use of a surfactant, which helps to stabilise the emulsion. The technique involves the dissolution of the polymer in a volatile solvent, the formation of an emulsion and the subsequent evaporation of the solvent, which leads to the formation of NPs. The solvent is evaporated by magnetic stirring at room temperature or under vacuum, followed by centrifugation to collect the nanoparticles, which are then purified to remove surfactant residues and finally lyophilised [111]. As one of the first methods developed, solvent evaporation has been greatly optimised and remains widely used thanks to its simplicity, reproducibility, and high encapsulation efficiency for lipophilic compounds [112]. However, this technique involves some disadvantages such as difficulties removing the surfactants and the potentially toxic nature of the used solvents [113].
Another traditional technique used is salting out, which allows the synthesis of PNPs without the use of surfactants and chlorinated solvents, thus reducing environmental impact and health risks [114]. This method exploits the salting-out phenomenon, which refers to the reduction of the miscibility between water and an organic solvent, and consequently the precipitation of a polymer, caused by the presence of high concentrations of dissolved salts in the aqueous phase [115]. In this process, the polymer is dissolved in an organic solvent that is completely miscible in water. The solution is emulsified in an aqueous phase that contains high concentrations of salts or sugars, which change the miscibility between the solvent and water, preventing the polymer from dissolving in the aqueous phase. In order to induce the precipitation of the polymer and the formation of NPs, the emulsion is subsequently diluted with a

large amount of water, reducing the concentration of salts or sugars in the aqueous phase, favouring the migration of the solvent from the emulsion droplets to the outside and causing the precipitation of the polymer in the form of nanoparticles [111]. This method is considered a safer and more environmentally friendly alternative to traditional techniques based on solvent evaporation, as it avoids the use of chlorinated solvents, which are harmful to both the environment and physiological systems [116]. Although the purification process can be complex, as residual salts or sugars must be completely removed from the NP solution [117]. It is not always effective with all types of polymers, especially those with low affinity for the solvents used [118].

The nanoprecipitation technique, also known as solvent displacement, is a widely used method for the rapid and simple production of PNPs [111]. The principle behind this method relies on the rapid diffusion of an organic solvent, in which the polymer is dissolved, into an aqueous phase. This process causes a reduction in the interfacial tension between the two phases, which promotes the formation of small droplets of the organic solvent and ultimately leads to the precipitation of the polymer as NPs with well-defined sizes [119]. The nanoprecipitation system consists of three main components: a polymer dissolved in an organic solvent (such as acetone, ethanol, or methylene chloride), a non-solvent (typically water), and, in some cases, a surfactant. The non-solvent is a liquid that is miscible with the organic solvent but does not dissolve the polymer; this incompatibility is what triggers the polymer's precipitation [111]. Although not strictly necessary, a surfactant is often added to improve the long-term stability of the NPs by preventing their aggregation [120]. During the process, the organic phase is added dropwise into the aqueous phase under moderate magnetic stirring, ensuring uniform mixing and controlled diffusion. The formation of NPs is not caused by the stirring itself, but rather by the rapid diffusion of the organic solvent into the aqueous medium. This leads to local supersaturation of the polymer, which immediately precipitates out of solution to form nanoparticles [111]. The mechanism of NP formation occurs in three stages: nucleation, growth, and aggregation. Initially, during nucleation, the supersaturation of the polymer results in the formation of small nuclei. In the growth phase, additional polymer molecules migrate toward these nuclei, increasing their size. Finally, in the aggregation phase, the particles may cluster together, unless properly stabilized. The key to obtaining uniform, well-defined nanoparticles lie in effectively separating the nucleation phase from the growth phase, which can be achieved by carefully controlling parameters such as polymer concentration, solvent addition rate, and stirring intensity. This separation prevents uncontrolled particle growth and ensures a narrow size distribution [121]. Some advantages of the nanoprecipitation technique are its simplicity, speed, and reproducibility and scalability. However, it involves the use of organic solvents, which may raise environmental and safety concerns and ensuring the long-term stability of the nanoparticles can be challenging without the use of appropriate stabilizing agents or optimized formulations [117].

The dialysis method is a rather simple technique for obtaining PNPs a solution containing the polymer dissolved in an organic solvent from an external medium consisting of a non-solvent, usually water. As the organic solvent diffuses through the membrane, the polymer becomes less and less soluble and eventually precipitates in the form of nanoparticles [111]. This method is simple and effective, allowing for the formation of homogeneous suspensions without the need for chemical additives or surfactants [119]. However, it is a very slow process, often taking several hours or even days, as the solvent must gradually diffuse through the membrane [122]. Moreover, the formation mechanism is not yet fully

understood, and the choice of solvent can affect the morphology and particle size distribution of the NPs [111].

One of the earliest methods developed to try to overcome the use of organic solvents and surfactants involves the use of supercritical fluids, which are fluids compressed and heated above a critical temperature and critical pressure [123]. Under these conditions, the physical and chemical properties of the fluid are intermediate between those of a gas and a liquid, behaving like a gas but with the typical density of a liquid [124]. Among the most common methods are Rapid Expansion of Supercritical Solutions (RESS), Rapid Expansion of Supercritical Solution into Liquid Solvent (RESOLV), the Gas Antisolvent process (GAS), the Supercritical Antisolvent process (SAS), and Particles from Gas-Saturated Solutions (PGSS) [111]. RESS involves dissolving a solute in a supercritical fluid, typically CO_2, and rapidly expanding the solution through a nozzle into ambient conditions. This results in supersaturation and particle precipitation [125]. While this method avoids organic solvents and produces relatively pure particles, its main limitation is the poor solubility of many polymers in supercritical CO_2 [111]. Additionally, RESS often leads to the formation of microparticles or aggregates due to particle growth during expansion [125]. To address these limitations, RESOLV was developed as a modification of RESS, where the supercritical solution is expanded into a liquid solvent instead of air [126]. This suppresses particle growth and favours the formation of smaller, nanoscale particles. However, issues such as particle aggregation over time and the need for stabilizing agents (e.g., NaCl in the receiving liquid) remain challenges [127]. Overall, the advantages of these supercritical fluid techniques include high product purity, reduced environmental impact and precise control over particle morphology [128] [129]. However, they are also associated with technical complexity, high equipment costs, sensitivity to processing parameters, and limited polymer solubility, which can restrict their broader application [111], [130]. Despite these drawbacks, such methods are increasingly explored: Meziani et al. [127] successfully synthesized poly(heptadecafluorodecyl acrylate) (PHDFDA) NPs with diameters below 50 nm using the RESOLV (Rapid Expansion of Supercritical Solution into Liquid Solvent) technique. These fluorinated PNPs demonstrated excellent colloidal stability in aqueous media and showed potential for therapeutic applications, particularly as contrast agents or drug delivery vehicles due to their unique surface properties and nanoscale dimensions. The authors achieved this by expanding supercritical CO_2 solutions into an aqueous NaCl receiving solution, which helped control particle growth and minimize aggregation.

2.1.7 Traditional synthesis of nanoparticles: Top-down

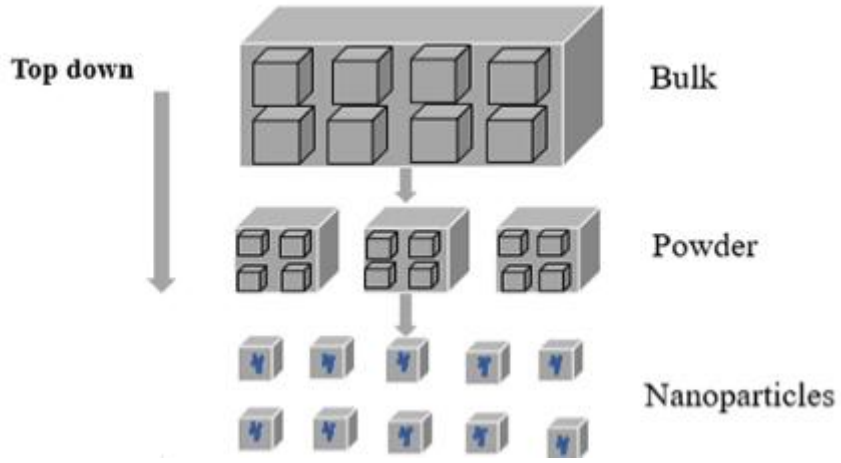

Figure 6: Top-down approach. Image taken from Abid et al. [108]

Figure 6 illustrates the top-down approach, that involves scaling down bulk materials to achieve structures at the nanoscale [108].

Ball milling is the simplest and most efficient mechanical method within the top-down approach, producing nanoparticles through attrition [108]. This technique is based on the application of mechanical energy to materials through impact, friction, shear, and compression within equipment called mills. These mills can be of different types: they can transmit kinetic energy directly to the particles through mechanical elements such as rotating shafts or rollers (direct mill), or the energy is transferred to the mill, which in turn transmits it to the material through friction and centrifugal forces (indirect mill). Compressive, impact, frictional and shear stresses are applied to the material, resulting in fracture, agglomeration and final dispersion of the material, which is the distribution and separation of nanoparticles due to shear effects [131]. This technique is simple, reliable, and safe; however, it is a destructive treatment that can alter the semicrystalline structure of the material and has as disadvantages the noise generated and the risk of contamination [108].

Laser ablation is a technique that uses pulsed laser beams to remove material from a substrate surface, enabling the creation of micro- and nanostructures [108]. The laser energy is absorbed by the electrons in the material, which transfer it to the crystal lattice by electron-photon coupling. If the pulse duration is longer than 1 picosecond the excess energy is converted into heat that melts the material, while if it is shorter the energy is confined to a small volume, leading to ablation by direct sublimation. Ablation generates a plume, a high-temperature, high-pressure cloud containing excited species that expands rapidly, compressing the surrounding gas and generating shock waves. With cooling, nucleation and condensation of the vaporized species occurs, leading to the formation of NPs. Finally, the particles diffuse into the background gas, completing the process [132]. This technique has the advantage of involving low energy loss, making it a very efficient process; on the other hand, to achieve high ablation

efficiency, a significant amount of energy must be used, which can be a limitation in terms of cost and practicality [108].

Another method for the synthesis of nanoparticles is the thermal evaporation that is part of the Physical Vapor Deposition (PVD) techniques and involves the use of heat to induce chemical breakdown [108]. Solid materials are vaporized under vacuum conditions; the atoms or small clusters thus generated condense on surfaces to form thin films or NPs. The use of low vapor pressure liquids, such as silicone oils, vegetable oils or room temperature ionic liquids (RTILs), allows these atoms to be trapped on or within the surface of the liquid, facilitating the controlled formation of dispersed NPs [133]. This process does not require the use of solvents and is particularly suitable for materials with a low melting point; however, it can be complex to deposit certain alloys, making it difficult to achieve certain compositions [108].

Among the various PVD techniques, sputtering is another commonly used method, also belonging to the top-down approach [108]. It is based on the generation of a plasma containing positive ions, usually obtained from noble gases such as argon, which bombard a target consisting of the material to be deposited. The impact causes atoms to be ejected from the target and deposited on the substrate. There are different sputtering configurations, including direct current (DC) sputtering, suitable for conductive materials, radio frequency (RF) sputtering, ideal for insulating materials, and magnetron sputtering, which uses magnetic fields to confine the plasma close to the target, increasing efficiency and deposition rate. The latter is particularly popular due to its high deposition rate and ability to work at lower pressures [134]. This method allows operation at low temperatures and provides a stable, long-lasting vaporization source. Nevertheless, it requires expensive equipment, and sputtering rates are generally low compared to thermal evaporation, which can limit productivity in nanoparticle synthesis [108].

2.2 Pyrrole

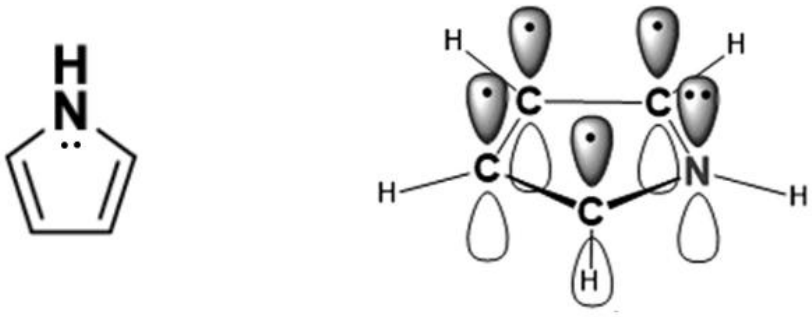

Figure 7: Chemical structure (left) and molecular orbitals (right) of pyrrole.
Images adapted from Su et al. [290] and taken from Szatylowicz et al. [291]7

Pyrrole is an electron-rich heteroaromatic compound, a five-membered ring with six π-electrons, composed of four carbon atoms and one nitrogen atom (**Figure 7**). The nitrogen atom exhibits coordinating properties, enabling the formation of a wide range of metal complexes with pyrrole

derivatives and macrocyclic pyrrolic structures [135]. The name "pyrrole" derives from the Greek word *pyrrols*, meaning "fiery", referring to the red coloration it imparts to wood when moistened with hydrochloric acid. Pyrroles display lower basicity compared to amines and other aromatic compounds containing a pyridine ring. This reduced basicity is due to the delocalization of the nitrogen lone pair within the aromatic system of the pyrrole ring. Pyrrole has a pKa value of 3.8, and protonation disrupts its aromaticity, leading to a loss of this stabilizing feature [136]. Pyrrole itself is not naturally derived, but its analogues are present in various natural products and cofactors such as vitamin B12, bile pigments like bilirubin and biliverdin [137], [138], and porphyrinoids including heme, chlorophyll, chlorins, bacteriochlorins, and porphyrinogens [139], [140], [141], [142].

The pyrrole subunit has a wide range of applications in therapeutically active compounds, including fungicides, antibiotics, anti-inflammatory drugs [143], cholesterol-lowering agents [144], antitumour drugs [145], and more. Pyrrole derivatives are known to inhibit reverse transcriptase from human immunodeficiency virus type 1 (HIV-1), as well as cellular DNA polymerases and protein kinases. Additionally, pyrrole-like units are found in polymers such as those based on thieno[3,4-c]pyrrole-4,6-dione (TPD), which are widely used in organic photovoltaics, [146], in indigoid dyes such as indigo and its derivatives (e.g., indirubin), which contain a fused pyrrole-like ring system that contributes to their intense coloration and electronic properties [144], and in larger aromatic systems such as porphyrins and related heteroaromatics, where the pyrrole unit contributes to the overall aromaticity and electronic delocalization, playing a key role in stability and function [147].

2.3 Polypyrrole

PPy is a conductive polymer with outstanding electrical, physicochemical, and biological properties, that emerged as a promising nanomaterial in various biomedical applications. Its electrical conductivity supports its use in electrically active tissue engineering, such as neural or cardiac regeneration, promoting cell signaling and tissue repair [148], [149]. Furthermore, its inherent biocompatibility, particularly when functionalized or incorporated with natural polymers like chitosan or alginate, enhances cell adhesion and proliferation [148]. This effect is attributed to PPy's tunable electrical properties, which can mimic the native electrical cues of nerve tissues, thus stimulating electrically responsive cells. Additionally, its good environmental and thermal stability, low toxicity, and mechanical properties contribute to creating a supportive microenvironment that promotes cell growth. When combined with hydrophilic and biodegradable polymers like alginate or nanochitosan, the scaffold surface becomes more hydrophilic, further facilitating cell attachment.

PPy NPs are stimuli-responsive materials that can react to a variety of external triggers, including electrical fields, NIR light, pH changes, and temperature variations, making them highly attractive for applications in controlled drug delivery and cancer therapy [150], [151]. Their electrical responsiveness stems from their intrinsic conductivity, due to delocalized π-electrons along their conjugated backbone. This feature enables PPy to be doped with negatively charged therapeutic molecules during synthesis and to subsequently release them upon application of an electric field, a mechanism that allows for precise, on-demand drug delivery with minimal systemic side effects [152]. PPy also exhibits excellent

photothermal properties under NIR irradiation; upon exposure to NIR light, PPy nanoparticles can convert light into heat, causing localized cell damage and enabling photothermal therapy. This approach was shown to effectively kill HEP G2 cells in vitro and enhance the uptake of chemotherapeutic agents such as allicin into tumour tissue, demonstrating synergistic potential when combined with chemotherapy [150]. In terms of pH responsiveness, PPy NPs can modulate drug release based on environmental acidity or alkalinity. Their degree of protonation increases in acidic environments, facilitating the binding of negatively charged drugs, whereas an increase in pH reduces protonation and promotes cargo release. This pH-sensitive behaviour allows PPy systems to be tailored for selective drug release in acidic tumour microenvironments or intracellular compartments [153]. Additionally, temperature-responsive systems incorporating PPy nanogels stabilized with triblock polymers have shown promise in controlled drug release. These soft, injectable platforms respond to temperature changes, forming in situ nanogels that load high amounts of doxorubicin and release it in a sustained manner. Upon NIR irradiation, these nanogels enable effective penetration and therapeutic action within tumours, demonstrating the versatility and potential of PPy-based systems in multi-modal cancer treatment [154].

Additionally, PPy NPs can be chemically modified with targeting ligands or bioactive molecules, enabling targeted delivery and multifunctional therapeutic platforms [5], [151]. The material also integrates well with other biocompatible scaffolds and hydrogels, leading to the development of electroconductive composite scaffolds for tissue engineering [148], [149]. In neural tissue engineering, Manzari-Tavakoli et al. [148] incorporated PPy into alginate and further reinforced it with nanochitosan, forming a nanocomposite scaffold with high conductivity, hydrophilicity, porosity, and mechanical stability. This composite supported excellent cytocompatibility and promoted the adhesion and proliferation of both OLN-93 neural cells and fibroblasts, making it a promising candidate for neural regeneration strategies. Additionally, the use of chitosan NPs enhanced surface hydrophilicity and provided a favourable microenvironment for cellular interactions. In bone tissue engineering, electrospun nanofibrous scaffolds composed of a polycaprolactone (PCL) matrix with in situ polymerized PPy NPs demonstrated a significant improvement in conductivity, surface roughness, and mechanical strength. These scaffolds closely mimicked the extracellular matrix, offering a high surface-area-to-volume ratio ideal for cell attachment. Under electrical stimulation, they significantly enhanced osteoblast-like MC3T3-E1 cell proliferation and differentiation, as evidenced by increased ALP activity and mineralization [149].

2.4 Plasma technology: overview

Conventional methods, as described above, are being widely used for the synthesis of NPs. However, several limitations, such as the use of toxic organic solvents, the presence of surfactants, complex purification procedures, limited polymer compatibility, colloidal instability, poor control over particle size and morphology, long processing times, high technical complexity, and elevated equipment costs, have driven research toward alternative approaches. Among these, plasma-based synthesis has gained increasing attention, offering several advantages [155]

2.4.1 Plasma, the fourth state of the matter

Plasma is defined as the `fourth state of the matter', and it is the predominant state of matter in the known universe, as it constitutes stars, the solar wind, and nebulae [156]

It is well-known that by supplying energy to matter, it transitions from the solid to the liquid state, and eventually to the gaseous state. However, if energy continues to be supplied to a gas, the gas particles absorb enough energy to overcome the attractive forces binding electrons to atomic nuclei, resulting in the partial or complete removal of electrons from atoms or molecules. This process, known as ionization, leads to the formation of an entirely new state of matter: plasma [157].

Plasma consists of a mixture of charged particles, including free electrons and positive ions, along with neutral particles such as non-ionized atoms and molecules [158].

Different parameters can be used to classify the diversity of plasma types that exist in nature or can be generated artificially. The main classification is based on their thermal equilibrium, whether the temperature or average energy of the particles that compose them is uniform across different particle types [159].

2.4.2 Thermal plasmas

Thermal plasmas are in ‘thermal equilibrium’ since both the electrons and the heavy species, such as neutral particles and ions, reach the same temperatures. These temperatures are extremely high, equivalent to millions of kelvins, typically in the range of 1,000,000 to 100,000,000 K [160].

Such high temperatures make thermal plasmas widely used in industrial applications [161]. Due to their high energy density and precision, thermal plasmas are widely used for cutting metals, a process that involves localized melting and removal of molten material by high-velocity plasma jets [162]. They are also employed for welding metals, particularly stainless steels and carbon steels, offering advantages such as deep penetration and minimal distortion [163]. Plasma spraying is another key application, where particles are melted in the plasma jet and accelerated onto substrates to form coatings for wear resistance, thermal insulation, and corrosion protection [164]. Thermal plasmas also play a critical role in metallurgical processes, including remelting and purification of metals like titanium and aluminium [165], as well as reheating molten steel in tundishes to maintain optimal casting temperatures [166]. In chemical synthesis, plasmas enable high-temperature reactions for producing acetylene [167] and TiO_2 pigments [168]. Finally, thermal plasmas are increasingly used in waste treatment, where they destroy

hazardous and radioactive materials through pyrolysis and vitrification, minimizing harmful byproducts [169], [170].

2.4.3 Non-thermal plasmas

In contrast, non-thermal plasmas, also referred to as cold plasmas, are characterized by a significant disparity between the temperatures of their constituent particles. The heavy species, including ions and neutral atoms, remain at relatively low temperatures, close to room temperature, typically ranging from 300 to 500 K. Meanwhile, the electrons in non-thermal plasmas exhibit much higher temperatures, often reaching values between 10,000 and 100,000 K, but due to their small mass the effect of the temperature on the plasma is negligible [160]. This thermal imbalance allows this type of plasmas to exist under conditions where the overall gas temperature remains low, making them suitable for a variety of applications [157].

In the last two decades, increasing attention has been given to non-equilibrium plasmas, particularly in the biomedical field, due to their singular properties. One of their key advantages lies in their ability to interact with materials without excessive heating, which is crucial for applications involving biological tissues or heat-sensitive materials [171]. Additionally, non-equilibrium plasmas are highly effective in generating a wide array of reactive components, including charged particles (electrons and ions), neutral metastable species, radicals, and a diverse group of reactive oxygen and nitrogen species (RONS), such as singlet oxygen ($^1O_2$), ozone (O_3), hydroxyl radicals (•OH), hydrogen peroxide (H_2O_2), nitric oxide (NO), and nitrogen dioxide (NO_2). [171]. These reactive species play a fundamental role in several biomedical applications, such as sterilization, wound healing, cancer therapy, and drug delivery [172].

2.4.4 Atmospheric Pressure Plasma

Cold plasmas can be generated under a wide range of conditions depending on the intended application. One of the key parameters is the gas pressure. At a fixed gas temperature, pressure determines the overall density of gas particles, which in turn affects the frequency of collisions between them. As pressure increases, collisions become more frequent, thereby increasing the likelihood that particles will eventually reach a steady-state energy equilibrium [173].

In the 20th century non-equilibrium plasmas at reduced gas pressure ($p < 133$ mbar) became a widely used industrial technology for coating and have been applied to surface processing. These systems require expensive vacuum systems and pumps, for this reason, there has been a growing interest, mainly over the last two decades, to replace these systems by non-equilibrium cold atmospheric plasmas [173]. APP can be generated using different techniques, each with specific characteristics and applications [174]. One common method is Dielectric Barrier Discharge (DBD), in which a high voltage alternating current is applied between two electrodes separated by a dielectric material. This configuration prevents arc formation and produces a uniform plasma, making it ideal for surface treatments such as polymer modification and sterilization [175]. Microwave Atmospheric Plasma is another technique that uses microwave energy to generate a stable, high-density plasma without direct electrode contact, which is particularly useful for advanced chemical processing and surface engineering [175]. Plasma Pens or Cold Plasma devices generate a localized, low-temperature plasma, often used in medicine for wound

healing, disinfection, and tissue activation. Another approach is the APPJ, in which a gas flow, typically helium or argon mixed with reactive species, is ionized by an electric field [175].
APPJs have been studied for over 50 years, during which their design and plasma generation mechanisms have evolved and been tailored to suit a wide range of applications [172]. These devices offer the significant advantage that the discharge region, where breakdown takes place, is separated from the treatment area. As a result, a plasma plume extending several centimetres into the surrounding air is generated, making them suitable for the direct treatment of targets of various sizes. [176].
One of the main benefits of APPJs is their ability to operate at low temperatures, making them ideal for substrates that are heat-sensitive [177]. Another significant advantage is that they do not require vacuum chambers or complex pumping systems, typically a major source of cost and maintenance in traditional plasma systems. This simplification not only reduces energy consumption but also facilitates system setup, making the technology more accessible for large-scale use [175]. Moreover, APPJs are highly versatile: they can operate at low power and across a wide frequency range, including direct current (DC), alternating current (AC), radio frequency (RF), and microwave sources [178].
A crucial environmental benefit of plasma-based processes is their eco-friendly nature, offering a clean alternative to conventional methods that often involve toxic chemicals and organic solvents. This reduces both environmental and health risks, promoting a more sustainable approach to NP production. As a result, APPJs are particularly suitable for biomedical and environmental applications, where compatibility with organic materials and low ecological impact are of central importance [8].
Recent studies have demonstrated that plasma-synthesised materials often exhibit superior chemical and physical properties compared to those produced through conventional methods [179]. For instance, NPs synthesised using plasma jets exhibit improved dimensional uniformity and a more homogeneous distribution on treated surfaces, making them particularly suitable for medical applications such as drug delivery systems and antibacterial coatings for implantable devices [180]. Furthermore, plasma's ability to activate surfaces and modify chemical properties expands its potential to a wide array of advanced applications, including catalysis [181], sensor development [182], and the fabrication of functional materials for electronics and energy sectors [183]. In conclusion, the synthesis of NPs using APPJ technology presents a compelling alternative to traditional methods. Shorter processing times, the elimination of hazardous chemicals, energy efficiency, and compatibility with a broad range of materials make this approach highly innovative, versatile, and sustainable [179]

2.4.5 Atmospheric Pressure Plasma Jet Devices

Plasma jets represent a versatile and constantly evolving technology, with different variants differing in terms of power mode, excitation frequencies and applications [172].
DC plasma jets operate at atmospheric pressure and are widely used due to their ability to generate reactive chemical species. Among the most studied configurations are micro cathode discharge jets, which can produce high ozone concentrations and allow control of plasma properties by varying the gas composition and discharge current [184]. These devices are promising for biomedical applications due to their flexibility in producing reactive species. Other models, such as the plasma jet with an internal electrode and external mesh, are used for thin film deposition [185], while pure oxygen plasma jets have

shown efficacy in sterilising bacteria such as Escherichia coli by exploiting reactive species such as ozone and singlet oxygen [186]. Applications range from medicine to decontamination, with the additional potential to reduce thermal damage on heat-sensitive materials [172].

Pulsed DC plasma jets are distinguished from DC models by their self-pulsed behaviour, in which plasma discharge occurs via high-voltage pulses or in self-oscillating mode. These devices, such as the pin-to-mesh configuration, generate plasma at controllable temperatures and reactive chemical species such as ozone and nitric oxide, finding applications in plasma medicine [187] . The use of nanosecond transient spark discharges in some studies has shown how rapid repetition of discharges can generate extremely short discharge events, optimising interaction with surfaces [188]. An interesting example of this type of device is the brush plasma jet developed for large surface treatments, where the discharge propagates in a wide jet thanks to a sliding arc between tungsten electrodes [189]. Furthermore, research on the sterilisation of bacterial biofilms highlights the potential of pulsed plasma jets in inactivating microorganisms on sensitive biological surfaces [172].

Plasma jets operating at kHz and RF frequencies represent an advanced class of devices operating at high frequencies, such as 30 kHz or 13.56 MHz, and are used in numerous fields, including surface modification and thin-film deposition. For example, 30 kHz plasma jets can operate in low-power and high-power modes, enabling the analysis of micro-discharges in relation to electrode geometry [190]. Other models, such as the radiofrequency Kinpen, are particularly relevant in biomedicine, where the modulation of reactive species in plasma, such as ozone and hydrogen peroxide, may have applications in wound treatment or sterilisation [191].

Microwave plasma jets are a further development that has led to devices capable of generating plasma without the use of mechanical ignition components, improving the stability and reproducibility of the process [192]. Such devices are capable of operating at low power, controllable temperatures, and are used in biomedical applications, such as the sterilisation of bacteria, where UV-C radiation and hydrogen peroxide formation contribute to microbial inactivation. Miniaturised microwave devices, operating at lower powers, also offer opportunities for portable applications, such as pollutant detection. The miniaturisation of microwave plasma jets has paved the way for more compact and efficient solutions for the sterilisation and treatment of delicate surfaces [193].

As result, the growing variety of plasma jet devices and different operating modes (continuous, pulsed, microwave) offer ample customisation possibilities for all kinds of applications. Current research focuses on optimising the production of reactive species, the manipulation of plasma chemistry and the effectiveness of treatments, with the aim of making these devices increasingly versatile and efficient for uses ranging from medicine to environmental technology [172].

2.4.6 Application of atmospheric pressure plasmas

Plasma treatment is widely used to modify polymer surfaces, with objectives ranging from surface activation to improve adhesion, cleaning, modification of hydrophobic or hydrophilic properties, and even etching of polymers. The use of atmospheric radiofrequency plasma jets has proven effective for the treatment of materials, especially heat-sensitive ones. For example, argon plasma treatment can improve the hydrophilic character of some materials, as demonstrated by the reduction in the contact

angle of water on PET surfaces after treatment [194]. Polymers, generally having a low surface energy, present adhesion problems. APPJ treatment has been successfully used to increase surface energy and improve adhesion. Tissues can also be treated with APPJ. Treatment with helium or oxygen plasma has been shown to be effective in cleaning cotton fabrics, making it a more efficient alternative to wet cleaning [194].

Another application can be found in the deposition of coatings by APPJs, a more complex process than simple surface treatment as it requires the introduction of a precursor in vapour form. Liquid precursors are atomised or vaporised before being transferred into the working volume of the APPJ [194]. These devices are widely used for the deposition of ZnO films, using organometallic precursors, organic or inorganic solutions. Such coatings have different functionalities, they can be exploited to improve a material's electrical properties, transparency, corrosion resistance or to fabricate micropatterns on the surface. Although most applications of APPJs involve the deposition of oxides, the possibility of depositing metallic coatings has also been demonstrated, resulting in high-purity coatings [195]. Plasma is widely used for applications such as sterilisation and tissue regeneration. However, the use of high-temperature plasma in therapeutic settings can cause serious damage to living tissue. The generation of low-temperature (30-50°C) atmospheric plasmas, which retain the same beneficial properties as hot plasma, offers great potential for biomedical applications, including sterilisation, bacterial inactivation, dentistry, wound healing and cancer treatment. Reactive species in plasma (such as O, NO and OH) have been shown to play a key role in sterilisation, causing the inactivation of bacteria such as Staphylococcus aureus and Escherichia coli [196], [197]. Factors such as the distance to the nozzle and the composition of the gas influence the effectiveness of the treatment. The use of helium with small amounts of oxygen (0.2 \%) showed a high bacterial inactivation efficiency. Plasma has also been used in dentistry to sterilise root canals [198] modify the surface of enamel and dentin [199] and improve the effectiveness of hydrogen peroxide bleaching [200]. APPJs have also been tested for the treatment of chronic infected wounds, demonstrating efficacy without causing pain to patients [201]. Furthermore, cold plasma has shown great potential in cancer therapy by selectively inducing oxidative stress in cancer cells without damaging healthy ones. Studies on melanoma, colon, breast and brain cancer cells have shown a reduction in their viability after plasma treatment, especially with the addition of oxygen to the working gas [194].

One of the most interesting applications of the APPJ, as illustrated above, is the generation of NPs. For example, a single-step process has been developed to synthesise crystalline Li4Ti5O12 (LTO) particles directly from a solution containing titanium ions and lithium, transported by carrier gas. By adjusting the operating conditions, particles with diameters ranging from 100 nm to several micrometres can be obtained [202]. Another study, by J. Cao et al, described the synthesis of hollow NPs using plasma polymerisation [203]. A low-pressure plasma was used to polymerise various organic precursors, sixteen different molecules were tested, and it was found that twelve of them formed hollow particles in a reproducible manner. The particle sizes ranged from 70 nm to almost 1 μm, with the hollow core diameter averaging 18\% of the particle diameter. The method described is a single-pass, low-temperature process that produces submicron-sized hollow particles. These particles could be useful for the encapsulation and controlled release of molecules. Habib et al investigated the synthesis of silver nanoparticles using a helium plasma jet at atmospheric pressure [204]. Silver nitrate was used as a precursor and trisodium citrate as a coating agent. The effect of various chemical parameters, such as

the concentration of silver nitrate and citrate, on NP synthesis was examined. The NPs were characterised by transmission electron microscopy and dynamic light scattering analysis. The results showed that the concentration of citrate significantly influences the morphology and size distribution of the NPs, with lower concentrations producing spherical and monodisperse particles, while higher concentrations lead to agglomerated and larger particles. The proposed methodology was found to be advantageous for the rapid production of silver NPs under favourable environmental conditions, with potential applications in catalysis, bioactivity, enhanced Raman scattering and photonics.

2.5 Formation of reactive species

The number of species generated is very large, making it very difficult to obtain complete experimental information on the chemical composition of the gas in the jet effluent. Several parameters, such as the gas flow, electrodynamic processes, discharge dynamics and kinetics, chemical transformations can influence the production of reactive species [205]. Additionally, the mixing of plasma-forming gases (usually He or Ar) with ambient air (N_2, O_2, H_2O) is typically described by coupled Navier–Stokes and diffusion equations, which yield the spatial distribution of neutral species and serve as a basis for discharge modelling [206].

However, based on the work of Lu X et al. [205], some of the main reactive species produced by Cold Atmospheric Pressure Plasma Jets (APPJs) can be identified as follows:

- Reactive Oxygen Species (ROS): Atomic Oxygen (O), Ozone (O_3), Hydrogen Peroxide (H_2O_2), Hydroxyl Radical ($OH^{\cdot}$), Superoxide Anion (O_2^{-})
- Reactive Nitrogen Species (RNS): Nitric Oxide (NO), Nitrogen Dioxide (NO_2)
- Electrons and Ions: Free electrons, positive and negative ions
- Metastable species: excited states of helium (He^*) and argon (Ar^*), depending on the chosen gas

The formation of these reactive species begins with ionization and dissociation processes. Collisions of high-energy electrons with neutral gas molecules such as oxygen, nitrogen, or water vapor can break molecular bonds, forming radicals and ions. Molecular oxygen can dissociate into two oxygen atoms, and nitrogen molecules can be excited to metastable states. These initiating reactions set the stage for further chemical processes [205].

One of the most significant reactions in APPJs is the production of ozone and atomic oxygen. Oxygen molecules, when impacted by high-energy electrons, can split into highly reactive atomic oxygen, which then combines with other oxygen molecules to form ozone. Similarly, reactive nitrogen species are formed when excited nitrogen molecules react with oxygen to produce nitric oxide and nitrogen dioxide, both of which play important roles in biological and environmental processes [207].

When plasma comes into contact with liquids, the process becomes even more complex. Reactive species can diffuse into the liquid phase, triggering additional reactions that produce hydrogen peroxide and other reactive compounds. [208].

The formation of these reactive species plays a central role in plasma medicine, where they are considered key therapeutic agents [205]. Early studies showed that these species can effectively inactivate a broad spectrum of pathogens, including antibiotic-resistant bacteria, without harming

surrounding healthy tissue [209]. Moreover, under carefully controlled conditions, plasma-generated reactive species can promote fibroblast proliferation, supporting wound healing [210], and selectively trigger apoptosis in cancer cells via redox-sensitive signaling pathways [211].

2.6 Helium

Helium is the second most abundant element in the universe. It is a very light (4 g/mol), odourless, tasteless, and colourless noble gas, characterized by its chemical inertness, non-flammability and low toxicity. These properties contribute to its excellent safety record, making it suitable for use in sensitive environments, including medical applications [212]. Helium's unique physical properties, such as low density, low solubility, and high thermal conductivity, enable its use in several fields, among which respiratory therapy [213], cardiovascular protection during ischemic events [214], abdominal insufflation in laparoscopic surgery [215], magnetic resonance imaging (MRI) imaging of the lungs using hyperpolarized helium [216], and high-resolution imaging via helium ion microscopy [217].

He as a discharge gas exhibits low breakdown voltage, low gas temperature, and a stable glow discharge, which is maintained over a wide range of operating conditions including varying, input RF power levels, gas flow rates, and discharge gap configurations [218].

Comparative studies of atmospheric pressure plasma characteristics between helium and argon as discharge gases have demonstrated the advantages of using helium for plasma generation at atmospheric pressure The results showed that the breakdown voltage required for helium was less than 3 kV, whereas argon required approximately 5.5 kV to initiate a plasma discharge in a jet. Furthermore, the current waveform was more stable in the case of helium, while argon exhibited greater distortion. The rotational temperature was found to be higher in argon plasma compared to helium plasma, which is a crucial parameter when aiming to avoid excessive heating during the nanoparticle formation process. This temperature difference was attributed to the disparity in thermal conductivity between the two gases: helium has a thermal conductivity of 0.1415 $W \cdot m^{-1} \cdot K^{-1}$, while argon has a much lower value of 0.0162 $W \cdot m^{-1} \cdot K^{-1}$. Helium's higher thermal conductivity enables more effective transfer and dissipation of thermal energy compared to argon. The plasma jet length, defined as the visible plume extending from the APPJ nozzle, was found to depend on the gas flow rate. Under the same flow conditions (2 to 5 L/min), the helium plasma effluent was longer than the argon plasma effluent. However, the helium jet was also more sensitive to variations in gas flow rate and applied voltage. This sensitivity, particularly the transition from laminar to turbulent flow in helium at higher flow rates (notably between 4 and 6 L/min), can be mitigated by optimizing the flow regime through careful adjustment of flow rate and nozzle geometry to maintain laminar conditions. Additionally, operating at voltages that balance jet stability and discharge length, avoiding extremes that promote instability, can further enhance effluent control [219].

2.7 Characterization techniques

This chapter provides an overview of the principles and applications of SEM, FTIR, XPS, and OES used in this study.

2.7.1 SEM (Scanning Electron Microscopy)

Scanning Electron Microscopy (SEM) is a powerful and widely used technique for characterizing the surface morphology and composition of materials at the micro- and nanoscale. Due to its versatility, SEM is employed across numerous scientific and engineering disciplines, from materials science to biology. It is particularly effective for analysing both organic and inorganic surfaces, offering high spatial resolution and depth of field [220].

Unlike conventional optical microscopy, which is limited to a maximum useful magnification of approximately 1000× due to the wavelength of visible light, SEM overcomes this limitation by utilising a focused beam of high-energy electrons. These electrons are typically accelerated to energies between 2 and 30 kiloelectronvolts (keV), with some instruments reaching up to 1000 keV. At such energies, the associated electron wavelengths are extremely short (ranging from 0.027 to 0.0009 nm), enabling magnifications of up to 300,000× or more, up to 1,000,000× in advanced systems [220], [221].

When the electron beam interacts with the surface of a specimen, it generates a variety of signals due to multiple types of interactions with the atoms in the sample. These signals include: secondary electrons (SEs), backscattered electrons (BSEs), characteristic X-rays, Auger electrons, cathodoluminescence (CL), electron beam-induced current (EBIC). Each of these carries different types of information, such as surface topography, elemental composition, electronic properties, and crystal structure [221]. Among these, secondary electrons (SEs) and backscattered electrons (BSEs) are the most commonly used for imaging. SEs are generated when the primary beam transfers energy to loosely bound electrons in the sample, causing their emission from the very surface (typically within a few nanometres depth). These low-energy electrons are highly surface-sensitive and provide excellent topographic contrast and high spatial resolution, making them ideal for observing surface morphology and fine details [221].

In contrast, backscattered electrons (BSEs) result from elastic collisions between the primary electrons and atomic nuclei. They originate from deeper regions within the sample and are more sensitive to the atomic number of the constituent elements. As a result, BSE images are particularly useful for compositional contrast, since heavier elements scatter electrons more effectively and appear brighter. Though BSE images offer slightly lower resolution than SE images, they are invaluable for distinguishing between materials and analysing phase distributions, especially in heterogeneous or multiphase samples [221].

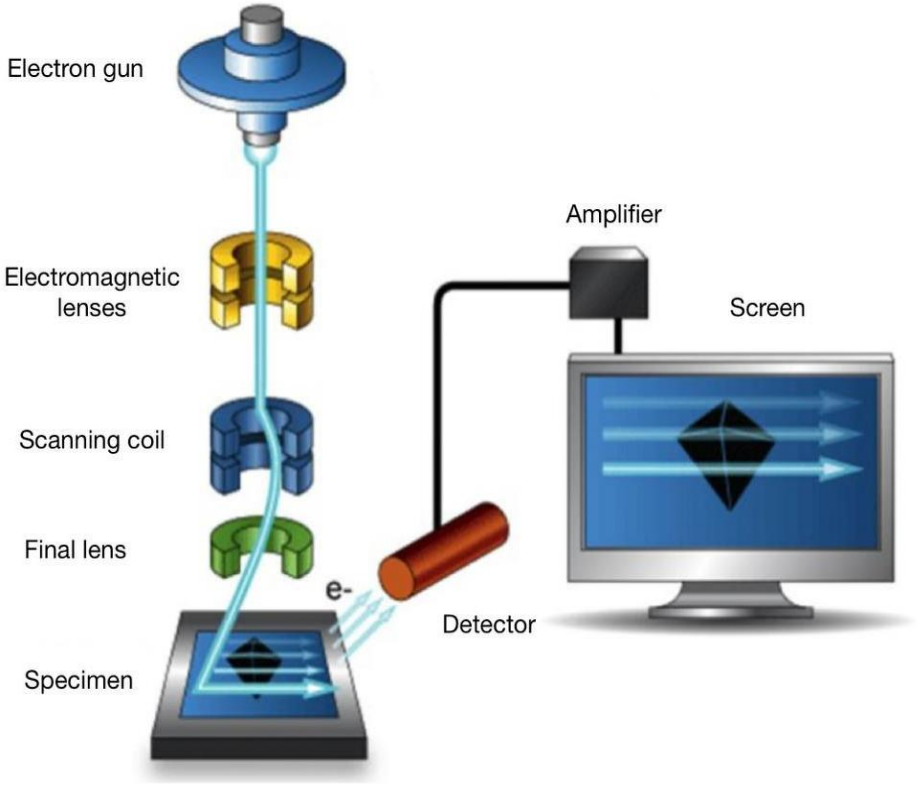

Figure 8: SEM components, adapted from Abdullah et al. [220].

To produce a finely focused electron beam, SEM instruments use a series of electromagnetic lenses and apertures, which narrow the beam diameter down to the nanometre scale. The imaging process takes place in a high-vacuum environment to prevent scattering of the electrons by air molecules. For non-conductive or low-contrast samples, such as polymers or biological materials mainly composed of light elements, it is common to apply a thin conductive coating (e.g., gold or platinum) to improve imaging quality and reduce charging effects. A typical SEM system includes several key components, as shown in the **Figure 8**: an electron gun to generate the electron beam, electromagnetic lenses for beam shaping and focusing, a scanning coil to raster the beam over the sample, detectors (such as SE and BSE detectors) to capture emitted signals, a specimen stage and a vacuum chamber to maintain the required environment [222].

SEM was employed to analyse the morphology of the synthesised NPs. SEM imaging revealed the presence of either nanoparticle deposition or continuous film formation, depending on the sample, through surface and cross-sectional analysis. To quantify NP size, ImageJ software was used to measure the diameters under each experimental condition. From these measurements, the average diameter and standard deviation were calculated.

2.7.2 Fourier transform Infrared spectroscopy (FTIR)

Fourier Transform Infrared (FTIR) spectroscopy is based on the interaction of infrared radiation with the functional groups within the analysed sample. As the infrared light passes through the sample, part of it is absorbed while the rest is transmitted. The resulting spectrum reflects the molecular absorption and transmission characteristics, effectively creating a molecular "fingerprint" of the sample. Each material exhibits a unique pattern of absorption peaks, which correspond to the vibrational frequencies of the chemical bonds between its atoms. these include stretching and bending vibrations such as symmetric and asymmetric stretching (e.g., C–H, N–H, O–H) and bending modes like scissoring, rocking, wagging, and twisting, typically observed in the mid-infrared region (4000–400 cm^{-1}) [223]

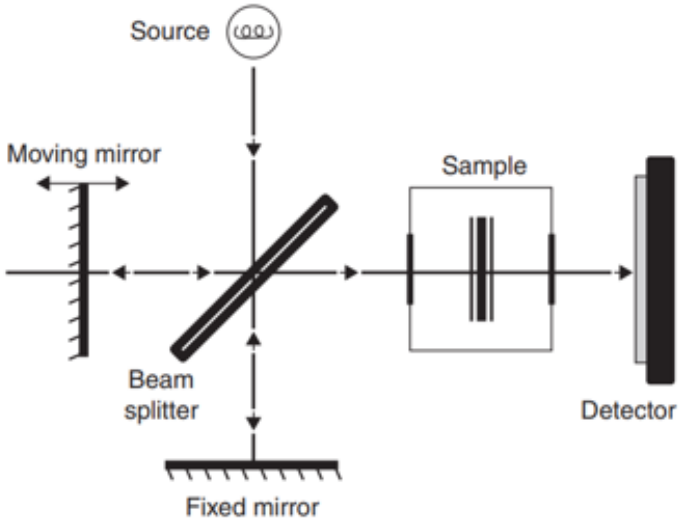

Figure 9: Schematic representation of a basic interferometer setup. Image taken from Mohamed et al. [292]

FTIR represents an advancement over traditional IR spectroscopy through the incorporation of a Michelson interferometer. This component is fundamental to FTIR instruments, as it splits a single beam of light into two separate paths, then recombines them and directs the resulting beam to the detector. The detector measures the intensity differences between the two beams as a function of their path length differences [224].

FTIR spectroscopy operates on the principle that the interference between these two beams produces an interferogram, a signal that varies with the optical path difference created by the mirrors in the interferometer block **(Figure 9)**. The data in the time (or distance) domain can then be converted into the frequency domain using a mathematical technique called Fourier transformation, which gives the method its name: Fourier Transform Infrared Spectroscopy [223].

Since each material is composed of a unique combination of atoms, no two compounds produce identical infrared spectra. As a result, infrared spectroscopy enables the reliable identification of different substances. Additionally, the intensity of the peaks in the spectrum directly correlates with the quantity of material present in the sample [225]

This device is widely used because of its high precision, accuracy, speed of analysis, enhanced sensitivity, ease of operation, and sample non-destructiveness. FTIR can quantify the components even

when present in low concentrations, and is particularly effective for assessing the composition, quality, and consistency of materials. Its ability to collect data over a wide spectral range in a single measurement significantly reduces analysis time while maintaining high spectral resolution. All these benefits contribute to the high accuracy and reproducibility of measurements obtained through FTIR [226].
FTIR was employed to obtain chemical analysis of the deposited NPs.

2.7.3 X-Ray Photoelectron Spectroscopy (XPS)

X-ray Photoelectron Spectroscopy (XPS) is widely recognized as a crucial technique for the surface characterization and analysis [227]. This technique enables comprehensive elemental analysis, excluding hydrogen and helium, of the top 10 to 200 Å of any solid surface that is vacuum-stable or can be stabilized under vacuum conditions through cooling. Additionally, it provides valuable information on the chemical bonding states of the detected elements [227]. As a result, this technique gives information on chemical composition, oxidation state, and coordination number [228].

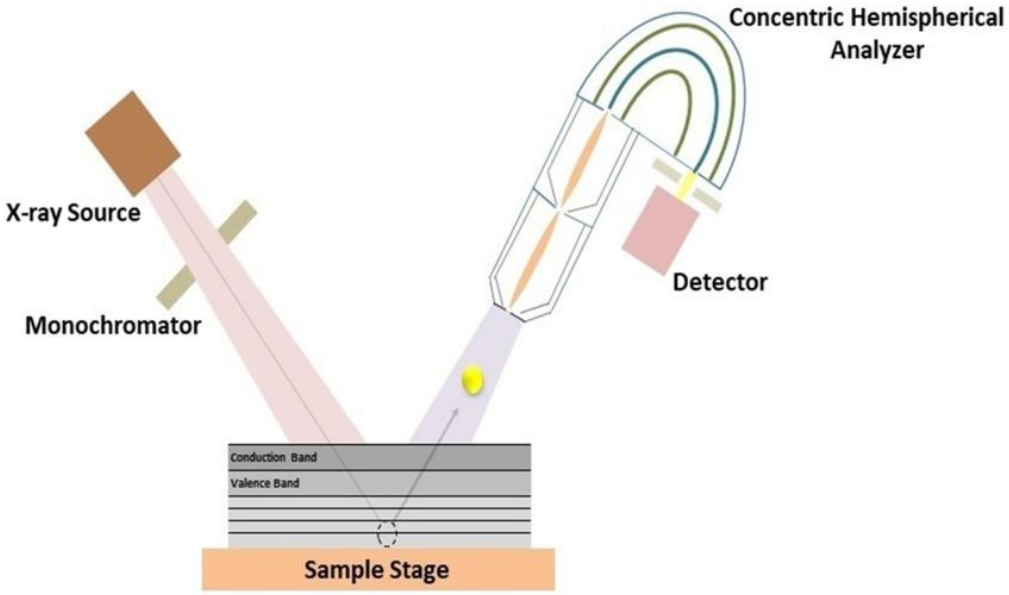

Figure 10: Basic schematic of an XPS measurement system. Image taken from Magdy et al. [230]

The principles of XPS are based on the photoelectric effect [229]. When a solid is bombarded with photons of energy *hv,* it emits photoelectrons from its surface. The kinetic energy of the photoelectrons is measured by a spectrometer, which provides a spectrum consisting in a series of discrete bands and the energy of these photo peaks reflects the electronic structure of the atoms present at the solid surface [228]. The device is composed of four main components: an X-ray source, a monochromator, an analyser and finally a detector [230] (**Figure 10**).
XPS is particularly useful for confirming the presence of surface functional groups and it was employed to study the chemical composition of the nanoparticles surface.

2.7.4 Optical Emission Spectroscopy (OES)

Optical Emission Spectroscopy emission is an analytical technique that involves the collection, spectral dispersion, and detection of light from 200–900 nm [231]. This characterization technique is widely used because it offers fast, accurate elemental analysis allowing for material certification, quality checking, or to identify an unknown material. OES provides both qualitative (element identification) and quantitative (element concentration) information about the analysed sample [232].

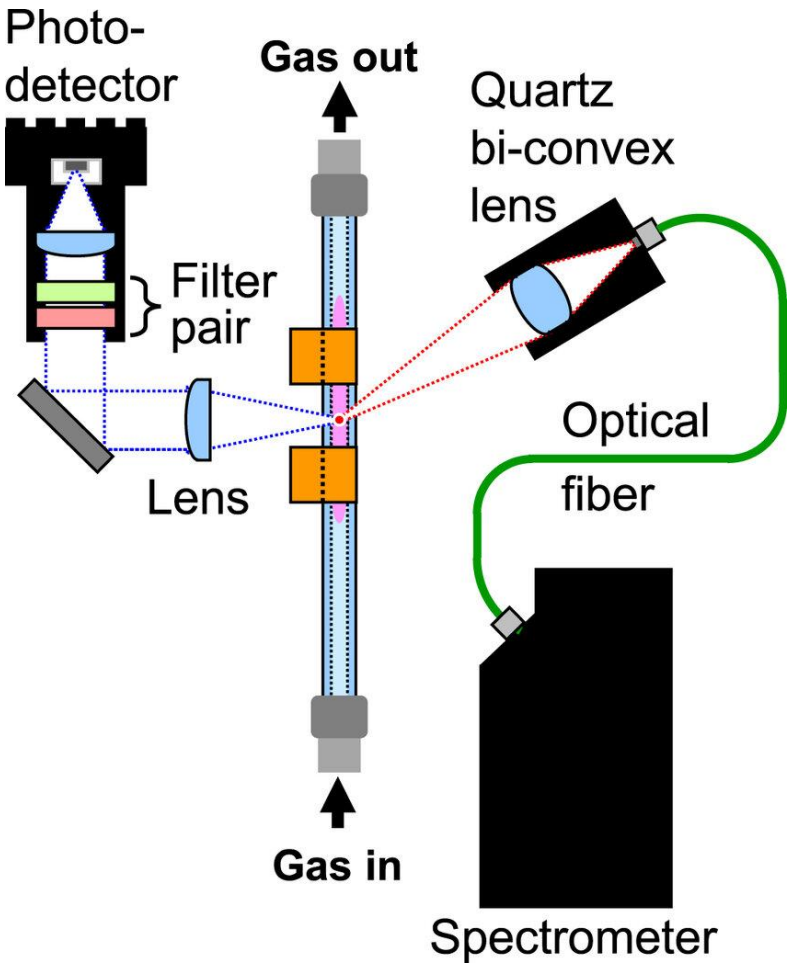

Figure 11: Basic schematic of an OES measurement system.
Image taken from Urabe et al. [293]

The four major components of an OES device are: an excitation generator, an optical device that captures light, a photodetector, and a spectrometer for signal read-out (**Figure 11**). When the energy from an electrical discharge interacts with an atom, outer-shell electrons are ejected, creating a vacancy that makes the atom unstable. To restore stability, an electron from a higher orbit falls into the vacancy, releasing excess energy as element-specific light. Each element produces a unique set of spectral lines resulting from electronic transitions between discrete energy levels. When electrons in the plasma

collide with atoms or ions, they can excite their electrons to higher energy states. As these electrons return to lower energy levels, they emit photons with specific wavelengths. The emitted light is directed into an optical system, where a diffraction grating separates the wavelengths. Detectors capture the intensity of each spectral line, generating a spectrum that plots light intensity versus wavelength [233]. With the resulting spectrum, it is possible to perform a qualitative analysis of the elemental composition and, to some extent, a quantitative one. However, quantitative analysis is more difficult because the intensity of the emitted light is not only related to the concentration of the species, but also depends on other factors, such as the number of electrons in the plasma and how efficiently these electrons can excite the species. Since these factors change with conditions like power, pressure, and gas mixture, the relationship between intensity and concentration is not fixed and can vary significantly [234].
OES was employed to study the chemical composition of the generated plasma.

CHAPTER 3

Materials and Methods

3.1 Experimental setup

This section describes the experimental apparatus used for the plasma-based synthesis of NPs, detailing the configuration of the system and the key components involved.

3.1.1 Description of the single electrode APPJ-array generator

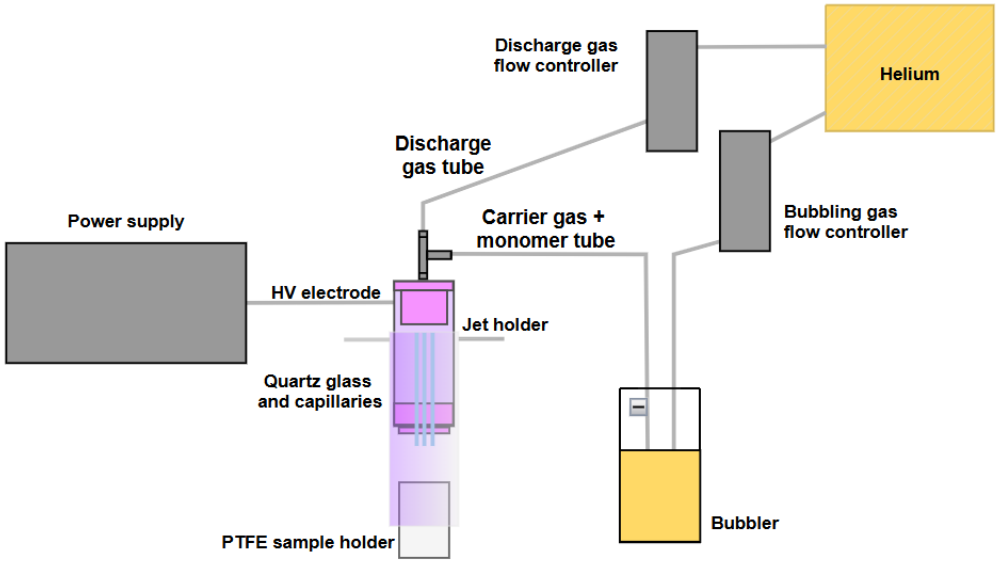

Figure 12: Schematic representation of the used single electrode APPJ- array

The employed device consists of seven quartz capillaries, each with a length of 7 cm, an inner diameter of 1 mm, and an outer diameter of 3 mm, enclosed in a quartz glass housing. It includes a high voltage electrode connected to an alternating current-driven, and custom-made power supply operating at 50 kHz frequency a bubbling gas and precursor tube, and a discharge gas tube.

For precise tuning of the bubbling and discharge gas flows, two separate mass flow controllers (Bronkhorst) were employed. The mass flow controller for the discharge gas has a maximum flow rate

of 500 standard cubic centimeters per minute (sccm), while the one for the precursor + bubbling gas has a maximum flow rate of 10 standard liters per minute (slm).
The bubbling gas (which, in this case, is the same as the discharge gas) passes through the bubbler containing the liquid precursor. This causes the precursor to vaporize and mix with the bubbling gas which is then pressurised by the incoming flow of the gas to the jet.
Inside the capillaries, where the plasma is present, the mixture of electrons, ions, excited species, and radicals interacts with the precursor molecules as it flows through the plasma zone, leading to fragmentation, polymerization and NP formation. Specifically, the plasma energy breaks the chemical bonds of the precursor, forming reactive radicals. These radicals recombine to initiate polymerization, resulting in the formation of oligomers. If enough radicals are present, they can also collide and form NPs. These NPs continue to grow either by further precursor addition or by particle-particle fusion [235].
The synthesised NPs were deposited and analysed on circular microscope glass cover slips with a 25 mm diameter.

3.1.2 Process Parameters of the Plasma Jet-array

Throughout the experiments, the discharge gas and bubbling gas used to generate the plasma remained unchanged: helium (Air Liquide-Alphagaz 1, 99.999% purity) was used in both cases. The liquid precursor was pyrrole (Sigma-Aldrich, reagent grade, 98%), which gave rise to pyrrole-based NPs.
Initial experiments were conducted by varying the ratios between the discharge gas and the precursor+bubbling gas, but keeping constant the total gas flow, to assess its influence on the deposition process. Once an optimal flow rate was identified, this was kept constant for subsequent experiments. Subsequent tests were then performed by varying, for each set, a single parameter at a time, while keeping all the others constant, to isolate the specific effect of each variable on nanoparticle formation.

3.2 Experimental conditions

In this section the process conditions applied during the experiments and the sample preparation procedure are outlined to provide context for the subsequent analysis.

3.2.1 Varied experimental conditions

The samples were prepared by exposing the substrates to the plasma jet-array under varying experimental conditions, according to the parameter being investigated. The parameters analysed were the ratio between the flow rate of the discharge gas and the flow rate of the bubbling gas and the liquid pyrrole, the distance between the tip of the capillaries and the substrate, and the input voltage applied to generate the plasma. For each set of experiments, a single parameter was varied at a time, while keeping all others constant, as described earlier.

Table 1: Tested ratios between discharge gas and monomer + carrier gas flows

Monomer + bubbling gas flow rate (sccm)	Discharge gas flow rate (slm)
10	1.99
25	1.975
50	1.95
100	1.90
150	1.85
200	1.80
250	1.75
300	1.70
350	1.65
400	1.60
450	1.55
500	1.50

In the first set of experiments, the parameter that was varied was the ratio between the discharge gas and the carrier gas carrying the precursor, while keeping the total gas flow constant at 2 slm. The ratios of the components are depicted in **Table 1.**
In this series of experiments, the following conditions were kept constant: an input voltage of 9 kV, a distance of 5 cm between the tip of the capillaries and the substrate, and a deposition time of 60 s.

Table 2: Tested capillaries-to-substrate distances

Distance from capillaries (cm)
3
4
5
6
7

Subsequently, the conditions that yielded the best results, specifically those that led to the formation of nanoparticles rather than continuous films, with size distributions closest to the typical nanoscience range of 1 to 100 nanometres, were selected for further analysis. Although some particle sizes slightly exceeded 100 nm, these conditions were chosen because they produced the best overall results. Under these conditions, the distance between the tip of the capillaries and the substrate was varied, with values of 3, 4, 5, 6, and 7 cm (**Table 2**).

Table 3: Tested input voltages

Input voltage (kV)
6
7
8
9
10

Based on these results, the next step was to vary the input voltage, testing the following values: 6, 7, 8, 9, and 10 kV (**Table 3**). The initial value of 6 kV was chosen as it was experimentally found to be the lowest voltage that allowed for the ignition of plasma and its maintenance.

All experiments were carried out under controlled laboratory conditions to ensure consistency. The following parameters were kept constant during the entire experimental campaign: ambient temperature (approximately 22 ± 1 °C), relative humidity (45–55%), plasma ignition time (a few seconds before deposition, to ensure stability), and environmental pressure (atmospheric). These fixed conditions ensured that any variations in nanoparticle deposition were solely due to the process parameters under investigation.

3.2.2 Substrate preparation

The substrate used for all experiments was standard microscope glass cover slips, a dielectric material, circular, with a diameter of 25 mm. The nature of the substrate can influence the results, as different substrates may exhibit variations in wettability, surface energy, and roughness [236]. These factors can affect the adhesion, distribution, and morphology of the deposited nanoparticles, and should therefore be taken into account when examining the outcomes of the deposition process.
Prior to plasma exposure, the glass slide substrates were cleaned using an ultrasonic bath for 20 minutes in acetone. After sonication, the substrates were rinsed with distilled water, followed by a second rinse with acetone, and subsequently dried using pressurized dry air gun.

Once cleaned, the substrate was placed on a cylindrical PTFE sample holder. The process parameters were then set, and the substrate was carefully aligned and positioned directly under the plasma to ensure accurate and reproducible exposure during deposition.

3.3 Characterization procedures

3.3.1 SEM (Scanning Electron Microscopy)

The morphological analysis and size distribution of the pyrrole-based nanoparticles were performed using a scanning electron microscope (JSM-6010PLUS, JEOL, Japan). SEM imaging was carried out to investigate both the top-view and cross-sectional perspectives of the samples, with magnifications of 700x and 10,000x, respectively. Prior to imaging, the samples were sputter-coated with a thin layer of gold using a JFC-130 auto fine coater (JEOL, Japan) to enhance conductivity and prevent charging effects during electron beam exposure. The images were acquired at an accelerating voltage of 7 or 5 kV, ensuring optimal resolution and contrast for detailed surface analysis.

The size distribution analysis of the nanoparticles was conducted using ImageJ software (National Institutes of Health, USA), where measurements were taken from SEM images by evaluating the diameter of individual particles. At least 100 nanoparticles from different areas of the samples were analysed to obtain statistically significant results.

3.3.2 FTIR (Fourier Transform Infrared Spectroscopy)

The chemical characterization of the pyrrole-based nanoparticles was performed using Fourier-Transform Infrared Spectroscopy (FTIR). The spectra were acquired with a Bruker Tensor 27 spectrometer equipped with a single attenuated total reflection (ATR) accessory. For the analysis, a zinc selenide (ZnSe) crystal was employed due to its high durability and wide infrared transparency range.

To prevent potential damage to the ATR crystal during measurements, the nanoparticles were first deposited onto a low-density polyethylene (LDPE) film with a thickness of 0.18 mm (Goodfellow Cambridge Limited). This layer served as a protective barrier while maintaining good infrared transmission properties. The spectra were processed using OPUS 7.0129 software.

The acquired spectra allowed for the identification of characteristic functional groups present in the pyrrole-based nanoparticles, providing insight into their chemical structure.

3.3.3 XPS (X-ray Photoelectron Spectroscopy)

To investigate the surface chemical composition of the deposited pyrrole-based nanoparticles, X-ray Photoelectron Spectroscopy (XPS) analysis was performed using a PHI 5000 Versaprobe II spectrometer equipped with a monochromatic Al Kα X-ray source ($h\nu$ = 1486.6 eV) operating at a power of 50 W, with a beam size of 200 μm. The analysis chamber was maintained under high vacuum conditions, with a pressure of at least 10^{-6} Pa to ensure minimal contamination during measurements.

Survey spectra were acquired to identify the elemental composition of the nanoparticle surfaces, focusing on the detection of N1s, C1s, and O1s signals. The measurements were performed with a pass energy of 187.85 eV, which allowed for the identification of the principal elements present. The quantification of these elements was carried out using Multipak software (V 9.6), which enabled elemental analysis based on the relative sensitivity factors (RSFs) provided by the instrument's manufacturer.

For each sample, measurements were conducted at six different locations to account for surface variability, and the average elemental composition was calculated to enhance the reliability of the data.

3.3.4 OES (Optical Emission Spectroscopy)

To investigate the excited species generated during the plasma discharge, Optical Emission Spectroscopy (OES) analysis was carried out. The measurements were performed using an Ocean Optics S2000 spectrometer with a spectral resolution of 1.4 nm, covering a wavelength range from 200 to 900 nm. The analysis was conducted in three distinct configurations: (1) helium plasma (He) without the PTFE sample holder, to study the baseline reactive species generated solely by the helium discharge; (2) helium plasma with the PTFE sample holder, to evaluate any additional species arising from the interaction with the holder material; and (3) helium plasma with pyrrole injection (He + Pyrrole), to observe the species formed during the polymerization process induced by the interaction of the plasma with the pyrrole monomer. The optical fiber was positioned near the plasma jet-array, approximately 1 cm from the discharge centre, to maximize signal acquisition while preventing potential damage from direct exposure. This setup enabled the identification of key emission lines corresponding to reactive species such as excited helium atoms, reactive nitrogen species, and molecular fragments generated during the interaction with pyrrole. The collected OES spectra provided critical insights into the active plasma chemistry and allowed for the estimation of physical parameters of the discharge.

CHAPTER 4

Results and Discussion

4.1 Nanoparticle morphology and size distribution (SEM)

The morphology of the nanoparticles was investigated by SEM under different synthesis parameters, both in top-view and cross-sectional imaging.

4.1.1. Effect of Precursor Flow Rate: Results

The first investigated condition involved varying the ratio between the discharge gas and the precursor flow but keeping the total flow constant at 2 standard litres per minute (slm). Other parameters such as input voltage were kept constant at 9 kV. The distance between the tips of the capillaries and the substrate was fixed at 5 cm. The reaction was carried out for 60 s.

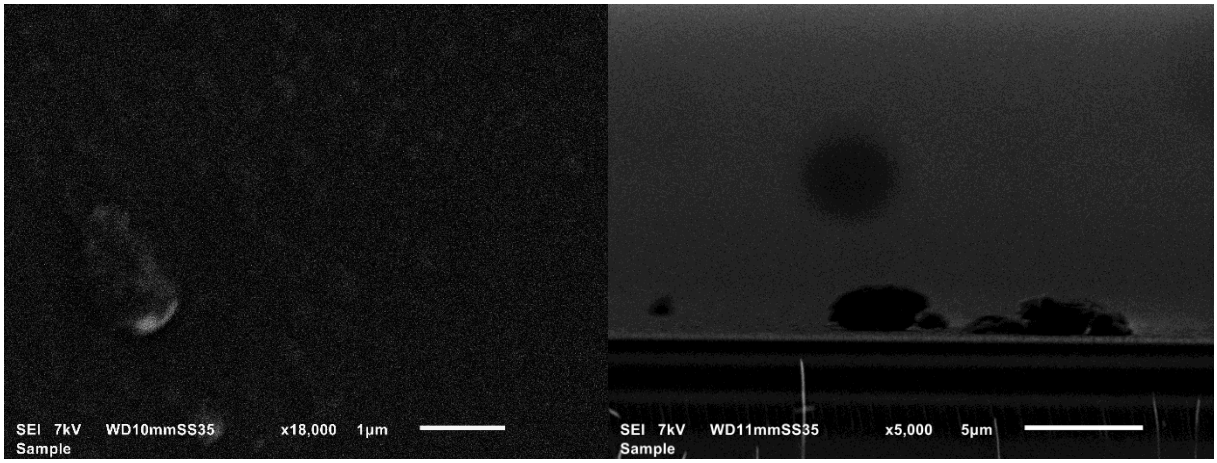

Figure 13: Top-view and cross-section SEM images with He 1.950 slm slm Q_{Py+He} 50 sccm

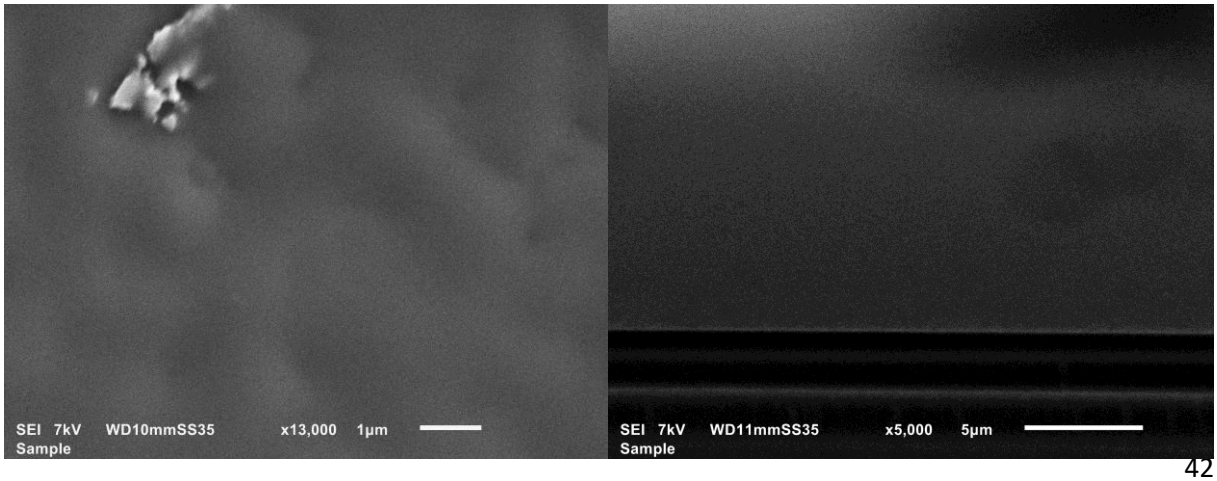

Figure 14: Top-view and cross-section SEM images with He 1.900 slm slm Q_{Py+He} 100 sccm

The first two conditions characterised by a very precursor (and bubbling gas) flow rate (50 and 100 sccm) showed the absence of distinct NPs on the substrate surface. Instead, the deposition resulted predominantly in the formation of continuous films.

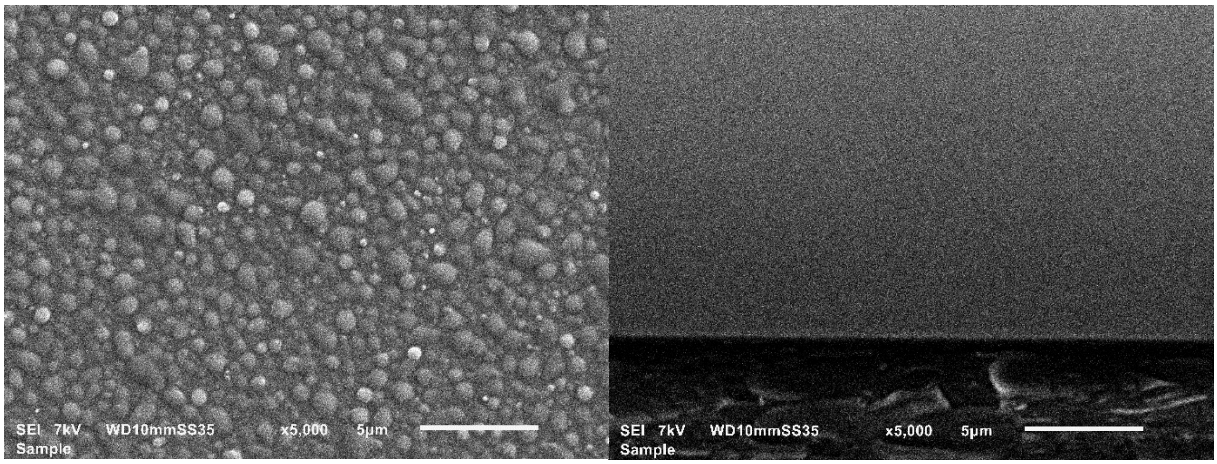

Figure 15: Top-view and cross-section SEM images with He 1.850 slm slm Q_{Py+He} 150 sccm

Under this condition, the nanoparticles exhibited the largest average diameter among all tested conditions, reaching approximately 544.3±199.9 nm. These values indicate a strong heterogeneity in particle size, followed by simultaneous film deposition across the inspected sample. The cross-sectional image indeed confirms the presence of a film, with an average thickness of 454 ± 90 nm.

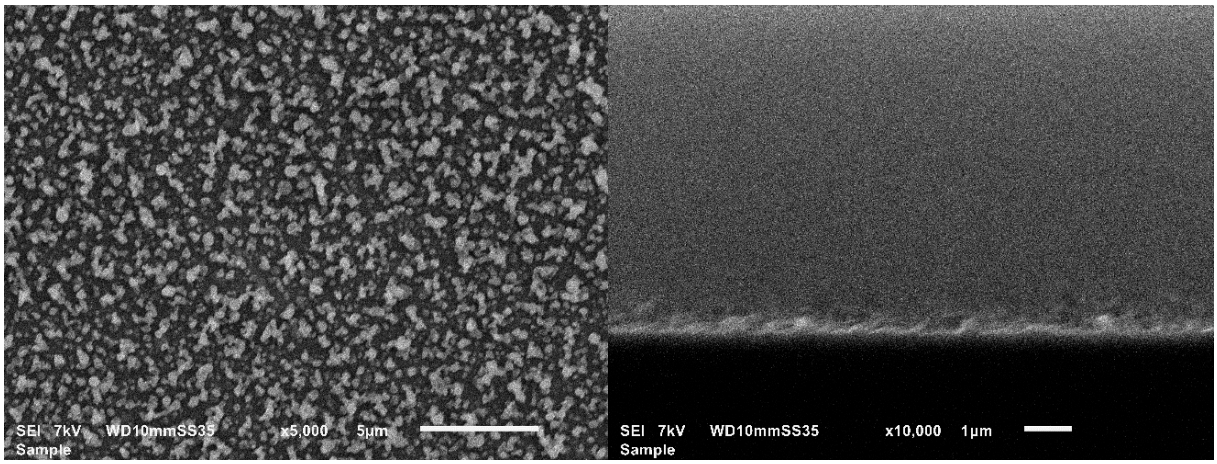

Figure 16: Top-view and cross-section SEM images with He 1.800 slm slm Q_{Py+He} 200 sccm

This condition resulted in nanoparticles with one of the smallest average diameters, approximately 248.6 ± 60.6 nm. However, the morphology was less spherical compared to all other conditions, and the average thickness was the lowest among this set of experiments, measuring 296 ± 77 nm.

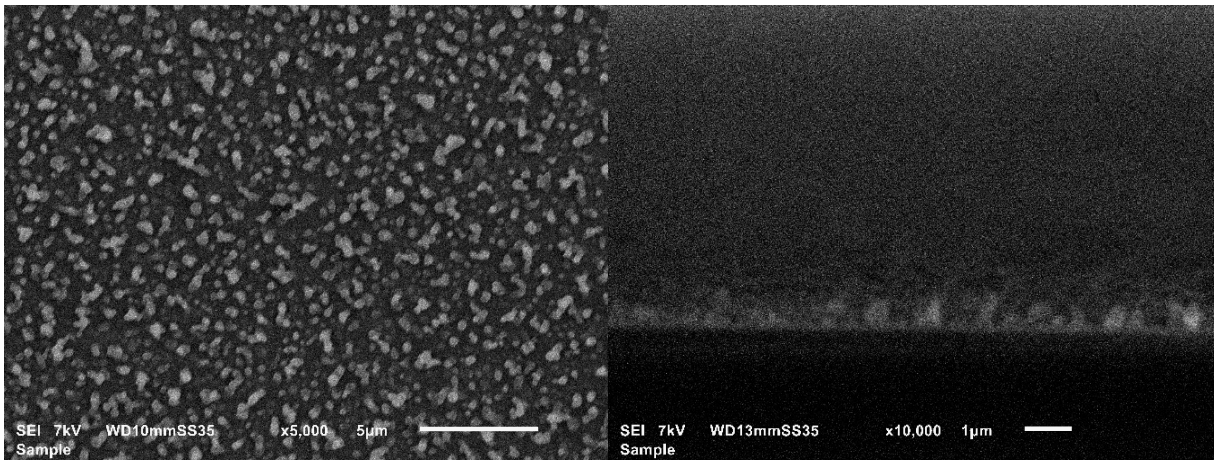

Figure 17: Top-view and cross-section SEM images with He 1.750 slm slm Q_{Py+He} 250 sccm

Like the previous case, this condition led to the formation of nanoparticles with no presence of film deposition. To some extent, the NPs coalesced together, but the average diameter remained relatively small at 296.5 ± 69.8 nm, with a narrower standard deviation indicating improved homogeneity in size. The average thickness, determined from the cross-sectional SEM analysis, was 552.7 ± 178.8 nm.

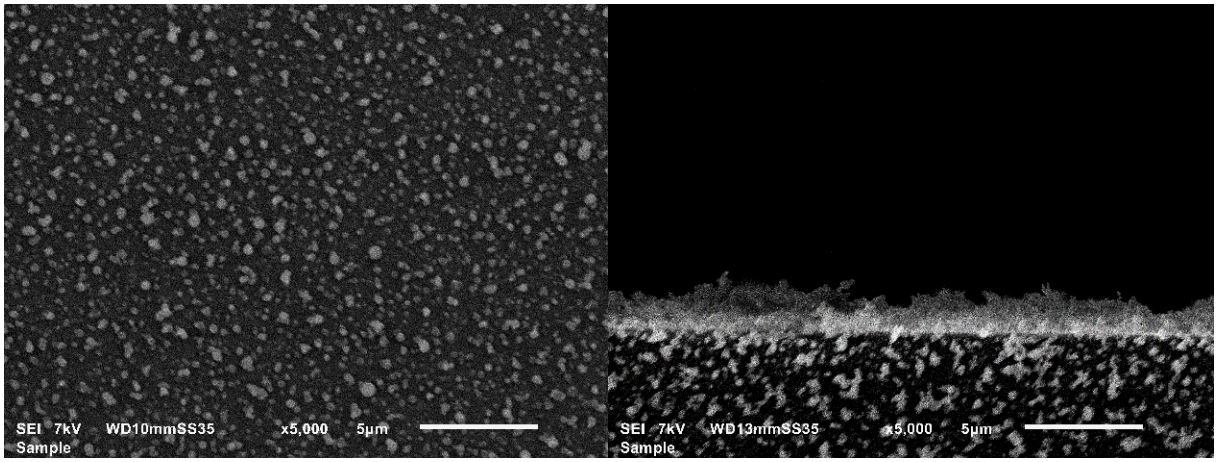

Figure 18: Top-view and cross-section SEM images with He 1.700 slm slm Q_{Py+He} 300 sccm

Under this condition, no film-like deposition was observed, and discrete NPs formation became predominant. The NPs showed a less spherical morphology compared to previous conditions; however, the average diameter decreased significantly to 249.0 ± 68.9 nm, with a lower standard deviation suggesting a more consistent size distribution despite the reduced shape uniformity. Additionally, the cross-sectional analysis revealed the greatest thickness among this experimental set, measuring 1506 ± 313 nm, which indicates a relatively larger amount of material deposited on the substrate compared to other conditions.

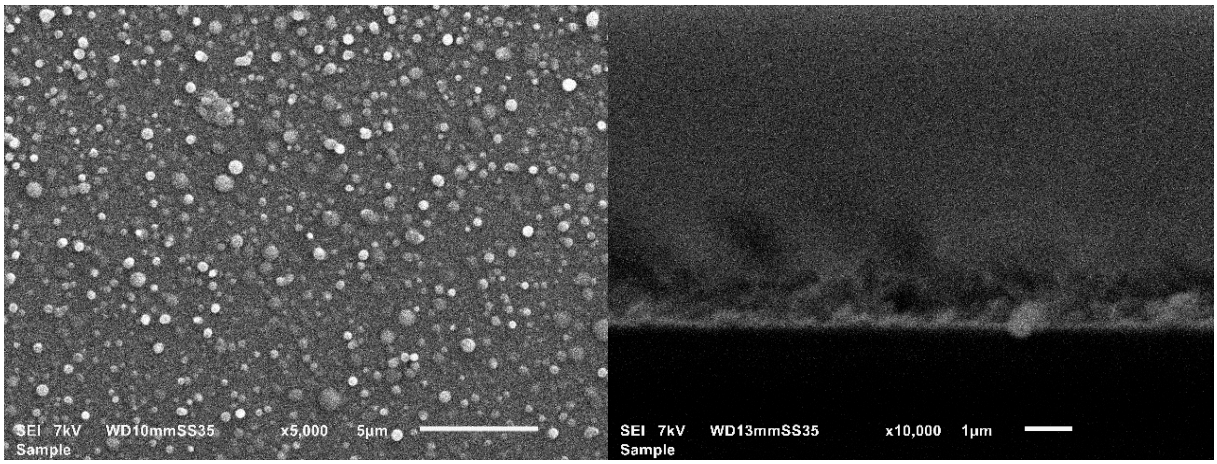

Figure 19: Top-view and cross-section SEM images with He 1.650 slm slm Q_{Py+He} 350 sccm

In this condition, the average particle diameter reached its highest value, approximately 441.3 nm ± 189.3 nm, accompanied by the largest standard deviation among all tested conditions. This non-uniformity in particle size distribution is likely due to the uncontrolled coalescence of multiple particles during deposition. The corresponding cross-sectional SEM image confirmed the presence of agglomerated nanoparticles, forming a discontinuous and irregular layer with an average thickness of 663.7 ± 145.5 nm.

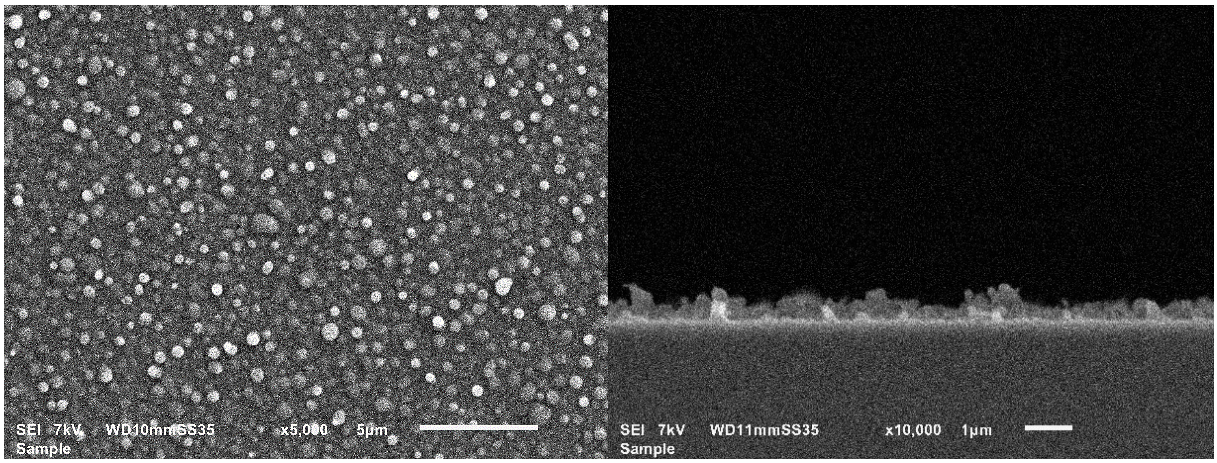

Figure 20*:* Top-view and cross-section SEM images with He 1.600 slm slm Q_{Py+He} 400 sccm

Under this condition, the synthesised nanoparticles were similar in morphology to those obtained in the first experimental set, displaying a large average diameter of approximately 355.7 ± 108.8 nm and a highly homogeneous spherical shape. The cross-sectional SEM analysis revealed a moderately thick nanoparticle layer, with an average thickness of 471.6 ± 141.8 nm. Despite not being among the thickest layers observed, the coverage appeared uniform, with no visible gaps, indicating effective particle deposition.

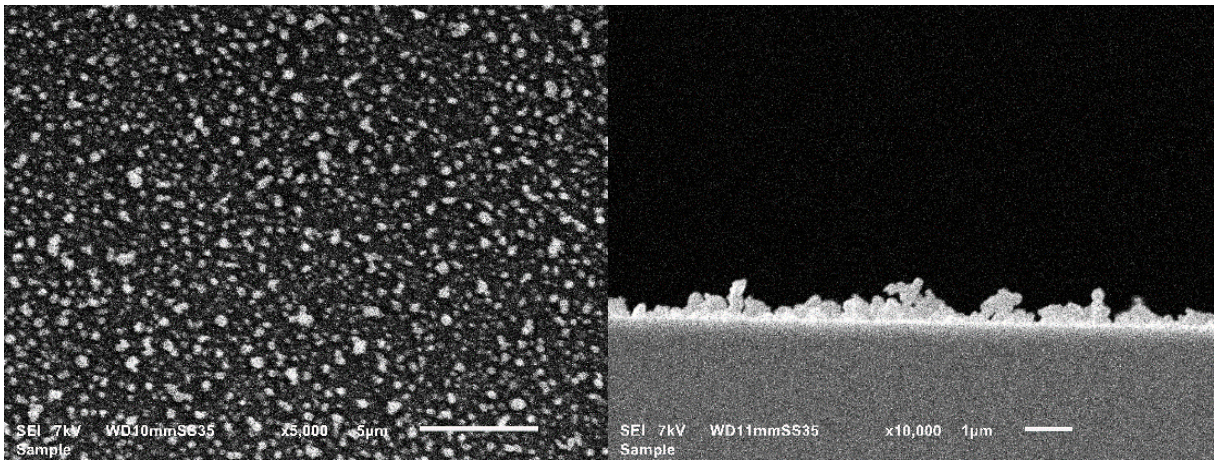

Figure 21: Top-view and cross-section SEM images with He 1.550 slm slm Q_{Py+He} 450 sccm

Under this condition, the nanoparticles exhibited an average diameter of approximately 344.4 ± 116.7. The top-view SEM suggested an irregular nanoparticle morphology, likely due to partial fusion during deposition. This was corroborated by the cross-sectional image, which revealed a discontinuous layer of agglomerated structures with non-uniform height and shape. The average thickness of the deposited material was 388.9 ± 120.2 nm.

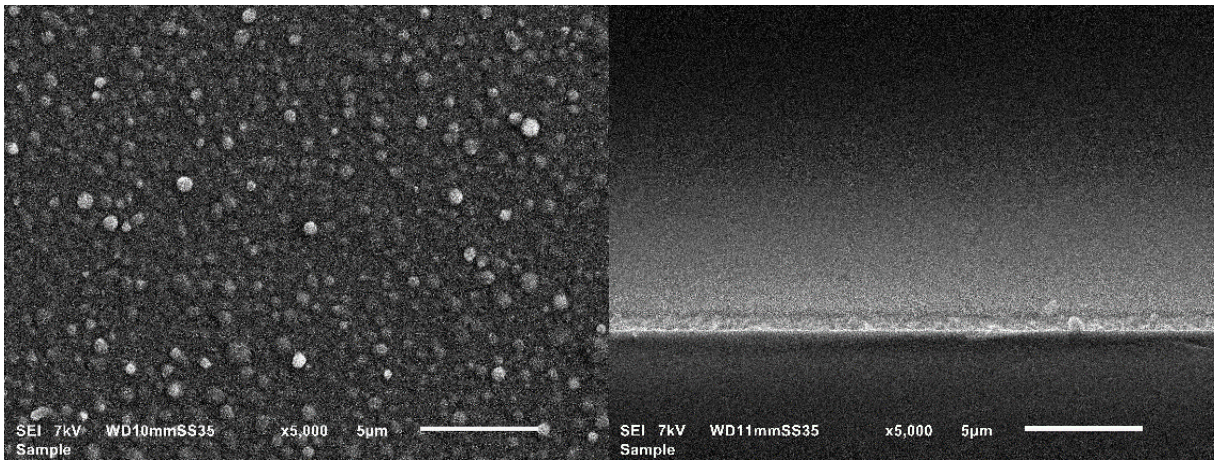

Figure 22: Top-view and cross-section SEM images with He 1.500 slm slm Q_{Py+He} 500 sccm

Using this condition, the resulting nanoparticles exhibited a relatively large average diameter of approximately 416 nm ± 122 nm, indicating a non-uniform size distribution. Morphologically, the particles appeared to be spherically shaped and homogeneous in terms of form and of distribution over the substrate. The average thickness, determined from the cross-sectional SEM analysis, was 471 ± 80 nm.

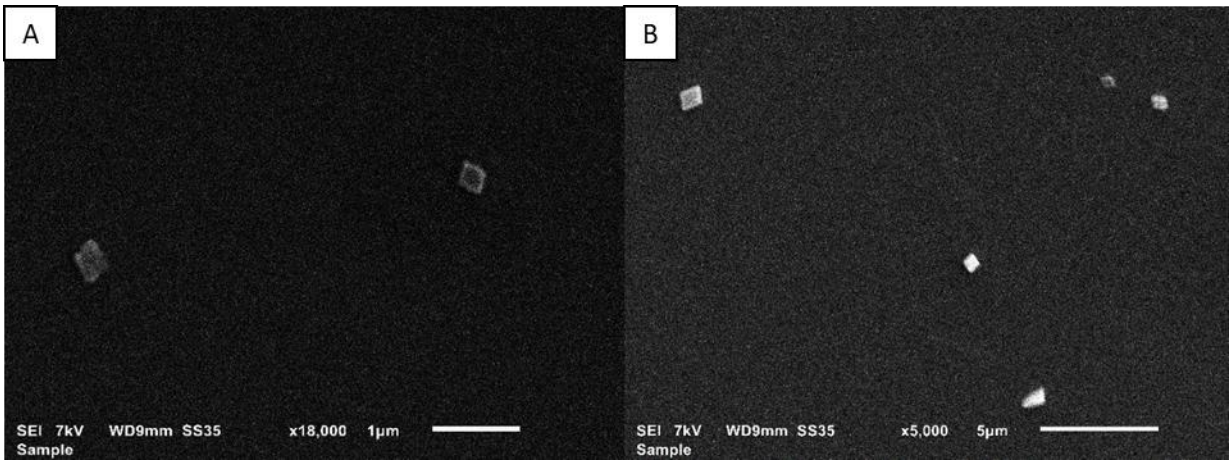

Figure 23: Top-view SEM images with (A) He 1.975 slm Q_{Py+He} 25 sccm and (B) He 1.990 slm Q_{Py+He} 10 sccm

Interesting results were also obtained under conditions of very low monomer flow rates, specifically at 10 and 25 sccm. Under these settings, the nanoparticles no longer exhibited a spherical morphology; instead, they exhibited a rhomboidal shape. The average dimensions of the particles were measured along their major and minor diagonals, yielding the following values: for 25 sccm, the major diagonal was 487 ± 337.5 nm and the minor diagonal was 332.2 ± 276.73 nm; for 10 sccm, the major diagonal was 426.4 ± 59.1 nm and the minor diagonal was 322.8 ± 30.4 nm. This shift in shape and aspect ratio suggests a different nucleation and growth dynamic at extremely low precursor concentrations.

4.1.2. Effect of Precursor Flow Rate: Interpretation and Comparison with Literature

The results on the average nanoparticles size for each condition of different precursor flow are synthesized in **Figure 24:**

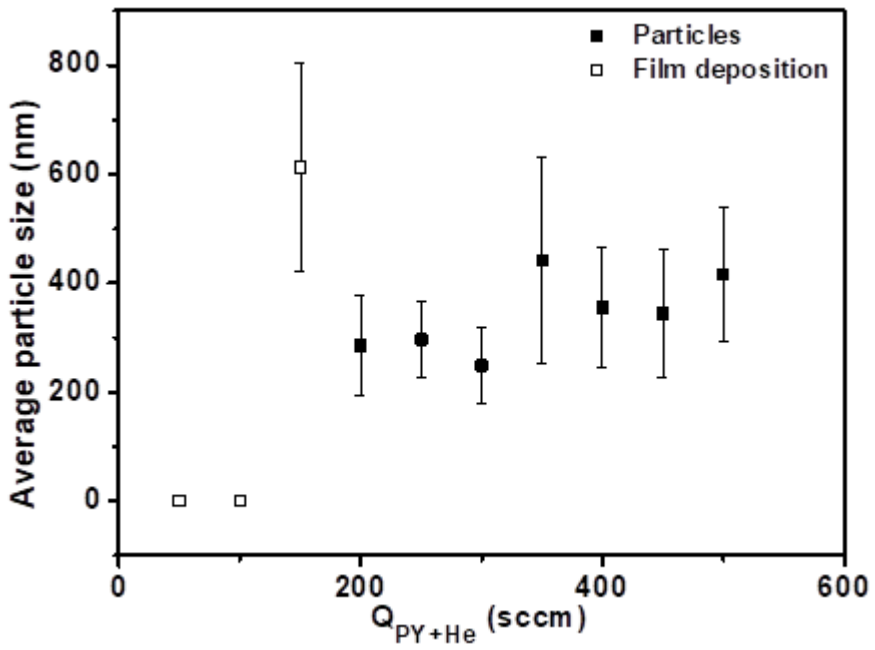

Figure 24: Size distribution of NPs for different tested precursor flow rates

The results obtained show how variations in the ratio between the flow of the discharge gas and that of the precursor significantly influence the formation and average size of the synthesised nanoparticles. The first two conditions, characterised by a very low pyrrole flux (50 and 100 sccm), showed the absence of nanoparticles and the exclusive formation of films, indicating that nucleation is severely limited at these concentrations. Under these conditions, the precursor tends to deposit directly on the surface in the form of a continuous film. The low monomer concentration results in a low presence of free radicals, which is not sufficient to promote nucleation and particle growth. Indeed, nucleation requires a critical concentration of radicals for it to occur: if this threshold is not exceeded, the radicals simply tend to adsorb onto the substrate surface, resulting in films rather than stable nuclei.

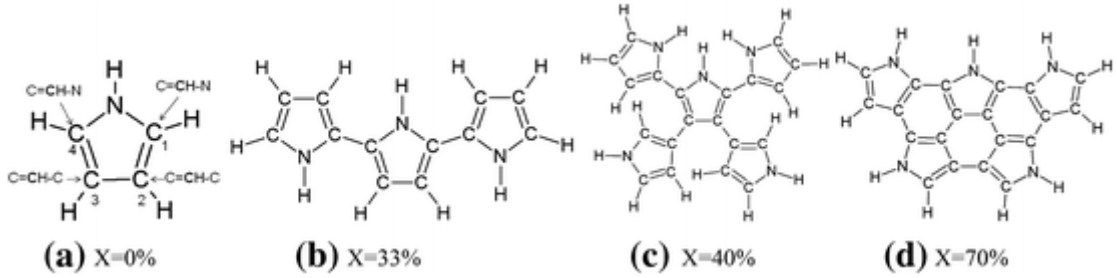

Figure 25: Schematic representation of pyrrole polymerization and crosslinking. (a) Pyrrole monomer with numbered carbon atoms. (b) Linear chain of five pyrrole rings showing X = 40%. (c) Branched structure with unchanged X but reduced C=CH–C states. (d) Highly crosslinked structure (X = 70%) resulting from dehydrogenation. Adapted from Gomez et al. [237]

These findings are consistent with the chemical analysis presented by Gomez et al.[237], who showed through XPS that the formation of crosslinked structures in plasma-synthesized polypyrrole particles strongly depends on the presence of reactive sites generated by dehydrogenation. In their work, a higher degree of crosslinking, indicative of particle growth, was observed only when sufficient energy and reactive monomer concentration were present, suggesting that under low-monomer conditions, the system lacks the necessary radical density to initiate effective nucleation. This concept is well illustrated in **Figure 25**, where different pyrrole configurations show how the crosslinking percentage (X) increases with the number of connected rings and decreases in hydrogenation, highlighting the structural evolution required for particle formation. Consequently, the formation process favours surface adsorption and film growth over the generation of stable three-dimensional nuclei.

In contrast, under conditions where the precursor flow is higher (350-500 sccm), a higher concentration of monomer is observed, which leads to excessive free radical formation. In this case, nucleation and crosslinking occurs very rapidly, favouring the formation of clusters and aggregates. This phenomenon results in an increase in the average diameter of the nanoparticles, compared to conditions with lower concentrations. A similar trend was observed by Heredia-Rivera et al. [238], who reported an increase in the crosslinking degree and conjugation length of plasma-synthesised PPy films with increasing precursor concentration, indicating enhanced polymerization activity under these conditions.

Under these conditions, the plasma energy is distributed among a larger number of molecules, reducing the amount of energy available to each individual molecule. As a result, fragmentation is limited, which can lead to incomplete reactions. This aligns with Friedrich's observations [239], who reported that when plasma energy is shared across many molecules, the lower energy per molecule restricts fragmentation and may cause the reaction to be incomplete. In addition, the large amount of monomer leads to greater interaction between the molecules (e.g., through van der Waals forces), favouring clumping and aggregation of nanoparticles. This occurs because higher monomer concentrations increase the proximity of particles, enhancing attractive van der Waals interactions that promote particle growth and formation of larger aggregates [240]. The combination of these factors leads to the formation of larger particles.

The most promising results, in terms of small average particle size, were obtained for intermediate precursor flows, particularly at flow rates of 200, 250 and 300 sccm. Under these conditions, the amount of precursor is adequate to ensure the formation of a sufficient concentration of free radicals, which is necessary to initiate and sustain nucleation. The NPs obtained are thus smaller, morphologically uniform and well dispersed over the analysed substrate surface. Similarly, in the chemical polymerization of PPy investigated by Liang et al. [241], intermediate oxidant concentrations produce thicker, more uniform nanowires, while too low or too high concentrations lead to less controlled morphologies. This suggests that, regardless of the method, there is an optimal parameter range that promotes high-quality nanostructure formation.

4.1.3 Effect of Distance from the Capillaries to the Substrate: Results

The three conditions that showed the most promising results in terms of a smaller nanoparticle size range (closer to 100 nm) and lower standard deviation were 300, 250, and 200 sccm of pyrrole and helium flow rate. For each given flow, the distance was varied from 3 to 7 cm in 1 cm increments. Other parameters, such as input voltage, total flow, and deposition time, were kept constant.

A. Condition: He 1.700 slm Q_{Py+He} 300 sccm

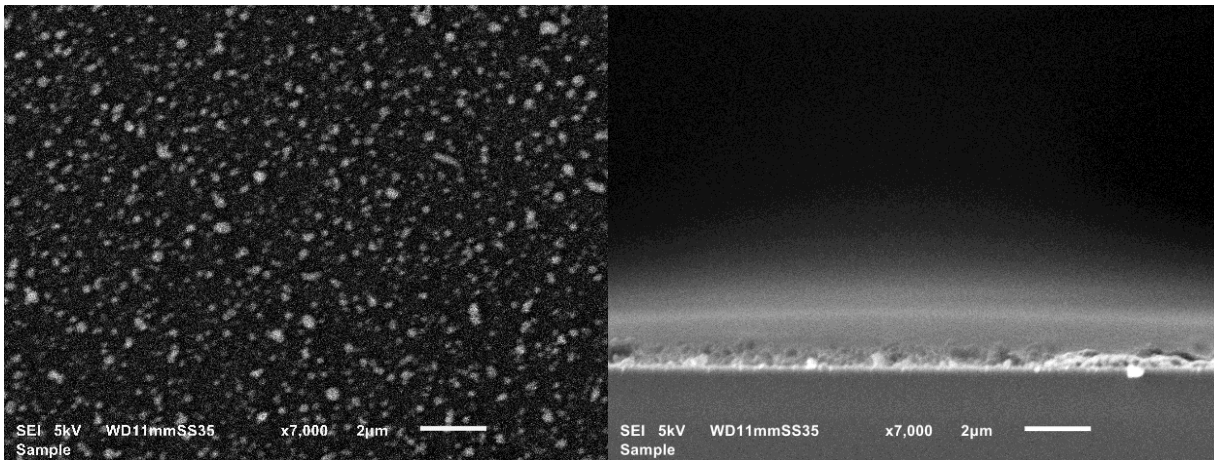

Figure 26: Top-view and cross-section SEM images with He 1.700 slm Q_{Py+He} 300 sccm - 3 cm

Under the first condition, corresponding to the shortest distance of 3 cm, the synthesized nanoparticles were relatively small, with an average diameter of 172.5 ± 48.1 nm. The particles appeared to be mostly spherical in shape. The cross-sectional image also confirmed the presence of deposited nanoparticles, with an average thickness of 352.6 ± 63.1 nm.

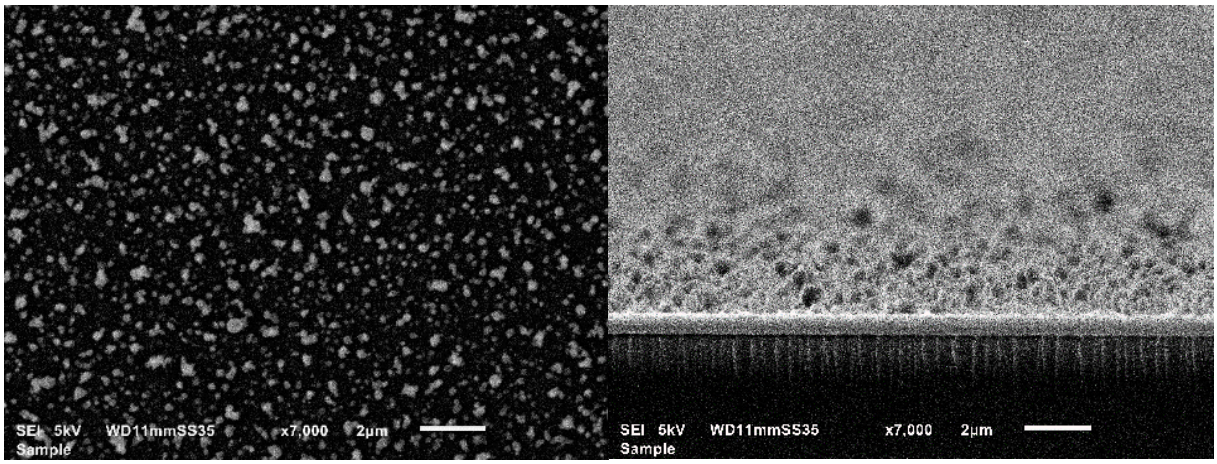

Figure 27: Top-view and cross-section SEM images with He 1.700 slm Q_{Py+He} 300 sccm - 4 cm

Increasing the distance to 4 cm resulted in the smallest average nanoparticle size, measured at 168.1 ± 52.5 nm. Under this condition, the overall deposition was high across the substrate, but the distribution was less homogeneous than in the previous cases. SEM analysis revealed areas where the nanoparticles

were well separated, while in other areas, aggregation and cluster formation were observed. This heterogeneity may be attributed to local fluctuations or asymmetries in the plasma jet, which can cause spatial variations in the nanoparticle nucleation and transport. As reported by Polonskyi et al, [242], the nanoparticle growth and deposition are highly sensitive to plasma parameters and local conditions within the gas aggregation source, which can lead to preferential deposition or aggregation in certain zones. Furthermore, the cross-sectional image showed a high presence of nanoparticles, with an average thickness of 1345.7 ± 180.6 nm, representing the highest value obtained in this set of experiments.

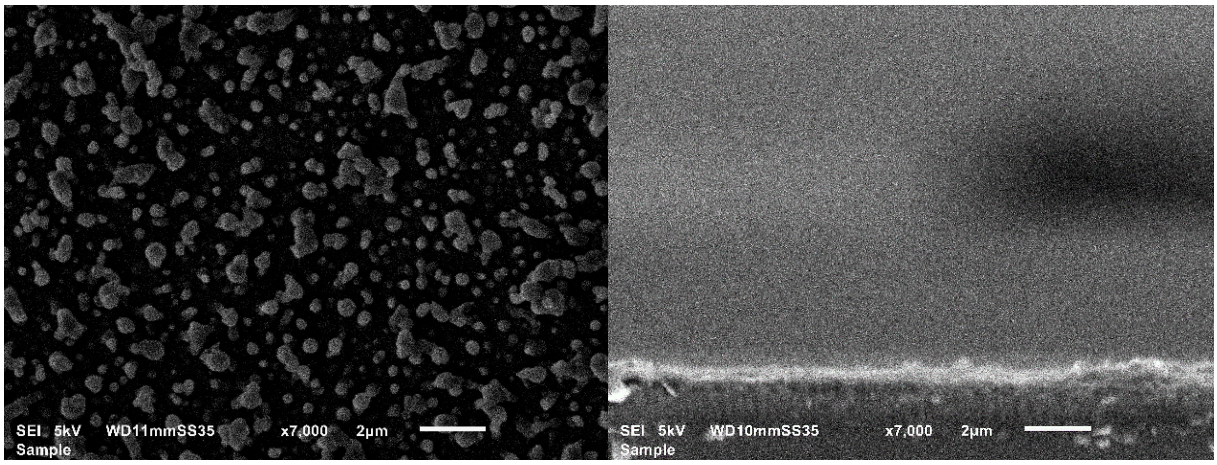

Figure 28: Top-view and cross-section SEM images with He 1.700 slm Q_{Py+He} 300 sccm - 5 cm

At 5 cm, there was a notable increase in particle size, with an average of 344.9 ± 116.0 nm. The standard deviation, the highest among all conditions reflects a broad size distribution, suggesting the simultaneous presence of both large and small particles, while the average thickness was 473.2 ± 101.8 nm.

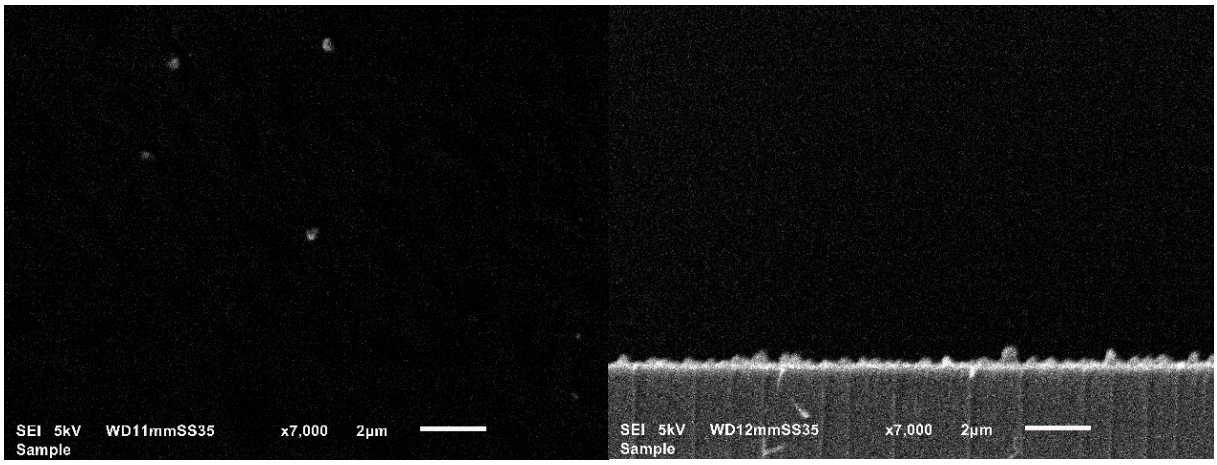

Figure 29: Top-view and cross-section SEM images with He 1.700 slm Q_{Py+He} 300 sccm - 6 cm

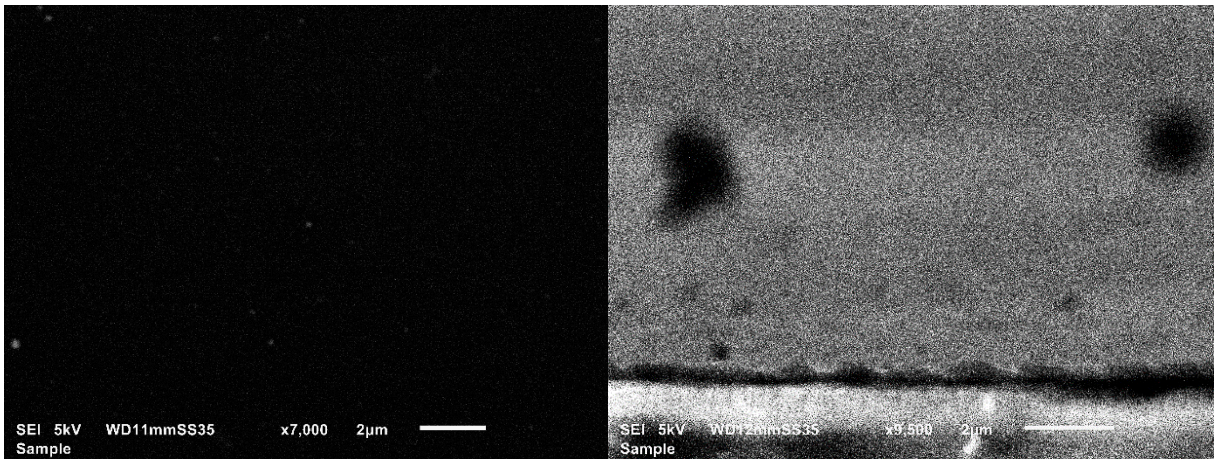

Figure 30: Top-view and cross-section SEM images with He 1.700 slm Q_{Py+He} 300 sccm - 7 cm

When the distance was further increased to 6 cm and 7 cm, a significant drop in deposition was observed, particularly at 7 cm, where nanoparticle presence was minimal. At 6 cm, although the particle concentration was low, the nanoparticles detected were relatively large, with an average size of 320.1 ± 66.0 nm. In contrast, at 7 cm, the few particles present were the smallest, with an average size of just 110.1 ± 48.2 nm. Regarding the average thickness measured from the cross-sectional analysis, for the 6 cm sample the value was 268.30 ± 95.77 nm, while for the 7 cm sample it was 387.26 ± 46.69 nm.

B. Condition: He 1.750 slm Q_{Py+He} 250 sccm

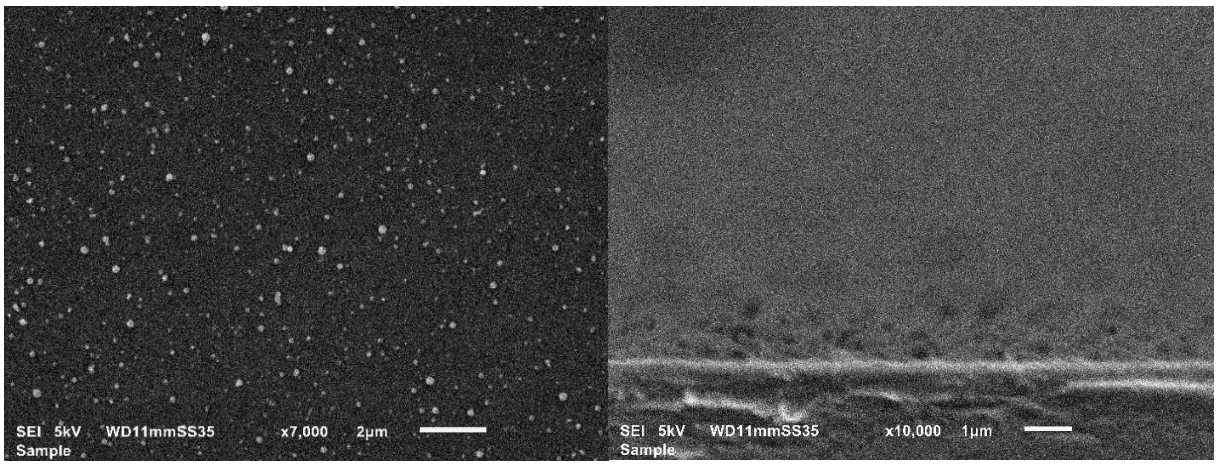

Figure 31: Top-view and cross-section SEM images with He 1.750 slm Q_{Py+He} 250 sccm - 3 cm

Under the first condition, with distance of 3 cm, the smallest average size was observed, reaching 111.9 ± 41.6 nm. The standard deviation was also the lowest of this set but still high compared to the average size, indicating a moderate dispersion in particle sizes. The average thickness measured was 397.5 ± 86.7 nm, reflecting a significant material deposition.

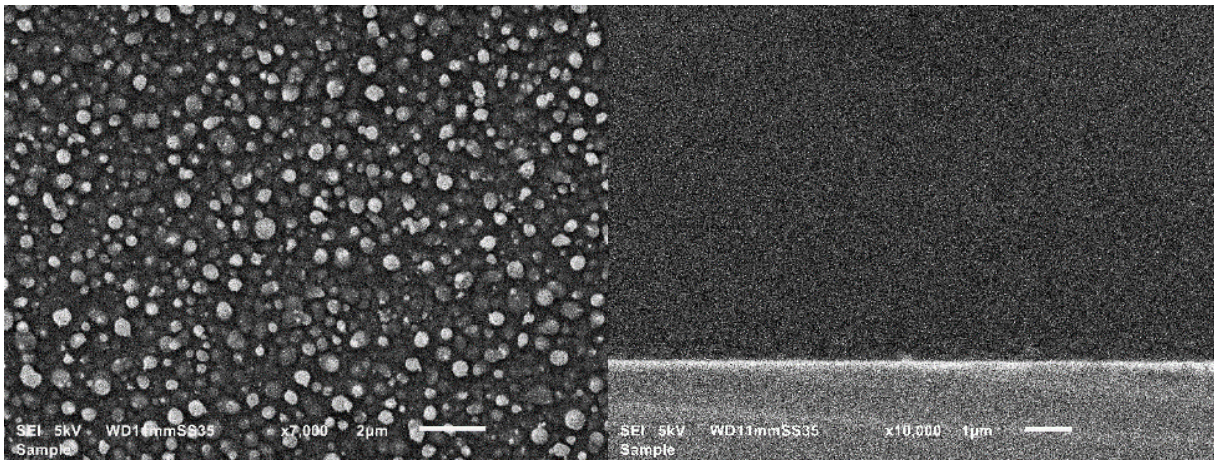

Figure 32: Top-view and cross-section SEM images with He 1.750 slm Q_{Py+He} 250 sccm - 4 cm

When the distance was increased to 4 cm, the average nanoparticle size increased significantly, reaching 207.1 ± 98.5 nm, which is almost double compared to the previous conditions. The standard deviation was also the highest and this variation was evident from the SEM images. Some regions of the sample showed high concentrations of aggregated particles forming clusters, while in others, the nanoparticles were smaller and well separated, as was already observed under the condition of He 1.700 slm Q_{Py+He} 300 sccm with a distance of 4 cm. Unlike the previous condition, the average thickness this time was 226.59 ± 60.78 nm, and the cross-sectional image confirms the actual presence of spherical nanoparticles.

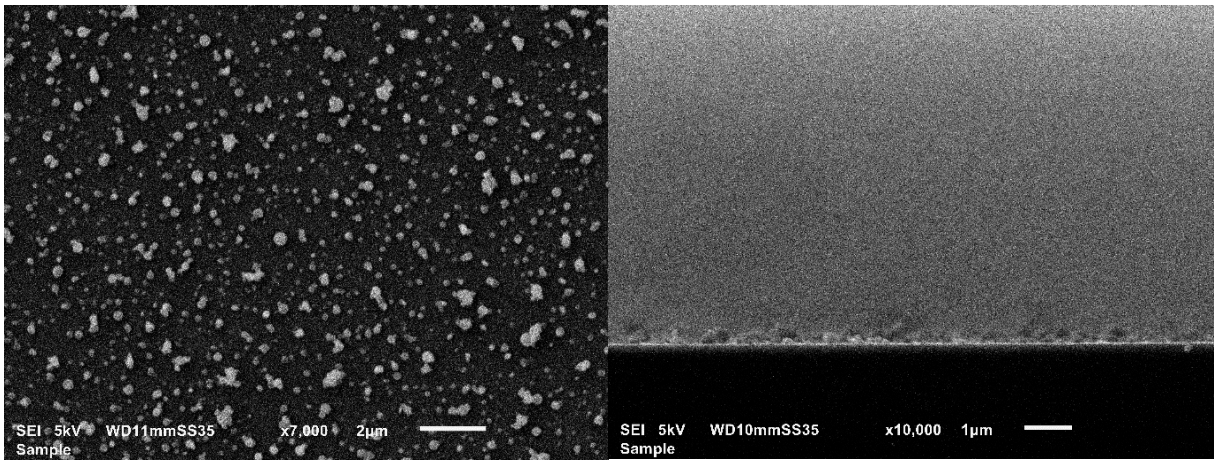

Figure 33: Top-view and cross-section SEM images with He 1.750 slm Q_{Py+He} 250 sccm - 5 cm

At a distance of 5 cm, the average nanoparticle size decreased again, down to 152.4 ± 55.6 nm. In terms of shape, the cross-section showed the presence of mostly spherical nanoparticles, with an average deposition thickness of 200.4 ± 64.4 nm.

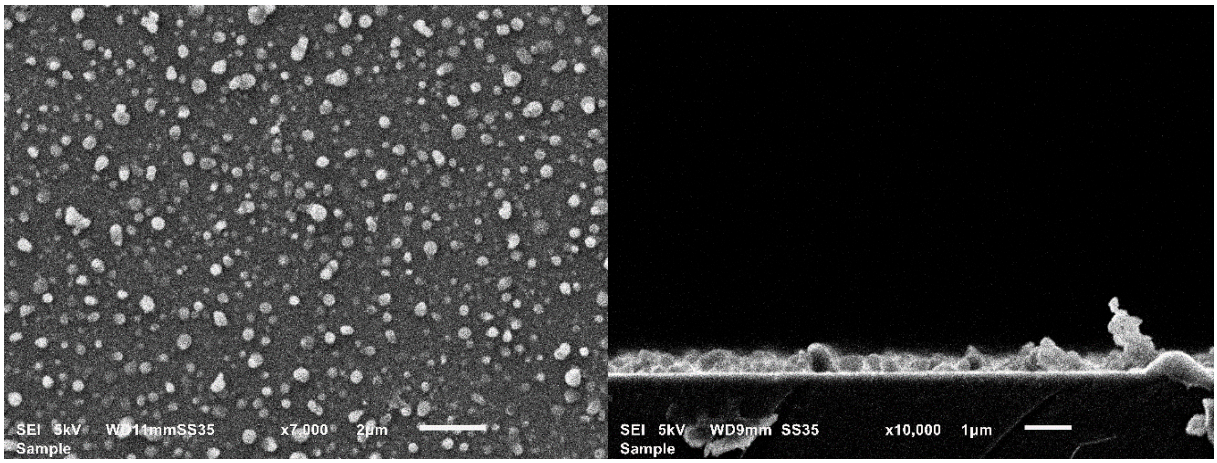

Figure 34: Top-view and cross-section SEM images with He 1.750 slm Q_{Py+He} 250 sccm - 6 cm

With a distance of 6 cm, the nanoparticles were the largest in the set, with an average diameter of 227.6 ± 67.1 nm. The relatively high standard deviation indicates a broad size distribution of nanoparticles present in the sample, reflecting variation in particle sizes. Cross-sectional analysis showed an average deposition thickness of 348.85 ± 96.92 nm. The image also allowed clear distinction of nanoparticles within the deposited material.

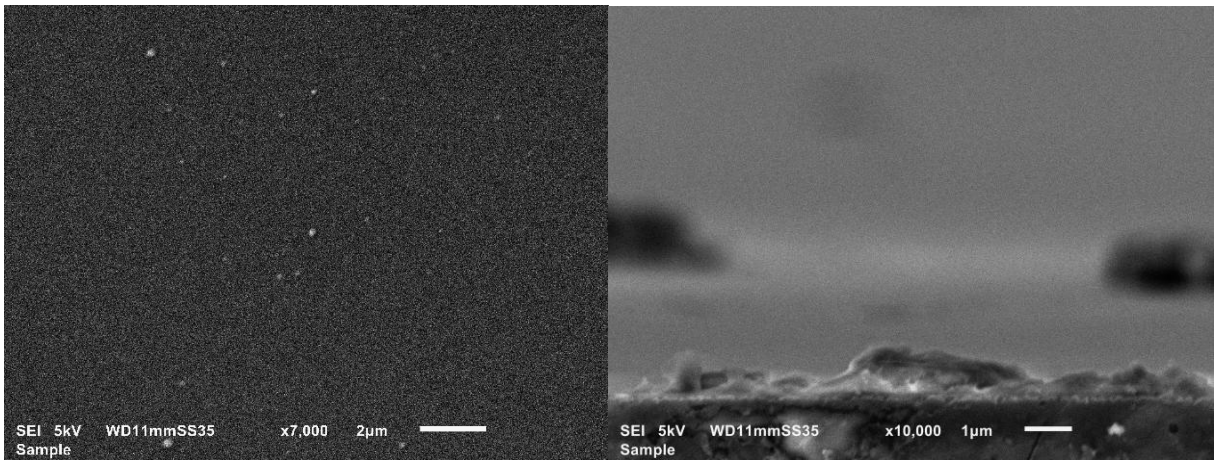

Figure 35: Top-view and cross-section SEM images with He 1.750 slm Q_{Py+He} 250 sccm - 7 cm

Finally, at 7 cm, the deposition drastically decreased, as also observed in the previous experimental set. The presence of nanoparticles on the substrate under this condition was quite sparse, and the few particles detected were very small, with an average size of 121.0 ± 46.4 nm.Cross-sectional analysis showed an average deposition thickness of 537.44 ± 172.35 nm.

C. Condition: He 1.800 slm Q_{Py+He} 200 sccm

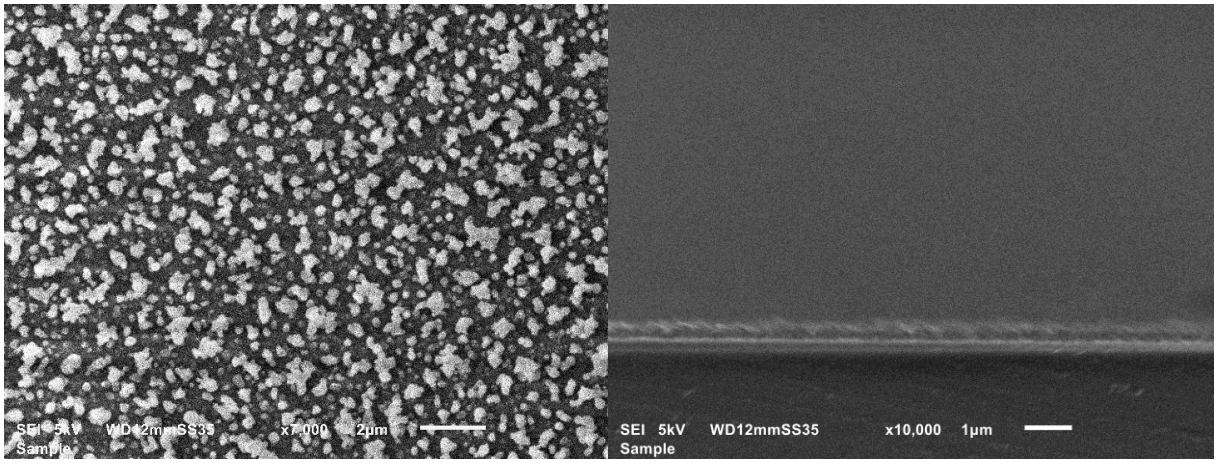

Figure 36: Top-view and cross-section SEM images with He 1.800 slm Q_{Py+He} 200 sccm - 3 cm

At a distance of 3 cm, the largest average nanoparticle size of this experimental set was recorded, reaching 217.4 ± 82.1 nm. Top-view images show the presence of aggregates in some areas, while the cross-sectional analysis indicates a relatively uniform deposition thickness within the analysed region. The average thickness measured from the cross section was 328.90 ± 44.55 nm.

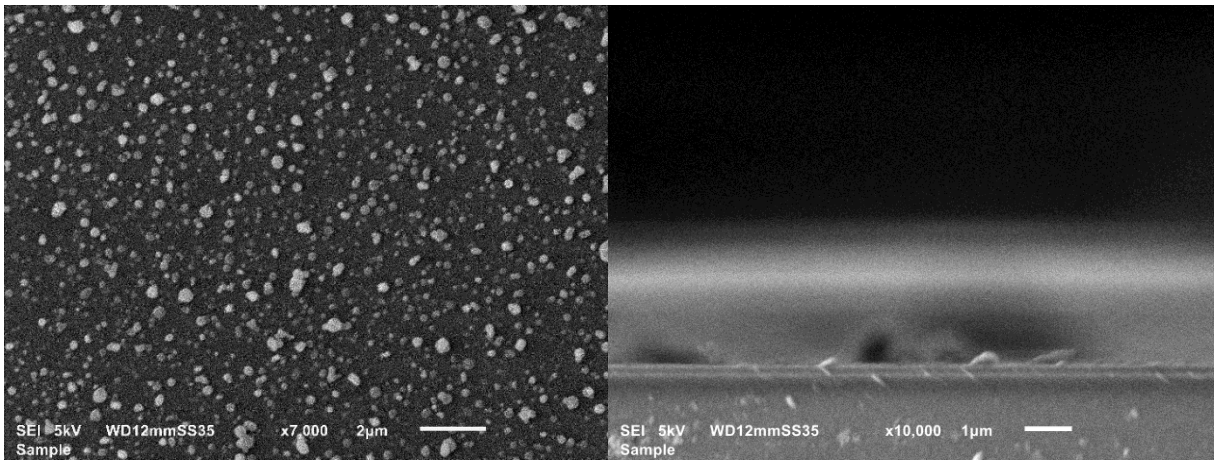

Figure 37: Top-view and cross-section SEM images with He 1.800 slm Q_{Py+He} 200 sccm - 4 cm

When the distance was increased to 4 cm, the average nanoparticle size decreased slightly to 170.3±70.4 nm. However, the standard deviation was relatively high indicating a wide variation in particle size. Despite the decrease in average size, the morphology remained mostly spherical. The average thickness, determined from the cross-sectional SEM analysis, was 529.0 ± 149.2 nm.

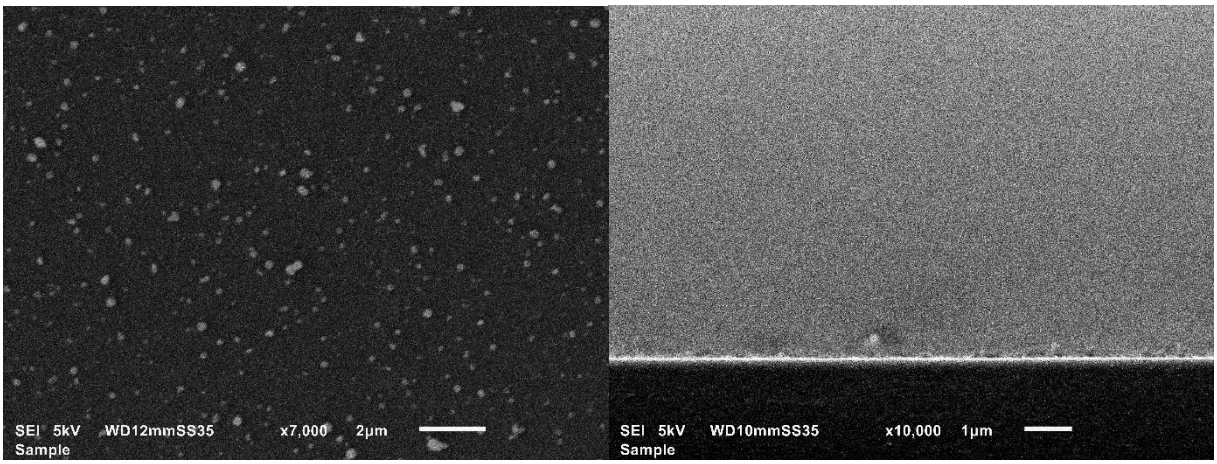

Figure 38: Top-view and cross-section SEM images with He 1.800 slm Q_{Py+He} 200 sccm - 5 cm

At 5 cm, the lowest average particle size of this set was achieved, with nanoparticles measuring 123.1 ± 47.8 nm. The standard deviation was also the smallest, suggesting better size uniformity. However, some large clusters were observed in specific regions of the substrate. Cross-sectional analysis confirmed the presence of spherical nanoparticles, showing a decreased thickness compared to the previous condition, with an average value of 321.7 ± 30.5 nm.

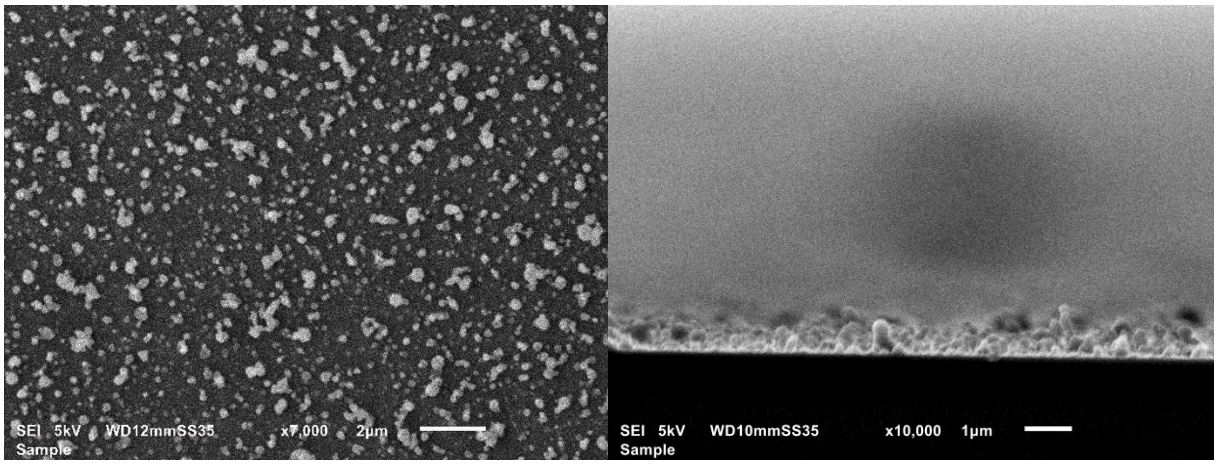

Figure 39: Top-view and cross-section SEM images with He 1.800 slm Q_{Py+He} 200 sccm - 6 cm

With a distance of 6 cm, the average nanoparticle size increased again to 177.4 ± 76.1 nm. This high standard deviation indicates a broad size distribution. Along with the spherical nanoparticles, the coalescence of multiple particles into large clusters was observable from the top view. The cross-sectional image also showed one of the highest average thicknesses measured in this set of experiments, at 482.16 ± 115.54 nm.

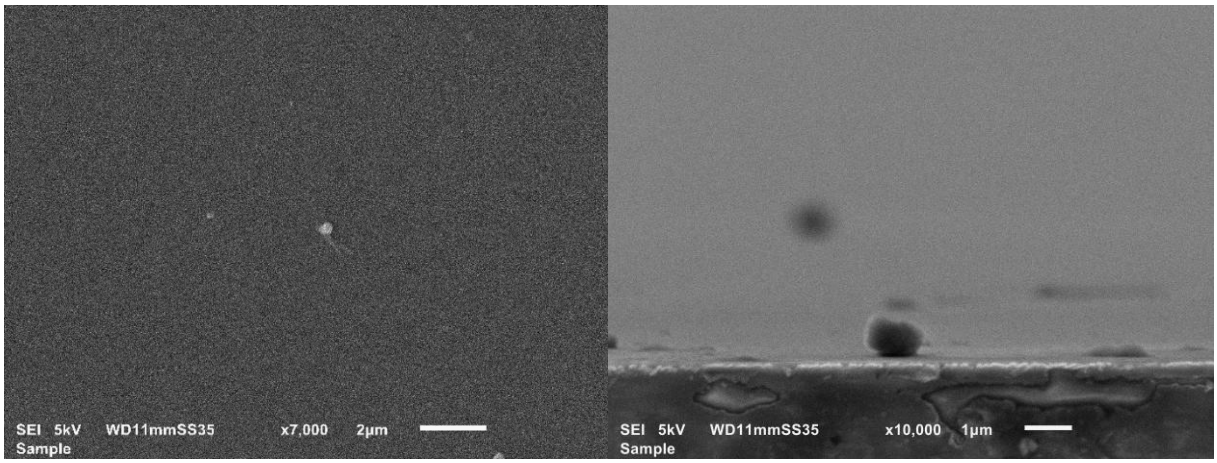

Figure 40: Top-view and cross-section SEM images with He 1.800 slm Q_{Py+He} 200 sccm - 7 cm

Finally, at 7 cm, the deposition drastically decreased, consistent with trends observed in previous experiments. The average size dropped again, reaching 131.1 ± 66.3 nm, and only a few features were observed on the substrate.

4.1.4 Effect of Distance from the Capillaries to the Substrate: Interpretation and Comparison with Literature

The results on the average particle size obtained varying the distance from the capillaries to the substrate (3-4-5-6-7 cm) for the first two best conditions (300 and 250 sccm of precursor) in terms of monomer flow are synthesised in the **Figure 41**:

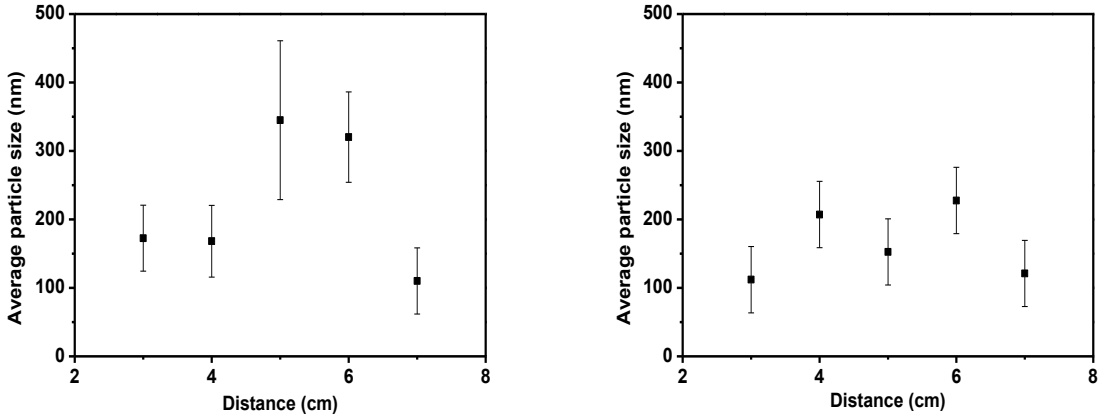

Figure 41: Size distribution of NPs for different tested distances with He 1.700 slm Q_{Py+He} 300 sccm (left) and He 1.750 slm Q_{Py+He} 250 sccm (right)

Using the first two sets of precursor flow rates, 300 sccm and 250 sccm, with identical process parameters except for the variation in the substrate-to-capillary tip distance, similar trends were observed.

When the distance between the substrate and the capillaries was short at 3 cm, the time the formed nuclei spent in the active plasma region was also short. This short residence time inhibited further growth of the nuclei as they quickly deposited on the substrate resulting in smaller nanoparticles., According to established plasma polymerization models showed in the publication of Friedrich [239], the energy dose imparted to monomer molecules and nuclei is directly related to their residence time in the plasma, which governs the extent of radical formation, chain growth, and recombination processes. A shorter residence time thus limits the exposure of nuclei to reactive plasma species and the energy necessary for further crosslinking. This results in the early deposition of smaller nuclei onto the substrate, effectively inhibiting their further growth and leading to smaller nanoparticle sizes. This behaviour aligns with the concept that plasma polymerization kinetics depend not only on plasma power and monomer concentration but also critically on the duration that reactive species spend within the plasma environment before deposition.

At intermediate distances (5 and 6 cm for 300 sccm; 4, 5, and 6 cm for 250 sccm), the residence time within the plasma increases, allowing nuclei more time to grow. However, as the distance increases, the reactive species and plasma-generated energy reaching the substrate progressively decrease. This energy decay, due to collisions and diffusion losses along the path, reduces the efficiency of monomer fragmentation and subsequent reactions. According to the CAP mechanism described by Dufour [243], this shift may limit plasma-induced polymerization, favouring instead less controlled deposition or

incomplete reactions. As result, polymerization becomes less efficient, and the formation of larger nanoparticles and local cluster aggregation is observed. This suggests that while longer residence times initially promote growth, the concurrent drop in energy input begins to affect polymerization kinetics and particle morphology.

A particularly distinct behaviour was observed at a distance of 7 cm for both conditions. Here, the average nanoparticle size decreased drastically, and the overall deposition density was very low. This phenomenon can be attributed to the fact that, at this distance, the sample holder was no longer positioned inside the quartz tube. Consequently, both the plasma plume and the bubbled precursor interacted directly with ambient air before reaching the substrate. The introduction of atmospheric oxygen at this stage likely altered the plasma chemistry, leading to premature reactions of plasma-generated radicals and precursor species. This scenario is consistent with findings from laser ablation plumes by Kautz et al. [244], where even trace amounts of O_2 in the ambient environment were shown to significantly influence the formation pathways of molecular species, clusters, and nanoparticles by promoting early molecular formation and reducing the persistence of atomic species within the plume. Although the plasma jet and laser ablation systems differ in their generation mechanisms and plasma dynamics, both contain highly reactive radical and atomic species that are susceptible to premature reactions with atmospheric oxygen. These oxygen-induced reactions reduce the availability and lifetime of reactive intermediates necessary for nanoparticle growth. In the APPJ case, this interaction likely reduced the density of reactive species reaching the substrate, thus hindering polymerization efficiency and resulting in smaller and sparser nanoparticles.

The main difference between the two flow conditions was that, overall, NPs synthesized with the 250 sccm pyrrole flow were smaller compared to those obtained with 300 sccm. This is likely due to the higher discharge gas flow rate used in the 250 sccm experiments, which led to increased radical generation, greater pyrrole fragmentation, and consequently, the formation of smaller and more numerous nuclei, ultimately resulting in smaller NPs. This trend is consistent with the findings reported by Müller et al. [245] in their study on tungsten nanoparticle synthesis using the HelixJet plasma source, where they showed that increasing the gas flow rate significantly affects nanoparticle size. Specifically, higher gas flow increases the flux of reactive species and radicals that influence nucleation dynamics, favouring the formation of more numerous and smaller nanoparticle. Although the system differs (metal vapor vs. pyrrole monomer), the underlying plasma chemistry principles agree: an increased discharge gas flow enhances radical generation and fragmentation, shifting the balance towards nucleation over growth and resulting in smaller nanoparticles.

The results on the average particle size obtained varying the distance from the capillaries to the substrate (3-4-5-6-7 cm) for the last best condition (200 sccm of precursor) in terms of monomer flow are synthesised in the **Figure 42**:

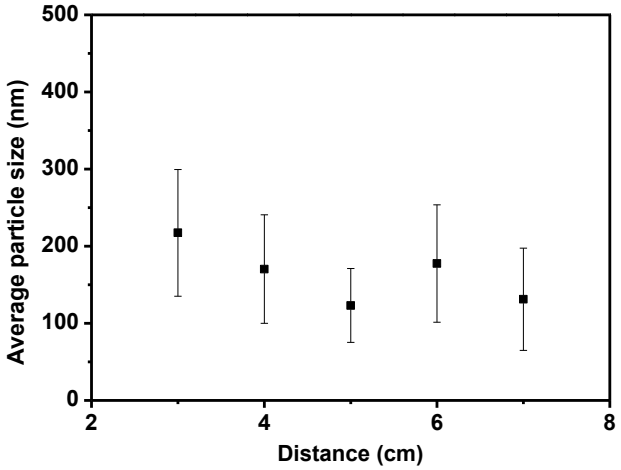

Figure 42: Size distribution of NPs for different tested distances with He 1.800 slm Q_{Py+He} 200 sccm

In the last tested condition, the precursor flow rate was the lowest among the three analysed. The results showed an increased system sensitivity to variations in the substrate-to-capillaries distance. Such enhanced sensitivity under low monomer availability was also observed by Kadhem [246], where slight changes in plasma parameters significantly affected the morphology of synthesized nanoparticles, especially when operating under monomer-limited regimes. At a slightly larger distance of 3 cm, a modest decrease in plasma energy resulted in a significant increase in nanoparticle size compared to the other distances. This suggests a shift in the dominant mechanism from nucleation toward growth, where existing nuclei had more time and energy to grow rather than new nuclei forming. As the distance increased further to 4 and 5 cm, the combined effects of reduced plasma energy and decreased monomer availability once again promoted nucleation over growth, resulting in smaller particles. This trend is consistent with the Cold Atmospheric Plasma (CAP) polymerization mechanism described by Dufour [243], which emphasizes the balance between energy input and monomer concentration in controlling the extent of polymerization and the resulting particle morphology. At 6 cm, the energy transferred by the plasma was no longer sufficient to ensure effective monomer fragmentation and polymerization. Due to the large distance between the substrate and the capillaries (with the substrate positioned very low at the end of the quartz tube) the reduced energy led to incomplete reactions and partial aggregation. This ultimately resulted in an increase in particle size. Similar trends have been observed in low-power plasma environments, where insufficient activation energy leads to disordered growth and particle clustering [247]. Finally, at 7 cm, the sample was located outside the quartz tube, exposing the plasma and precursor to ambient air. This interaction led again to a dramatic drop in nanoparticle deposition and the formation of very small, sparse particles, as was already explained for the other sets of precursor flow rates. In summary, as was anticipated earlier, this last condition revealed great sensitivity to small variations in plasma parameters, particularly substrate distance, resulting in significant shifts in the balance between nucleation and growth, and ultimately affecting nanoparticles size and morphology.

4.1.5 Effect of Input Voltage: Results

For each precursor flow rate condition, an ideal distance was selected based on the smallest average NPs size and the highest deposition on the substrate. Using the best combination of precursor flow and distance, the influence of the input voltage was then investigated by testing 6, 7, 8, 9, and 10 kV. For the 300 sccm precursor flow, the selected distance was 4 cm; for the 250 sccm flow, it was 3 cm; and for the 200 sccm flow, it was 5 cm. All other parameters remained unchanged.

A. Condition: He 1.700 slm Q_{Py+He} 300 sccm

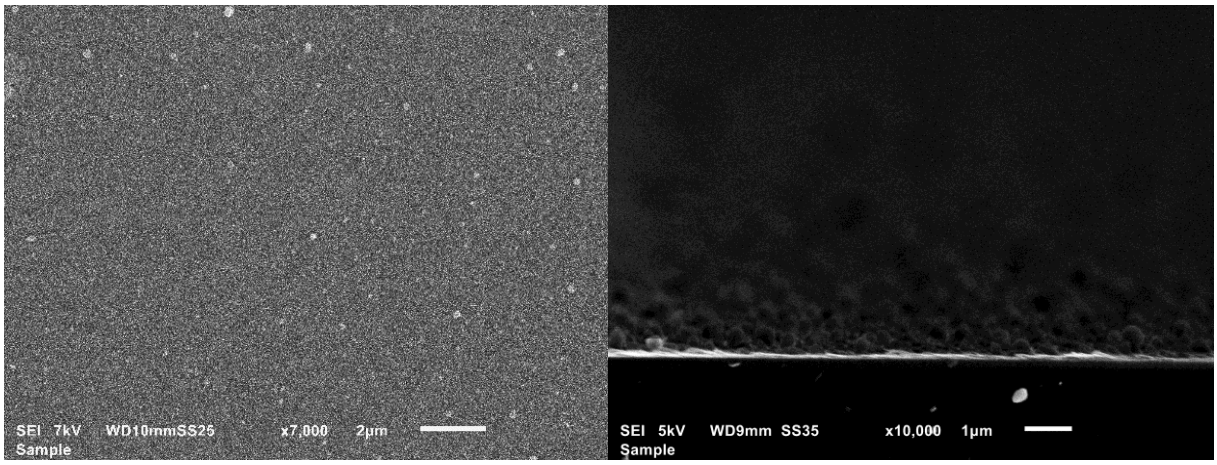

Figure 43: Top-view and cross-section SEM images with He 1.700 slm Q_{Py+He} 300 sccm - 4 cm - 6 kV

Under the first condition, with the lowest input voltage of 6 kV, the smallest average nanoparticle size was achieved, measuring 77.1 ± 36.9 nm. The standard deviation was also the lowest in this experimental set, suggesting a higher degree of size uniformity. Cross-sectional analysis confirmed the presence of spherical nanoparticles, and the measured average deposition thickness was among the highest observed, reaching 650.8 ± 191.5 nm.

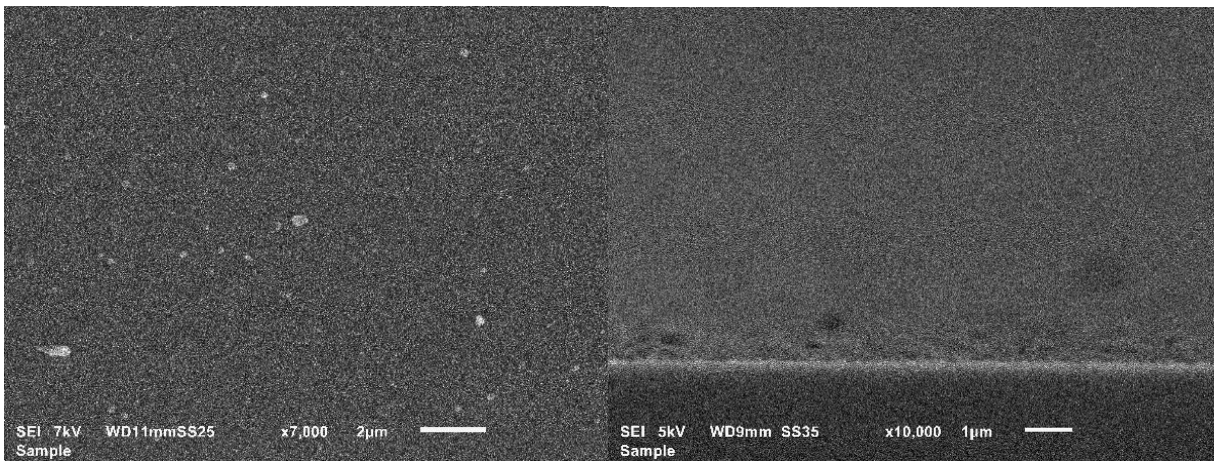

Figure 44: Top-view and cross-section SEM images with He 1.700 slm Q_{Py+He} 300 sccm - 4 cm - 7 kV

By increasing the voltage to 7 kV, SEM images taken from various areas of the substrate revealed a reduced presence of nanoparticles compared to the previous condition. Both the average nanoparticle size and its variability increased, with a mean diameter of 131.3 ± 62.5 nm. Cross-sectional analysis showed a deposition thickness of 385.1 ± 38.9 nm.

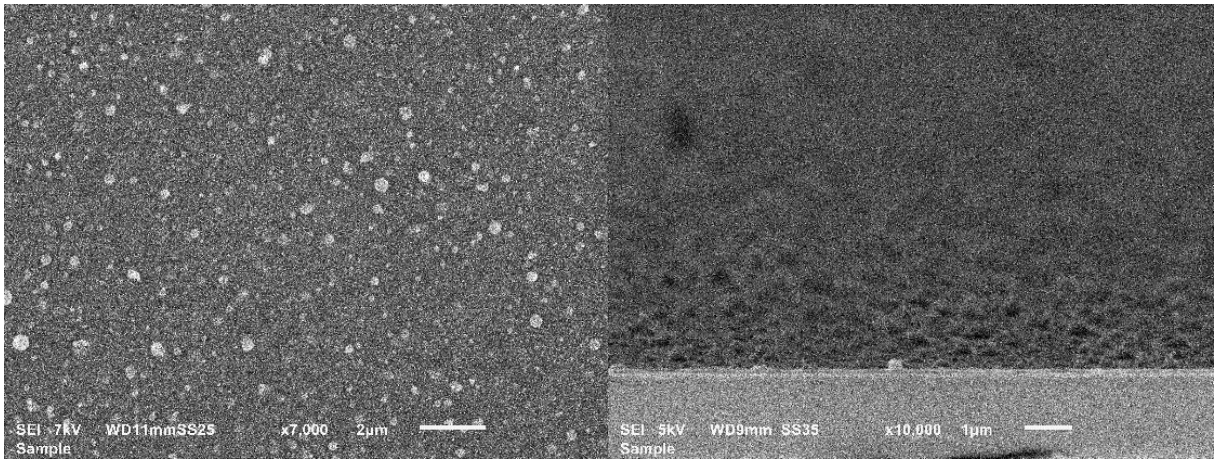

Figure 45: Top-view and cross-section SEM images with He 1.700 slm Q_{Py+He} 300 sccm - 4 cm - 8 kV

At an input voltage of 8 kV, the average nanoparticle size rose slightly to 151 ± 81.6 nm. SEM analysis of multiple regions of the substrate revealed a more consistent coverage, indicating improved deposition uniformity. Well-defined spherical nanoparticles were visible in both top-view and cross-sectional images. The cross-sectional analysis also confirmed the morphology and allowed the estimation of the average deposition thickness, which was 233.4 ± 45.3 nm.

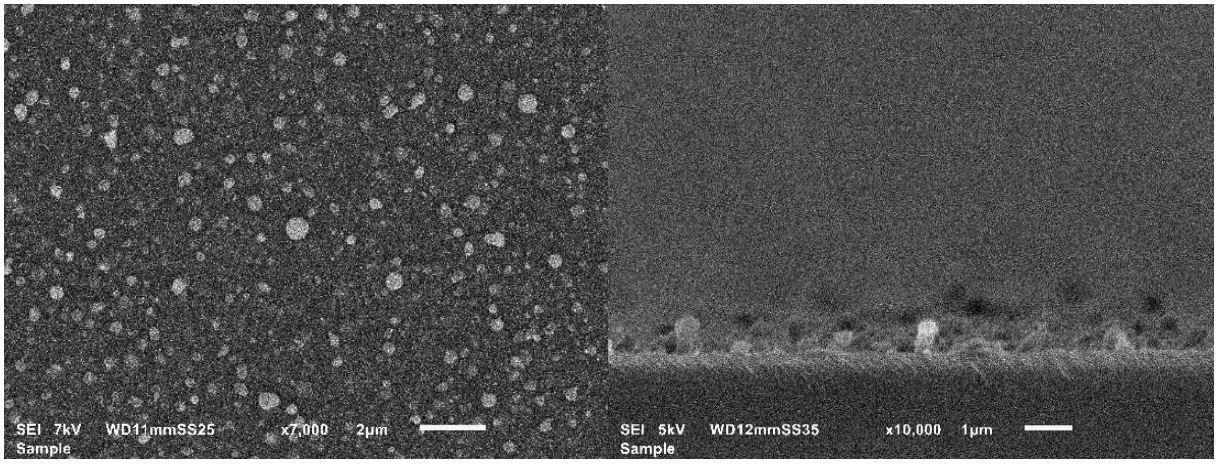

Figure 46: Top-view and cross-section SEM images with He 1.700 slm Q_{Py+He} 300 sccm - 4 cm - 9 kV

A similar behaviour was observed at 9 kV, where the average nanoparticle size further increased, reaching the highest value in this experimental set (169.7 ± 93.7 nm). The nanoparticles maintained a spherical morphology, and the cross-sectional analysis showed a slightly higher average deposition thickness of 291.6 ± 41.6 nm.

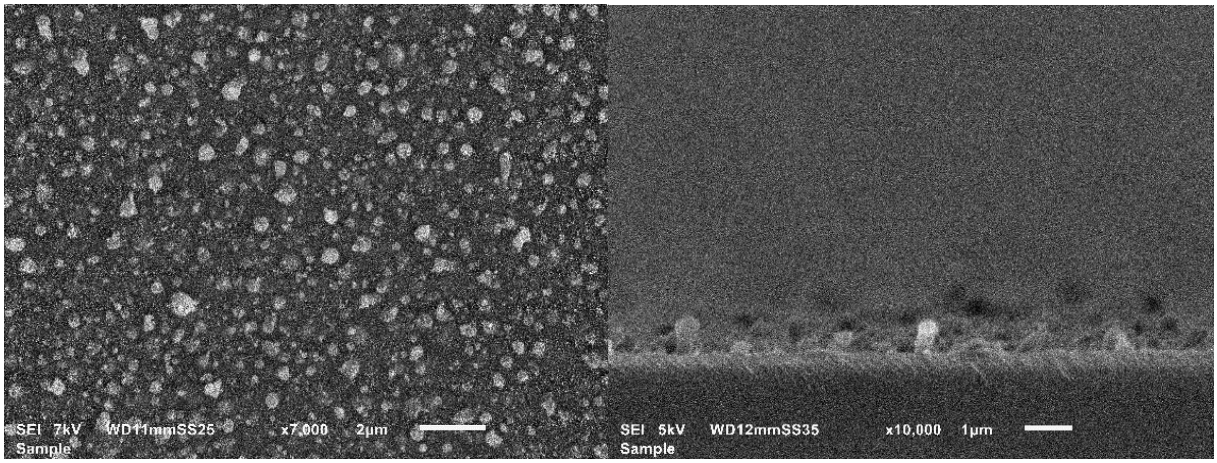

Figure 47: Top-view and cross-section SEM images with He 1.700 slm Q_{Py+He} 300 sccm - 4 cm - 10 kV

Finally, at the highest input voltage of 10 kV, the morphology of the nanoparticles remained comparable to that observed under the previous two conditions. However, the average nanoparticle size slightly decreased to 158.2 ± 89.5 nm. The relatively high standard deviation indicates a broader size distribution and lower uniformity. Additionally, the average deposition thickness increased, reaching 424.3 ± 185.3 nm, as confirmed by cross-sectional analysis.

B. Condition: He 1.750 slm Q_{Py+He} 250 sccm

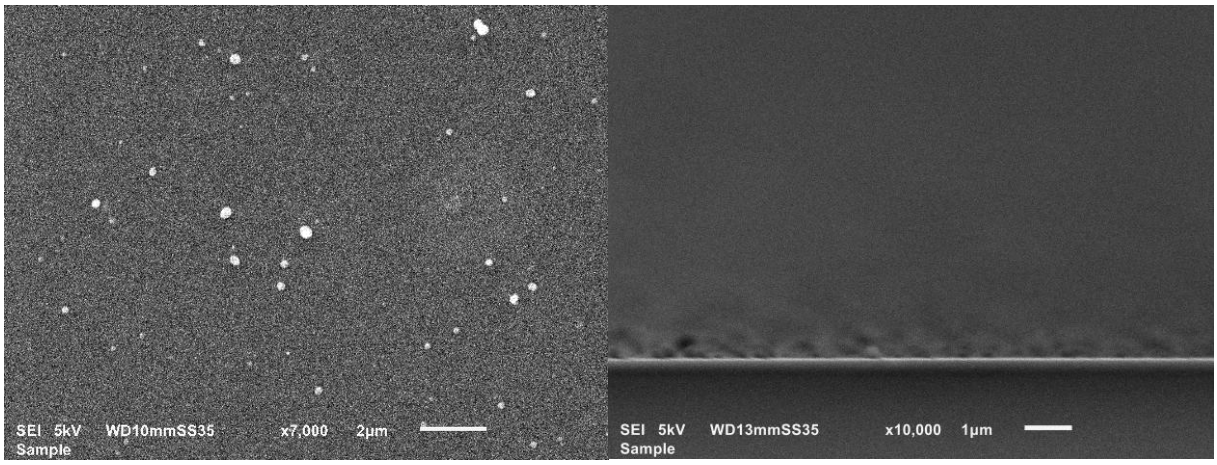

Figure 48: Top-view and cross-section SEM images with He 1.750 slm Q_{Py+He} 250 sccm - 3 cm - 6 kV

In this set of experiments, the lowest input voltage (6 kV) resulted in the smallest average nanoparticle size, measuring 113 ± 55.9 nm. The nanoparticles exhibited a spherical morphology, and top-view SEM images from different areas of the substrate showed a sparse distribution. Their presence was further confirmed by cross-sectional analysis, which revealed an average deposition thickness of 400.0 ± 102.7 nm.

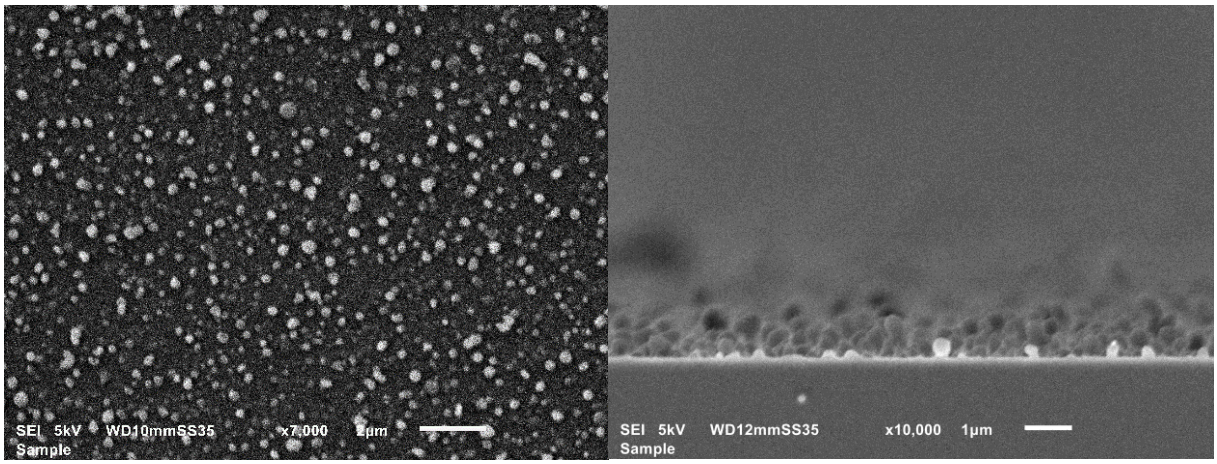

Figure 49: Top-view and cross-section SEM images with He 1.750 slm Q_{Py+He} 250 sccm - 3 cm - 7 kV

When the input voltage was increased to 7 kV, the deposition improved significantly, with a noticeably higher presence of nanoparticles compared to the previous condition. The average nanoparticle size also increased substantially to 169.9 ± 60.4 nm. Cross-sectional analysis confirmed this enhancement, revealing a considerable increase in the average deposition thickness, which reached 650.4 ± 143.9 nm.

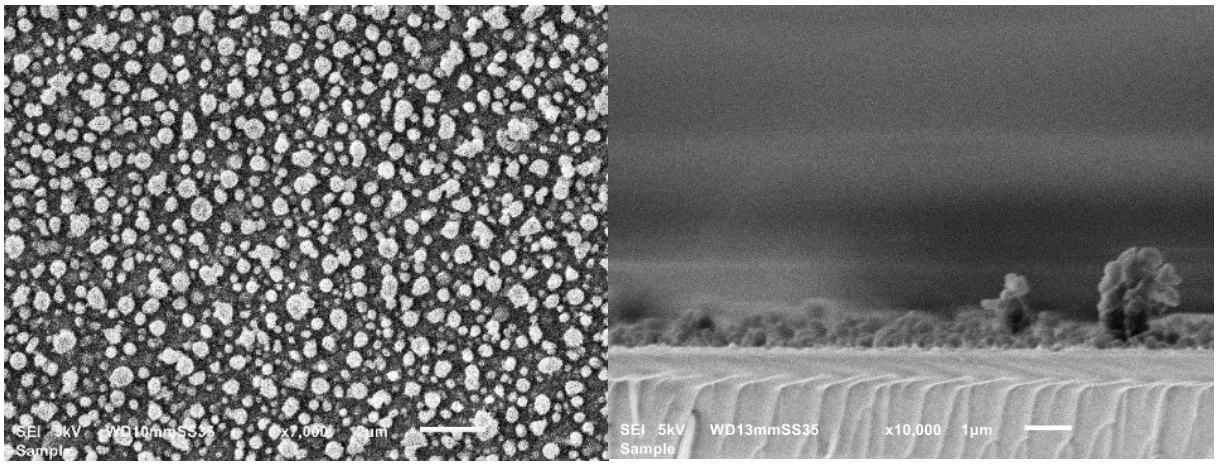

Figure 50*:* Top-view and cross-section SEM images with He 1.750 slm Q_{Py+He} 250 sccm - 3 cm - 8 kV

At 8 kV, the trend of increasing particle size continued, with an average size of 208.3 ± 91.7 nm and the highest standard deviation recorded in this experimental set. The distribution across the substrate appeared less uniform, with some areas visually showing a greater number of nanoparticles and aggregates, while others had more sparsely distributed particles, a pattern also observed under some

previous conditions. Cross-sectional analysis revealed the highest average deposition thickness of the set, measuring 620.6 ± 142.1 nm.

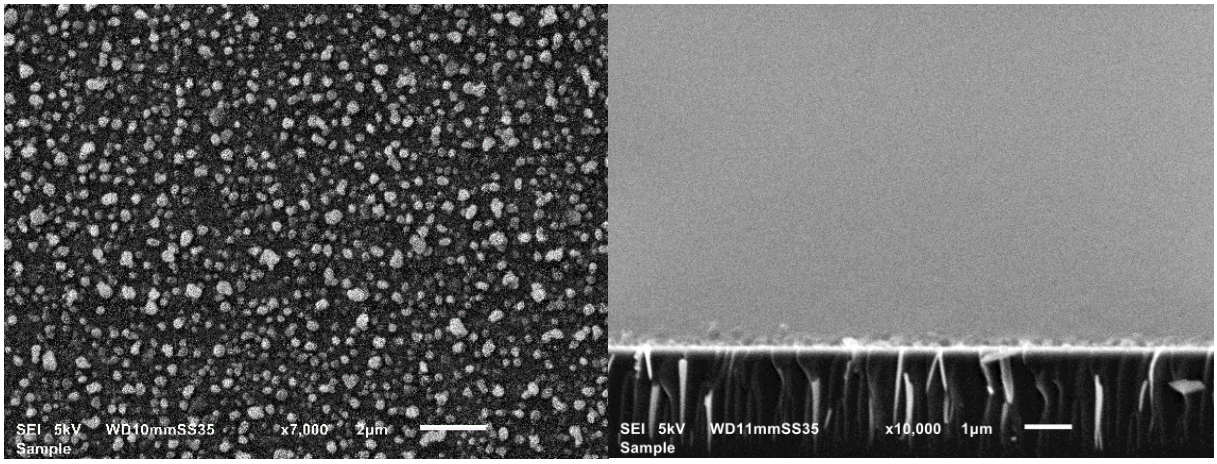

Figure 51: Top-view and cross-section SEM images with He 1.750 slm Q_{Py+He} 250 sccm - 3 cm - 9 kV

Under the condition of 9 kV, the average nanoparticle size remained similar to that observed at 8 kV, reaching 214.7 ± 84.1 nm. However, the standard deviation decreased, indicating a narrower size distribution. Top-view SEM images from different regions of the substrate showed no clearly densely populated areas. In contrast, the average thickness of the deposited nanoparticles decreased to 241.2 ± 47.5 nm, as revealed by cross-sectional analysis.

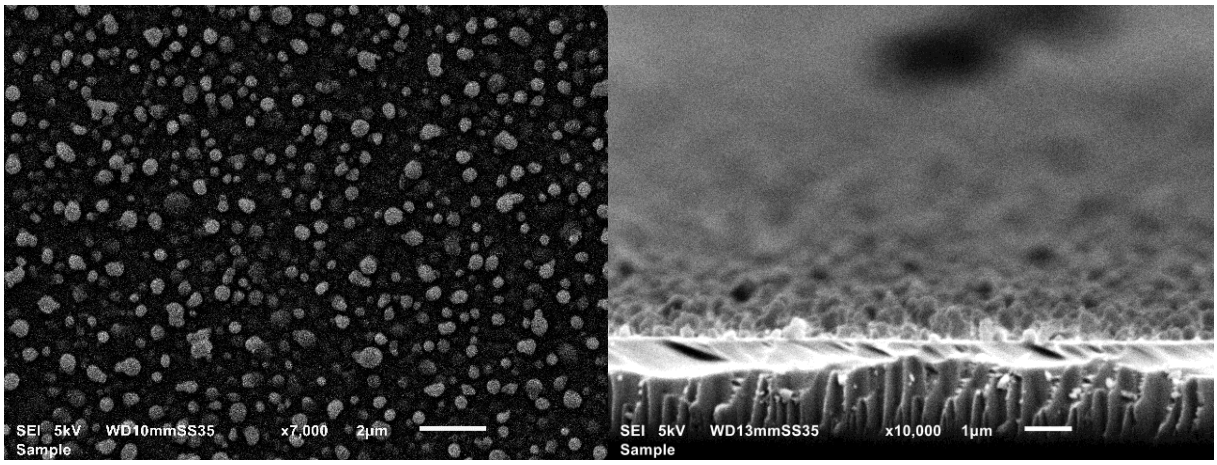

Figure 52: Top-view and cross-section SEM images with He 1.750 slm Q_{Py+He} 250 sccm - 3 cm - 10 kV

Finally, at the highest voltage tested (10 kV), the largest average nanoparticle size was observed, reaching 245.2 ± 90.4 nm—more than double the size recorded at 6 kV. Most of the particles exhibited a spherical morphology, as confirmed by both top-view and cross-sectional SEM images. Under this condition, the average thickness also increased compared to the previous condition, reaching 378.1 ± 78.5 nm.

C. Condition: He 1.800 slm Q_{Py+He} 200 sccm

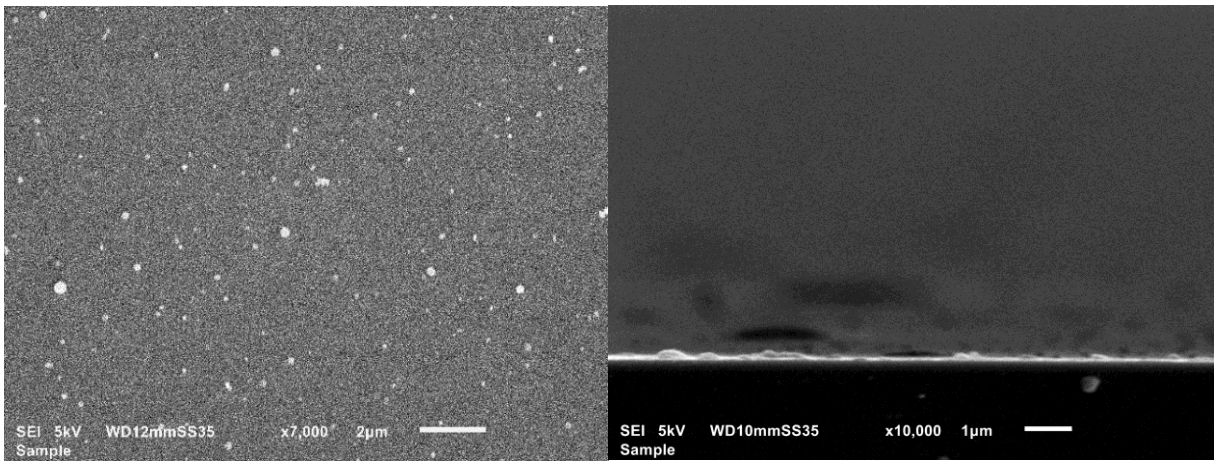

Figure 53: Top-view and cross-section SEM images with He 1.800 slm Q_{Py+He} 200 sccm - 5 cm - 6 kV

In this set of experiments, the lowest input voltage of 6 kV once again resulted in the smallest average nanoparticle size, measuring 117.9 ± 49.8 nm, along with the lowest standard deviation. The nanoparticles exhibited a predominantly spherical morphology, and both top-view and cross-sectional SEM images from different areas revealed a sparse distribution of particles. This condition also produced the lowest average deposition thickness of the set, measured at 161.3 ± 19.8 nm.

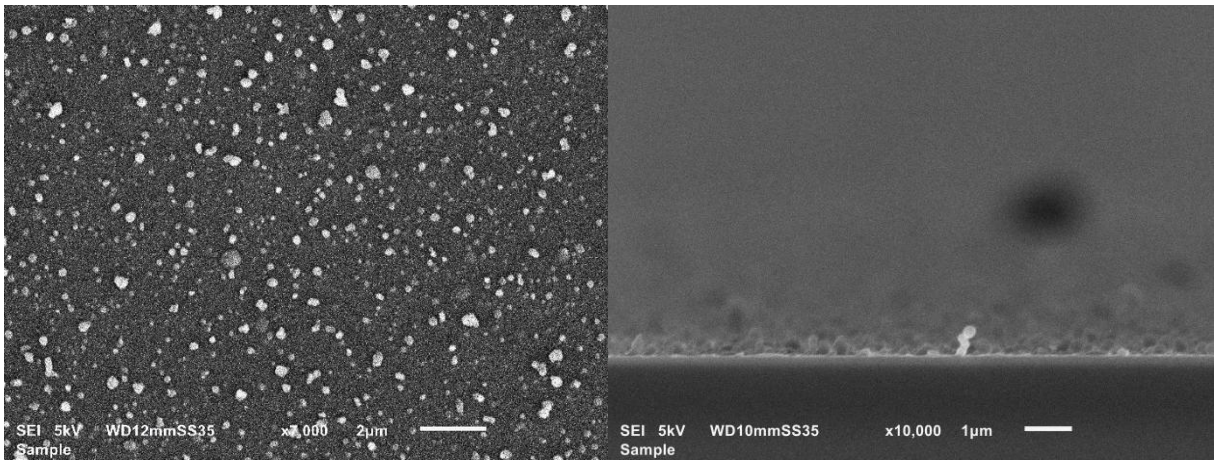

Figure 54: Top-view and cross-section SEM images with He 1.800 slm Q_{Py+He} 200 sccm - 5 cm – 7 kV

Increasing the voltage to 7 kV led to a slight increase in the average nanoparticle size, which rose to 137.5 nm. The presence of nanoparticles also appeared slightly greater compared to the 6 kV condition, and they maintained a predominantly spherical shape. Cross-sectional analysis further revealed a higher average deposition thickness of 363.8 ± 90.8 nm.

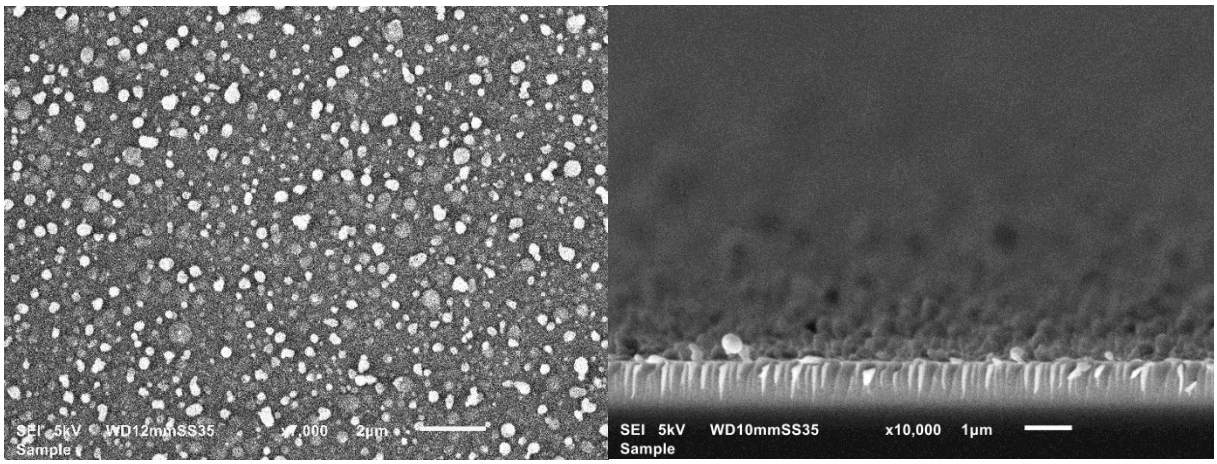

Figure 55: Top-view and cross-section SEM images with He 1.800 slm Q_{Py+He} 200 sccm - 5 cm - 8 kV

A more substantial change was observed at 8 kV, where a significant increase in nanoparticle size occurred. The average nanoparticle size nearly doubled compared to 7 kV, measuring 234.6 ± 85.9nm. Both top-view and cross-sectional images showed a high presence of nanoparticles in the areas and sections of the substrate analysed. Additionally, an increase in the average deposition thickness was recorded, reaching 409.5 ± 137.0 nm.

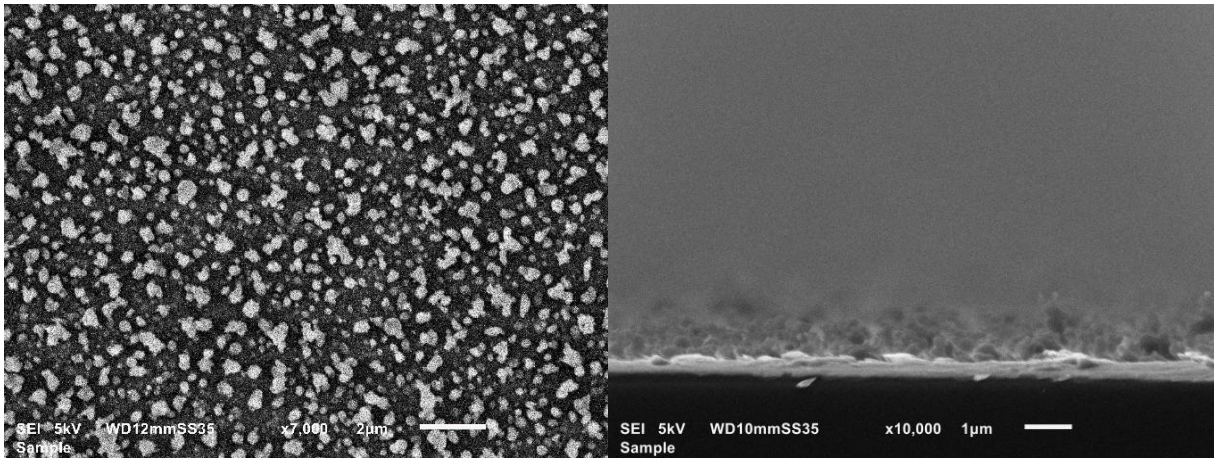

Figure 56: Top-view and cross-section SEM images with He 1.800 slm Q_{Py+He} 200 sccm - 5 cm - 9 kV

At 9 kV, the nanoparticles attained one of their largest average sizes, measuring 268.8 ± 93.9 nm. A noticeable change in morphology was observed: the particles appeared less spherical and exhibited a greater variety of shapes. The standard deviation also increased significantly, indicating greater variability in nanoparticle dimensions. Additionally, the average thickness further increased to 694.4 ± 141.8 nm.

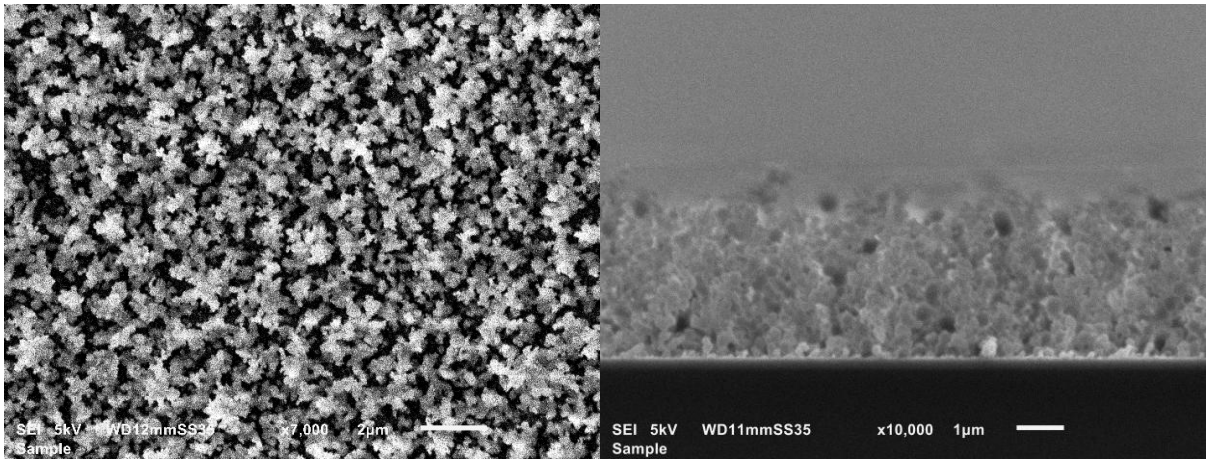

Figure 57: Top-view and cross-section SEM images with He 1.800 slm Q_{Py+He} 200 sccm - 5 cm - 10 kV

Under the highest voltage condition of 10 kV, a marked transformation in the deposition pattern was observed. The nanoparticles were no longer clearly distinguishable as individual entities but had instead merged into large clusters and aggregates. As a result, the average nanoparticle size increased to 462.8 ± 172.6 nm, representing the highest value recorded in this experimental set, accompanied by the largest standard deviation, indicating a broad size distribution and significant particle coalescence. Cross-sectional analysis supported these observations, revealing an exceptionally high average thickness of 3283.2 ± 108.3 nm.

4.1.6 Effect of Input Voltage: Interpretation and Comparison with Literature

The results on the average particle size obtained varying the input voltage (6, 7, 8, 9, and 10 kV) for the three best conditions in terms of monomer flow and distance are summarized in the **Figure 58, Figure 59** and **Figure 60**:

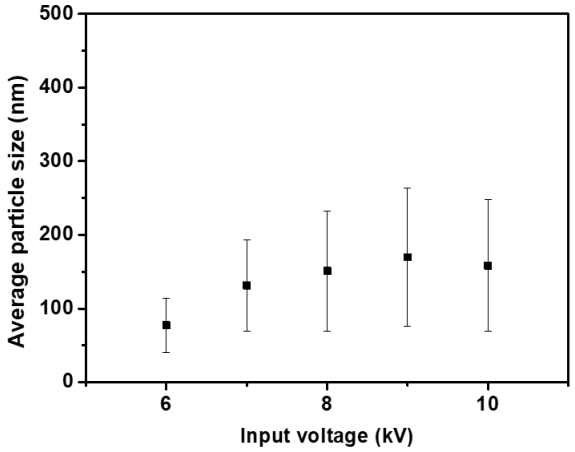

Figure 58: Size distribution of NPs for different input voltages with He 1.700 slm Q_{Py+He} 300 sccm – 4 cm

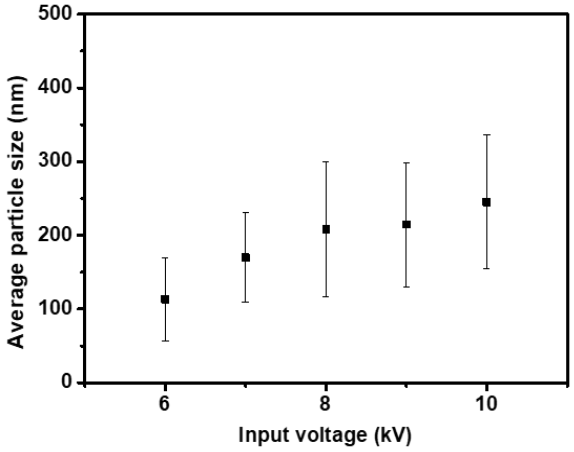

Figure 59*:* Size distribution of NPs for different input voltages with He 1.750 slm Q_{Py+He} 250 sccm – 3 cm

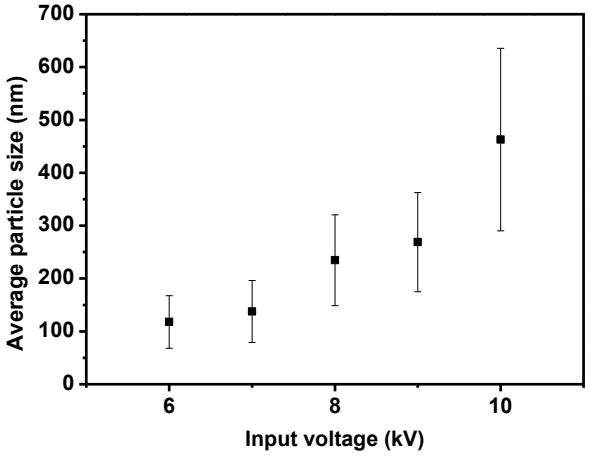

Figure 60: Size distribution of NPs for different input voltages with He 1.800 slm Q_{Py+He} 200 sccm – 5 cm

Varying the input voltage for all three conditions, the same trend was observed: increasing the input voltage led to an increase in the average nanoparticle size, indicating a strong relationship between this parameter and nanoparticle dimensions. The input voltage influences the energy delivered to the plasma, which, together with gas flow and composition, affects the formation of reactive species and consequently the fragmentation and nucleation processes [248]. When the electric field is higher, the plasma energy increases, leading to a more rapid and extensive reaction. Under these conditions, formed nuclei can grow more easily before new nuclei are generated, resulting in reduced nucleation and enhanced growth [249]. This leads to nanoparticles with a larger average size compared to conditions with lower input voltages. In addition, in some cases, SEM images showed the formation of clusters, which may be attributed to aggregation or partial melting of closely spaced nanoparticles caused by the elevated plasma energy associated with higher input voltages.

The main factors contributing to this behaviour are higher density of electrons and reactive radicals in the plasma, and the increase in local temperature, which results in more heat transferred to the precursor, For instance, the study by Xu et al. [250] on ferroelectric barrier discharges demonstrated that the presence of strong surface charge on ferroelectric electrodes significantly amplifies the local electric field, leading to elevated electron densities and electron temperatures, and thus promoting plasma reactivity and instability. This rise in electron temperature and current also results in greater Joule heating within the plasma region. The increased local temperature can cause more thermal energy to be transferred to precursor molecules or nanoparticles on the substrate, thereby favouring growth dynamics and, under some conditions, partial melting and agglomeration.

4.2 Chemical analysis (FTIR)

The surface chemistry of the nanoparticles was investigated by FTIR under different synthesis parameters.

4.2.1. Analysis of Optimal Flow Conditions

FTIR analysis was performed on the samples obtained under three optimal precursor flow conditions (200, 250, and 300 sccm). The first analysis was conducted with a deposition time of 1 minute, an input voltage of 9 kV, and a fixed distance of 5 cm. Zinc selenide (ZnSe) crystal was employed for the analysis, and the spectra were obtained at a range from 700 to 4000 cm^{-1}. The nanoparticles were deposited on a low-density polyethylene (LDPE) film of 0.18 mm thickness (Goodfellow Cambridge Limited) to prevent potential damaging of the crystal upon pressing the analytes against the crystal.

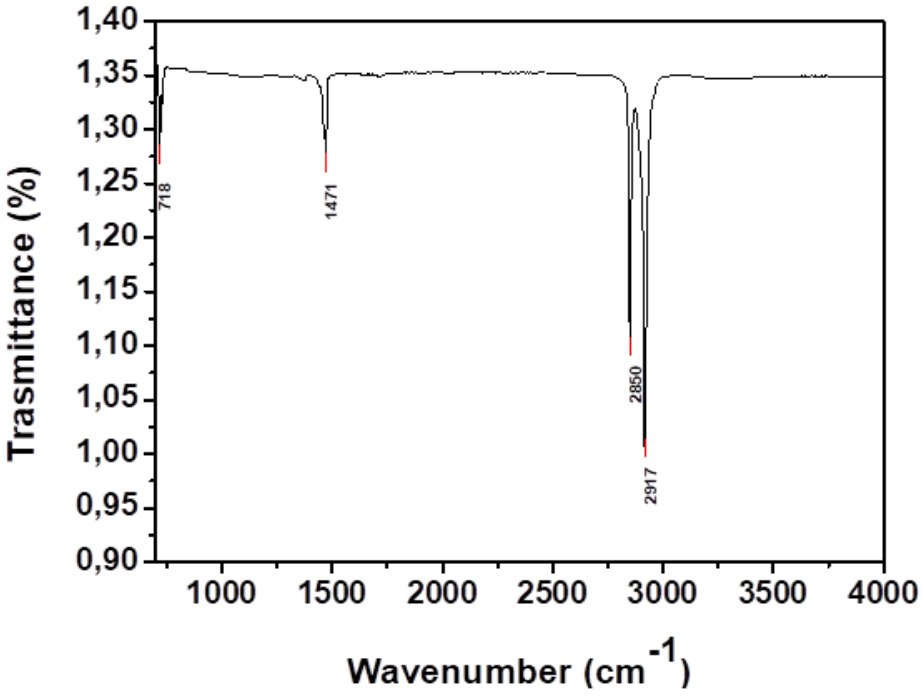

Figure 61: FTIR spectra PE

The first spectrum analysed corresponds to the polyethylene (PE) substrate alone, to identify peaks attributable solely to the substrate. Four main absorption bands are observed at 2917, 2850, 1471, and 718 cm^{-1}. These peaks are characteristic of PE, as reported by Gulmine et al. (2002), and correspond to CH_2 asymmetric stretching (2917 cm^{-1}), CH_2 symmetric stretching (2850 cm^{-1}), CH_2 bending deformation (1471 cm^{-1}), and CH_2 rocking deformation (718 cm^{-1}) [251].

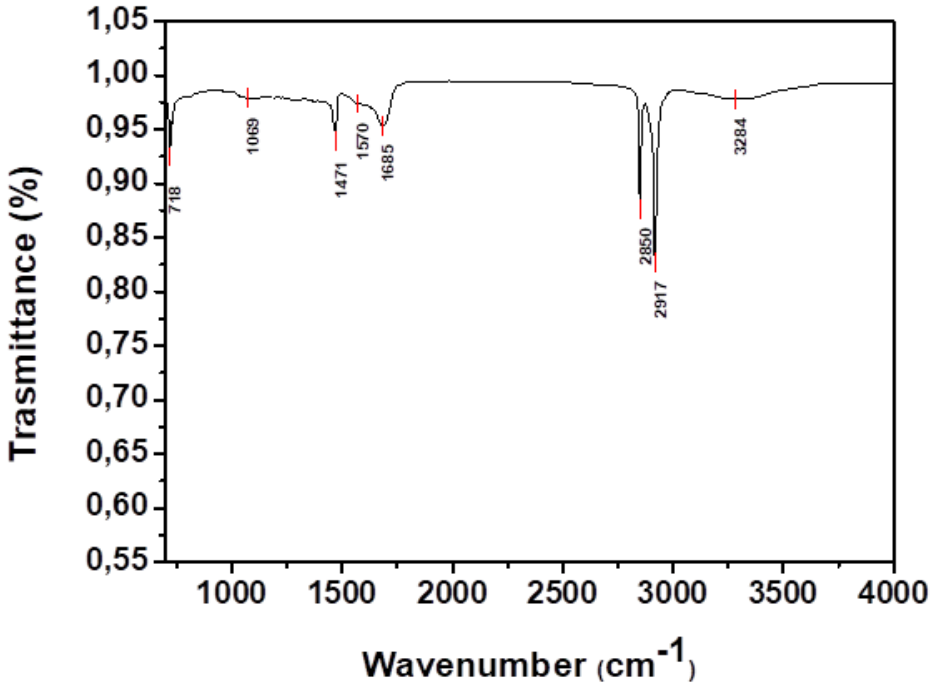

Figure 62: FTIR spectra He 1.700 slm + 300 sccm Py – 9 kV – 5 cm

Under the condition He 1.700 slm + 300 sccm Py, additional peaks emerge at 3284 and 1685 cm^{-1}. The broad band at 3284 cm^{-1} is attributed to N–H stretching vibrations of the pyrrole ring [252], consistent with literature values. The peak at 1685 cm^{-1} corresponds to in-plane C=C stretching within the aromatic pyrrole ring [253]. A shoulder near 1570 cm^{-1} may also be observed, which is attributed to C–C and C=C stretching vibrations associated with interchain crosslinking in the PPy structure [252], [253]. Such crosslinking likely arises from recombination reactions involving reactive plasma species during the polymerization process. Also using this flow, a new peak appears at 1069 cm^{-1}, which can be attributed to the aromatic C–H in-plane bending mode of the pyrrole ring [253]. This assignment is consistent with previous studies on PPy synthesized via solution plasma, which report bands in the 1100–1000 cm^{-1} region.

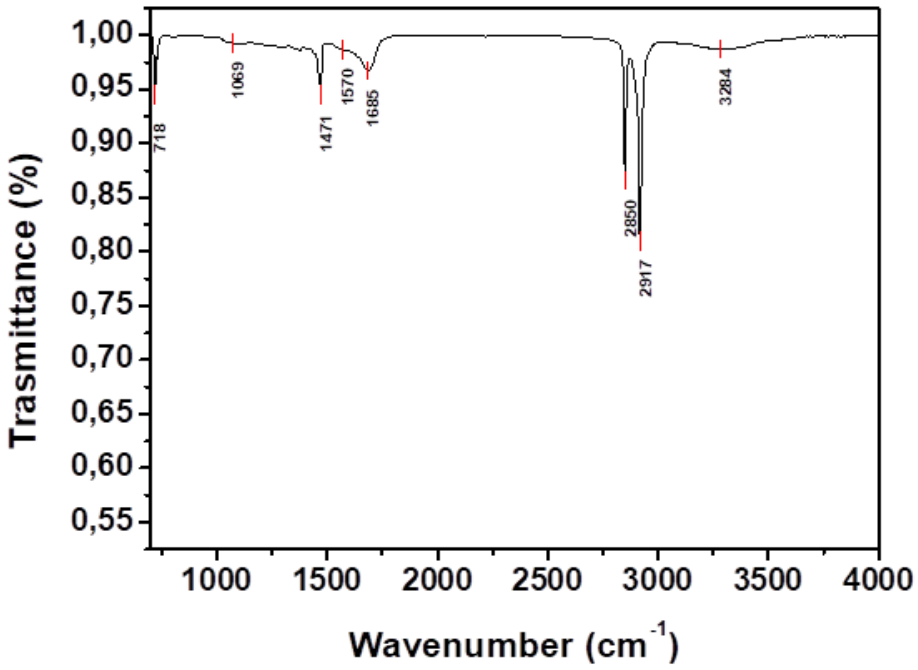

Figure 63: FTIR spectra He 1.750 slm + 250 sccm Py – 9 kV – 5 cm

A comparable spectrum is observed under He 1.750 slm + 250 sccm Py, indicating that the slight variation in monomer flow does not significantly affect the chemical structure of the deposited material. The same peaks are observed at 3284, 2917, 2850, 1685, 1570, 1471, 1069, and 718 cm^{-1}, confirming the consistency of the chemical composition.

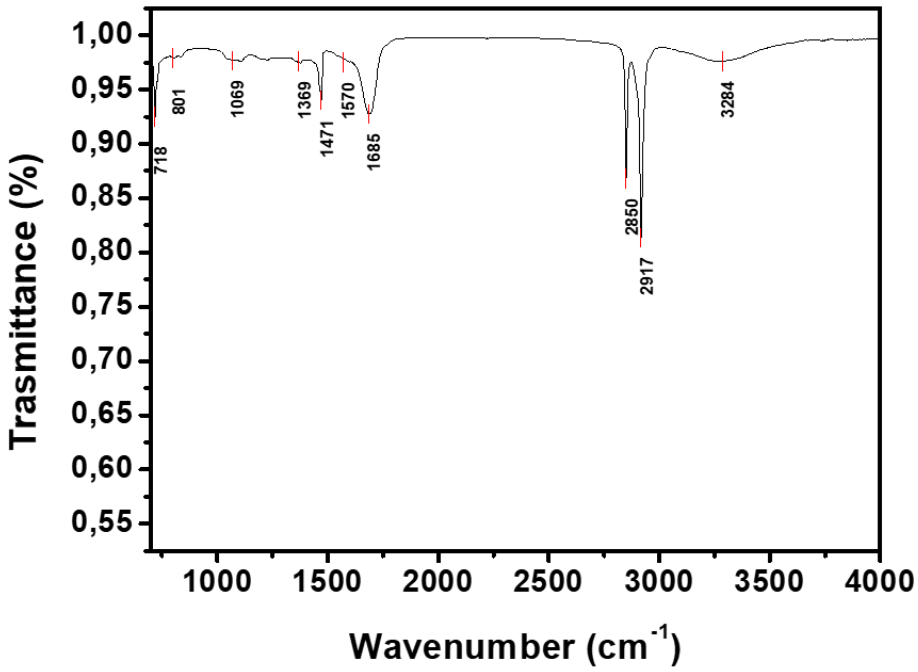

Figure 64: FTIR spectra He 1.800 slm + 200 sccm Py – 9 kV – 5 cm

At He 1.800 slm + 200 sccm Py, a more intense peak is detected at 1685 cm^{-1}, attributed to in-plane C=C stretching vibrations of the aromatic pyrrole ring. Additionally, a potential overlap is observed near 718 cm^{-1}, characteristic of the PE substrate, with a new band emerging around 801 cm^{-1}, that may be assigned to out-of-plane C–H bending in substituted alkenes or ring-opened structures [254]. These are likely formed due to plasma-induced fragmentation of the pyrrole, accompanied by branching and crosslinking processes during polymerization, resulting in a complex PPy nanoparticle matrix. This spectrum shows also a new peak at 1369 cm^{-1}, which has been associated with C–N stretching vibrations in polypyrrole, as reported in the literature [255].

4.2.2. Analysis at SEM-Optimised Distances

The second FTIR analysis considered the optimal distance obtained for each of the three previously analysed precursor flow conditions: 4 cm for 300 sccm, 3 cm for 250 sccm, and 5 cm for 200 sccm.

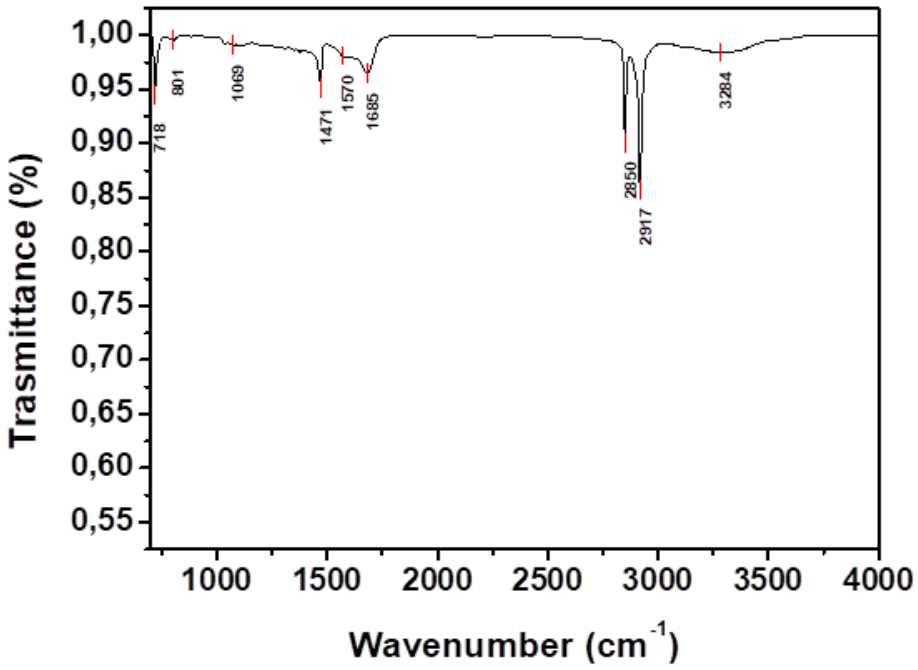

Figure 65: FTIR spectra He 1.700 slm + 300 sccm Py – 9 kV – 4 cm

For the conditions of a helium flow of 1.700 slm and 300 sccm of Py with an input voltage of 9 kV, the best results in terms of nanoparticle morphology were obtained at 4 cm. The spectrum shows the presence of all the characteristic peaks of the PE substrate, including CH_2 asymmetric stretching (2917 cm^{-1}), CH_2 symmetric stretching (2850 cm^{-1}), CH_2 bending deformation (1471 cm^{-1}), and CH_2 rocking deformation (718 cm^{-1}). In addition, several peaks characteristic of pyrrole and PPy are observed: the N–H stretching vibration of the pyrrole ring (3284 cm^{-1}), in-plane C=C stretching within the aromatic pyrrole ring (1685 cm^{-1}), overlapped with C–C and C=C stretching vibrations (1570 cm^{-1}), and the aromatic C–H in-plane bending (1069 cm^{-1}). A small peak is also visible at 801 cm^{-1}, which may indicate the presence of alkene groups or ring-opened structures, likely formed due to plasma-induced fragmentation [254]. However, in general, the PPy-related peaks, except for the one at 1685 cm^{-1}, appear relatively weak. We speculate that the low intensity of the peaks could be attributed to the reduced deposition yield resulting in a thinner coating or due to the fragmentation of these species by highly energetic plasma species.

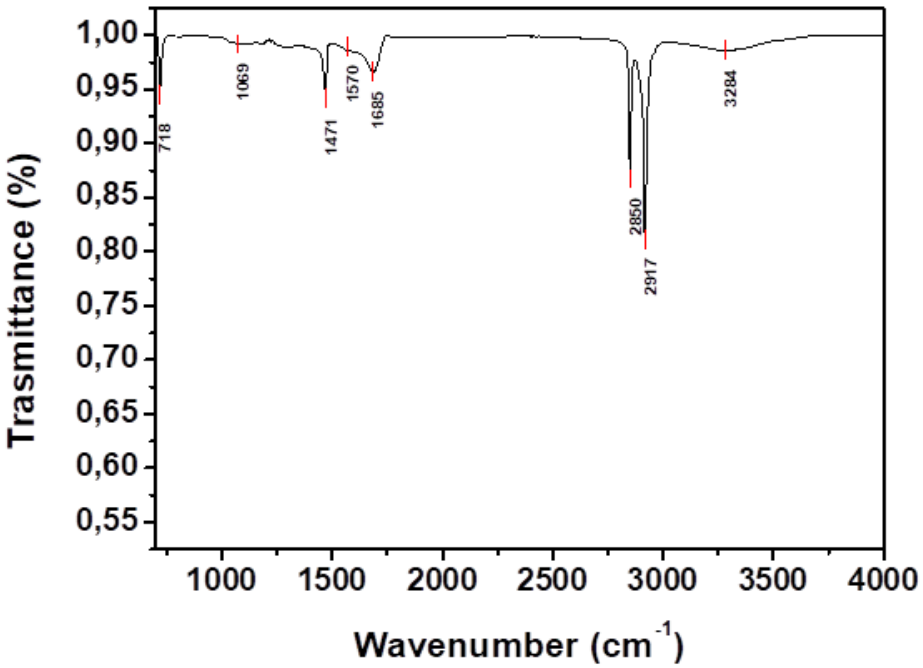

Figure 66: FTIR spectra He 1.750 slm + 250 sccm Py – 9 kV – 3 cm

A very similar spectrum was obtained under the flow of He of 1.750 slm and 250 sccm of Py with an input voltage of 9 kV and the optimal distance of 3 cm. The main difference lies in the absence of the 801 cm^{-1} peak, suggesting a lower presence of substituted alkenes or open-ring structures in this case. These results indicate that no significant chemical differences are observed between the two monomer flow conditions, and that although the optimal distances (3 cm vs. 4 cm) differ, the distance does not substantially influence the chemistry of the deposited material under these conditions. This observation aligns with previous experiments, where comparable spectra were obtained for both flow conditions.

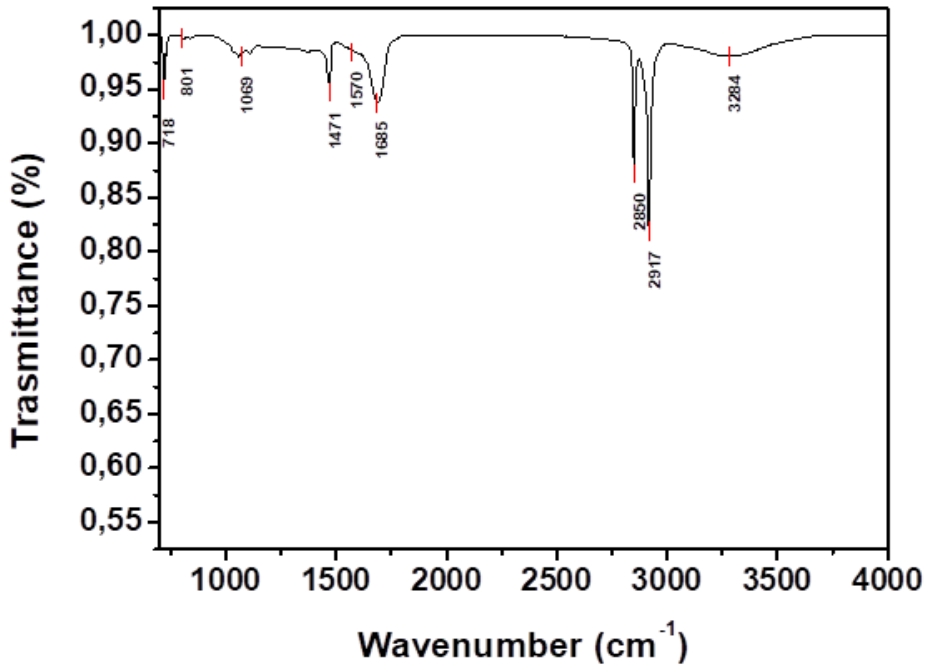

Figure 67: FTIR spectra He 1.800 slm + 200 sccm Py – 9 kV – 5 cm

In contrast, under the flow of He of 1.800 slm and 200 sccm of Py at an input voltage of 9 kV and a distance of 5 cm, all characteristic peaks of PE and pyrrole/polypyrrole are present, and many appear more intense than in the previous conditions. We hypothesize that under these specific conditions, the deposition yield of pyrrole is higher, potentially leading to a higher coating density or greater incorporation of functional groups related to the PPy structure, as higher FTIR signal intensity has been associated with increased deposition yield in plasma-polymerized coatings [256].

4.2.3. Analysis at Final Optimised Conditions

Starting from the three optimal flow conditions and distances, the input voltage was subsequently varied. For each flow, the FTIR analysis focused on the voltage value that resulted in the most effective deposition in terms of particle size and morphology (6 kV for 300 sccm, 7 kV for 250 sccm, and 7 kV for 200 sccm).

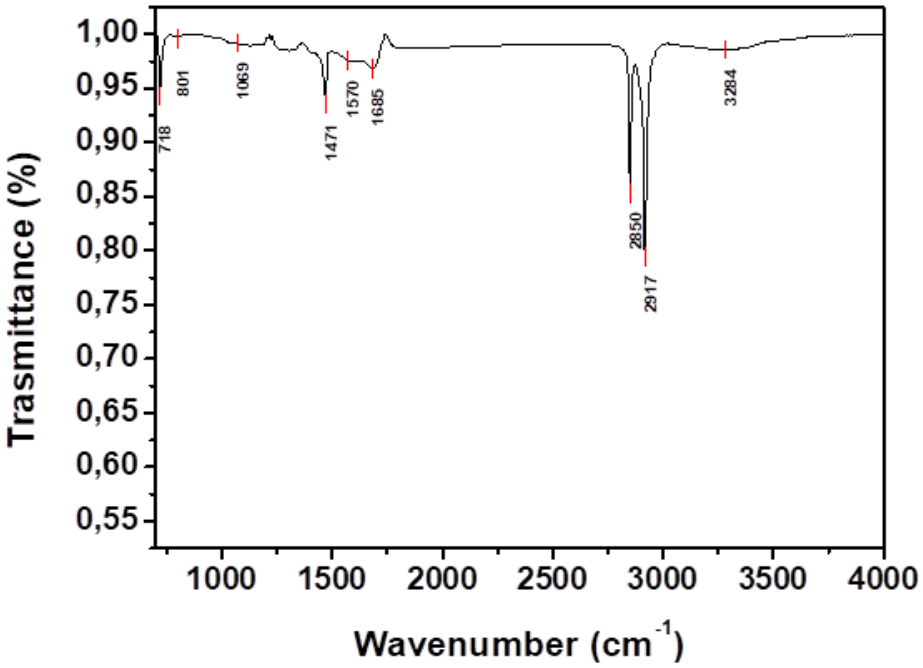

Figure 68: FTIR spectra He 1.700 slm + 300 sccm Py – 6 kV – 4 cm

Under the condition of He 1.700 slm with 300 sccm of pyrrole, a 4 cm distance, 6 kV input voltage, and 1-minute deposition time, the FTIR spectrum revealed clear signals from the polyethylene (PE) substrate. These included the CH_2 asymmetric stretching at 2917 cm^{-1}, symmetric stretching at 2850 cm^{-1}, bending deformation at 1471 cm^{-1}, and rocking deformation at 718 cm^{-1}. In addition, several characteristic peaks associated with pyrrole or polypyrrole were detected: a broad N–H stretching shoulder at 3284 cm^{-1} corresponding to the pyrrole ring, in-plane C=C stretching at 1685 cm^{-1}, overlapping with C–C/C=C vibrations at 1570 cm^{-1}, and aromatic C–H in-plane bending at 1069 cm^{-1}. The signal intensities were strong and well-defined, indicating effective deposition of NPs.

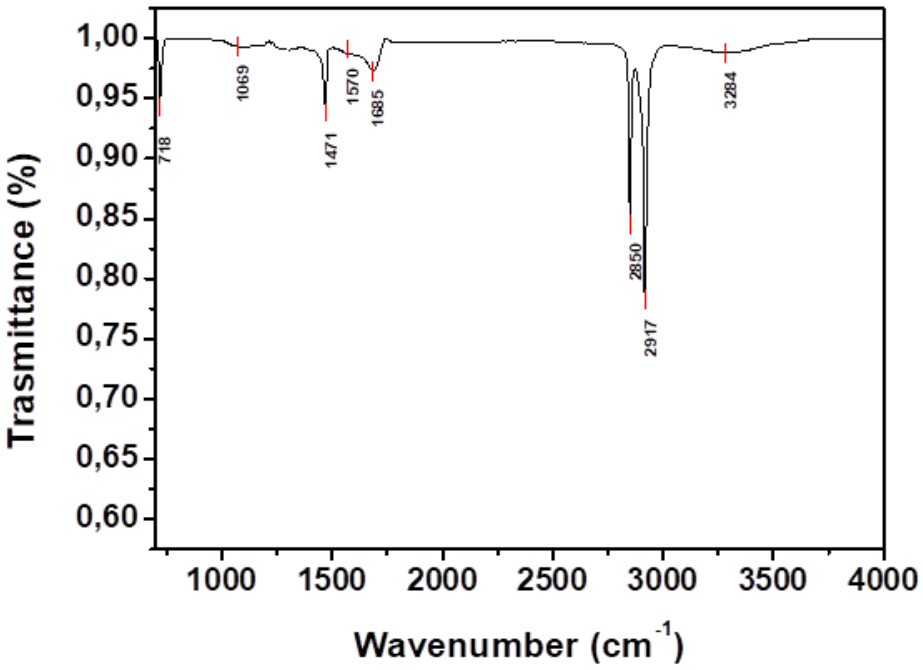

Figure 69: FTIR spectra He 1.750 slm + 250 sccm Py – 7 kV – 3 cm

Under the condition He 1.750 slm + 250 sccm Py – 3 cm – 7 kV – 1 min, the same set of characteristic peaks was observed, with slightly reduced intensity. The peak at 801 cm^{-1}, which was occasionally present in previous spectra and attributed to alkenes or ring-opened structures, was no longer visible. The moderate reduction in peak intensity suggests a slightly lower deposition efficiency compared to the 300 sccm condition, but overall, the chemical features of PPy remain clearly identifiable. This further supports the previous observation that the deposition behaviour between 250 and 300 sccm is comparable, with only minor variations.

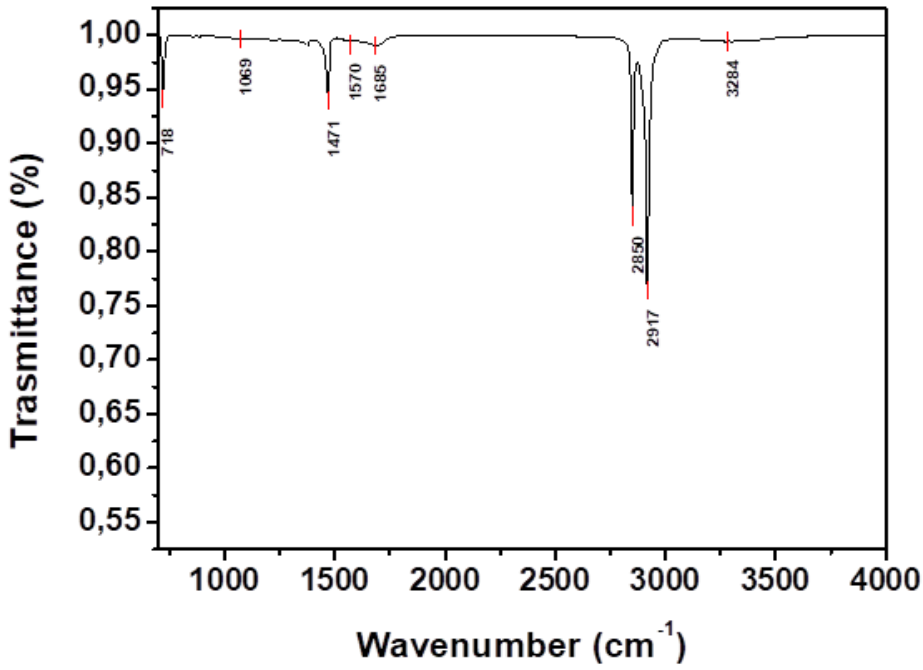

Figure 70: FTIR spectra He 1.800 slm + 200 sccm Py – 7 kV – 5 cm

In contrast, the sample synthesised under He flow of 1.800 slm and 200 sccm of Py at a 5 cm distance and an input voltage of 7 kV exhibited considerably weaker pyrrole-related peaks. While all key bands associated with PPy and PE were still present, their intensities were significantly diminished.

4.2.4. Interpretation and Comparison with literature

Table 4 summarises the main FTIR absorption bands identified under all tested conditions.

Table 4: Main FTIR absorption bands

Wavenumber (cm^{-1})	Functional Group / Bond	Type of Vibration
3284	N–H (pyrrole ring)	Stretching (broad)
2917	CH_2 (PE)	Asymmetric stretching
2850	CH_2 (PE)	Symmetric stretching
1685	C=C (aromatic pyrrole ring)	In-plane stretching
1570	C–C / C=C (PPy interchain)	Stretching (crosslinking related)
1471	CH_2 (PE)	Bending deformation
1369	C–N (polypyrrole)	Stretching
1069	C–H (aromatic pyrrole ring)	In-plane bending
801	Substituted alkenes / ring opening	Out-of-plane C–H bending
718	CH_2 (PE)	Rocking deformation

The FTIR spectra obtained by varying the monomer flow from 300 to 200 sccm showed the functionalities present on the surface. with no substantial chemical differences among the three tested conditions. This observation suggests that minor variations in precursor flow do not significantly impact the chemical structure of the deposited material. Within this range, several key points were identified. Firstly, the appearance of characteristic polypyrrole peaks (N–H stretching, C=C stretching, C–N bending) [252], and secondly, signals that suggest the aromatic ring is retained to some extent, along with crosslinking and branching, highlighted by secondary or overlapping bands (e.g., the shoulder at 1570 cm^{-1}) [253]. Thirdly, the emergence of peaks at 801 cm^{-1}, which are associated with alkene fragments or open-ring structures, suggesting structural rearrangement of the monomer induced by plasma energy.[254] . This flow range represents an optimal balance between monomer availability and plasma energy, which is capable of triggering efficient and complex polymerization reactions. The stability of the chemical structure across different flow rates also suggests that the APP process is resilient to slight variations in precursor input, ensuring surface chemistry reproducibility in nanoparticle synthesis.

The analysis of the FTIR spectra at the optimal distances for each monomer flow condition, 4 cm for 300 sccm, 3 cm for 250 sccm, and 5 cm for 200 sccm of precursor, revealed important insights into the influence of the distance on the chemical structure of the deposited material. The spectra for 300 and 250 sccm showed comparable chemical profiles, with well-defined peaks corresponding to both the

polyethylene substrate and pyrrole/polypyrrole, indicating stable deposition chemistry within this flow range. Notably, the spectrum obtained at 200 sccm and 5 cm exhibited more intense absorption bands, suggesting that the increased distance at lower flow rates may facilitate more efficient polymerization. This could be due to an extended residence time of the precursor in the plasma zone, allowing for more effective interactions with reactive plasma species and thus promoting nanoparticle formation, in agreement with the SEM results, which showed the relationship between residence time and particle growth and crosslinking [239]. One distinct feature observed was the disappearance of the 801 cm^{-1} peak under the 250 sccm - 3 cm condition. This band, typically associated with substituted alkenes or ring-opened structures, was present under other conditions and its absence indicates structural rearrangement of the monomer. This can be attributed to the higher energy density near the jet nozzle. In this region, reactive species impact the substrate with minimal energy dissipation, potentially leading to further fragmentation of labile functional groups. As reported in previous studies, the preservation of such chemical functionalities in plasma polymerization is highly sensitive to energy input and exposure time, with milder conditions generally being more favourable for maintaining the precursor's chemical identity [257]. This finding is consistent with the SEM observations, where smaller nanoparticles were formed at shorter substrate distances. The increased plasma energy at proximity promotes precursor fragmentation, while the reduced residence time limits further growth and crosslinking, resulting in smaller and less interconnected particles.

Finally, the effect of input voltage on nanoparticle synthesis was evaluated for the three optimal flow-distance combinations. At 300 sccm of precursor flow rate and 6 kV of input voltage, FTIR spectra showed strong signals related to the presence of pyrrole and/or polypyrrole, confirming effective nanoparticle deposition. At 250 sccm and 7 kV, the signals slightly weakened, while at 200 sccm and 7 kV, the peaks became very faint, despite previously being strong at the same flow but different distance. This suggests that at lower flow rates, higher voltages may alter the plasma chemistry in a way that reduces the efficiency of nanoparticle formation. This interpretation aligns with prior studies reporting the strong influence of plasma power on nanoparticles formation, demonstrating that increasing plasma power beyond a certain threshold can disrupt polymer growth and alter polymer structure, with higher plasma energy leading to partial ring breakage and the formation of less conjugated polymer fragments, ultimately affecting nanoparticle morphology and chemical integrity [254]. This contrasts with the results observed when varying the distance, where the same 200 sccm condition led to stronger nanoparticles-related peaks, indicating improved deposition and highlighting how plasma energy density must be finely balanced with precursor concentration.

4.3 Surface Elemental Composition Analysis (XPS)

In addition to FTIR, XPS was performed to further investigate the surface chemistry of the nanoparticles under different synthesis parameters.

4.3.1. Analysis of Optimal Flow Conditions

To evaluate the best conditions concerning the morphology of the synthesized nanoparticles, XPS analysis was performed. Initially, the three optimal monomer flow rates were selected and analysed: He 1.700 + 300 sccm Py - 9 kV - 5 cm - 1 min, He 1.750 slm + Py 250 sccm - 9 kV - 5 cm - 1 min and He 1.800 slm + Py 200 sccm - 9 kV - 5 cm - 1 min. For each sample, six different points were analysed, and the results represent the average elemental composition across these measurements.

Table 5: Average atomic percentages of C1s, N1s, O1s for optimal monomer flow rates

He (slm)	Q_{PY+He} (sccm)	Voltage (kV)	Deposition Time (min)	Distance (cm)	C1s (%)	N1s (%)	O1s (%)
1.7	300	9	1	5	71,0 ± 1,2	14,3 ± 0,5	14,7 ± 1,0
1.75	250	9	1	5	74,9 ± 1,0	14,9 ± 0,6	10,2 ± 0,6
1.8	200	9	1	5	69,7 ± 1,4	13,9 ± 0,7	16,3 ± 1,6

The XPS survey spectra revealed the presence of three main elements: Carbon (C 1s), Nitrogen (N 1s), and Oxygen (O 1s). In all three conditions, carbon exhibited the highest percentage, with values of 71.0 ± 1,2 %, 74.9 ± 1,0 %, and 69.7 ± 1,4 % for the precursor flow rates of 300 sccm, 250 sccm, and 200 sccm, respectively. Regarding the other elements, nitrogen has concentrations of 14.3 ± 0,5 %, 14,9 ± 0,6 %, and 13.9 ± 0,7 % for the three conditions, respectively. Finally, oxygen was detected with percentages of 14,7 ± 1,0 %, 10,2 ± 0,6 %, and 16.3 ± 1,6 %.

4.3.2. Analysis at SEM-Optimised Distances

Secondly, for each of the three optimal flow rates, XPS was performed under the condition with the identified best distance. The three conditions were as follows: He 1.700 + 300 sccm Py - 4 cm - 1 min - 9 kV, He 1.750 slm + Py 250 sccm - 9 kV - 3 cm - 1 min and He 1.800 slm + Py 200 sccm - 9 kV - 5 cm - 1 min.

Table 6: Average atomic percentages of C1s, N1s, O1s for optimal precurso flow rates and distances

He (slm)	**Q_{PY+He} (sccm)**	**Voltage (kV)**	**Deposition Time (min)**	**Distance (cm)**	**C1s (%)**	**N1s (%)**	**O1s (%)**
1.7	300	9	1	4	77,3 ± 0,5	14,6 ± 0,5	8,0 ± 0,5
1.75	250	9	1	3	76,5 ± 0,8	15,0 ± 0,5	8,5 ± 0,4
1.8	200	9	1	5	75,9 ± 0,9	15,3 ± 0,5	8,7 ± 0,8

Under the optimized distances, only minor changes were observed in the atomic composition. Carbon remained the predominant element, with atomic percentages of $77.3 \pm 0.5\%$, $76.5 \pm 0.8\%$, and $75.9 \pm 0.9\%$ for monomer flow rates of 300, 250, and 200 sccm, respectively. Nitrogen was the second most abundant, showing values of $14.6 \pm 0.5\%$, $15.0 \pm 0.5\%$, and $15.3 \pm 0.5\%$ across the same conditions. Oxygen content was slightly lower, with corresponding values of $8.0 \pm 0.5\%$, $8.5 \pm 0.4\%$, and $8.7 \pm 0.8\%$. Overall, the elemental composition remained highly consistent, with variations within 2%, suggesting no significant influence of flow rate at this stage.

4.3.3. Analysis at Final Optimised Conditions

After testing different input voltages for the three optimal combinations of pyrrole flow and distances, the three voltages that yielded the best results in terms of deposition and nanoparticle size were selected for further analysis. Each sample was examined at six different points, and the average values were recorded. The selected parameters were as follows: He 1.700 + 300 sccm Py - 4 cm - 1 min - 6 kV, He 1.750 slm + Py 250 sccm - 7 kV - 3 cm - 1 min and He 1.800 slm + Py 200 scmm - 7 kV - 5 cm - 1 min.

Table 7: Average atomic percentages of C1s, N1s, O1s for optimal monomer flow rates, distances and input voltages

He (slm)	**Q_{PY+He} (sccm)**	**Voltage (kV)**	**Deposition Time (min)**	**Distance (cm)**	**C1s (%)**	**N1s (%)**	**O1s (%)**
1.7	300	6	1	4	75,8 ± 0,7	14,7 ± 0,5	9,5 ± 0,6
1.75	250	7	1	3	77,4 ± 0,3	14,5 ± 0,3	8,0 ± 0,5
1.8	200	7	1	5	73,2 ± 1,5	14,3 ± 0,8	12,4 ± 1,5

Under the optimized input voltage conditions, the same elements were detected as in the previous experiments: carbon (C 1s), nitrogen (N 1s), and oxygen (O 1s). Carbon remained the most abundant element, followed by nitrogen and oxygen. For the 300 sccm monomer flow rate, the elemental composition was 75.8 ± 0,7 % for carbon, 14.7 ± 0,5 % for nitrogen, and 9.5 ± 0,6 % for oxygen. Compared to the values obtained with the previous voltage configuration (9 kV), a slight decrease in carbon content (from 77.3 ± 0,5 % to 75.8 ± 0,7 %) and an increase in oxygen content (from 8,0 ± 0,5 % to 9.5 ± 0,6 %) were observed, while the nitrogen percentage remained nearly constant. For the 250 sccm monomer flow rate, the results showed 77.4 ± 0,3 % of carbon, 14.5 ± 0,3 % of nitrogen, and 8,0 ± 0,5 % of oxygen. In this case, there was a slight increase in carbon content compared to the previous condition (from 76.5 ± 0,8 % to 77.4 ± 0,3%) and a reduction in oxygen presence (from 8.5 ± 0,4 % to 8 ± 0,5 %). Finally, for the 200 sccm monomer flow rate, nitrogen content remained almost unchanged (14.3 ± 0,8 % compared to 15.3 ± 0,5 % at 9 kV), while a notable decrease in carbon percentage (73.2 ± 1,5 % compared to 75.9 ± 0,9 %) and a significant increase in oxygen percentage (12.4 ± 1,5 % compared to 8.7 ± 0,8 %) was observed.

4.3.4. Interpretation and Comparison with Literature

The results obtained from the first set of XPS analyses, performed at fixed distance (5 cm) and voltage (9 kV) for all flow rates, showed noticeable inconsistencies compared to the following optimised conditions. Notably, the condition using 200 sccm was repeated in the second set and yielded significantly different elemental ratios, particularly for oxygen. These discrepancies may indicate that the first set was affected by suboptimal deposition or plasma instability, Unstable plasma conditions can lead to poor deposition adhesion, which in turn affect the reliability of surface-sensitive techniques such as XPS [258]. Therefore, the subsequent experiments, based on SEM-identified optimal distances and voltages, are considered more representative and consistent.

The main elements detected in all samples were carbon (C 1s), nitrogen (N 1s), and oxygen (O 1s). This elemental composition reflects the presence of carbon and nitrogen-rich fragments originating from pyrrole [259]. Although not intrinsic to the monomer structure, oxygen was detected in significant amounts, which can be attributed to surface modifications induced by plasma treatment and atmospheric contamination during synthesis and handling. Plasma exposure is known to activate the surface, facilitating the incorporation of oxygen-containing functional groups such as carboxyl, hydroxyl, and ester groups [260], [261]. These surface oxidation processes can enhance the material's reactivity and hydrophilicity [262].

Pure pyrrole (C_4H_5N) does not contain oxygen in its structure and has an atomic N/C ratio of 0.25 [263]. Therefore, the atomic percentages expected from XPS analysis should be approximately 80% carbon and 20% nitrogen. The obtained results showed lower atomic percentages for both carbon (74–77%) and nitrogen (14–15%) compared to the theoretical values. The reduction is particularly significant for nitrogen, with a loss of about 25–30%. These values are highly consistent with those reported for plasma-polymerized pyrrole films, where after just one day of exposure to ambient air, the surface composition showed 76,7 % C, 15.4% N and 7.9% O [264].

In this study the reduction of nitrogen content was associated with the specific degradation pathways induced by plasma and air exposure. One of the key mechanisms involves the formation of nitrile groups during plasma polymerization, which are highly reactive and susceptible to hydrolysis in the presence of water vapor contained in the air. This reaction converts nitrile groups into carboxylic acids, with nitrogen being lost in the form of volatile ammonia. This mechanism provides a strong rationale for the observed decrease in nitrogen and the concurrent increase in oxygen content. Therefore, the surface composition of the nanoparticles not only reflects the effects of plasma-induced fragmentation and polymerization, but also secondary reactions driven by environmental exposure, especially involving humidity and oxygen, which selectively reduce the nitrogen content over time.

Overall, the elemental percentages remained relatively stable, with variations generally below the 2% threshold, indicating that most differences can be attributed to measurement uncertainties. However, a notable change was observed under the condition of 200 sccm of monomer with 7kV and 5 cm, where the oxygen content increased significantly alongside a decrease in carbon percentage. This shift suggests enhanced surface oxidation, likely induced by plasma irradiation, which promotes the formation of oxygen-containing functional groups on the nanoparticle surface. These modifications are documented in the literature, highlighting how plasma treatment can introduce reactive sites that facilitate oxygen incorporation, altering the surface chemistry and improving hydrophilicity [260], [261].

These findings from the XPS analysis align well with the FTIR results, offering a coherent picture of the chemical transformations induced by plasma polymerization and environmental exposure. The presence of characteristic PPy bands in the FTIR spectra, such as N–H stretching, C=C in-plane stretching, and C–N vibrations, confirms the formation of pyrrole-based polymeric structures. Simultaneously, XPS detected a surface enrichment in oxygen, which complements the FTIR observation of increased band intensities, particularly at lower monomer flow and greater substrate distance, suggesting enhanced incorporation of oxygen-containing groups. This is consistent with the proposed formation of polar functionalities such as carboxylic acids or hydroxyls, inferred from both techniques. Moreover, the reduction in nitrogen content detected by XPS can be linked to the structural changes observed in FTIR, such as the disappearance or weakening of certain pyrrole-associated peaks under more intense plasma conditions. Together, these data support the hypothesis that plasma exposure, coupled with post-deposition air humidity, leads to partial hydrolysis and structural rearrangements, modifying the surface chemistry of the nanoparticles. Therefore, the correlation between the two spectroscopic techniques strengthens the interpretation that both plasma parameters and ambient environment critically shape the final chemical nature of the synthesized nanoparticles.

4.4 Plasma composition (OES)

The plasma composition was investigated through OES, using different process parameters.

4.4.1. Effect of Sample Holder

The generated plasma species were analysed using Optical emission spectroscope (OES - S2000, Ocean Optics). To enable comparison, all spectra were normalized by dividing the recorded intensities by the respective integration times used for each condition. As a control and for reference purposes, emission spectra were obtained for pure helium plasma generated with and without the sample holder. NP synthesis conditions which yielded the smallest NP diameters both without the monomer (in the absence and presence of the sample holder) and with the monomer (under optimized conditions in terms of monomer flow, distance from the substrate to the tip of the capillaries, and input voltage).

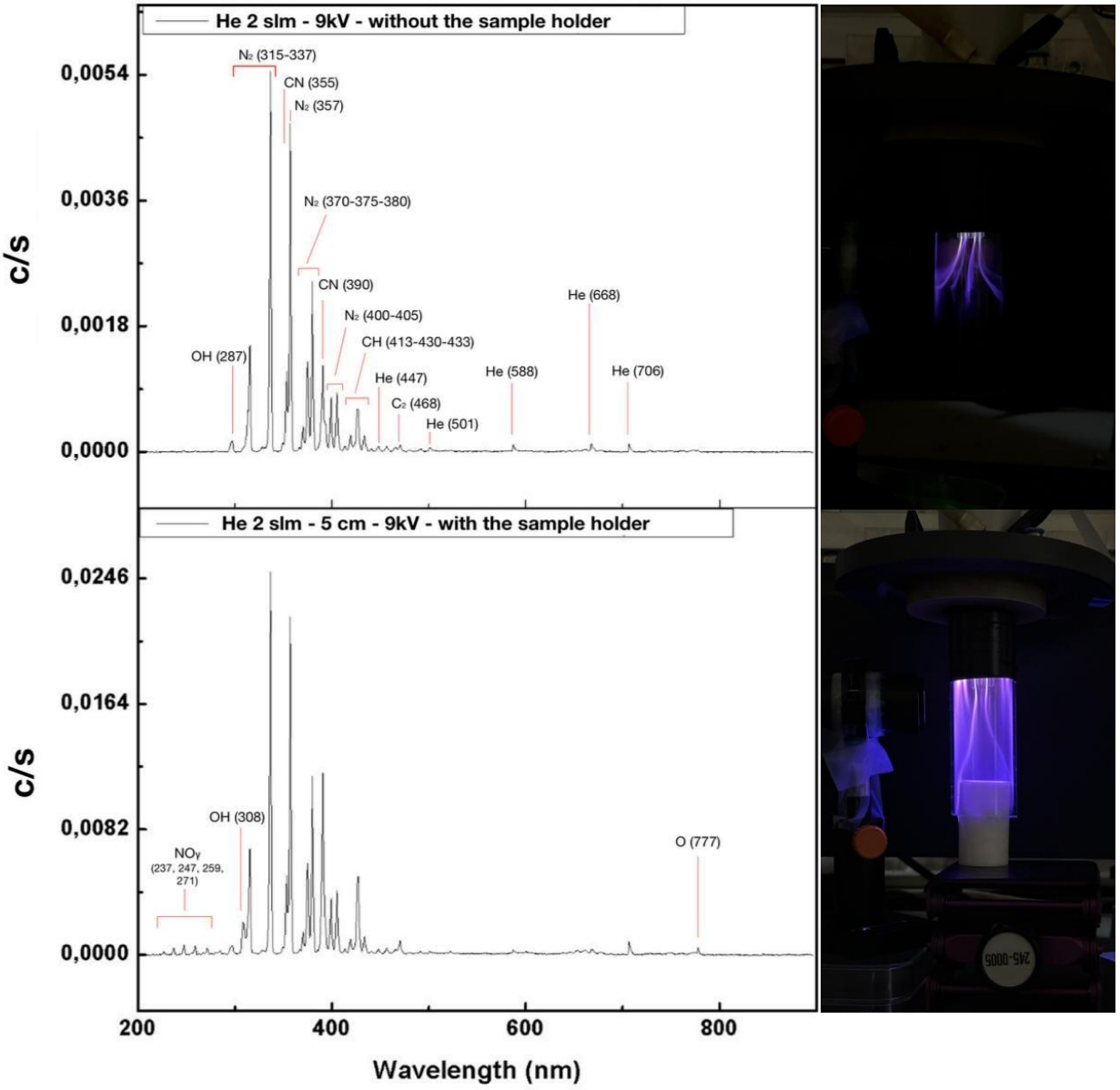

Figure 71: OES spectra of He 2 slm with sample holder and without sample holder (left) and photography of the APPJ-array (right) during the analysis

The first analysis was performed to evaluate the species present in the plasma without the influence of the sample holder. The spectrum in this case showed a high concentration of peaks between 300 and 450 nm, mainly attributed to different plasma components. The first peak at 287 nm corresponds to the OH transition $A^2\Sigma^+$ (v = 0, 1) → $X^2\Pi$ ($\Delta v = 1$) [265]. The peaks at 315, 337, 370, 375, and 380 nm are related to the presence of excited N_2 molecules, specifically corresponding to the $C^3\Pi_u$ → $B^3\Pi g$ electronic transition of the Second Positive System ($\Delta v = 0$) [266]. The peak at 355 nm and 390 nm are attributed to C—N fragmentation transitions ($B^2\Sigma$ → $X^2\Sigma$, $\Delta v \pm 1$), which are typical of nitrogen-containing species [267]. Furthermore, the peaks at 400 nm and 405 nm are part of the extended N_2 emission band (400-470 nm), representing additional vibrational-rotational transitions of the Second Positive System (SPS, $C^3\Pi u \rightarrow B^3\Pi g$). These emissions, along with the 315-390 nm bands, demonstrate the sustained presence of excited N_2 molecules in the plasma, generated through direct electron impact excitation of atmospheric nitrogen [266]. At 413, 430 and 433 nm, the emission corresponds to the CH radical ($B^2\Sigma^-$ → $X^2\Pi$), which is a common fragment in plasma polymerization processes [267]. The peak at 447 nm represents the He transition $4d^3D \rightarrow 2p^3P$ [268], while the next one at 468 nm is associated with C_2 ($d^3\Pi$ → $a^3\Pi$), suggesting the presence of carbon dimers potentially formed from plasma-induced fragmentation of pyrrole [267]. The last four peaks are all related to He transition, in particular: at 501 nm $3p^1P_o \rightarrow 2s^1S_o$, at 588 nm $3d^3D \rightarrow 2p^3P_o$, at 668 nm $3d^1D \rightarrow 2p^1P_o$ and at 706 nm is $3s^3S_1 \rightarrow 2p^3P_o$ [265].

In the case where plasma was generated while the sample holder was inserted into the quartz tube at a 5 cm distance from the tip of the capillaries, the spectrum resembled the one obtained without the sample holder, suggesting that the sample holder did not significantly influence the formation of radicals. However, some new, although low intensity, peaks were observed at 237, 247, 259, 271, 308, 777 nm. The first four peaks (at 237 nm, 247 nm, 259 nm, and 271 nm) belong to the 200-300 nm emission band, corresponding to excited atmospheric NO (NOγ system) [266], while the 308 nm peak indicates OH transition $A^2\Sigma^+$ (v = 0, 1) → $X^2\Pi$ ($\Delta v = 0$) [265] . Finally, emissions at 777 is attributed to the O transition $3p^5P \rightarrow 2s^5S$ [267]

4.4.2. Analysis of Optimised Process Conditions per Flow Rate

For each of the three selected precursor flow rates (200, 250, and 300 sccm), the emission spectra obtained under progressively optimised conditions were analysed. These include the spectra acquired using the optimal precursor flow with 5 cm of distance and 9 kV of input voltage, then with the addition of the optimal distance (determined from SEM analysis) and still 9 kV, and finally under the fully optimised settings (best precursor flow, best distance and best input voltage).

Condition: He 1.700 slm Py 300 sccm

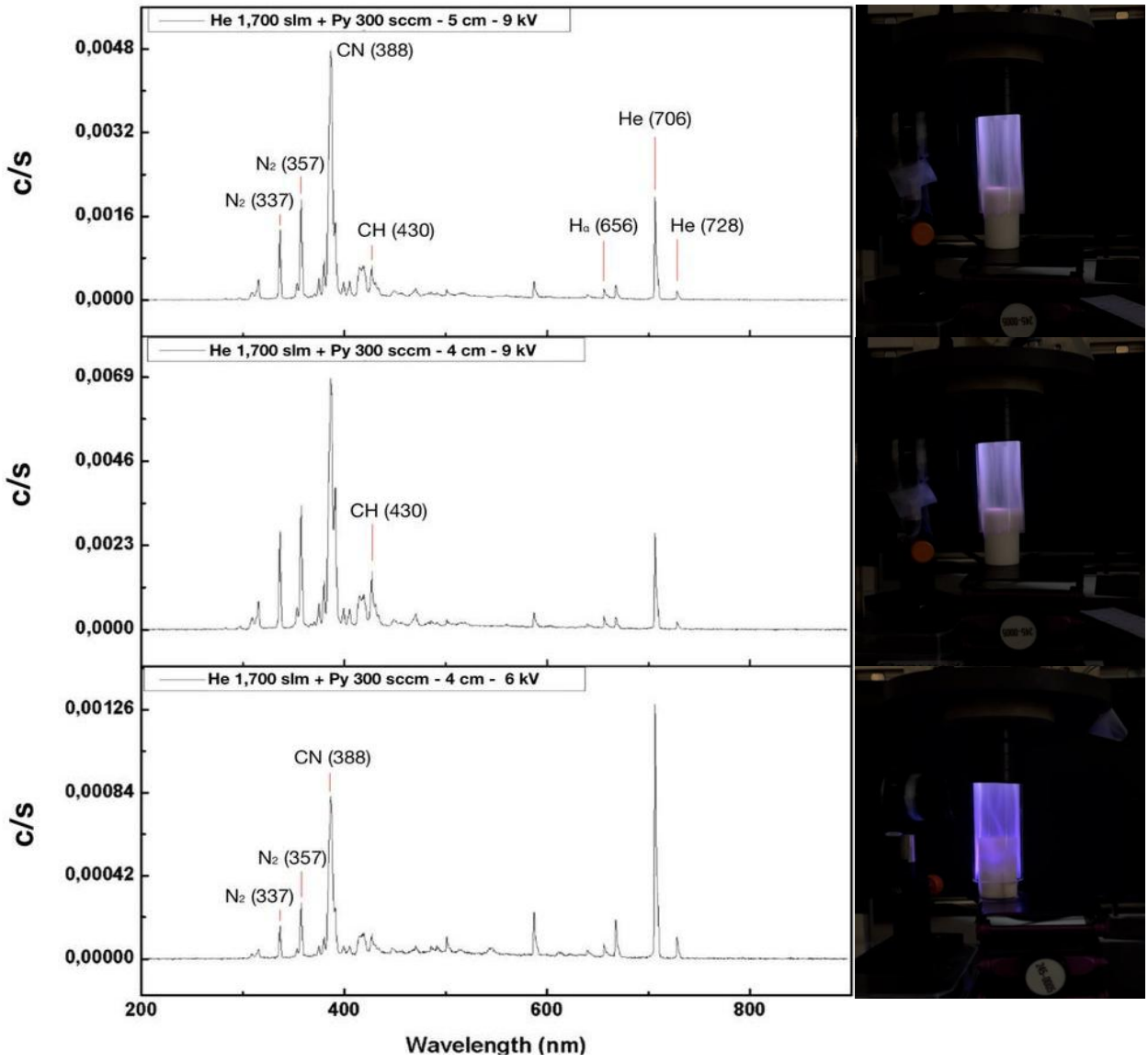

Figure 72: OES spectra of He 1,7 sccm + Py 300 sccm (left) and photography of the APPJ-array (right) during the analysis

Some of the peaks observed in pure helium plasma were also present in 1.70 slm helium plasma with 300 sccm of pyrrole. The main differences were observed with the peaks at 337, 357, and 430 nm, which are significantly lower in intensity compared to the pure helium plasma. The first two are associated with the presence of N_2, while the third is attributed to CH. There was a notable increase of the intensity of the peak at 706 nm, which is associated with the $3s^3S_1 \rightarrow 2p^3P_0$ helium transition. Additionally, three new peaks appeared at 388, 656 nm and 728 nm. The first peak at 388 nm indicates the presence of the CN radical ($B^2\Sigma^+ \rightarrow X^2\Sigma^+$ transition) [267], the second one at 656 nm corresponds to the Hα transition ($2p \rightarrow 3d$), while the peak at 728 nm is associated with a helium transition ($3s^1S_0 \rightarrow 2p^1P_0$) [265].
By changing the distance and using the optimal one at 4 cm, the spectrum remained more or less the same, with both the position and the intensity of the peaks being consistent. The only noticeable variation was a slight increase in the peak associated with the CH radical ($B^2\Sigma^- \rightarrow X^2\Pi$) at 430 nm. This indicates that small variations in distance do not significantly influence the generated species of the plasma.
The last spectrum corresponds to the analysis performed under the optimal input voltage of 6 kV. All the peaks appeared with a lower intensity, particularly the one at 388 nm, as well as a slight decrease in the peak intensities at 357 nm and 337 nm, all associated with nitrogen-related emissions.

Condition: He 1.750 slm Py 250 sccm

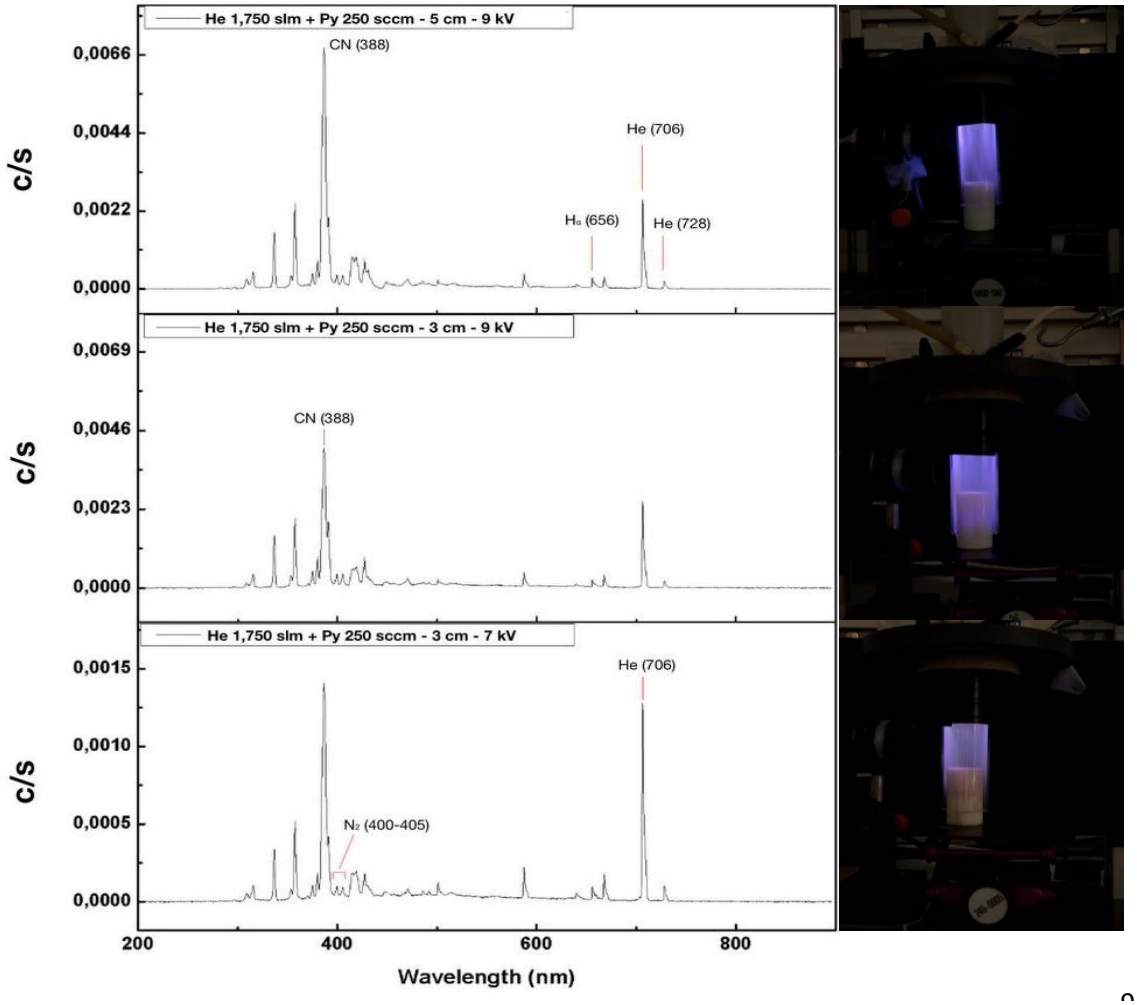

Figure 73: OES spectra of He 1,750 sccm + Py 250 sccm (left) and photography of the APPJ-array (right) during the analysis

The results obtained under the condition of a 250 sccm of pyrrole were analysed first at 5 cm and an input voltage of 9 kV. The spectrum appeared very similar to that obtained with a flow of 300 sccm, showing the same peaks and demonstrating that small variations in flow do not significantly influence the formation of the chemical species. The most intense peak was observed at 388 nm, corresponding to the CN radical transition, followed by the peak at 706 nm, representative of helium. Apart from these, under this condition as well, compared to the pure helium condition, additional peaks appeared at 656 and 728 nm. In this case, varying the distance from 5 to 3 cm did not significantly change the appearance of the spectrum. The primary difference was that most peaks appeared with lower intensity, indicating a reduced presence of some species. For instance, the peak at 388 nm decreased compared to the 5 cm condition, suggesting a reduced occurrence of CN radical transitions. Small differences were observed when using the optimal input voltage of 7 kV while maintaining the same distance as the previous case. In this spectrum, the 706 nm peak became one of the most intense peaks. This indicates a stronger helium transition ($3s^3S_1 \rightarrow 2p^3P_0$). Meanwhile, the peaks corresponding to nitrogen species (at 400 and 405 nm) appeared weaker, suggesting a decrease in nitrogen fragmentation.

Condition: He 1.800 slm Py 200 sccm

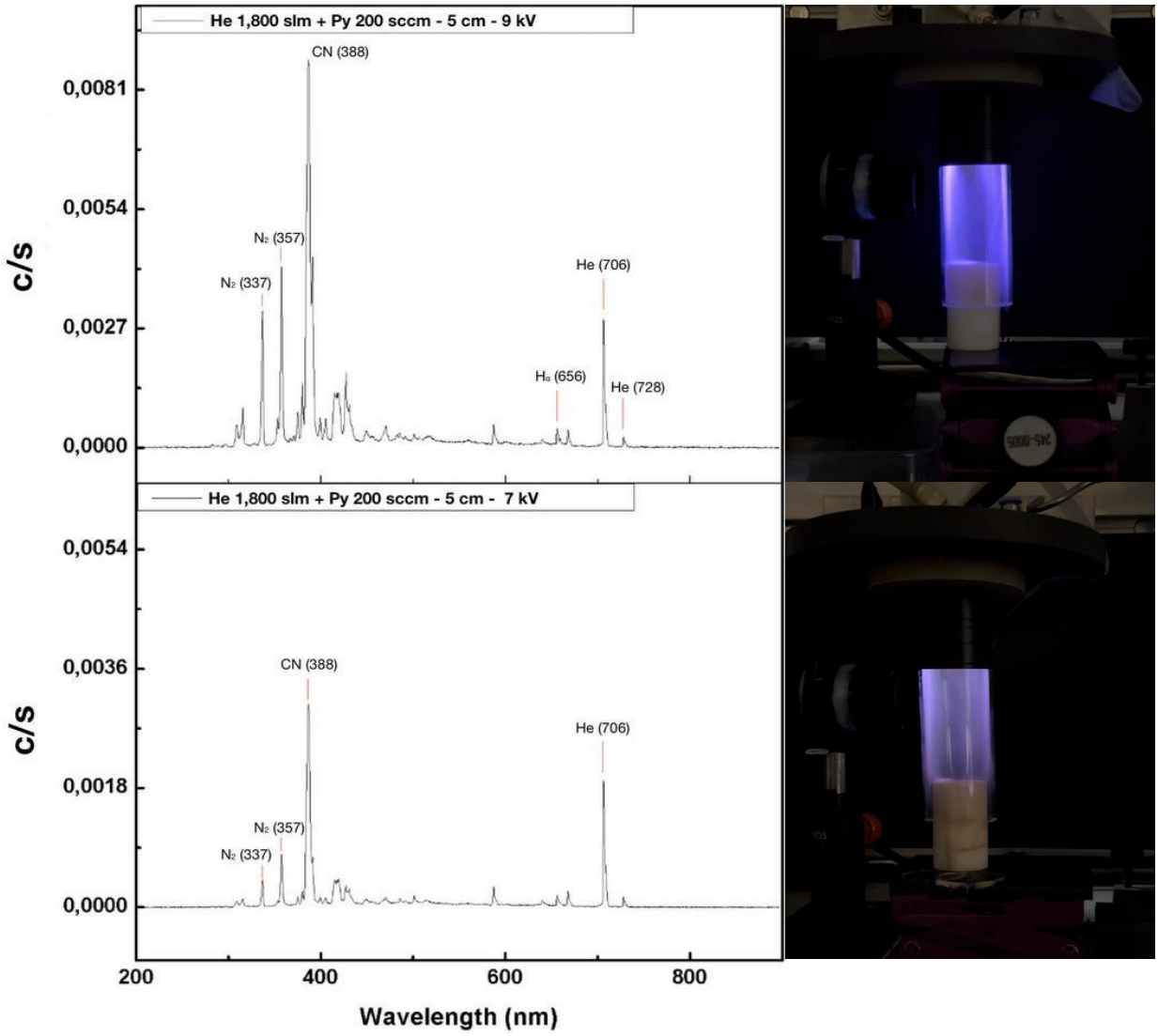

Figure 74: OES spectra of He 1,800 sccm + Py 200 sccm (left) and photography of the APPJ-array (right) during the analysis

For the condition of a 200 sccm of precursor, the analysis was first conducted at a distance of 5 cm and an input voltage of 9 kV. The resulting spectrum was largely comparable to those obtained at 300 and 250 sccm also showing the appearance of peaks at 388, 656, and 728 nm. This indicates that variations in flow rate within this range have a minimal impact on species formation. However, two noticeable differences emerged: the peaks at 337 nm and 357 nm were slightly more intense, suggesting a higher concentration of nitrogen-related species. The most significant change was observed at 388 nm, where the CN radical emissions displayed a marked increase in intensity compared to the other conditions.

When the input voltage was set to 7 kV, distinct changes in the spectrum were observed. The 706 nm peak, associated with the He ($3s^3S_1 \rightarrow 2p^3P_0$) transition, significantly increased, becoming one of the dominant emissions. Conversely, the peak at 388 nm, which had previously shown strong intensity, was notably reduced, along with the nitrogen-associated peaks at 337 nm and 357 nm. This behaviour suggests that lowering the voltage alters the energy distribution within the plasma, favouring metastable helium excitation while reducing the fragmentation of nitrogen and carbon species.

4.3.1. Interpretation and Comparison with Literature

Table 8 summarises the main OES emission wavelengths identified under all tested conditions.

Table 8: Summary of the emission wavelengths observed in the optical emission spectroscopy (OES):

Wavelengths (nm)	**Species**	**Transitions**
237, 247, 259, 271	NO	NOγ system (excited atmospheric NO)
287, 308	OH	$A^2\Sigma^+$ (v = 0,1) → $X^2\Pi$ (Δv = 1 and 0)
315, 337, 357, 370, 375, 380, 400–405	N_2	$C^3\Pi_u$ → $B^3\Pi g$ (Second Positive System, Δv = 0), extended vibrational-rotational transitions
355, 390, 388	C–N / CN	C–N ($B^2\Sigma \rightarrow X^2\Sigma$), CN radical ($B^2\Sigma^+ \rightarrow X^2\Sigma^+$)
413, 430, 433	CH radical	$B^2\Sigma^- \rightarrow X^2\Pi$
468	C_2	$d^3\Pi \rightarrow a^3\Pi$ (carbon dimers from pyrrole)
447, 501, 588, 668, 706, 728	He	Various atomic transitions (e.g., $4d^3D \rightarrow 2p^3P$, $3p^1P_o \rightarrow 2s^1S_o$, etc.)
656	H	Hα line: 2p → 3d
777	O	$3p^5P \rightarrow 2s^5S$

In the absence of pyrrole, the plasma exhibits prominent emission peaks, notably at 308 nm (OH radical), 337 and 357 nm (N_2 second positive system) and 390 nm (CN transition). These emissions are characteristic of helium plasmas interacting with ambient air, leading to the excitation of nitrogen and oxygen species. The presence of OH radicals, for instance, is attributed to the dissociation of water vapor, present in ambient air, adsorbed on the inner surfaces of the helium line and the quartz tube [269]. Introducing the sample holder into the plasma environment does not significantly alter the overall emission spectrum. However, minor peaks emerge at wavelengths such as 247 nm, 308 nm, and 777 nm, indicating slight modifications in the plasma-surface interactions. This behaviour can be attributed to changes in the local electric field and energy distribution caused by the introduction of a solid surface

near the plasma jet, that leads to the appearance of additional spectral lines [270]. However, these subtle changes suggest that while the PTFE sample holder introduces new interfaces, its impact on the generation of reactive species remains minimal.

Introducing pyrrole at a flow rate of 300 sccm led to significant spectral changes, including the reduction of nitrogen-related peaks (337 nm, 357 nm), enhancement of helium emissions (706 nm), and the emergence of new peaks at 656 nm (Hα transition) and 728 nm (He transition), suggesting pyrrole fragmentation and energy transfer modifications; similar modifications in plasma chemistry upon monomer introduction have been reported in low-pressure DC plasmas [271]. Adjusting the distance to 4 cm didn't alter the spectrum, while reducing the voltage to 6 kV decreased overall emission intensities, except for the 706 nm helium peak, which increased. This behaviour can be attributed to a greater accumulation of metastable helium species at lower voltages, as reported by Naidis [272], where reduced electric fields favour the formation of long-lived excited states such as $He(2^3S)$, which emit at 706 nm and play a key role in sustaining the plasma through stepwise excitation and energy transfer. At 250 sccm and 200 sccm flow rates of pyrrole, the spectra remained consistent, with slight intensity variations. Interestingly, lower flow rates enhanced nitrogen-related peaks (337 nm, 357 nm, and 388 nm), suggesting more efficient excitation and energy transfer to ambient air species. According to Bárdos and Baránková [173], this is due to the reduced concentration of organic monomer in the plasma, which decreases the competition for electron energy and allows more efficient excitation of N_2 molecules, thereby intensifying their characteristic emission lines. Voltage optimization at these flow rates of pyrrole confirmed the dominance of the 706 nm helium peak at 7 kV, aligning with findings that helium plasmas maintain stable reactive species across different conditions [272].

4.5 Voltage Characterization

For the different conditions, different input voltages were applied on the power supply itself. However, to assess the actual voltage delivered to the plasma, the peak-to-peak voltage (Vpp) were calculated from the voltage-current waveforms, and for the conditions that yielded best results in terms of morphology and size distributions of synthesized NPs. The measurements were performed using a PicoScope PC Oscilloscope equipped with a Tektronix P6015A high-voltage probe. The Vpp was determined using the following equation:

$$Vpp = Vmax - Vmin$$

where Vmax and Vmin are the maximum and minimum voltage values observed in the waveform, respectively [273]. Five measurements were taken under the same conditions to ensure reproducibility; for each, the peak-to-peak voltage was determined, and the average of these values was considered. The results are shown in the following **Table 9**:

Table 9: Measured Peak-to-Peak Voltages Delivered to the Plasma Under Different Operating Conditions

He (slm)	Py (sccm)	Distance (cm)	Input Voltage (kV)	Average Vpp (kV)
1.7	300	4	6	9,1 ± 0,1
1.7	300	4	9	12,5 ± 0,1
1.7	300	5	9	12,6 ± 0,1
1.75	250	3	7	10,3 ± 0,1
1.75	250	3	9	12,6 ± 0,1
1.75	250	5	9	12,6 ± 0,1
1.8	200	5	7	10,4 ± 0,1
1.8	200	5	9	12,7 ± 0,1
2	0	NO sample holder	9	12,6 ± 0,1
2	0	5	9	12,7 ± 0,1

As shown in **Table 9**. the measured peak-to-peak voltages are consistently higher than the nominal input voltage set on the power supply. This discrepancy may be attributed to the characteristics of the electrical circuit and the impedance mismatch between the power supply and the plasma discharge, especially in the capacitive effects near the electrode [274]. The peak-to-peak voltage appears to increase with increasing input voltage, as expected, but slight variations are observed depending on the gas flow and the inter-electrode distance. For instance, longer distances (e.g., 5 cm) tend to show slightly higher or more variable Vpp values, which may suggest changes in the plasma impedance or the onset of different discharge modes. The configuration without the sample holder (He = 2 slm, Py = 0 sccm) also exhibits comparable Vpp value, confirming that the plasma can be maintained in free mode and that the presence of the sample holder does not significantly affect the delivered voltage.

CHAPTER 5

Conclusions

5.1 Summary of the main findings

In this study, the synthesis of pyrrole-based nanoparticles using an atmospheric pressure plasma jet array (APPJ-array) was investigated. A particular focus was given to how variations in process parameters (precursor flow rate, substrate distance, and input voltage) influence nanoparticle morphology, chemical structure, and plasma characteristics. This was achieved through a comprehensive characterization approach, including scanning electron microscopy (SEM) for nanoparticle morphology, X-ray photoelectron spectroscopy (XPS) for surface atomic composition, Fourier-transform infrared spectroscopy (FTIR) for chemical functional groups, and optical emission spectroscopy (OES) for analysing plasma-generated species.

SEM analysis revealed that intermediate flow rates, between 200 and 300 sccm, yielded the most uniform and smallest nanoparticles (down to ~77 nm), while extremely high or low flows resulted in either aggregation or continuous film formation. Excess monomer led to agglomeration due to several possible factors, including enhanced van der Waals interactions, rapid nucleation and crosslinking driven by high radical formation, and the distribution of plasma energy among a larger number of molecules, which reduces the energy available per molecule and consequently limits monomer fragmentation. Among the tested distances, those between 3 and5 cm were found to be optimal. It was observed that short distances increased energy density, favouring nucleation over growth and resulting in small, spherical nanoparticles. At larger distances (>6 cm), decreased plasma reactivity and increased interaction with ambient air reduced deposition efficiency. The input voltage consistently showed the same trend, indicating a strong correlation between size distribution and applied voltage. An increase in this parameter generally led to larger particle sizes due to enhanced plasma energy, which favoured growth. However, beyond 9 kV, the energy became excessive, disrupting polymerization and reducing uniformity.

FTIR analysis revealed the presence of characteristic pyrrole/polypyrrole peaks, indicating retention of the aromatic ring, crosslinking, and structural rearrangements. Analysis at optimal flow–distance combinations (300 sccm–4 cm, 250 sccm–3 cm, 200 sccm–5 cm) showed that increased distance at lower flow (200 sccm) led to stronger absorption bands, likely due to longer precursor residence time and more efficient interaction with plasma species. Increasing the input voltage resulted in weaker FTIR signals at 200 sccm–7 kV, suggesting that excessive plasma energy may hinder polymer growth and reduce nanoparticle formation efficiency. In general, apart from peaks related to the substrate, all conditions (with varying different parameters) showed the presence of NH, C=C, C–C, C–N, and C–H groups.

The surface composition, analysed through XPS, revealed a clear trend in elemental content: increasing substrate distance or voltage generally enhanced oxygen incorporation (likely due to oxidation) and reduced nitrogen content. These changes were consistent with FTIR results and confirmed the sensitivity of surface chemistry to plasma conditions. However, in general, these results were only slightly influenced by changes in distance and voltage, with average atomic percentages of C1s, N1s, and O1s remaining similar across conditions. Further studies could acquire high-resolution spectra to identify the different bonds present and gain deeper insight into the chemical functionalities.

OES measurements identified reactive species such as excited He, OH, and N_2. Plasma chemistry was affected by the sample holder, the presence of the precursor, and the process parameters. From the interaction between helium and air, the generation of •OH, N_2, and CN was observed. The introduction of pyrrole to the plasma led to the appearance of new signals, a reduction in nitrogen-associated peaks, and an increase in helium-associated emissions, indicating that pyrrole altered the plasma chemistry. Varying the other parameters (monomer flow, input voltage, and distance) did not lead to significant differences in the spectral lines, suggesting that the main species remained present under all tested conditions: NO, OH, N_2, CN, C_2, He, H, and O. Greater distances and input voltages modified the emission profile, reflecting changes in reactive species generation and energy distribution within the array.

These findings demonstrate that plasma polymerization via APPJ-array is a highly tunable and solvent-free method for producing pyrrole-based nanoparticles with tailored properties, offering strong potential for biomedical applications.

5.2 Biomedical potential of the synthesised nanoparticles

The synthesis of pyrrole-based nanoparticles via atmospheric pressure plasma jet array (APPJ-array) has yielded promising physicochemical features that strongly support their potential use in various biomedical applications. The results of morphological, chemical, and plasma characterization highlight the versatility and tunability of the produced nanoparticles, aligning them with key requirements in nanomedicine, particularly in the areas of drug delivery, photoacoustic imaging, photothermal therapy, and biosensing [1].

The nanoparticles synthesized under optimal plasma conditions (flow rate of 300 sccm, distance of 4 cm, and input voltage of 6 kV) exhibited spherical and homogeneous morphology with an average diameter 77.1 ± 36.9 nm. These dimensional characteristics are crucial for systemic biomedical applications. Particles in this size range are known to avoid rapid renal clearance (which typically occurs for particles <5 nm) [275], evade splenic retention (particles >200 nm) [276], resulting in prolonged blood circulation and enhanced permeability and retention (EPR) effect in tumour tissues [277]. This makes the synthesized PPy NPs particularly suitable for targeted drug delivery and tumour imaging.

FTIR, XPS, and OES provided insights into the chemistry of both the surface deposition and the plasma, demonstrating that, from a chemical perspective as well, the synthesised nanoparticles are suitable for biomedical applications. For instance, the group NH, in the protonate form NH+, is known to have bactericidal activity. The presence of this positive charge enables strong electrostatic interactions with negatively charged bacterial membranes, leading to membrane disruption and cell death [151]. Inspired by this mechanism, nanoparticles containing protonable nitrogen functionalities (such as –NH or $–NH_2$)

may exhibit similar antibacterial behaviour, especially when surface-modified or doped to enhance positive charge density. In addition, N-containing functional groups enhance the biocompatibility and hemocompatibility of the materials by improving cell adhesion, proliferation, and viability, while also reducing platelet adhesion and haemolysis. These functional groups can modulate surface properties such as charge distribution, wettability, and surface energy, which in turn influence the interactions between the material and biological components, leading to better cellular responses and reduced cytotoxic or thrombogenic effects [278]. The presence of C–H groups in the synthesized nanoparticles offers potential for biomedical applications, as these groups can participate in C,H insertion reactions, enabling further surface functionalization, that are normally used in the formation of bioactive hydrogel coatings on organic materials [279].

Moreover, the analysis of the APPJ-array plasma plume through OES revealed the presence of several reactive species, including OH, N_2, CH, C_2, and He transitions. Among those, OH radicals are known for their potent oxidative properties that contribute to the inactivation of pathogens and cancer cells. Specifically, OH, along with other reactive oxygen and nitrogen species (RONS), has been shown to induce DNA damage, promote cytotoxicity, and trigger selective apoptosis in various cancer cell lines [280], [281].

To fully harness the promising structural and chemical properties of the synthesized nanoparticles for clinical applications, several additional analyses are recommended.

Zeta potential and colloidal stability assessments provide information on surface charge and predict nanoparticle stability in physiological fluids, guiding further surface modifications to enhance dispersion and prevent aggregation [282].

Given that conventional polypyrrole nanoparticles are widely used in photothermal therapy (PTT) and photoacoustic imaging (PAI) due to their strong absorption in the near-infrared (NIR) region, UV-Vis-NIR spectroscopy should be performed to verify the NIR absorption profile and evaluate the photothermal conversion efficiency [283].

In vitro cytotoxicity and hemocompatibility assays using relevant cell lines and blood components to assess the biocompatibility of the plasma-synthesized nanoparticles [284].

Lastly, drug loading and release studies should be conducted to explore the capacity of the nanoparticles to adsorb or encapsulate therapeutic agents and to evaluate their release profiles in response to specific stimuli such as pH, temperature, or NIR light, enabling the development of stimuli-responsive delivery systems [285].

5.3 Societal reflection

This work comes under the convergence of nanotechnology, green chemistry, and biomedical innovation. The step of synthesis of biocompatible pyrrole-based nanoparticles through a non-thermal Atmospheric Pressure Plasma Jet (APPJ) array not only can be discussed from the technical and scientific points of view but also considering societal responsibility. The selected method, plasma-assisted nanoparticle synthesis, is an intentional deviation away from traditional chemical pathways that often include organic solvents, toxic reagents, and energy-intensive processes. This transition to greener,

safer, and more sustainable synthesis pathways puts this work at the forefront of an international movement toward ethical innovation and aligns with several of the United Nations' Sustainable Development Goals (SDGs) [286].

The APPJ-array process developed in this thesis is consistent with SDG 12 [286]: Responsible Consumption and Production, as it does not demand organic solvents and lowers chemical waste. Compared to conventional bottom-up approaches to the synthesis of nanoparticles, where surfactants, crosslinkers, or further surface functionalization by subsequent procedures may be employed, the APPJ-array process offers in-synthesis functionalization at significantly lower environmental cost. Furthermore, the process is carried out at room temperature and atmospheric pressure, which lowers the energy requirement significantly compared to high-temperature or vacuum-based systems, which contributes to SDG 13 [286]: Climate Action by having a lower carbon footprint.

This shift towards green nanomanufacturing is particularly opportune since the field of nanomedicine advances rapidly. While nanotechnology holds vast therapeutic potential, social acceptance and long-term adoption of such technologies will increasingly depend on their environmental fit throughout the product life cycle. By showing that high-quality biomedical nanoparticles can be fabricated clean, scalable, and solvent-free, this research makes sustainable medical technology with lowered ecological perturbation as a future prospect possible.

The potential applications of the synthesized nanoparticles, such as drug delivery, photoacoustic imaging, photothermal therapy, and biosensing, are directly related to SDG 3 [286]: Good Health and Well-being. These technologies can potentially enable early disease diagnosis, targeted treatment, and real-time disease monitoring for diseases such as cancer, and improve clinical outcomes while reducing side effects and treatment burden overall.

Significantly, plasma-mediated synthesis can be a low-cost, reproducible alternative to conventional nanoparticle synthesis, improving the availability of complex therapies, especially in low-resource settings. The simplicity of operation of the APPJ system, combined with the absence of requirement for expensive reagents or cleanroom facilities, may facilitate technology transfer to the developing world, improving more equitable global access to medical innovation.

Ethically, the use of inherently biocompatible materials is critical for biomedical use. As a potentially more degradable and biologically compatible alternative to some metal-based nanoparticles, which may have long-term toxicity and bioaccumulation concerns, pyrrole-based nanoparticles are an appealing alternative. Nevertheless, it is pertinent to note that biocompatibility needs to be demonstrated through in vitro tests as an initial step, followed by exhaustive toxicological studies to determine their safety for clinical use.

This thesis was conducted in an international academic environment and illustrates the merit of international cooperation in addressing health and sustainability issues. The interdisciplinarity of the project, covering materials science, physics, chemistry, and biomedical engineering, shows the importance of cross-sectoral communication in making technological innovations responsive to societal values and needs.

In conclusion, this thesis is part of a growing literature trying to bring sustainability, equity, and safety into nanotechnology innovation, helping attain a number of SDGs and creating a vision of healthcare that is not just technologically innovative, but socially and environmentally sustainable.

REFERENCES

[1] K. McNamara and S. A. M. Tofail, “Nanoparticles in biomedical applications,” *Adv Phys X*, vol. 2, no. 1, pp. 54–88, Jan. 2017, doi: 10.1080/23746149.2016.1254570.

[2] S. Roszkowski and Z. Durczynska, “Advantages and limitations of nanostructures for biomedical applications,” *Advances in Clinical and Experimental Medicine*, vol. 34, no. 3, pp. 447–456, Jun. 2024, doi: 10.17219/acem/186846.

[3] S. Andrade, M. J. Ramalho, and J. A. Loureiro, “Polymeric Nanoparticles for Biomedical Applications,” *Polymers (Basel)*, vol. 16, no. 2, p. 249, Jan. 2024, doi: 10.3390/polym16020249.

[4] U. Omar, O. Roberto, G. Rafael, and M. Juan, “Interaction of polypyrrole nanoparticles synthesized by plasma with cell lines whit potential biomedical applications,” *Front Bioeng Biotechnol*, vol. 4, 2016, doi: 10.3389/conf.FBIOE.2016.01.01382.

[5] L. Hao, C. Dong, L. Zhang, K. Zhu, and D. Yu, “Polypyrrole Nanomaterials: Structure, Preparation and Application,” *Polymers (Basel)*, vol. 14, no. 23, p. 5139, Nov. 2022, doi: 10.3390/polym14235139.

[6] S. Geetha, C. R. K. Rao, M. Vijayan, and D. C. Trivedi, “Biosensing and drug delivery by polypyrrole,” *Anal Chim Acta*, vol. 568, no. 1–2, pp. 119–125, May 2006, doi: 10.1016/j.aca.2005.10.011.

[7] B. V. N. Nagavarma, H. Yadav, A. Ayaz, L. Vasudha, and H. Shivakumar, “Different techniques for preparation of polymeric nanoparticles - A review,” *Asian Journal of Pharmaceutical and Clinical Research*, vol. 5, pp. 16–23, 2012.

[8] M. Singh, M. Vajpayee, and L. Ledwani, “Eco-friendly Surface Modification and Nanofinishing of Textile Polymers to Enhance Functionalisation,” 2020, pp. 529–559. doi: 10.1007/978-3-030-33774-2_23.

[9] H. Shang, W. Ning, S. Shen, R. Wang, D. Dai, and S. Jia, “Atmospheric pressure plasma jet for surface treatment: a review,” *Rev Mod Plasma Phys*, vol. 9, no. 1, p. 3, Dec. 2024, doi: 10.1007/s41614-024-00177-0.

[10] M. Chen, X. Fang, S. Tang, and N. Zheng, “Polypyrrole nanoparticles for high-performance in vivo near-infrared photothermal cancer therapy,” *Chemical Communications*, vol. 48, no. 71, p. 8934, 2012, doi: 10.1039/c2cc34463g.

[11] M. Wang, “Emerging Multifunctional NIR Photothermal Therapy Systems Based on Polypyrrole Nanoparticles,” *Polymers (Basel)*, vol. 8, no. 10, p. 373, Oct. 2016, doi: 10.3390/polym8100373.

[12] R. Chen, F. Yang, Y. Xue, X. Wei, L. Song, and X. Liu, “Polypyrrole confined in dendrimer-like silica nanoparticles for combined photothermal and chemotherapy of cancer,” *RSC Adv*, vol. 6, no. 45, pp. 38931–38942, 2016, doi: 10.1039/C6RA03314H.

[13] Z. Zha *et al.*, “Biocompatible polypyrrole nanoparticles as a novel organic photoacoustic contrast agent for deep tissue imaging,” *Nanoscale*, vol. 5, no. 10, p. 4462, 2013, doi: 10.1039/c3nr00627a.

[14] O. S. Kwon *et al.*, “Ultrasensitive and Selective Recognition of Peptide Hormone Using Close-Packed Arrays of hPTHR-Conjugated Polymer Nanoparticles,” *ACS Nano*, vol. 6, no. 6, pp. 5549–5558, Jun. 2012, doi: 10.1021/nn301482x.

[15] Y. Tao, E. Ju, J. Ren, and X. Qu, “Polypyrrole nanoparticles as promising enzyme mimics for sensitive hydrogen peroxide detection,” *Chem. Commun.*, vol. 50, no. 23, pp. 3030–3032, 2014, doi: 10.1039/C4CC00328D.

[16] A. Junk and F. Riess, “From an idea to a vision: There’s plenty of room at the bottom,” *Am J Phys*, vol. 74, no. 9, pp. 825–830, Sep. 2006, doi: 10.1119/1.2213634.

[17] R. Feynman, “There’s Plenty of Room at the Bottom,” in *Feynman and Computation*, 2018, pp. 63–76.

[18] S. Bayda, M. Adeel, T. Tuccinardi, M. Cordani, and F. Rizzolio, “The History of Nanoscience and Nanotechnology: From Chemical-Physical Applications to Nanomedicine.,” *Molecules*, vol. 25, no. 1, Dec. 2019, doi: 10.3390/molecules25010112.

[19] V. Harish *et al.*, “Review on Nanoparticles and Nanostructured Materials: Bioimaging, Biosensing, Drug Delivery, Tissue Engineering, Antimicrobial, and Agro-Food Applications.,” *Nanomaterials (Basel)*, vol. 12, no. 3, Jan. 2022, doi: 10.3390/nano12030457.

[20] E. Roduner, “Size matters: why nanomaterials are different,” *Chem Soc Rev*, vol. 35, no. 7, pp. 583–592, 2006, doi: 10.1039/b502142c.

[21] J. Biener, A. Wittstock, T. F. Baumann, J. Weissmüller, M. Bäumer, and A. V. Hamza, “Surface Chemistry in Nanoscale Materials,” *Materials*, vol. 2, no. 4, pp. 2404–2428, Dec. 2009, doi: 10.3390/ma2042404.

[22] C. Buzea, I. I. Pacheco, and K. Robbie, “Nanomaterials and nanoparticles: Sources and toxicity,” *Biointerphases*, vol. 2, no. 4, pp. MR17–MR71, Dec. 2007, doi: 10.1116/1.2815690.

[23] S. J. Ikhmayies, “Characterization of Nanomaterials,” *JOM*, vol. 66, no. 1, pp. 28–29, Jan. 2014, doi: 10.1007/s11837-013-0826-6.

[24] X. Bai *et al.*, “The Basic Properties of Gold Nanoparticles and their Applications in Tumor Diagnosis and Treatment,” *Int J Mol Sci*, vol. 21, no. 7, p. 2480, Apr. 2020, doi: 10.3390/ijms21072480.

[25] Y. Mikami, A. Dhakshinamoorthy, M. Alvaro, and H. García, “Catalytic activity of unsupported gold nanoparticles,” *Catal. Sci. Technol.*, vol. 3, no. 1, pp. 58–69, 2013, doi: 10.1039/C2CY20068F.

[26] W. Luo, W. Hu, and S. Xiao, “Size Effect on the Thermodynamic Properties of Silver Nanoparticles,” *The Journal of Physical Chemistry C*, vol. 112, no. 7, pp. 2359–2369, Feb. 2008, doi: 10.1021/jp0770155.

[27] M. Cain and R. Morrell, “Nanostructured ceramics: a review of their potential,” *Appl Organomet Chem*, vol. 15, no. 5, pp. 321–330, May 2001, doi: 10.1002/aoc.153.

[28] H. Tanaka, N. Morioka, S. Mori, J. Suda, and T. Kimoto, “Quantum-confinement effects on conduction band structure of rectangular cross-sectional GaAs nanowires,” *J Appl Phys*, vol. 115, no. 5, Feb. 2014, doi: 10.1063/1.4864490.

[29] L. D. Geoffrion and G. Guisbiers, “Quantum confinement: Size on the grill!,” *Journal of Physics and Chemistry of Solids*, vol. 140, p. 109320, May 2020, doi: 10.1016/j.jpcs.2019.109320.

[30] M. C. Troparevsky, L. Kronik, and J. R. Chelikowsky, “Optical properties of CdSe quantum dots,” *Journal of Chemical Physics*, vol. 119, no. 4, pp. 2284–2287, Jul. 2003, doi: 10.1063/1.1585013.

[31] D. L. Leslie-Pelecky and R. D. Rieke, “Magnetic Properties of Nanostructured Materials,” *Chemistry of Materials*, vol. 8, no. 8, pp. 1770–1783, Jan. 1996, doi: 10.1021/cm960077f.

[32] International Organization for Standardization, “Nanotechnologies — Vocabulary — Part 2: Nano-objects,” 2015.

[33] N. Joudeh and D. Linke, “Nanoparticle classification, physicochemical properties, characterization, and applications: a comprehensive review for biologists,” *J Nanobiotechnology*, vol. 20, no. 1, p. 262, Jun. 2022, doi: 10.1186/s12951-022-01477-8.

[34] S. Anu Mary Ealia and M. P. Saravanakumar, “A review on the classification, characterisation, synthesis of nanoparticles and their application,” *IOP Conf Ser Mater Sci Eng*, vol. 263, p. 032019, Nov. 2017, doi: 10.1088/1757-899X/263/3/032019.

[35] S. Machado, J. G. Pacheco, H. P. A. Nouws, J. T. Albergaria, and C. Delerue-Matos, “Characterization of green zero-valent iron nanoparticles produced with tree leaf extracts,” *Science of The Total Environment*, vol. 533, pp. 76–81, Nov. 2015, doi: 10.1016/j.scitotenv.2015.06.091.

[36] A. Z. Wilczewska, K. Niemirowicz, K. H. Markiewicz, and H. Car, “Nanoparticles as drug delivery systems,” *Pharmacological Reports*, vol. 64, no. 5, pp. 1020–1037, Sep. 2012, doi: 10.1016/S1734-1140(12)70901-5.

[37] E. Trave *et al.*, “Towards controllable optical properties of silicon based nanoparticles for applications in opto-electronics,” *Opt Mater (Amst)*, vol. 27, no. 5, pp. 1014–1019, Feb. 2005, doi: 10.1016/j.optmat.2004.08.055.

[38] S. Jiang, K. Y. Win, S. Liu, C. P. Teng, Y. Zheng, and M.-Y. Han, “Surface-functionalized nanoparticles for biosensing and imaging-guided therapeutics,” *Nanoscale*, vol. 5, no. 8, p. 3127, 2013, doi: 10.1039/c3nr34005h.

[39] P. T. Sekoai *et al.*, “Application of nanoparticles in biofuels: An overview,” *Fuel*, vol. 237, pp. 380–397, Feb. 2019, doi: 10.1016/j.fuel.2018.10.030.

[40] M. Das, N. Saxena, and P. D. Dwivedi, “Emerging trends of nanoparticles application in food technology: Safety paradigms,” *Nanotoxicology*, vol. 3, no. 1, pp. 10–18, Jan. 2009, doi: 10.1080/17435390802504237.

[41] R. Mishra *et al.*, “The production, characterization and applications of nanoparticles in the textile industry,” *Textile Progress*, vol. 46, no. 2, pp. 133–226, Apr. 2014, doi: 10.1080/00405167.2014.964474.

[42] S. Kumari and L. Sarkar, “A Review on Nanoparticles: Structure, Classification, Synthesis & Applications,” *JOURNAL OF SCIENTIFIC RESEARCH*, vol. 65, no. 08, pp. 42–46, 2021, doi: 10.37398/JSR.2021.650809.

[43] K. Loza, M. Heggen, and M. Epple, “Synthesis, Structure, Properties, and Applications of Bimetallic Nanoparticles of Noble Metals,” May 01, 2020, *Wiley-VCH Verlag*. doi: 10.1002/adfm.201909260.

[44] I. Khan, K. Saeed, and I. Khan, “Nanoparticles: Properties, applications and toxicities,” *Arabian Journal of Chemistry*, vol. 12, no. 7, pp. 908–931, Nov. 2019, doi: 10.1016/j.arabjc.2017.05.011.

[45] M. Fan, F.-J. Lai, H.-L. Chou, W.-T. Lu, B.-J. Hwang, and A. G. Brolo, “Surface-enhanced Raman scattering (SERS) from Au:Ag bimetallic nanoparticles: the effect of the molecular probe,” *Chem. Sci.*, vol. 4, no. 1, pp. 509–515, 2013, doi: 10.1039/C2SC21191B.

[46] G. Guisbiers, G. Abudukelimu, and D. Hourlier, “Size-dependent catalytic and melting properties of platinum-palladium nanoparticles,” *Nanoscale Res Lett*, vol. 6, no. 1, p. 396, Dec. 2011, doi: 10.1186/1556-276X-6-396.

[47] S. Abbasi, “The thermal conductivity modeling of nanofluids involving modified Cu nanorods by Ag nanoparticles,” *Heat and Mass Transfer*, vol. 55, no. 3, pp. 891–897, Mar. 2019, doi: 10.1007/s00231-018-2476-2.

[48] M.-H. Chan *et al.*, “Magnetically guided theranostics: montmorillonite-based iron/platinum nanoparticles for enhancing in situ MRI contrast and hepatocellular carcinoma treatment,” *J Nanobiotechnology*, vol. 19, no. 1, p. 308, Oct. 2021, doi: 10.1186/s12951-021-01052-7.

[49] A.-I. Moreno-Vega, T. Gómez-Quintero, R.-E. Nuñez-Anita, L.-S. Acosta-Torres, and V. Castaño, “Polymeric and Ceramic Nanoparticles in Biomedical Applications,” *J Nanotechnol*, vol. 2012, pp. 1–10, 2012, doi: 10.1155/2012/936041.

[50] R. D’Amato *et al.*, “Synthesis of ceramic nanoparticles by laser pyrolysis: From research to applications,” *J Anal Appl Pyrolysis*, vol. 104, pp. 461–469, Nov. 2013, doi: 10.1016/j.jaap.2013.05.026.

[51] S. Thomas, B. S. P. Harshita, P. Mishra, and S. Talegaonkar, “Ceramic Nanoparticles: Fabrication Methods and Applications in Drug Delivery,” *Curr Pharm Des*, vol. 21, no. 42, pp. 6165–6188, Dec. 2015, doi: 10.2174/1381612821666151027153246.

[52] I. Roy *et al.*, “Ceramic-Based Nanoparticles Entrapping Water-Insoluble Photosensitizing Anticancer Drugs: A Novel Drug−Carrier System for Photodynamic Therapy,” *J Am Chem Soc*, vol. 125, no. 26, pp. 7860–7865, Jul. 2003, doi: 10.1021/ja0343095.

[53] H. Hao, “ADVANCEMENTS IN THE USE OF CERAMIC NANOPARTICLES IN 3D PRINTED TISSUE ENGINEERING,” *Ceramics - Silikaty*, pp. 96–115, Feb. 2024, doi: 10.13168/cs.2024.0009.

[54] K.-J. Chen *et al.*, “White light emitting diodes with enhanced CCT uniformity and luminous flux using ZrO 2 nanoparticles,” *Nanoscale*, vol. 6, no. 10, pp. 5378–5383, 2014, doi: 10.1039/C3NR06894C.

[55] J. Wang *et al.*, “Silicon oxycarbonitride ceramic containing nickel nanoparticles: from design to catalytic application,” *Mater Adv*, vol. 2, no. 5, pp. 1715–1730, 2021, doi: 10.1039/D0MA00917B.

[56] S. Zinatloo-Ajabshir, Z. Mehrabadi, H. Khojasteh, and F. Sharifianjazi, “Innovative fabrication of highly efficient CeO2 ceramic nanomaterials for enhanced photocatalytic degradation of toxic contaminants under sunlight,” *Ceram Int*, vol. 50, no. 23, pp. 49263–49276, Dec. 2024, doi: 10.1016/j.ceramint.2024.09.271.

[57] Y. Khan *et al.*, “Classification, Synthetic, and Characterization Approaches to Nanoparticles, and Their Applications in Various Fields of Nanotechnology: A Review,” *Catalysts*, vol. 12, no. 11, p. 1386, Nov. 2022, doi: 10.3390/catal12111386.

[58] B. C. Yadav and R. Kumar, “Structure, properties and applications of fullerenes,” *Int J Nanotechnol Appl*, vol. 2, no. 1, pp. 15–24, 2008.

[59] S. Margadonna and K. Prassides, “Recent Advances in Fullerene Superconductivity,” *J Solid State Chem*, vol. 168, no. 2, pp. 639–652, Nov. 2002, doi: 10.1006/jssc.2002.9762.

[60] R. M. Ahmed and S. M. El-Bashir, “Structure and Physical Properties of Polymer Composite Films Doped with Fullerene Nanoparticles,” *International Journal of Photoenergy*, vol. 2011, pp. 1–6, 2011, doi: 10.1155/2011/801409.

[61] A. J. Ferguson, J. L. Blackburn, and N. Kopidakis, “Fullerenes and carbon nanotubes as acceptor materials in organic photovoltaics,” *Mater Lett*, vol. 90, pp. 115–125, Jan. 2013, doi: 10.1016/j.matlet.2012.08.145.

[62] J. Conyers, “Biomedical applications of functionalized fullerene-based nanomaterials,” *Int J Nanomedicine*, p. 261, Nov. 2009, doi: 10.2147/IJN.S5964.

[63] J. Shi *et al.*, “A tumoral acidic pH-responsive drug delivery system based on a novel photosensitizer (fullerene) for in vitro and in vivo chemo-photodynamic therapy,” *Acta Biomater*, vol. 10, no. 3, pp. 1280–1291, Mar. 2014, doi: 10.1016/j.actbio.2013.10.037.

[64] E. N. Ganesh, “Single walled and multi walled carbon nanotube structure, synthesis and applications,” *International Journal of Innovative Technology and Exploring Engineering*, vol. 2, no. 4, pp. 311–320, 2013.

[65] P. M. Ajayan and O. Z. Zhou, “Applications of Carbon Nanotubes,” in *Carbon Nanotubes*, Berlin, Heidelberg: Springer Berlin Heidelberg, pp. 391–425. doi: 10.1007/3-540-39947-X_14.

[66] L.-M. Peng, Z. Zhang, and C. Qiu, “Carbon nanotube digital electronics,” *Nat Electron*, vol. 2, no. 11, pp. 499–505, Nov. 2019, doi: 10.1038/s41928-019-0330-2.

[67] A. Mazzatenta *et al.*, “Interfacing Neurons with Carbon Nanotubes: Electrical Signal Transfer and Synaptic Stimulation in Cultured Brain Circuits,” *Journal of Neuroscience*, vol. 27, no. 26, pp. 6931–6936, Jun. 2007, doi: 10.1523/JNEUROSCI.1051-07.2007.

[68] L. G. Zhang, O. Im, J. Li, and M. Keidar, “Biomimetic three-dimensional nanocrystalline hydroxyapatite and magnetically synthesized single-walled carbon nanotube chitosan nanocomposite for bone regeneration,” *Int J Nanomedicine*, p. 2087, Apr. 2012, doi: 10.2147/IJN.S29743.

[69] E. Hammel *et al.*, “Carbon nanofibers for composite applications,” *Carbon N Y*, vol. 42, no. 5–6, pp. 1153–1158, 2004, doi: 10.1016/j.carbon.2003.12.043.

[70] V. Leung and F. Ko, “Biomedical applications of nanofibers,” *Polym Adv Technol*, vol. 22, no. 3, pp. 350–365, Mar. 2011, doi: 10.1002/pat.1813.

[71] M. R. Carvalho, R. L. Reis, and J. M. Oliveira, “Dendrimer nanoparticles for colorectal cancer applications,” *J Mater Chem B*, vol. 8, no. 6, pp. 1128–1138, 2020, doi: 10.1039/C9TB02289A.

[72] T. Nakanishi *et al.*, “Positively charged liposome functions as an efficient immunoadjuvant in inducing cell-mediated immune response to soluble proteins,” *Journal of Controlled Release*, vol. 61, no. 1–2, pp. 233–240, Aug. 1999, doi: 10.1016/S0168-3659(99)00097-8.

[73] H. Yang *et al.*, “Glucose-responsive complex micelles for self-regulated release of insulin under physiological conditions,” *Soft Matter*, vol. 9, no. 35, p. 8589, 2013, doi: 10.1039/c3sm51538a.

[74] K. K. Ng and G. Zheng, “Molecular Interactions in Organic Nanoparticles for Phototheranostic Applications,” *Chem Rev*, vol. 115, no. 19, pp. 11012–11042, Oct. 2015, doi: 10.1021/acs.chemrev.5b00140.

[75] M. Geszke-Moritz and M. Moritz, “Biodegradable Polymeric Nanoparticle-Based Drug Delivery Systems: Comprehensive Overview, Perspectives and Challenges,” *Polymers (Basel)*, vol. 16, no. 17, p. 2536, Sep. 2024, doi: 10.3390/polym16172536.

[76] A. Nasir, A. Kausar, and A. Younus, “A Review on Preparation, Properties and Applications of Polymeric Nanoparticle-Based Materials,” *Polym Plast Technol Eng*, vol. 54, no. 4, pp. 325–341, Mar. 2015, doi: 10.1080/03602559.2014.958780.

[77] M. Elsabahy and K. L. Wooley, “Design of polymeric nanoparticles for biomedical delivery applications,” *Chem Soc Rev*, vol. 41, no. 7, p. 2545, 2012, doi: 10.1039/c2cs15327k.

[78] X. Wang *et al.*, “Synthesis, Characterization, and Application of Novel Polymeric Nanoparticles,” *Macromolecules*, vol. 40, no. 3, pp. 499–508, Feb. 2007, doi: 10.1021/ma0613739.

[79] R. M. Overney, C. Buenviaje, R. Luginbühl, and F. Dinelli, “GLASS AND STRUCTURAL TRANSITIONS MEASURED AT POLYMER SURFACES ON THE NANOSCALE,” 2000.

[80] C. Zhang, Y. Guo, and R. D. Priestley, “Glass Transition Temperature of Polymer Nanoparticles under Soft and Hard Confinement,” *Macromolecules*, vol. 44, no. 10, pp. 4001–4006, May 2011, doi: 10.1021/ma1026862.

[81] J. Khan, S. E. Harton, P. Akcora, B. C. Benicewicz, and S. K. Kumar, “Polymer crystallization in nanocomposites: spatial reorganization of nanoparticles,” *Macromolecules*, vol. 42, no. 15, pp. 5741–5744, Aug. 2009, doi: 10.1021/ma900794t.

[82] B. Begines *et al.*, “Polymeric Nanoparticles for Drug Delivery: Recent Developments and Future Prospects,” *Nanomaterials*, vol. 10, no. 7, p. 1403, Jul. 2020, doi: 10.3390/nano10071403.

[83] C. Adhikari, “Polymer nanoparticles-preparations, applications and future insights: a concise review,” *Polymer-Plastics Technology and Materials*, pp. 1–29, Jul. 2021, doi: 10.1080/25740881.2021.1939715.

[84] Y. EL-Ghoul, F. M. Alminderej, F. M. Alsubaie, R. Alrasheed, and N. H. Almousa, “Recent Advances in Functional Polymer Materials for Energy, Water, and Biomedical Applications: A Review,” *Polymers (Basel)*, vol. 13, no. 24, p. 4327, Dec. 2021, doi: 10.3390/polym13244327.

[85] D. Bahamonde-Norambuena, A. Molina-Pereira, M. Cantin, M. Muñoz, K. Zepeda, and C. Vilos, “Polymeric Nanoparticles in Dermocosmetic,” *International Journal of Morphology*, vol. 33, no. 4, pp. 1563–1568, Dec. 2015, doi: 10.4067/S0717-95022015000400061.

[86] B. L. Banik, P. Fattahi, and J. L. Brown, “Polymeric nanoparticles: the future of nanomedicine,” *WIREs Nanomedicine and Nanobiotechnology*, vol. 8, no. 2, pp. 271–299, Mar. 2016, doi: 10.1002/wnan.1364.

[87] L. Cismaru and M. Popa, “POLYMERIC NANOPARTICLES WITH BIOMEDICAL APPLICATIONS,” *Revue Roumaine de Chimie*, vol. 55, pp. 433–442, Aug. 2010.

[88] K. B. Sutradhar and Md. L. Amin, “Nanotechnology in Cancer Drug Delivery and Selective Targeting,” *ISRN Nanotechnology*, vol. 2014, pp. 1–12, Jan. 2014, doi: 10.1155/2014/939378.

[89] C. GOMEZGAETE, N. TSAPIS, M. BESNARD, A. BOCHOT, and E. FATTAL, “Encapsulation of dexamethasone into biodegradable polymeric nanoparticles,” *Int J Pharm*, vol. 331, no. 2, pp. 153–159, Mar. 2007, doi: 10.1016/j.ijpharm.2006.11.028.

[90] N. Bertrand, J. Wu, X. Xu, N. Kamaly, and O. C. Farokhzad, “Cancer nanotechnology: The impact of passive and active targeting in the era of modern cancer biology,” *Adv Drug Deliv Rev*, vol. 66, pp. 2–25, Feb. 2014, doi: 10.1016/j.addr.2013.11.009.

[91] H. Maeda, “The enhanced permeability and retention (EPR) effect in tumor vasculature: the key role of tumor-selective macromolecular drug targeting,” *Adv Enzyme Regul*, vol. 41, no. 1, pp. 189–207, May 2001, doi: 10.1016/S0065-2571(00)00013-3.

[92] J. D. Byrne, T. Betancourt, and L. Brannon-Peppas, “Active targeting schemes for nanoparticle systems in cancer therapeutics,” *Adv Drug Deliv Rev*, vol. 60, no. 15, pp. 1615–1626, Dec. 2008, doi: 10.1016/j.addr.2008.08.005.

[93] S. Tanaka *et al.*, “Antiapoptotic effect of haem oxygenase-1 induced by nitric oxide in experimental solid tumour,” *Br J Cancer*, vol. 88, no. 6, pp. 902–909, Mar. 2003, doi: 10.1038/sj.bjc.6600830.

[94] S. K. Sahoo *et al.*, “Pegylated Zinc Protoporphyrin: A Water-Soluble Heme Oxygenase Inhibitor with Tumor-Targeting Capacity,” *Bioconjug Chem*, vol. 13, no. 5, pp. 1031–1038, Sep. 2002, doi: 10.1021/bc020010k.

[95] A. K. Iyer, K. Greish, J. Fang, R. Murakami, and H. Maeda, “High-loading nanosized micelles of copoly(styrene–maleic acid)–zinc protoporphyrin for targeted delivery of a potent heme oxygenase inhibitor,” *Biomaterials*, vol. 28, no. 10, pp. 1871–1881, Apr. 2007, doi: 10.1016/j.biomaterials.2006.11.051.

[96] S. Wilhelm *et al.*, “Analysis of nanoparticle delivery to tumours,” *Nat Rev Mater*, vol. 1, no. 5, p. 16014, Apr. 2016, doi: 10.1038/natrevmats.2016.14.

[97] C. M. Dawidczyk *et al.*, “State-of-the-art in design rules for drug delivery platforms: Lessons learned from FDA-approved nanomedicines,” *Journal of Controlled Release*, vol. 187, pp. 133–144, Aug. 2014, doi: 10.1016/j.jconrel.2014.05.036.

[98] T. Araki *et al.*, “Formulation and Evaluation of Paclitaxel-Loaded Polymeric Nanoparticles Composed of Polyethylene Glycol and Polylactic Acid Block Copolymer,” *Biol Pharm Bull*, vol. 35, no. 8, pp. 1306–1313, 2012, doi: 10.1248/bpb.b12-0020.

[99] S. Pieper *et al.*, “Incorporation of doxorubicin in different polymer nanoparticles and their anticancer activity,” *Beilstein Journal of Nanotechnology*, vol. 10, pp. 2062–2072, Oct. 2019, doi: 10.3762/bjnano.10.201.

[100] J. Kreuter, R. N. Alyautdin, D. A. Kharkevich, and A. A. Ivanov, “Passage of peptides through the blood-brain barrier with colloidal polymer particles (nanoparticles),” *Brain Res*, vol. 674, no. 1, pp. 171–174, Mar. 1995, doi: 10.1016/0006-8993(95)00023-J.

[101] W. Wang, B. Wang, X. Ma, S. Liu, X. Shang, and X. Yu, “Tailor-Made pH-Responsive Poly(choline phosphate) Prodrug as a Drug Delivery System for Rapid Cellular Internalization,” *Biomacromolecules*, vol. 17, no. 6, pp. 2223–2232, Jun. 2016, doi: 10.1021/acs.biomac.6b00455.

[102] D. Liu *et al.*, “Thermoresponsive Nanogel-Encapsulated PEDOT and HSP70 Inhibitor for Improving the Depth of the Photothermal Therapeutic Effect,” *Adv Funct Mater*, vol. 26, no. 26, pp. 4749–4759, Jul. 2016, doi: 10.1002/adfm.201600031.

[103] S. Nappini, S. Fogli, B. Castroflorio, M. Bonini, F. Baldelli Bombelli, and P. Baglioni, “Magnetic field responsive drug release from magnetoliposomes in biological fluids,” *J Mater Chem B*, vol. 4, no. 4, pp. 716–725, 2016, doi: 10.1039/C5TB02191J.

[104] R. Staruch, R. Chopra, and K. Hynynen, “Hyperthermia in Bone Generated with MR Imaging–controlled Focused Ultrasound: Control Strategies and Drug Delivery,” *Radiology*, vol. 263, no. 1, pp. 117–127, Apr. 2012, doi: 10.1148/radiol.11111189.

[105] C. Qian *et al.*, “Light-Activated Hypoxia-Responsive Nanocarriers for Enhanced Anticancer Therapy,” *Advanced Materials*, vol. 28, no. 17, pp. 3313–3320, May 2016, doi: 10.1002/adma.201505869.

[106] K. Yang, H. Xu, L. Cheng, C. Sun, J. Wang, and Z. Liu, “In Vitro and In Vivo Near-Infrared Photothermal Therapy of Cancer Using Polypyrrole Organic Nanoparticles,” *Advanced Materials*, vol. 24, no. 41, pp. 5586–5592, Nov. 2012, doi: 10.1002/adma.201202625.

[107] P. M. George *et al.*, “Fabrication and biocompatibility of polypyrrole implants suitable for neural prosthetics,” *Biomaterials*, vol. 26, no. 17, pp. 3511–3519, Jun. 2005, doi: 10.1016/j.biomaterials.2004.09.037.

[108] N. Abid *et al.*, “Synthesis of nanomaterials using various top-down and bottom-up approaches, influencing factors, advantages, and disadvantages: A review,” *Adv Colloid Interface Sci*, vol. 300, p. 102597, Feb. 2022, doi: 10.1016/j.cis.2021.102597.

[109] P. Christian, F. Von der Kammer, M. Baalousha, and Th. Hofmann, “Nanoparticles: structure, properties, preparation and behaviour in environmental media,” *Ecotoxicology*, vol. 17, no. 5, pp. 326–343, Jul. 2008, doi: 10.1007/s10646-008-0213-1.

[110] J. W. Vanderhoff, M. S. El Aasser, and J. Ugelstad, “Polymer emulsification process,” US 4,177,177, 1979

[111] J. P. Rao and K. E. Geckeler, “Polymer nanoparticles: Preparation techniques and size-control parameters,” 2011, *Elsevier Ltd*. doi: 10.1016/j.progpolymsci.2011.01.001.

[112] S. Desgouilles *et al.*, “The Design of Nanoparticles Obtained by Solvent Evaporation: A Comprehensive Study,” *Langmuir*, vol. 19, no. 22, pp. 9504–9510, Oct. 2003, doi: 10.1021/la034999q.

[113] P. B. O’Donnell and J. W. McGinity, “Preparation of microspheres by the solvent evaporation technique,” *Adv Drug Deliv Rev*, vol. 28, no. 1, pp. 25–42, Oct. 1997, doi: 10.1016/S0169-409X(97)00049-5.

[114] C. Bindschaedler, R. Gurny, and E. Doelker, “Process for preparing a powder of water-insoluble polymer which can be redispersed in a liquid phase, the resulting powder and utilization thereof,” US 4,968,350, 1990

[115] N. Mendoza-Munoz, D. Quintanar-Guerrero, and E. Allemann, “The Impact of the Salting-Out Technique on the Preparation of Colloidal Particulate Systems for Pharmaceutical Applications,” *Recent Pat Drug Deliv Formul*, vol. 6, no. 3, pp. 236–249, Aug. 2012, doi: 10.2174/187221112802652688.

[116] K. Krishnamoorthy and M. Mahalingam, “Selection of a suitable method for the preparation of polymeric nanoparticles: multi-criteria decision making approach.,” *Adv Pharm Bull*, vol. 5, no. 1, pp. 57–67, Mar. 2015, doi: 10.5681/apb.2015.008.

[117] T. Pulingam, P. Foroozandeh, J.-A. Chuah, and K. Sudesh, “Exploring Various Techniques for the Chemical and Biological Synthesis of Polymeric Nanoparticles.,” *Nanomaterials (Basel)*, vol. 12, no. 3, Feb. 2022, doi: 10.3390/nano12030576.

[118] N. Mendoza-Munoz, D. Quintanar-Guerrero, and E. Allemann, “The Impact of the Salting-Out Technique on the Preparation of Colloidal Particulate Systems for Pharmaceutical Applications,” *Recent Pat Drug Deliv Formul*, vol. 6, no. 3, pp. 236–249, Aug. 2012, doi: 10.2174/187221112802652688.

[119] H. Fessi, F. Puisieux, J. Ph. Devissaguet, N. Ammoury, and S. Benita, “Nanocapsule formation by interfacial polymer deposition following solvent displacement,” *Int J Pharm*, vol. 55, no. 1, pp. R1–R4, Oct. 1989, doi: 10.1016/0378-5173(89)90281-0.

[120] I. Limayem Blouza, C. Charcosset, S. Sfar, and H. Fessi, “Preparation and characterization of spironolactone-loaded nanocapsules for paediatric use,” *Int J Pharm*, vol. 325, no. 1–2, pp. 124–131, Nov. 2006, doi: 10.1016/j.ijpharm.2006.06.022.

[121] F. Lince, D. L. Marchisio, and A. A. Barresi, “Strategies to control the particle size distribution of poly-ε-caprolactone nanoparticles for pharmaceutical applications,” *J Colloid Interface Sci*, vol. 322, no. 2, pp. 505–515, Jun. 2008, doi: 10.1016/j.jcis.2008.03.033.

[122] C. Zhang, J. W. Chung, and R. D. Priestley, “Dialysis Nanoprecipitation of Polystyrene Nanoparticles,” *Macromol Rapid Commun*, vol. 33, no. 20, pp. 1798–1803, Oct. 2012, doi: 10.1002/marc.201200335.

[123] P. York, “Strategies for particle design using supercritical fluid technologies,” *Pharm Sci Technol Today*, vol. 2, no. 11, pp. 430–440, Nov. 1999, doi: 10.1016/S1461-5347(99)00209-6.

[124] R. Noyori, “Supercritical Fluids: Introduction,” *Chem Rev*, vol. 99, no. 2, pp. 353–354, Feb. 1999, doi: 10.1021/cr980085a.

[125] M. Weber and M. C. Thies, “Understanding the RESS Process,” in *Supercritical Fluid Technology in Materials Science and Engineering: Synthesis, Properties, and Applications*, Y. P. Sun, Ed., New York: Marcel Dekker, 2002, pp. 387–437.

[126] Y. P. Sun, H. W. Rolling, J. Bandara, J. M. Meziani, and C. E. Bunker, “Preparation and Processing of Nanoscale Materials by Supercritical Fluid Technology,” in *Supercritical Fluid Technology in Materials Science and Engineering: Synthesis, Properties, and Applications*, Y. P. Sun, Ed., New York: Marcel Dekker, 2002, pp. 491–576.

[127] M. J. Meziani, P. Pathak, R. Hurezeanu, M. C. Thies, R. M. Enick, and Y. Sun, “Supercritical-Fluid Processing Technique for Nanoscale Polymer Particles,” *Angewandte Chemie International Edition*, vol. 43, no. 6, pp. 704–707, Jan. 2004, doi: 10.1002/anie.200352834.

[128] E. Reverchon, “Supercritical antisolvent precipitation of micro- and nano-particles,” *J Supercrit Fluids*, vol. 15, no. 1, pp. 1–21, May 1999, doi: 10.1016/S0896-8446(98)00129-6.

[129] Y. Sun, M. J. Meziani, P. Pathak, and L. Qu, “Polymeric Nanoparticles from Rapid Expansion of Supercritical Fluid Solution,” *Chemistry – A European Journal*, vol. 11, no. 5, pp. 1366–1373, Feb. 2005, doi: 10.1002/chem.200400422.

[130] A. Blasig, C. Shi, R. M. Enick, and M. C. Thies, “Effect of Concentration and Degree of Saturation on RESS of a CO 2 -Soluble Fluoropolymer,” *Ind Eng Chem Res*, vol. 41, no. 20, pp. 4976–4983, Oct. 2002, doi: 10.1021/ie0201819.

[131] G. Gorrasi and A. Sorrentino, “Mechanical milling as a technology to produce structural and functional bio-nanocomposites,” *Green Chemistry*, vol. 17, no. 5, pp. 2610–2625, 2015, doi: 10.1039/C5GC00029G.

[132] N. G. Semaltianos, “Nanoparticles by Laser Ablation,” *Critical Reviews in Solid State and Materials Sciences*, vol. 35, no. 2, pp. 105–124, May 2010, doi: 10.1080/10408431003788233.

[133] T. Torimoto, T. Kameyama, and S. Kuwabata, “Top-Down Synthesis Methods for Nanoscale Catalysts,” in *Nanocatalysis in Ionic Liquids*, Wiley, 2016, pp. 171–205. doi: 10.1002/9783527693283.ch9.

[134] S. Shahidi, B. Moazzenchi, and M. Ghoranneviss, “A review-application of physical vapor deposition (PVD) and related methods in the textile industry,” *The European Physical Journal Applied Physics*, vol. 71, no. 3, p. 31302, Sep. 2015, doi: 10.1051/epjap/2015140439.

[135] T. Koide, T. Ono, H. Shimakoshi, and Y. Hisaeda, “Functions of bioinspired pyrrole cobalt complexes–recently developed catalytic systems of vitamin B12 related complexes and porphycene complexes–,” *Coord Chem Rev*, vol. 470, p. 214690, Nov. 2022, doi: 10.1016/j.ccr.2022.214690.

[136] S. Ahmad, O. Alam, Mohd. J. Naim, M. Shaquiquzzaman, M. M. Alam, and M. Iqbal, “Pyrrole: An insight into recent pharmacological advances with structure activity relationship,” *Eur J Med Chem*, vol. 157, pp. 527–561, Sep. 2018, doi: 10.1016/j.ejmech.2018.08.002.

[137] D. Osman, A. Cooke, T. R. Young, E. Deery, N. J. Robinson, and M. J. Warren, “The requirement for cobalt in vitamin B12: A paradigm for protein metalation.,” *Biochim Biophys Acta Mol Cell Res*, vol. 1868, no. 1, p. 118896, Jan. 2021, doi: 10.1016/j.bbamcr.2020.118896.

[138] M. L. Santos, M. D’Ambrosio, A. P. Rodrigo, A. J. Parola, and P. M. Costa, “A Transcriptomic Approach to the Metabolism of Tetrapyrrolic Photosensitizers in a Marine Annelid,” *Molecules*, vol. 26, no. 13, p. 3924, Jun. 2021, doi: 10.3390/molecules26133924.

[139] D. D. Haines and A. Tosaki, “Heme Degradation in Pathophysiology of and Countermeasures to Inflammation-Associated Disease,” *Int J Mol Sci*, vol. 21, no. 24, p. 9698, Dec. 2020, doi: 10.3390/ijms21249698.

[140] M. Ritter *et al.*, “Pyrrolic and Dipyrrolic Chlorophyll Degradation Products in Plants and Herbivores,” *Chemistry – A European Journal*, vol. 26, no. 28, pp. 6205–6213, May 2020, doi: 10.1002/chem.201905236.

[141] M. Dukh *et al.*, “*meso* - and β-Pyrrole-Linked Chlorin-Bacteriochlorin Dyads for Promoting Far-Red FRET and Singlet Oxygen Production,” *Chemistry – A European Journal*, vol. 26, no. 65, pp. 14996–15006, Nov. 2020, doi: 10.1002/chem.202003042.

[142] H. L. Bonkovsky, N. Dixon, and S. Rudnick, “Pathogenesis and clinical features of the acute hepatic porphyrias (AHPs),” *Mol Genet Metab*, vol. 128, no. 3, pp. 213–218, Nov. 2019, doi: 10.1016/j.ymgme.2019.03.002.

[143] W. W. Wilkerson, R. A. Copeland, M. Covington, and J. M. Trzaskos, “Antiinflammatory 4,5-Diarylpyrroles. 2. Activity as a Function of Cyclooxygenase-2 Inhibition,” *J Med Chem*, vol. 38, no. 20, pp. 3895–3901, Sep. 1995, doi: 10.1021/jm00020a002.

[144] R. P. Wurz and A. B. Charette, “Doubly Activated Cyclopropanes as Synthetic Precursors for the Preparation of 4-Nitro- and 4-Cyano-dihydropyrroles and Pyrroles,” *Org Lett*, vol. 7, no. 12, pp. 2313–2316, Jun. 2005, doi: 10.1021/ol050442l.

[145] H. Lee *et al.*, “A novel class of highly potent, selective, and non-peptidic inhibitor of ras farnesyltransferase (FTase),” *Bioorg Med Chem Lett*, vol. 11, no. 23, pp. 3069–3072, Dec. 2001, doi: 10.1016/S0960-894X(01)00624-2.

[146] C. Piliego, T. W. Holcombe, J. D. Douglas, C. H. Woo, P. M. Beaujuge, and J. M. J. Fréchet, “Synthetic Control of Structural Order in *N* -Alkylthieno[3,4- *c*]pyrrole-4,6-dione-Based Polymers for Efficient Solar Cells,” *J Am Chem Soc*, vol. 132, no. 22, pp. 7595–7597, Jun. 2010, doi: 10.1021/ja103275u.

[147] A. R. Katritzky, P. Barczynski, G. Musumarra, D. Pisano, and M. Szafran, “Aromaticity as a quantitative concept. 1. A statistical demonstration of the orthogonality of classical and magnetic aromaticity in five- and six-membered heterocycles,” *J Am Chem Soc*, vol. 111, no. 1, pp. 7–15, Jan. 1989, doi: 10.1021/ja00183a002.

[148] A. Manzari-Tavakoli, R. Tarasi, R. Sedghi, A. Moghimi, and H. Niknejad, “Fabrication of nanochitosan incorporated polypyrrole/alginate conducting scaffold for neural tissue engineering,” *Sci Rep*, vol. 10, no. 1, p. 22012, Dec. 2020, doi: 10.1038/s41598-020-78650-2.

[149] B. Maharjan *et al.*, “In-situ polymerized polypyrrole nanoparticles immobilized poly(ε-caprolactone) electrospun conductive scaffolds for bone tissue engineering,” *Materials Science and Engineering: C*, vol. 114, p. 111056, Sep. 2020, doi: 10.1016/j.msec.2020.111056.

[150] R. M. Hathout *et al.*, “Dual stimuli-responsive polypyrrole nanoparticles for anticancer therapy,” *J Drug Deliv Sci Technol*, vol. 47, pp. 176–180, Oct. 2018, doi: 10.1016/j.jddst.2018.07.002.

[151] E. N. Zare *et al.*, “Electroconductive multi-functional polypyrrole composites for biomedical applications,” *Appl Mater Today*, vol. 24, p. 101117, Sep. 2021, doi: 10.1016/j.apmt.2021.101117.

[152] D. D. Ateh, H. A. Navsaria, and P. Vadgama, “Polypyrrole-based conducting polymers and interactions with biological tissues,” *J R Soc Interface*, vol. 3, no. 11, pp. 741–752, Dec. 2006, doi: 10.1098/rsif.2006.0141.

[153] D. Samanta, J. L. Meiser, and R. N. Zare, “Polypyrrole nanoparticles for tunable, pH-sensitive and sustained drug release,” *Nanoscale*, vol. 7, no. 21, pp. 9497–9504, 2015, doi: 10.1039/C5NR02196K.

[154] S. Geng, H. Zhao, G. Zhan, Y. Zhao, and X. Yang, “Injectable in Situ Forming Hydrogels of Thermosensitive Polypyrrole Nanoplatforms for Precisely Synergistic Photothermo-Chemotherapy,” *ACS Appl Mater Interfaces*, vol. 12, no. 7, pp. 7995–8005, Feb. 2020, doi: 10.1021/acsami.9b22654.

[155] A. Choukourov *et al.*, “Advances and challenges in the field of plasma polymer nanoparticles,” *Beilstein Journal of Nanotechnology*, vol. 8, pp. 2002–2014, Sep. 2017, doi: 10.3762/bjnano.8.200.

[156] F. F. Chen, “Introduction,” in *Introduction to Plasma Physics and Controlled Fusion*, Cham: Springer International Publishing, 2016, pp. 1–18. doi: 10.1007/978-3-319-22309-4_1.

[157] A. Fridman, “ Introduction to Theoretical and Applied Plasma Chemistry,” in *Plasma Chemistry*, 2008, pp. 1–2.

[158] S. A. Ermolaeva, O. F. Petrov, B. S. Naroditsky, V. E. Fortov, G. E. Morfill, and A. L. Gintsburg, “Cold Plasma Therapy,” in *Comprehensive Biomedical Physics*, Elsevier, 2014, pp. 343–367. doi: 10.1016/B978-0-444-53632-7.01021-2.

[159] D. Wang *et al.*, “Low-temperature plasma technology for electrocatalysis,” *Chinese Chemical Letters*, vol. 30, no. 4, pp. 826–838, Apr. 2019, doi: 10.1016/j.cclet.2019.03.051.

[160] F. L. Tabares and I. Junkar, “Cold Plasma Systems and their Application in Surface Treatments for Medicine.,” *Molecules*, vol. 26, no. 7, Mar. 2021, doi: 10.3390/molecules26071903.

[161] S. Samal, “Thermal plasma technology: The prospective future in material processing,” *J Clean Prod*, vol. 142, pp. 3131–3150, Jan. 2017, doi: 10.1016/j.jclepro.2016.10.154.

[162] K. V Vasil’ev, “Plasma-arc cutting – a promising method of thermal cutting,” *Welding International*, vol. 17, no. 2, pp. 147–151, Jan. 2003, doi: 10.1533/wint.2003.3096.

[163] M. Ushio, “Plasma application in the steel industry in Japan,” *Pure and Applied Chemistry*, vol. 64, no. 5, pp. 677–683, Jan. 1992, doi: 10.1351/pac199264050677.

[164] P. Fauchais and A. Vardelle, “Thermal Spray Coatings,” in *Wiley Encyclopedia of Electrical and Electronics Engineering*, Wiley, 2007. doi: 10.1002/047134608X.W5923.pub2.

[165] R. Burkhard, W. Hoffelner, and R. C. Eschenbach, “Recycling of metals from waste with thermal plasma,” *Resour Conserv Recycl*, vol. 10, no. 1–2, pp. 11–16, Apr. 1994, doi: 10.1016/0921-3449(94)90033-7.

[166] H. Fujimoto, H. Tokunaga, and H. Iritani, “A high-powered A.C. plasma torch for the arc heating of molten steel in the tundish,” *Plasma Chemistry and Plasma Processing*, vol. 14, no. 3, pp. 361–382, Sep. 1994, doi: 10.1007/BF01447086.

[167] I. V. Bilera and Yu. A. Lebedev, “Plasma-Chemical Production of Acetylene from Hydrocarbons: History and Current Status (A Review),” *Petroleum Chemistry*, vol. 62, no. 4, pp. 329–351, Apr. 2022, doi: 10.1134/S0965544122010145.

[168] S.-M. Oh, J.-G. Li, and T. Ishigaki, “Nanocrystalline TiO 2 powders synthesized by in-flight oxidation of TiN in thermal plasma: Mechanisms of phase selection and particle morphology evolution,” *J Mater Res*, vol. 20, no. 2, pp. 529–537, Feb. 2005, doi: 10.1557/JMR.2005.0070.

[169] M. F. S. Gonçalves, G. Petraconi Filho, A. A. Couto, A. S. da Silva Sobrinho, F. S. Miranda, and M. Massi, “Evaluation of thermal plasma process for treatment disposal of solid radioactive waste,” *J Environ Manage*, vol. 311, p. 114895, Jun. 2022, doi: 10.1016/j.jenvman.2022.114895.

[170] C.-C. Tzeng, Y.-Y. Kuo, T.-F. Huang, D.-L. Lin, and Y.-J. Yu, “Treatment of radioactive wastes by plasma incineration and vitrification for final disposal,” *J Hazard Mater*, vol. 58, no. 1–3, pp. 207–220, Feb. 1998, doi: 10.1016/S0304-3894(97)00132-5.

[171] G. Fridman, G. Friedman, A. Gutsol, A. B. Shekhter, V. N. Vasilets, and A. Fridman, “Applied Plasma Medicine,” *Plasma Processes and Polymers*, vol. 5, no. 6, pp. 503–533, Aug. 2008, doi: 10.1002/ppap.200700154.

[172] J. Winter, R. Brandenburg, and K.-D. Weltmann, “Atmospheric pressure plasma jets: an overview of devices and new directions,” *Plasma Sources Sci Technol*, vol. 24, no. 6, p. 064001, Oct. 2015, doi: 10.1088/0963-0252/24/6/064001.

[173] L. Bárdos and H. Baránková, “Cold atmospheric plasma: Sources, processes, and applications,” *Thin Solid Films*, vol. 518, no. 23, pp. 6705–6713, Sep. 2010, doi: 10.1016/j.tsf.2010.07.044.

[174] G. Y. Park *et al.*, "Atmospheric-pressure plasma sources for biomedical applications," *Plasma Sources Sci Technol*, vol. 21, no. 4, p. 043001, Aug. 2012, doi: 10.1088/0963-0252/21/4/043001.

[175] C. Tendero, C. Tixier, P. Tristant, J. Desmaison, and P. Leprince, "Atmospheric pressure plasmas: A review," *Spectrochim Acta Part B At Spectrosc*, vol. 61, no. 1, pp. 2–30, Jan. 2006, doi: 10.1016/j.sab.2005.10.003.

[176] X. Lu, Z. Jiang, Q. Xiong, Z. Tang, X. Hu, and Y. Pan, "An 11cm long atmospheric pressure cold plasma plume for applications of plasma medicine," *Appl Phys Lett*, vol. 92, no. 8, Feb. 2008, doi: 10.1063/1.2883945.

[177] H. W. Herrmann, I. Henins, J. Park, and G. S. Selwyn, "Decontamination of chemical and biological warfare (CBW) agents using an atmospheric pressure plasma jet (APPJ)," *Phys Plasmas*, vol. 6, no. 5, pp. 2284–2289, May 1999, doi: 10.1063/1.873480.

[178] H. W. Lee, G. Y. Park, Y. S. Seo, Y. H. Im, S. B. Shim, and H. J. Lee, "Modelling of atmospheric pressure plasmas for biomedical applications," *J Phys D Appl Phys*, vol. 44, no. 5, p. 053001, Feb. 2011, doi: 10.1088/0022-3727/44/5/053001.

[179] N. K. Kaushik *et al.*, "Plasma and Nanomaterials: Fabrication and Biomedical Applications," *Nanomaterials*, vol. 9, no. 1, p. 98, Jan. 2019, doi: 10.3390/nano9010098.

[180] A. Patelli *et al.*, "Nanoroughness, Surface Chemistry, and Drug Delivery Control by Atmospheric Plasma Jet on Implantable Devices," *ACS Appl Mater Interfaces*, vol. 10, no. 46, pp. 39512–39523, Nov. 2018, doi: 10.1021/acsami.8b15886.

[181] L. Zhang, X. Liu, and M. S. Scurrell, "Cold plasmas in the modification of catalysts," *Reviews in Chemical Engineering*, vol. 34, no. 2, pp. 201–213, Feb. 2018, doi: 10.1515/revce-2016-0043.

[182] E.-Y. Jung, H. O. Suleiman, H.-S. Tae, and C.-S. Park, "A Review of Plasma-Synthesized and Plasma Surface-Modified Piezoelectric Polymer Films for Nanogenerators and Sensors.," *Polymers (Basel)*, vol. 16, no. 11, May 2024, doi: 10.3390/polym16111548.

[183] F. L. Tabarés, *Plasma Applications for Material Modification*. New York: Jenny Stanford Publishing, 2021. doi: 10.1201/9781003119203.

[184] W. Zhu and J. L. Lopez, "A dc non-thermal atmospheric-pressure plasma microjet," *Plasma Sources Sci Technol*, vol. 21, no. 3, p. 034018, Jun. 2012, doi: 10.1088/0963-0252/21/3/034018.

[185] X. Deng, A. Y. Nikiforov, N. De Geyter, R. Morent, and C. Leys, "Deposition of a TMDSO-Based Film by a Non-Equilibrium Atmospheric Pressure DC Plasma Jet," *Plasma Processes and Polymers*, vol. 10, no. 7, pp. 641–648, Jul. 2013, doi: 10.1002/ppap.201200166.

[186] J. Li, N. Sakai, M. Watanabe, E. Hotta, and M. Wachi, "Study on Plasma Agent Effect of a Direct-Current Atmospheric Pressure Oxygen-Plasma Jet on Inactivation of E. coli Using Bacterial Mutants," *IEEE Transactions on Plasma Science*, vol. 41, no. 4, pp. 935–941, Apr. 2013, doi: 10.1109/TPS.2013.2248395.

[187] X. L. Deng, A. Yu. Nikiforov, P. Vanraes, and Ch. Leys, "Direct current plasma jet at atmospheric pressure operating in nitrogen and air," *J Appl Phys*, vol. 113, no. 2, Jan. 2013, doi: 10.1063/1.4774328.

[188] T. Gerling, T. Hoder, R. Bussiahn, R. Brandenburg, and K.-D. Weltmann, "On the spatio-temporal dynamics of a self-pulsed nanosecond transient spark discharge: a spectroscopic and

electrical analysis," *Plasma Sources Sci Technol*, vol. 22, no. 6, p. 065012, Nov. 2013, doi: 10.1088/0963-0252/22/6/065012.

[189] X. Li, W. Bao, P. Jia, and C. Di, "A brush-shaped air plasma jet operated in glow discharge mode at atmospheric pressure," *J Appl Phys*, vol. 116, no. 2, Jul. 2014, doi: 10.1063/1.4889923.

[190] A. Sobota, O. Guaitella, and A. Rousseau, "The influence of the geometry and electrical characteristics on the formation of the atmospheric pressure plasma jet," *Plasma Sources Sci Technol*, vol. 23, no. 2, p. 025016, Mar. 2014, doi: 10.1088/0963-0252/23/2/025016.

[191] Th. von Woedtke, S. Reuter, K. Masur, and K.-D. Weltmann, "Plasmas for medicine," *Phys Rep*, vol. 530, no. 4, pp. 291–320, Sep. 2013, doi: 10.1016/j.physrep.2013.05.005.

[192] A. V Pipa, M. Andrasch, K. Rackow, J. Ehlbeck, and K.-D. Weltmann, "Observation of microwave volume plasma ignition in ambient air," *Plasma Sources Sci Technol*, vol. 21, no. 3, p. 035009, Jun. 2012, doi: 10.1088/0963-0252/21/3/035009.

[193] F. Judée, G. Wattieaux, N. Merbahi, M. Mansour, and M. P. Castanié-Cornet, "The antibacterial activity of a microwave argon plasma jet at atmospheric pressure relies mainly on UV-C radiations," *J Phys D Appl Phys*, vol. 47, no. 40, p. 405201, Oct. 2014, doi: 10.1088/0022-3727/47/40/405201.

[194] O. V. Penkov, M. Khadem, W.-S. Lim, and D.-E. Kim, "A review of recent applications of atmospheric pressure plasma jets for materials processing," *J Coat Technol Res*, vol. 12, no. 2, pp. 225–235, Mar. 2015, doi: 10.1007/s11998-014-9638-z.

[195] P. Zhao, W. Zheng, Y. D. Meng, and M. Nagatsu, "Characteristics of high-purity Cu thin films deposited on polyimide by radio-frequency Ar/H2 atmospheric-pressure plasma jet," *J Appl Phys*, vol. 113, no. 12, Mar. 2013, doi: 10.1063/1.4795808.

[196] X. Guimin, Z. Guanjun, S. Xingmin, M. Yue, W. Ning, and L. Yuan, "Bacteria Inactivation Using DBD Plasma Jet in Atmospheric Pressure Argon," *Plasma Science and Technology*, vol. 11, no. 1, pp. 83–88, Feb. 2009, doi: 10.1088/1009-0630/11/1/17.

[197] X. Liu, F. Hong, Y. Guo, J. Zhang, and J. Shi, "Sterilization of Staphylococcus Aureus by an Atmospheric Non-Thermal Plasma Jet," *Plasma Science and Technology*, vol. 15, no. 5, pp. 439–442, May 2013, doi: 10.1088/1009-0630/15/5/09.

[198] X. Lu *et al.*, "An RC Plasma Device for Sterilization of Root Canal of Teeth," *IEEE Transactions on Plasma Science*, vol. 37, no. 5, pp. 668–673, 2009.

[199] A. Lehmann *et al.*, "Modification of Enamel and Dentin Surfaces by Non-Thermal Atmospheric Plasma," *Plasma Processes and Polymers*, vol. 10, no. 3, pp. 262–270, Mar. 2013, doi: 10.1002/ppap.201200088.

[200] H. W. Lee, G. J. Kim, J. M. Kim, J. K. Park, J. K. Lee, and G. C. Kim, "Tooth Bleaching with Nonthermal Atmospheric Pressure Plasma," *J Endod*, vol. 35, no. 4, pp. 587–591, Apr. 2009, doi: 10.1016/j.joen.2009.01.008.

[201] G. Isbary *et al.*, "A first prospective randomized controlled trial to decrease bacterial load using cold atmospheric argon plasma on chronic wounds in patients," *British Journal of Dermatology*, vol. 163, no. 1, pp. 78–82, Jul. 2010, doi: 10.1111/j.1365-2133.2010.09744.x.

[202] S. Chang *et al.*, "One-Step Fast Synthesis of <scp> <scp>Li</scp> </scp> 4 <scp> <scp>Ti</scp> </scp> 5 <scp> <scp>O</scp> </scp> 12 Particles Using an Atmospheric Pressure Plasma Jet,"

Journal of the American Ceramic Society, vol. 97, no. 3, pp. 708–712, Mar. 2014, doi: 10.1111/jace.12728.

[203] J. Cao and T. Matsoukas, "Synthesis of hollow nanoparticles by plasma polymerization," *Journal of Nanoparticle Research*, vol. 6, no. 5, pp. 447–455, Oct. 2004, doi: 10.1007/s11051-004-2716-x.

[204] T. Habib, J. M. A. Caiut, and B. Caillier, "Synthesis of silver nanoparticles by atmospheric pressure plasma jet," *Nanotechnology*, vol. 33, no. 32, p. 325603, Aug. 2022, doi: 10.1088/1361-6528/ac6528.

[205] X. Lu, G. V. Naidis, M. Laroussi, S. Reuter, D. B. Graves, and K. Ostrikov, "Reactive species in non-equilibrium atmospheric-pressure plasmas: Generation, transport, and biological effects," May 04, 2016, *Elsevier B.V.* doi: 10.1016/j.physrep.2016.03.003.

[206] X. Lu, G. V. Naidis, M. Laroussi, and K. Ostrikov, "Guided ionization waves: Theory and experiments," *Phys Rep*, vol. 540, no. 3, pp. 123–166, Jul. 2014, doi: 10.1016/j.physrep.2014.02.006.

[207] G. V Naidis, "Production of active species in cold helium–air plasma jets," *Plasma Sources Sci Technol*, vol. 23, no. 6, p. 065014, Sep. 2014, doi: 10.1088/0963-0252/23/6/065014.

[208] S. Hamaguchi, "Chemically reactive species in liquids generated by atmospheric-pressure plasmas and their roles in plasma medicine," 2013, pp. 214–222. doi: 10.1063/1.4815857.

[209] M. Laroussi, C. Tendero, X. Lu, S. Alla, and W. L. Hynes, "Inactivation of Bacteria by the Plasma Pencil," *Plasma Processes and Polymers*, vol. 3, no. 6–7, pp. 470–473, Aug. 2006, doi: 10.1002/ppap.200600005.

[210] N. Barekzi and M. Laroussi, "Fibroblast Cell Morphology Altered by Low-Temperature Atmospheric Pressure Plasma," *IEEE Transactions on Plasma Science*, vol. 42, no. 10, pp. 2738–2739, Oct. 2014, doi: 10.1109/TPS.2014.2315787.

[211] S. Mohades, N. Barekzi, and M. Laroussi, "Efficacy of Low Temperature Plasma against SCaBER Cancer Cells," *Plasma Processes and Polymers*, vol. 11, no. 12, pp. 1150–1155, Dec. 2014, doi: 10.1002/ppap.201400108.

[212] C. J. Berganza and J. H. Zhang, "The role of helium gas in medicine," *Med Gas Res*, vol. 3, no. 1, p. 18, 2013, doi: 10.1186/2045-9912-3-18.

[213] S. Yilmaz, K. Daglioglu, D. Yildizdas, I. Bayram, D. Gumurdulu, and S. Polat, "The effectiveness of heliox in acute respiratory distress syndrome," *Ann Thorac Med*, vol. 8, no. 1, p. 46, 2013, doi: 10.4103/1817-1737.105719.

[214] P. S. Pagel *et al.*, "Noble Gases Without Anesthetic Properties Protect Myocardium Against Infarction by Activating Prosurvival Signaling Kinases and Inhibiting Mitochondrial Permeability Transition In Vivo," *Anesth Analg*, vol. 105, no. 3, pp. 562–569, Sep. 2007, doi: 10.1213/01.ane.0000278083.31991.36.

[215] M. R. Brackman, F. C. Finelli, T. Light, O. Llorente, K. McGill, and J. Kirkpatrick, "Helium Pneumoperitoneum Ameliorates Hypercarbia and Acidosis Associated with Carbon Dioxide Insufflation during Laparoscopic Gastric Bypass in Pigs," *Obes Surg*, vol. 13, no. 5, pp. 768–771, Oct. 2003, doi: 10.1381/096089203322509363.

[216] H. Middleton *et al.*, "MR Imaging with Hyperpolarized 3 He Gas," *Magn Reson Med*, vol. 33, no. 2, pp. 271–275, Feb. 1995, doi: 10.1002/mrm.1910330219.

[217] W. L. Rice *et al.*, "High Resolution Helium Ion Scanning Microscopy of the Rat Kidney," *PLoS One*, vol. 8, no. 3, p. e57051, Mar. 2013, doi: 10.1371/journal.pone.0057051.

[218] S. Y. Moon, J. Han, and W. Choe, "Control of radio-frequency atmospheric pressure argon plasma characteristics by helium gas mixing," *Phys Plasmas*, vol. 13, no. 1, Jan. 2006, doi: 10.1063/1.2161173.

[219] Y. S. Seo, A.-A. H. Mohamed, K. C. Woo, H. W. Lee, J. K. Lee, and K. T. Kim, "Comparative Studies of Atmospheric Pressure Plasma Characteristics Between He and Ar Working Gases for Sterilization," *IEEE Transactions on Plasma Science*, vol. 38, no. 10, pp. 2954–2962, Oct. 2010, doi: 10.1109/TPS.2010.2058870.

[220] A. Abdullah and A. Mohammed, "Scanning Electron Microscopy (SEM): A Review." [Online]. Available: https://www.researchgate.net/publication/330169176

[221] K. D. Vernon-Parry, "Scanning electron microscopy: an introduction," *III-Vs Review*, vol. 13, no. 4, pp. 40–44, Jul. 2000, doi: 10.1016/S0961-1290(00)80006-X.

[222] M. Kannan, "Scanning Electron Microscopy: Principle, Components and Applications," in *A Textbook on Fundamentals and Applications of Nanotechnology*, New Delhi: Daya Publishing House (A Division of Astral International Pvt. Ltd.), 2018, pp. 81–92.

[223] B. C. Smith, *Fundamentals of Fourier Transform Infrared Spectroscopy*, 2nd ed. Boca Raton: CRC Press, 2011.

[224] P. R. Griffiths and J. A. de Haseth, *Fourier Transform Infrared Spectrometry*. Wiley, 2007. doi: 10.1002/047010631X.

[225] H. Chen, C. Ferrari, M. Angiuli, J. Yao, C. Raspi, and E. Bramanti, "Qualitative and quantitative analysis of wood samples by Fourier transform infrared spectroscopy and multivariate analysis," *Carbohydr Polym*, vol. 82, no. 3, pp. 772–778, Oct. 2010, doi: 10.1016/j.carbpol.2010.05.052.

[226] S. P. Levine, Y. Li-Shi, C. R. Strang, and X. Hong-Kui, "Advantages and Disadvantages in the Use of Fourier Transform Infrared (FTIR) and Filter Infrared (FIR) Spectrometers for Monitoring Airborne Gases and Vapors of Industrial Hygiene Concern," *Applied Industrial Hygiene*, vol. 4, no. 7, pp. 180–187, Jul. 1989, doi: 10.1080/08828032.1989.10390419.

[227] J. D. Andrade, "X-ray Photoelectron Spectroscopy (XPS)," in *Surface and Interfacial Aspects of Biomedical Polymers*, Boston, MA: Springer US, 1985, pp. 105–195. doi: 10.1007/978-1-4684-8610-0_5.

[228] P. Simon, V. G. Baldovino-Medrano, and R. Wojcieszak, "X-Ray Photoelectron Spectroscopy (XPS): Principles and Application for the Analysis of Photoactive Materials," 2022, pp. 249–271. doi: 10.1007/978-3-030-63713-2_10.

[229] D. Schild, "X-ray Photoelectron Spectroscopy," in *Hydrogen Technology*, Berlin, Heidelberg: Springer Berlin Heidelberg, pp. 575–601. doi: 10.1007/978-3-540-69925-5_23.

[230] M. Magdy, "X-Ray Techniques Dedicated to Materials Characterization in Cultural Heritage," *ChemistrySelect*, vol. 8, no. 33, Sep. 2023, doi: 10.1002/slct.202301306.

[231] I. P. Herman, "Optical Emission Spectroscopy," in *Optical Diagnostics for Thin Film Processing*, Elsevier, 1996, ch. 6, pp. 157–213. doi: 10.1016/B978-012342070-1/50007-3.

[232] A. Sanz-Medel, R. Pereiro, and J. M. Costa-Fernández, “A General Overview of Atomic Spectrometric Techniques,” in *Basic Chemometric Techniques in Atomic Spectroscopy*, The Royal Society of Chemistry, 2009, pp. 1–50. doi: 10.1039/9781847559661-00001.

[233] PerkinElmer, “Concepts, Instrumentation and Techniques in Inductively Coupled Plasma Optical Emission Spectrometry.” [Online]. Available: www.perkinelmer.com

[234] W. G. J. H. M. Van Sark, “Methods of Deposition of Hydrogenated Amorphous Silicon for Device Applications,” 2002, pp. 1–215. doi: 10.1016/S1079-4050(02)80004-7.

[235] X. Zheng *et al.*, “Different Polymerizing Characteristics of Ar/He Atmospheric Pressure Plasma Jets at Room Temperature,” *Plasma Processes and Polymers*, vol. 10, no. 4, pp. 379–387, Apr. 2013, doi: 10.1002/ppap.201200125.

[236] T. Smith, D. H. Kaelble, and C. L. Hamermesh, “Mechanism of plasma polymerization: The effect of substrate and substrate topography,” *Surf Sci*, vol. 76, no. 1, pp. 203–231, Sep. 1978, doi: 10.1016/0039-6028(78)90076-6.

[237] L. M. Gomez, G. J. Cruz, M. G. Olayo, M. Gonzalez-Torres, F. Gonzalez-Salgado, and O. G. Lopez-Gracia, “Analysis of crosslinking in polypyrrole particles synthesized by plasma,” *Polymer Bulletin*, vol. 71, no. 12, pp. 3275–3287, Dec. 2014, doi: 10.1007/s00289-014-1249-4.

[238] U. Heredia-Rivera *et al.*, “Cold atmospheric plasma deposition of antibacterial polypyrrole–silver nanocomposites on wearable electronics for prolonged performance,” *J Mater Chem C Mater*, vol. 12, no. 31, pp. 11861–11876, 2024, doi: 10.1039/D4TC00844H.

[239] J. Friedrich, “Mechanisms of Plasma Polymerization – Reviewed from a Chemical Point of View,” *Plasma Processes and Polymers*, vol. 8, no. 9, pp. 783–802, Sep. 2011, doi: 10.1002/ppap.201100038.

[240] M. A. Boles, M. Engel, and D. V. Talapin, “Self-Assembly of Colloidal Nanocrystals: From Intricate Structures to Functional Materials,” *Chem Rev*, vol. 116, no. 18, pp. 11220–11289, Sep. 2016, doi: 10.1021/acs.chemrev.6b00196.

[241] L. Liang, G. Chen, and C.-Y. Guo, “Polypyrrole nanostructures and their thermoelectric performance,” *Mater Chem Front*, vol. 1, no. 2, pp. 380–386, 2017, doi: 10.1039/C6QM00061D.

[242] O. Polonskyi *et al.*, “Plasma based formation and deposition of metal and metal oxide nanoparticles using a gas aggregation source,” *The European Physical Journal D*, vol. 72, no. 5, p. 93, May 2018, doi: 10.1140/epjd/e2017-80419-8.

[243] T. Dufour, “From Basics to Frontiers: A Comprehensive Review of Plasma-Modified and Plasma-Synthesized Polymer Films,” *Polymers (Basel)*, vol. 15, no. 17, p. 3607, Aug. 2023, doi: 10.3390/polym15173607.

[244] E. J. Kautz *et al.*, “Impact of environmental oxygen on nanoparticle formation and agglomeration in aluminum laser ablation plumes,” *J Chem Phys*, vol. 159, no. 17, Nov. 2023, doi: 10.1063/5.0167400.

[245] M. Müller, M. Dworschak, J. Benedikt, and L. Kienle, “Tungsten Nanoparticles Generated in an Atmospheric Pressure Plasma Jet,” *Particle & Particle Systems Characterization*, vol. 41, no. 9, Sep. 2024, doi: 10.1002/ppsc.202400037.

[246] S. J. Kadhem, “Studying of Plasma- Polymerized Pyrrole at Variable Gas Flow Rates Via Plasma Jet,” *Iraqi Journal of Physics*, vol. 19, no. 48, pp. 44–51, Mar. 2021, doi: 10.30723/ijp.v19i48.593.

[247] E. Y. Jung *et al.*, “Optimization of Atmospheric Pressure Plasma Jet with Single-Pin Electrode Configuration and Its Application in Polyaniline Thin Film Growth,” *Polymers (Basel)*, vol. 14, no. 8, p. 1535, Apr. 2022, doi: 10.3390/polym14081535.

[248] H. K. Yasuda, “Some Important Aspects of Plasma Polymerization,” *Plasma Processes and Polymers*, vol. 2, no. 4, pp. 293–304, May 2005, doi: 10.1002/ppap.200400071.

[249] T. Wang *et al.*, “Effect of electrode configurations on the characteristics of the ring–ring typed atmospheric pressure plasma jet and its modification on polymer film,” *Plasma Processes and Polymers*, vol. 19, no. 2, Feb. 2022, doi: 10.1002/ppap.202100139.

[250] Y. Xu *et al.*, “Enhancements of electric field and afterglow of non-equilibrium plasma by Pb(ZrxTi1−x)O3 ferroelectric electrode,” *Nat Commun*, vol. 15, no. 1, p. 3092, Apr. 2024, doi: 10.1038/s41467-024-47230-7.

[251] J. V. Gulmine, P. R. Janissek, H. M. Heise, and L. Akcelrud, “Polyethylene characterization by FTIR,” *Polym Test*, vol. 21, no. 5, pp. 557–563, 2002, doi: 10.1016/S0142-9418(01)00124-6.

[252] U. Heredia-Rivera *et al.*, “Cold Atmospheric Plasma-Assisted Direct Deposition of Polypyrrole-Ag Nanocomposites for Flexible Electronic Sensors,” *ACS Appl Mater Interfaces*, vol. 15, no. 13, pp. 17078–17090, Apr. 2023, doi: 10.1021/acsami.2c20798.

[253] H. J. Jang, B. J. Shin, E. Y. Jung, G. T. Bae, J. Y. Kim, and H.-S. Tae, “Polypyrrole film synthesis via solution plasma polymerization of liquid pyrrole,” *Appl Surf Sci*, vol. 608, p. 155129, Jan. 2023, doi: 10.1016/j.apsusc.2022.155129.

[254] P. Yang, J. Zhang, and Y. Guo, “Synthesis of intrinsic fluorescent polypyrrole nanoparticles by atmospheric pressure plasma polymerization,” *Appl Surf Sci*, vol. 255, no. 15, pp. 6924–6929, May 2009, doi: 10.1016/j.apsusc.2009.03.016.

[255] M. Vasquez-Ortega, M. Ortega, J. Morales, M. G. Olayo, G. J. Cruz, and R. Olayo, “Core–shell polypyrrole nanoparticles obtained by atmospheric pressure plasma polymerization,” *Polym Int*, vol. 63, no. 12, pp. 2023–2029, Dec. 2014, doi: 10.1002/pi.4756.

[256] J. Schäfer, R. Foest, A. Quade, A. Ohl, and K.-D. Weltmann, “Local deposition of SiO *x* plasma polymer films by a miniaturized atmospheric pressure plasma jet (APPJ),” *J Phys D Appl Phys*, vol. 41, no. 19, p. 194010, Oct. 2008, doi: 10.1088/0022-3727/41/19/194010.

[257] C. Oehr, “Plasma surface modification of polymers for biomedical use,” *Nucl Instrum Methods Phys Res B*, vol. 208, pp. 40–47, Aug. 2003, doi: 10.1016/S0168-583X(03)00650-5.

[258] M. P. Seah and W. A. Dench, “Quantitative electron spectroscopy of surfaces: A standard data base for electron inelastic mean free paths in solids,” *Surface and Interface Analysis*, vol. 1, no. 1, pp. 2–11, Feb. 1979, doi: 10.1002/sia.740010103.

[259] S.-K. Pang, “Comprehensive study of polymerization of pyrrole: A theoretical approach,” *Journal of Electroanalytical Chemistry*, vol. 859, p. 113886, Feb. 2020, doi: 10.1016/j.jelechem.2020.113886.

[260] P. Chu, “Plasma-surface modification of biomaterials,” *Materials Science and Engineering: R: Reports*, vol. 36, no. 5–6, pp. 143–206, Mar. 2002, doi: 10.1016/S0927-796X(02)00004-9.

[261] J. Siegel, A. Řezníčková, A. Chaloupka, P. Slepička, and V. Švorčík, “Ablation and water etching of plasma-treated polymers,” *Radiation Effects and Defects in Solids*, vol. 163, no. 9, pp. 779–788, Sep. 2008, doi: 10.1080/10420150801969654.

[262] R. Ghobeira, P. S. Esbah Tabaei, A. Nikiforov, R. Morent, and N. De Geyter, “Unraveling Exclusive In-Plasma Initiated Oxidation Processes Occurring at Polymeric Surfaces upon O2 Admixtures to Medium Pressure Ar and N2 DBD Treatments,” *Polymers (Basel)*, vol. 15, no. 14, p. 2978, Jul. 2023, doi: 10.3390/polym15142978.

[263] M. González-Torres, Ma. G. Olayo, G. J. Cruz, L. Ma. Gómez, V. Sánchez-Mendieta, and F. González-Salgado, “XPS Study of the Chemical Structure of Plasma Biocopolymers of Pyrrole and Ethylene Glycol,” *Advances in Chemistry*, vol. 2014, pp. 1–8, Aug. 2014, doi: 10.1155/2014/965920.

[264] Y. Iriyama and M. Hanawa, “Plasma Polymerization of Pyrrole and Structures and Properties of the Polymerized Films,” *Polym J*, vol. 33, no. 5, pp. 419–423, May 2001, doi: 10.1295/polymj.33.419.

[265] M. Thiyagarajan, A. Sarani, and C. Nicula, “Optical emission spectroscopic diagnostics of a non-thermal atmospheric pressure helium-oxygen plasma jet for biomedical applications,” *J Appl Phys*, vol. 113, no. 23, Jun. 2013, doi: 10.1063/1.4811339.

[266] I. Burducea *et al.*, “Helium Atmospheric Pressure Plasma Jet Effects on Two Cultivars of Triticum aestivum L.,” *Foods*, vol. 12, no. 1, p. 208, Jan. 2023, doi: 10.3390/foods12010208.

[267] C. Li, J. H. Hsieh, and Y. T. Lee, “Effects of radio frequency power on the microstructures and properties of plasma polymerized polypyrrole thin films,” *Vacuum*, vol. 140, pp. 132–138, Jun. 2017, doi: 10.1016/j.vacuum.2016.09.009.

[268] Q. Xiong, A. Y. Nikiforov, M. Á. González, C. Leys, and X. P. Lu, “Characterization of an atmospheric helium plasma jet by relative and absolute optical emission spectroscopy,” *Plasma Sources Sci Technol*, vol. 22, no. 1, p. 015011, Dec. 2012, doi: 10.1088/0963-0252/22/1/015011.

[269] H. M. Joh, H. R. Kang, T. H. Chung, and S. J. Kim, “Electrical and Optical Characterization of Atmospheric-Pressure Helium Plasma Jets Generated With a Pin Electrode: Effects of the Electrode Material, Ground Ring Electrode, and Nozzle Shape,” *IEEE Transactions on Plasma Science*, vol. 42, no. 12, pp. 3656–3667, Dec. 2014, doi: 10.1109/TPS.2014.2332171.

[270] A. Schutze, J. Y. Jeong, S. E. Babayan, Jaeyoung Park, G. S. Selwyn, and R. F. Hicks, “The atmospheric-pressure plasma jet: a review and comparison to other plasma sources,” *IEEE Transactions on Plasma Science*, vol. 26, no. 6, pp. 1685–1694, 1998, doi: 10.1109/27.747887.

[271] W. J. van Ooij, S. Eufinger, and T. H. Ridgway, “DC-plasma polymerization of pyrrole,” *Plasmas Polym*, vol. 1, no. 3, pp. 229–260, Sep. 1996, doi: 10.1007/BF02532818.

[272] G. V. Naidis, “Modeling of helium plasma jets emerged into ambient air: Influence of applied voltage, jet radius, and helium flow velocity on plasma jet characteristics,” *J Appl Phys*, vol. 112, no. 10, Nov. 2012, doi: 10.1063/1.4766297.

[273] L. Jiang, M. Wong, and Y. Zohar, “Transient temperature performance of an integrated micro-thermal system,” *Journal of Micromechanics and Microengineering*, vol. 10, no. 3, pp. 466–476, Sep. 2000, doi: 10.1088/0960-1317/10/3/324.

[274] P. J. Bruggeman, F. Iza, and R. Brandenburg, “Foundations of atmospheric pressure non-equilibrium plasmas,” *Plasma Sources Sci Technol*, vol. 26, no. 12, p. 123002, Nov. 2017, doi: 10.1088/1361-6595/aa97af.

[275] H. Soo Choi *et al.*, “Renal clearance of quantum dots,” *Nat Biotechnol*, vol. 25, no. 10, pp. 1165–1170, Oct. 2007, doi: 10.1038/nbt1340.

[276] L.-T. Chen and L. Weiss, “The Role of the Sinus Wall in the Passage of Erythrocytes Through the Spleen,” *Blood*, vol. 41, no. 4, pp. 529–537, Apr. 1973, doi: 10.1182/blood.V41.4.529.529.

[277] E. Blanco, H. Shen, and M. Ferrari, “Principles of nanoparticle design for overcoming biological barriers to drug delivery,” *Nat Biotechnol*, vol. 33, no. 9, pp. 941–951, Sep. 2015, doi: 10.1038/nbt.3330.

[278] M. Guo *et al.*, “N-containing functional groups induced superior cytocompatible and hemocompatible graphene by NH2 ion implantation,” *J Mater Sci Mater Med*, vol. 24, no. 12, pp. 2741–2748, Dec. 2013, doi: 10.1007/s10856-013-5016-0.

[279] O. Prucker, T. Brandstetter, and J. Rühe, “Surface-attached hydrogel coatings via C,H-insertion crosslinking for biomedical and bioanalytical applications (Review),” *Biointerphases*, vol. 13, no. 1, Feb. 2018, doi: 10.1116/1.4999786.

[280] Y. Li, M. Ho Kang, H. Sup Uhm, G. Joon Lee, E. Ha Choi, and I. Han, “Effects of atmospheric-pressure non-thermal bio-compatible plasma and plasma activated nitric oxide water on cervical cancer cells,” *Sci Rep*, vol. 7, no. 1, p. 45781, Mar. 2017, doi: 10.1038/srep45781.

[281] M. Keidar, “Plasma for cancer treatment,” *Plasma Sources Sci Technol*, vol. 24, no. 3, p. 033001, May 2015, doi: 10.1088/0963-0252/24/3/033001.

[282] S. Bhattacharjee, “DLS and zeta potential – What they are and what they are not?,” *Journal of Controlled Release*, vol. 235, pp. 337–351, Aug. 2016, doi: 10.1016/j.jconrel.2016.06.017.

[283] Y. Wang *et al.*, “Comparison Study of Gold Nanohexapods, Nanorods, and Nanocages for Photothermal Cancer Treatment,” *ACS Nano*, vol. 7, no. 3, pp. 2068–2077, Mar. 2013, doi: 10.1021/nn304332s.

[284] M. A. Dobrovolskaia and S. E. McNeil, “Immunological properties of engineered nanomaterials,” *Nat Nanotechnol*, vol. 2, no. 8, pp. 469–478, Aug. 2007, doi: 10.1038/nnano.2007.223.

[285] J. H. Lee and Y. Yeo, “Controlled Drug Release from Pharmaceutical Nanocarriers.,” *Chem Eng Sci*, vol. 125, pp. 75–84, Mar. 2015, doi: 10.1016/j.ces.2014.08.046.

[286] United Nations, “Sustainable Development Goals.”

[287] M. Bouloudenine and M. Bououdina, “Toxic Effects of Engineered Nanoparticles on Living Cells,” pp. 35–68. doi: 10.4018/978-1-4666-9811-6.ch002.

[288] A. A. Tikhomirov, V. S. Nedzvetskii, M. V. Lipka, G. V. Andrievskii, and V. K. Klochkov, “Chronic alcoholization-induced damage to astroglia and intensification of lipid peroxidation in the rat brain: Protector effect of hydrated form of fullerene C60,” *Neurophysiology*, vol. 39, no. 2, pp. 105–111, Mar. 2007, doi: 10.1007/s11062-007-0015-8.

[289] B. D. Malhotra, S. Srivastava, and S. Augustine, “Biosensors for Food Toxin Detection: Carbon Nanotubes and Graphene,” *MRS Proceedings*, vol. 1725, pp. mrsf14-1725-i05-02, Feb. 2015, doi: 10.1557/opl.2015.165.

[290] H. Su, D. N. Sredojevic, H. Bronstein, T. J. Marks, B. C. Schroeder, and M. Al-Hashimi, “Bithiazole: An Intriguing Electron-Deficient Building for Plastic Electronic Applications,” *Macromol Rapid Commun*, vol. 38, no. 10, May 2017, doi: 10.1002/marc.201600610.

[291] H. Szatylowicz, O. A. Stasyuk, and T. M. Krygowski, “Calculating the Aromaticity of Heterocycles,” 2016, pp. 301–327. doi: 10.1016/bs.aihch.2016.03.007.

[292] M. A. Mohamed, J. Jaafar, A. F. Ismail, M. H. D. Othman, and M. A. Rahman, “Fourier Transform Infrared (FTIR) Spectroscopy,” in *Membrane Characterization*, Elsevier, 2017, pp. 3–29. doi: 10.1016/B978-0-444-63776-5.00001-2.

[293] K. Urabe, M. Toyoda, Y. Matsuoka, and K. Eriguchi, “Investigation of small-fraction molecular impurities in high-pressure helium plasmas using optical plasma diagnostic methods,” *Plasma Sources Sci Technol*, vol. 33, no. 2, p. 025011, Feb. 2024, doi: 10.1088/1361-6595/ad1f38.

APPENDICES

Non-included results

Additional SEM images

Varying the precursor flow between 150-500 sccm

9 kV – 5 cm – 1 min

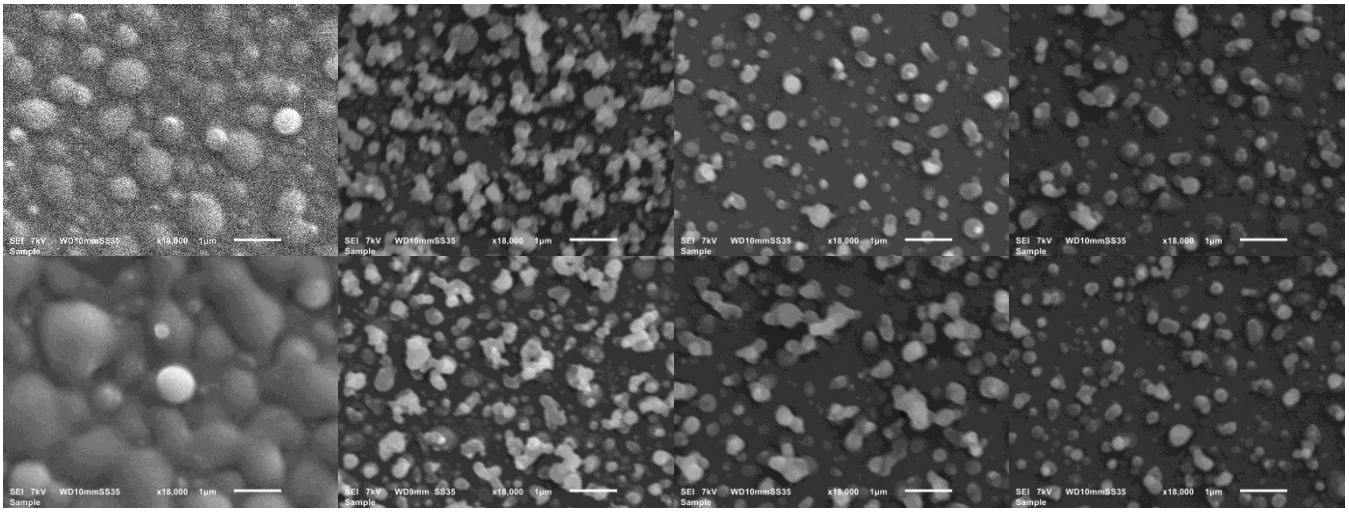

Py 150 sccm | Py 200 sccm | Py 250 sccm | Py 300 sccm

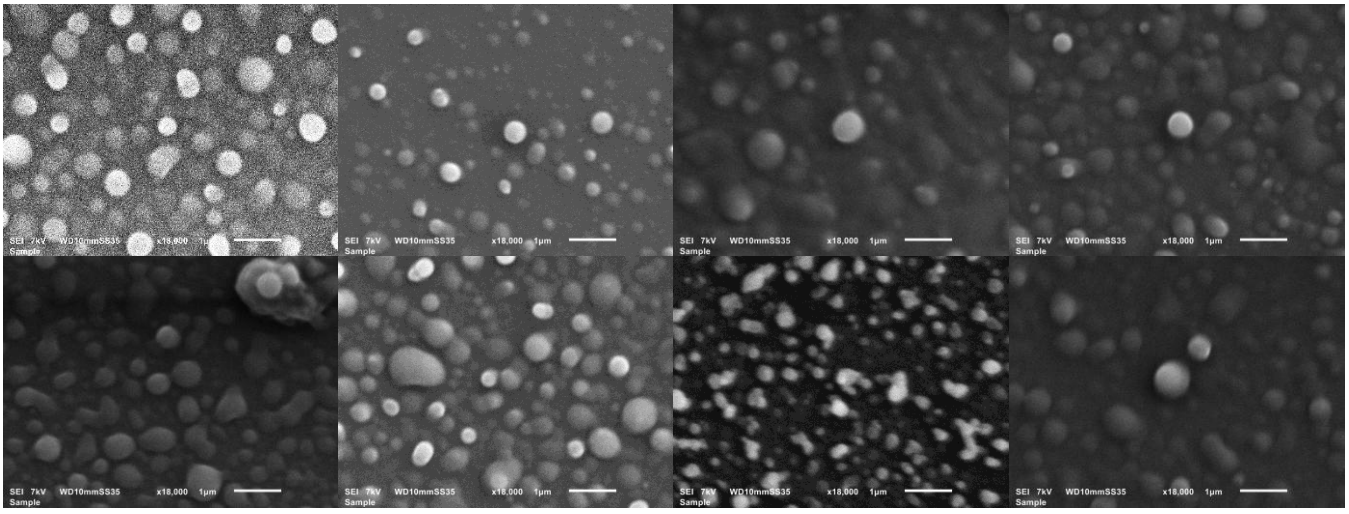

Py 350 sccm | Py 400 sccm | Py 450 sccm | Py 500 sccm

Rhomboidal nanoparticles

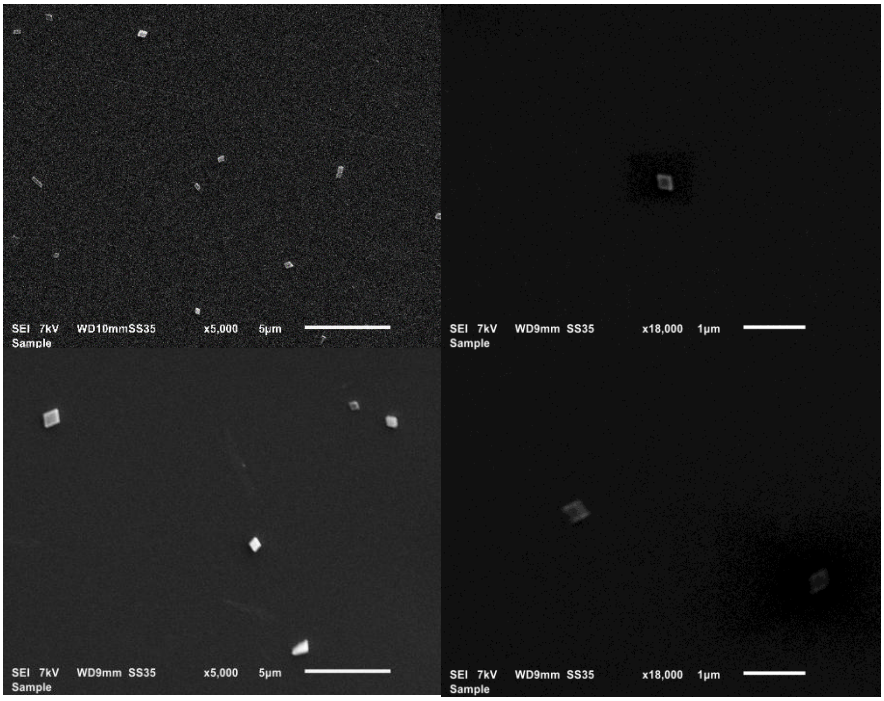

Py 10 sccm Py 25 sccm

Under these conditions (He 1.990 slm + Py 10 sccm – 5 cm – 9 kV – 1 min and He 1.975 slm + Py 10 sccm – 5 cm – 9 kV – 1 min) particular results were obtained with the formation of rhomboidal nanoparticles. However, the experiment was not reproducible, as subsequent attempts using the same conditions did not lead to the formation of nanoparticles with this shape.

Varying the distance substrate-to-capillaries

He 1,700 slm + Py 300 sccm – 9 kV – 1 min

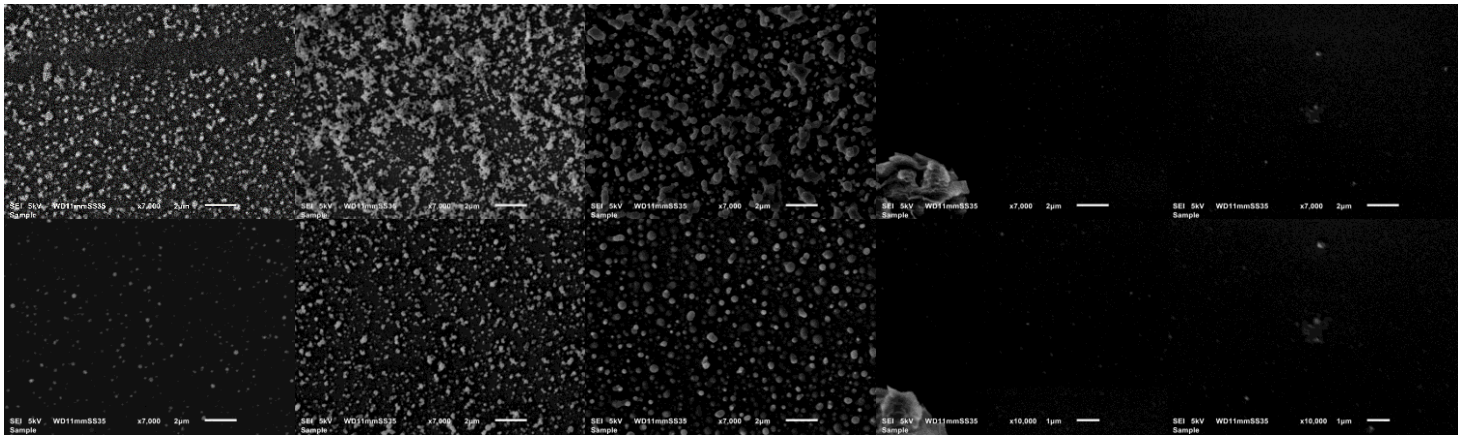

3 cm 4 cm 5 cm 6 cm 7 cm

He 1,750 slm + Py 250 sccm – 9 kV – 1 min

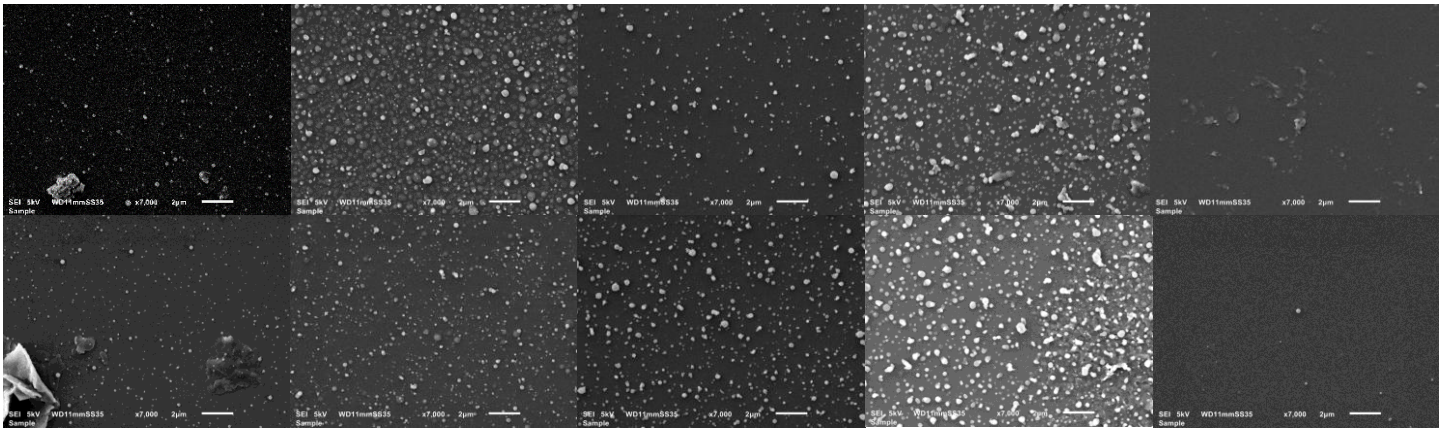

3 cm 4 cm 5 cm 6 cm 7 cm

He 1,800 slm + Py 200 sccm – 9 kV – 1 min

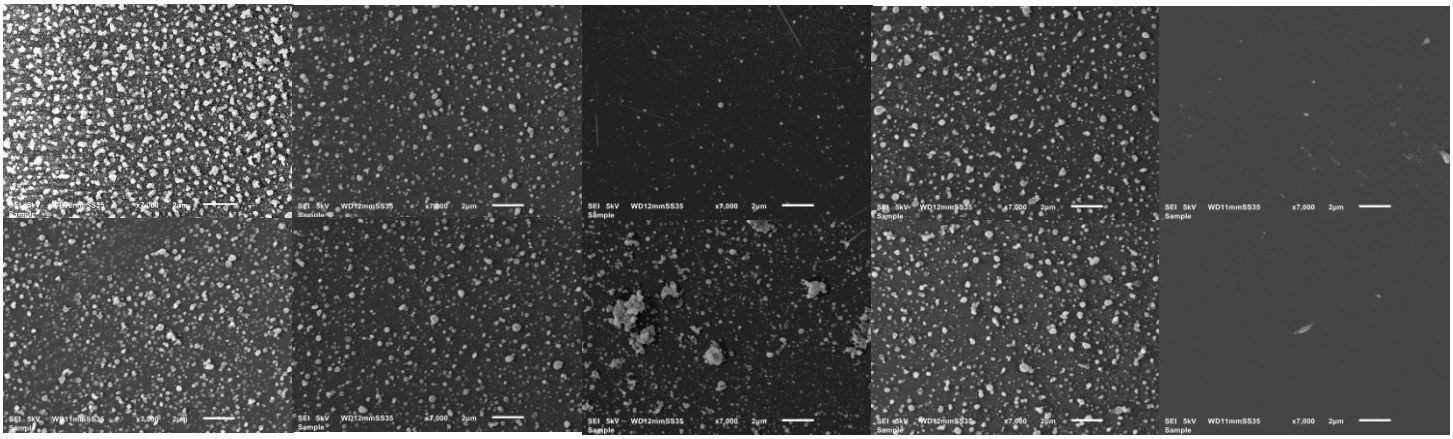

3 cm 4 cm 5 cm 6 cm 7 cm

Varying the input flow

He 1,700 slm + Py 300 sccm – 4 cm– 1 min

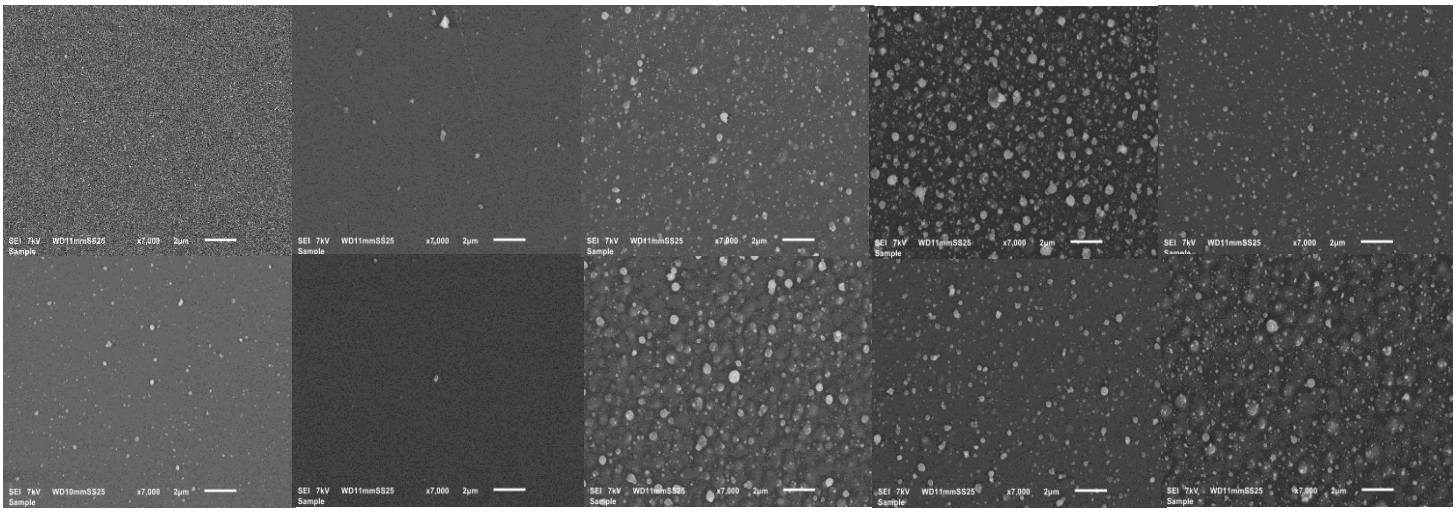

6 kV | 7 kV | 8 kV | 9 kV | 10 kV

He 1,750 slm + Py 250 sccm – 3 cm– 1 min

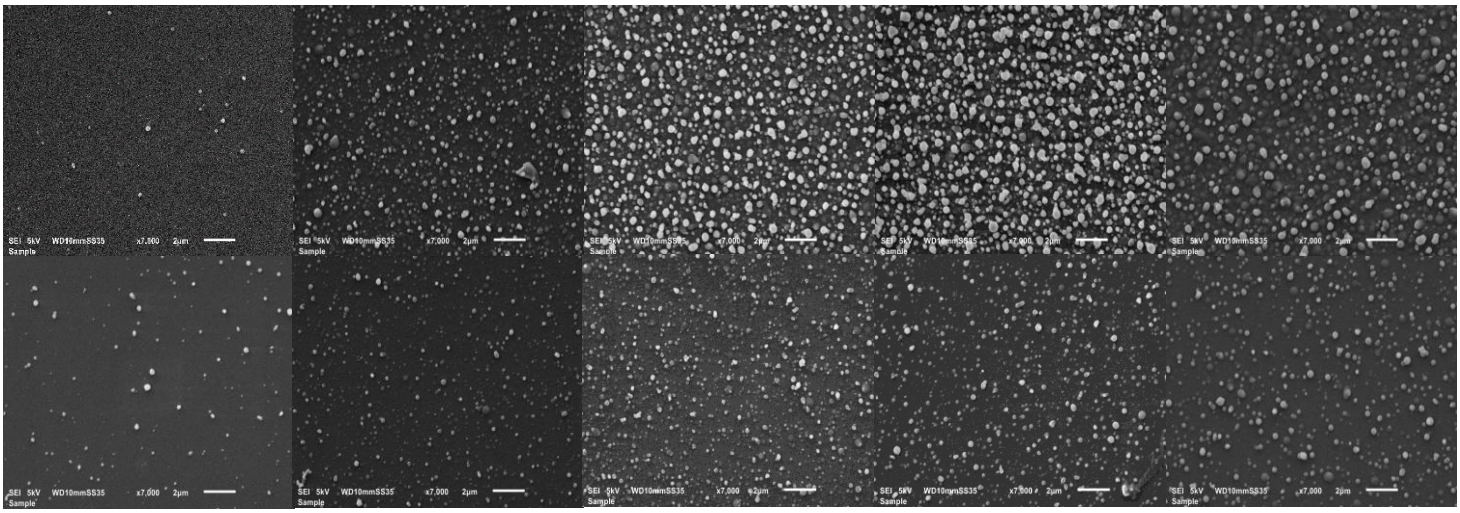

6 kV | 7 kV | 8 kV | 9 kV | 10 kV

He 1,800 slm + Py 200 sccm – 5 cm– 1 min

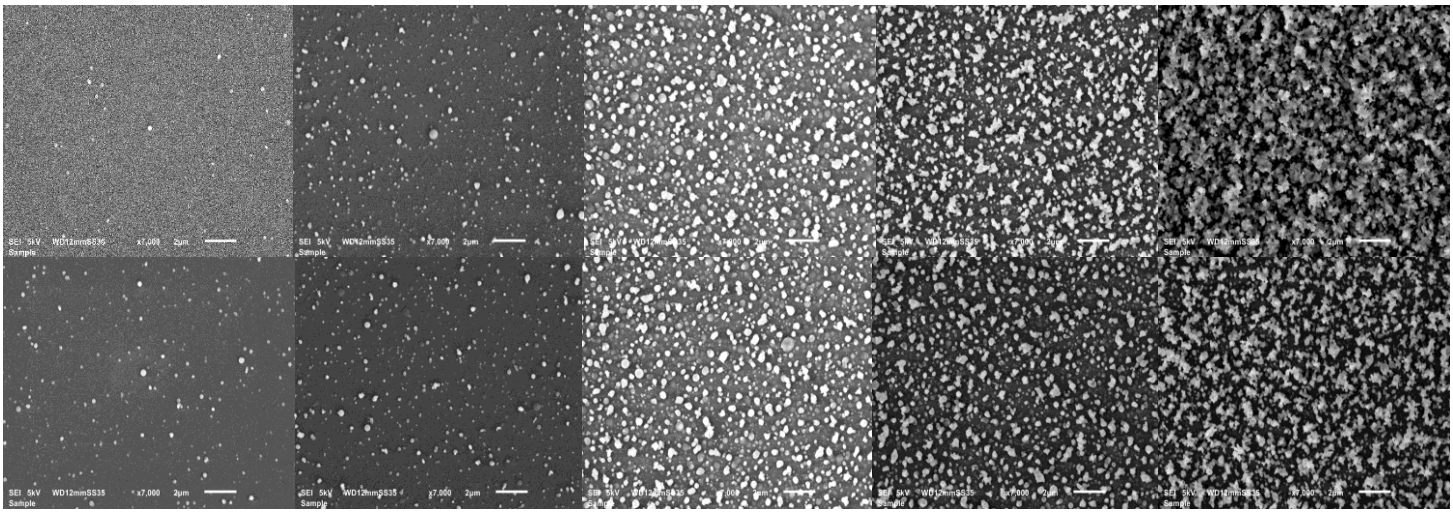

6 kV 7 kV 8 kV 9 kV 10 kV

XPS atomic percentages

Varying the precursor flow – 9 kV – 5 cm – 1 min

He 1,700 slm + Py 300 sccm

C1s (%)	N1s (%)	O1s (%)
70,05	14,72	15,23
69,51	14,19	16,3
71,7	14,06	14,24
70,89	15,01	14,1
73,06	13,43	13,51

He 1,750 slm + Py 250 sccm

C1s (%)	N1s (%)	O1s (%)
75,99	13,92	10,09
76,09	14,65	9,26
73,43	15,38	11,19
73,67	15,34	10,98
75,47	14,62	9,91
74,85	15,44	9,71

He 1,800 slm + Py 200 sccm

C1s (%)	N1s (%)	O1s (%)
67,93	13	19,07
68,37	14,35	17,28
70,06	13,73	16,21
69,1	14,62	16,28
71,68	13,21	15,11
71,28	14,68	14,05

Varying the distance – 9 kV – 1 min

He 1,700 slm + Py 300 sccm

C1s (%)	N1s (%)	O1s (%)
77,54	14,21	8,25
76,65	15,4	7,95
76,98	14,77	8,25
77,46	13,72	8,82
78,25	14,65	7,09
76,91	14,91	8,18

He 1,750 slm + Py 250 sccm

C1s (%)	N1s (%)	O1s (%)
75,31	15,55	9,14
77,23	14,65	8,12
77,14	14,37	8,49
75,66	15,57	8,77
76,15	15,35	8,49
77,54	14,6	7,86

He 1,800 slm + Py 200 sccm

C1s (%)	N1s (%)	O1s (%)
77,51	14,41	8,08
76,54	15,86	7,6
76,09	15,7	8,22
75,97	14,78	9,26
74,88	15,49	9,63
74,93	15,49	9,58

Varying the input flow – 1 min

He 1,700 slm + Py 300 sccm – 4 cm

C1s (%)	N1s (%)	O1s (%)
76,55	15,13	8,32
75,99	14,27	9,74
76,56	14,01	9,43
75,83	14,52	9,65
74,33	15,47	10,2
75,73	14,76	9,51

He 1,750 slm + Py 250 sccm – 3 cm

C1s (%)	N1s (%)	O1s (%)
77,1	14,25	8,66
77,13	14,26	8,61
77,29	15,1	7,61
77,15	14,56	8,3
77,62	14,9	7,48
77,92	14,27	7,8

He 1,800 slm + Py 200 sccm – 5 cm

C1s (%)	N1s (%)	O1s (%)
70,77	13,79	15,44
73,76	13,47	12,77
75,69	13,56	10,75
73,6	15,11	11,29
72,53	15,63	11,84
73,11	14,49	12,4

Voltage waveforms

He 2 slm – 9 kV – no sample holder

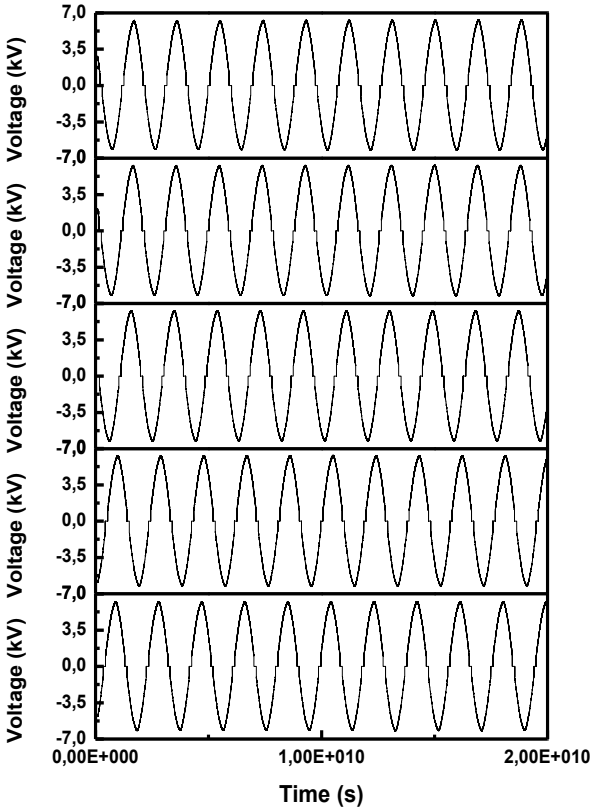

He 2 slm – 9 kV – 5 cm

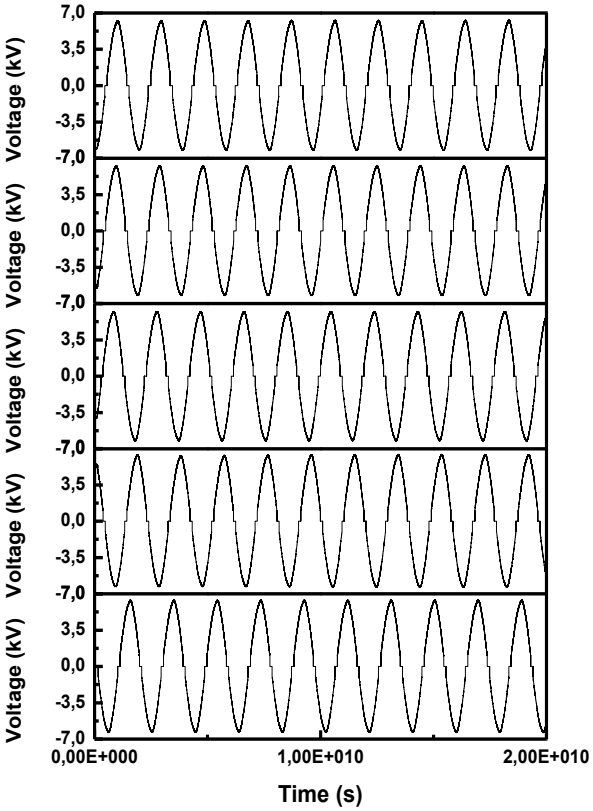

He 1,700 slm + Py 300 sccm – 6 kV – 4 cm

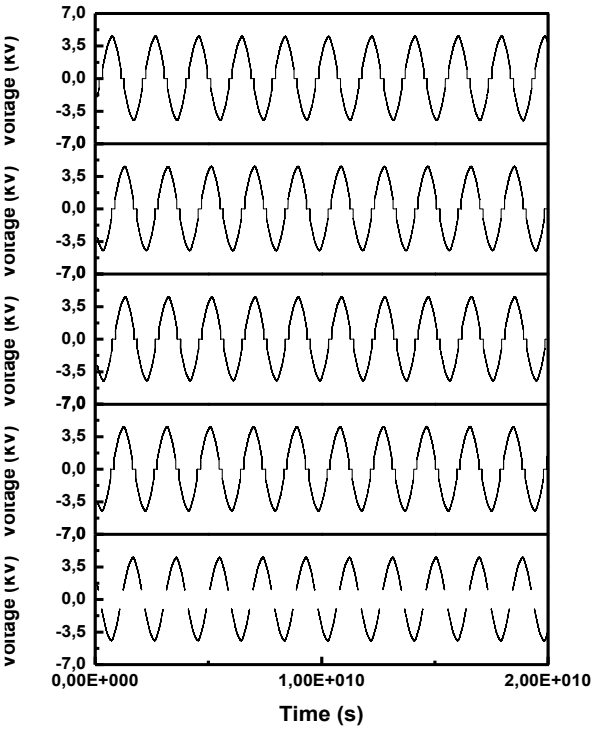

He 1,700 slm + Py 300 sccm – 6 kV – 5 cm

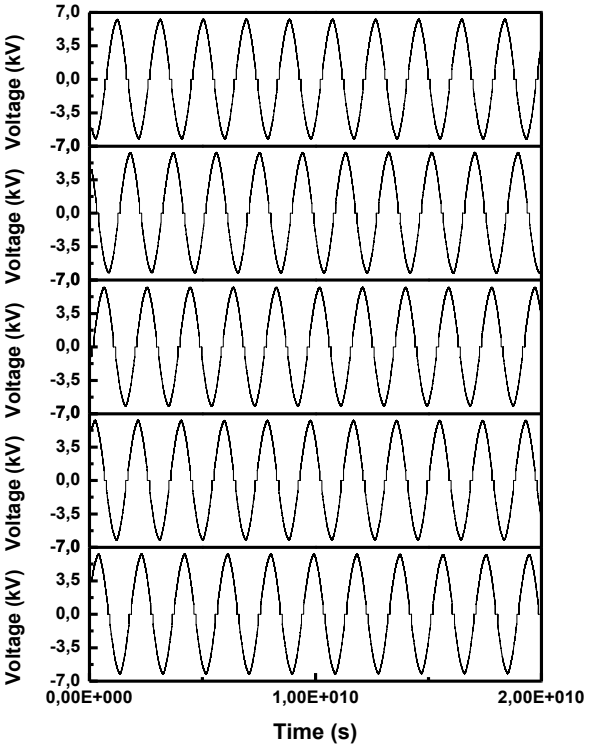

He 1,700 slm + Py 300 sccm – 9 kV – 5 cm

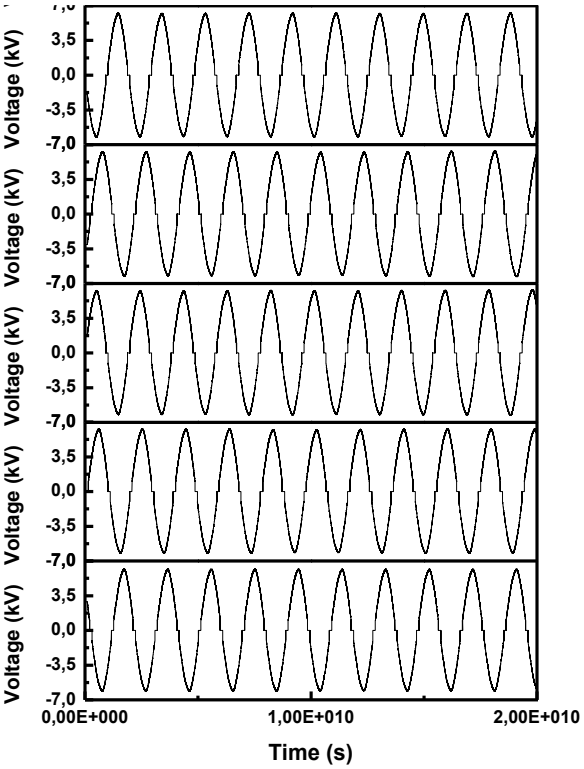

He 1,750 slm + Py 250 sccm – 7 kV – 3 cm

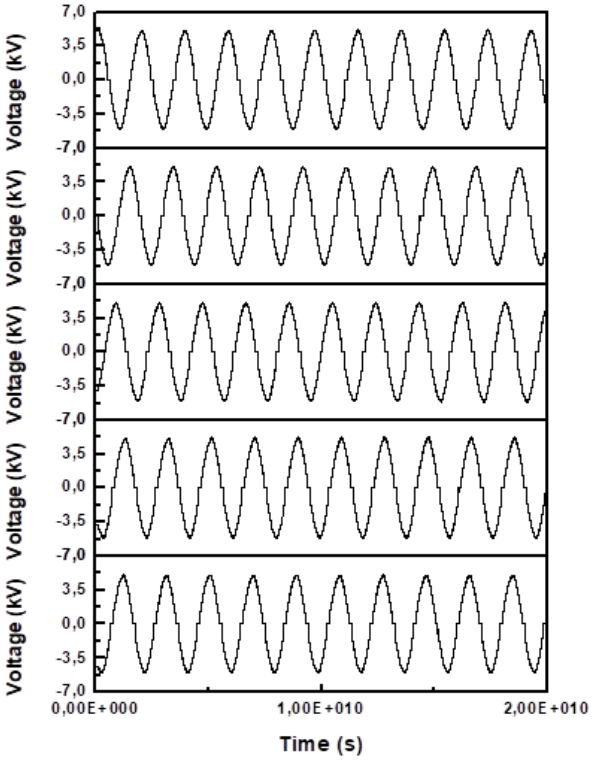

He 1,750 slm + Py 250 sccm – 9 kV – 3 cm

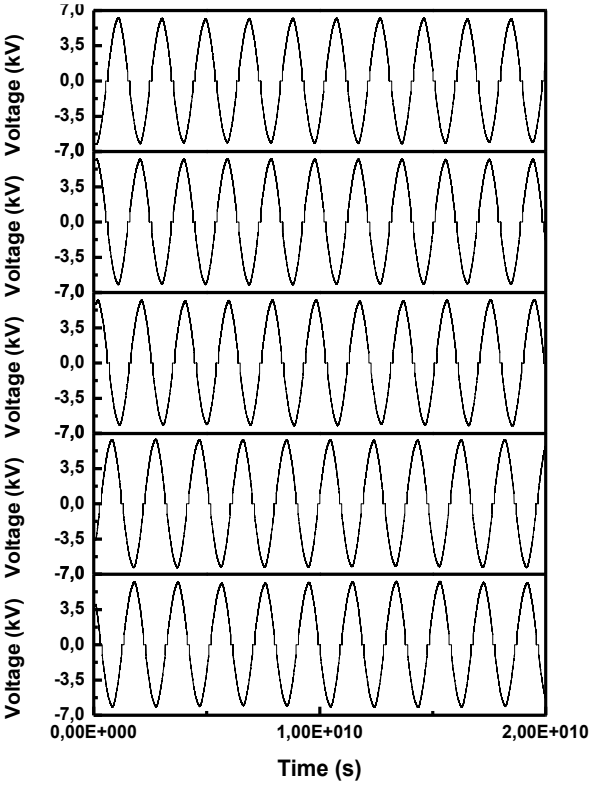

He 1,750 slm + Py 250 sccm – 9 kV – 5 cm

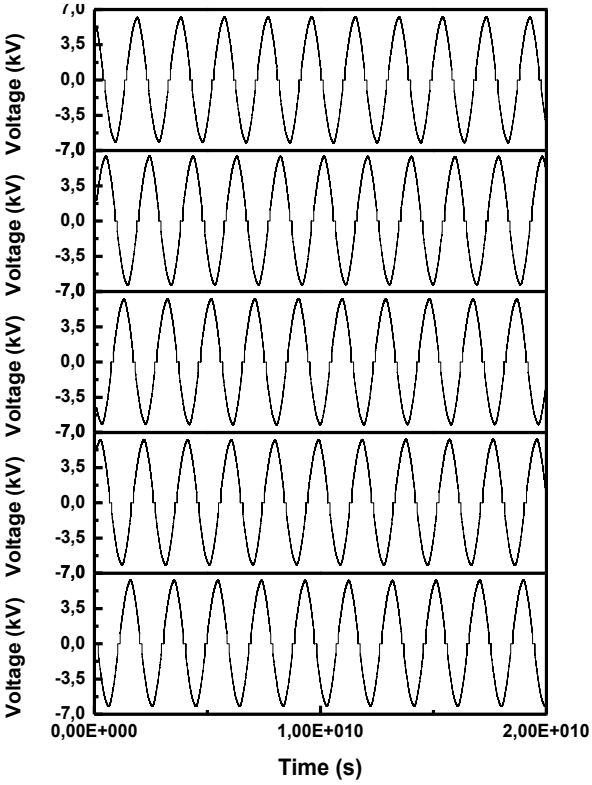

He 1,800 slm + Py 200 sccm – 7 kV – 5 cm

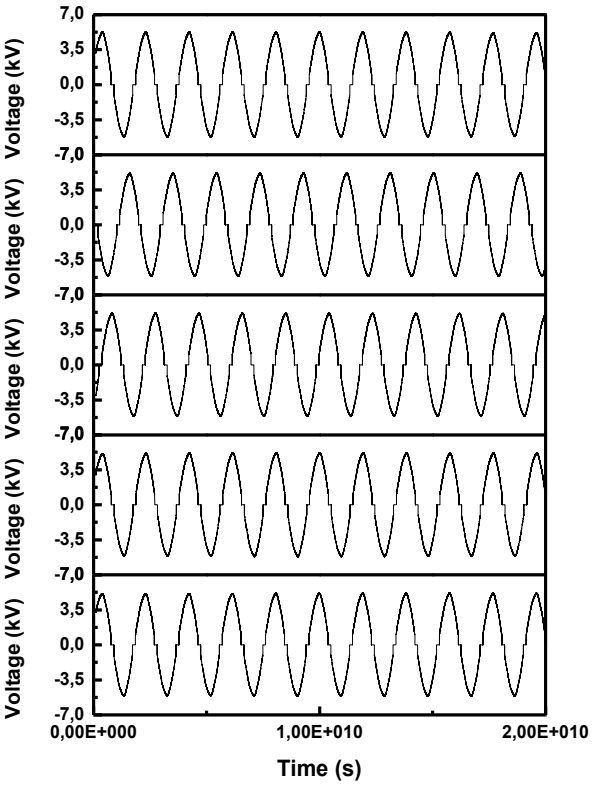

He 1,800 slm + Py 200 sccm – 9 kV – 5 cm